Exemplar für

Inaugural - Dissertation

zur

Erlangung der Doktorwürde

der

Naturwissenschaftlich-Mathematischen

Gesamtfakultät

der Ruprecht - Karls - Universität

Heidelberg

vorgelegt von

Dipl.-Phys. Johann-Philipp von Hase

aus München

Tag der mündlichen Prüfung: 18. Dezember 2002

Digitale Bildanalyse der radialen Verteilungen von spezifischen Subregionen im Zellkern

Gutachter: Prof. Dr. Dr. Christoph Cremer

Prof. Dr. Josef Bille

Meinen lieben Eltern

Zusammenfassung

In der vorliegenden Arbeit wurde die Struktur von Zellkernen während der Interphase mit konfokaler Laser-Scanning-Mikroskopie und Software zur Kartierung des Kerns in konzentrischen Schalen untersucht. Besonderes Augenmerk wurde hierbei auf die Lage der Chromosomen Nr. 18 und Nr. 19 gerichtet, welche in etwa die gleiche genomische Größe, aber eine unterschiedliche Gendichte und einen unterschiedlichen Replikationszeitpunkt aufweisen. Es zeigte sich, dass das früher replizierende und gendichtere Chromosom Nr. 19 eher im Inneren des Kerns zu finden ist. Chromosom Nr. 18 hat in Fibroblasten eine innere Position und in Lymphozyten eine Randposition. (hierbei ist zu beachten, dass Lymphozyten kugelförmig sind und in 3D ausgewertet werden können, während bei den flachen Fibroblasten nur Raum für eine 2D Auswertung existiert).

In Lymphozyten von 7 verschiedenen Primatenarten wurden diese Befunde bestätigt. Somit blieb die radiale Lage dieser Chromosomen über 30 Millionen Jahren Evolution erhalten.

In Karzinomzellen traten meistens chromosomale Umbauten mit Abweichungen in der Verteilung von Chromosom Nr. 18 und Nr. 19 gegenüber gesunden Zellen korreliert auf.

Zudem wurden Modelle von kugelförmigen menschlichen Zellkernen im PC erzeugt, und die Wirkung der eingesetzten Wahrscheinlichkeitsfunktionen für die Chromosomenpositionierung gemessen. Das Modell mit den realistischsten Verteilungen kann für weitergehende Berechnungen wie Translokationsraten nach Doppelstrangbrüchen verwendet werden.

Es wurden auch die Verteilungen von Centromeren untersucht. Während in der G0 Phase alle Centromere zu den betrachteten 8 Chromosomen am Kernrand lagen, lagen sie in den anderen Interphasen zum Teil im Kerninneren, woraus auf eine Bewegung der Centromere während der Interphase des Teilungszyklus geschlossen wird.

Schließlich wurde die räumliche Korrelation von RNA und DNA im Zellkern untersucht.

Abstract

This thesis deals with analysing the structure of nuclei in the interphase using laser scanning microscopy and software for mapping the nucleus in concentrical shells. The focus of attention is the position of chromosomes number 18 and 19, having the same size, but differing in gene density and replicating time. Chromosome no. 19 replicating earlier and being more gene-dense was situated in the interior of the nucleus, while chromosome no. 18 was positioned in fibroblasts at the interior and in lymphocytes at the nuclear rim. The spherical lymphocytes could be analysed in three-dimensional, the flat fibroblasts in two-dimensional models for lack of space.

The analysis of lymphocytes of different species such as 7 primates confirmed these findings. Thus this has been remaining the same during 30 million years of evolution.

The analysis of 8 carcinoma types showed in most cases a positive correlation between chromosomal involvement in aberrations and in an untypical radial distribution in chromosomes no. 18 and 19.

Furthermore spherical human nuclei were generated by a computer. The validity and suitability of the model depended on how realistic the chromosome distributions were.

Furthermore spherical human nuclei were generated by a computer and the resulting chromosome distributions measured to test the validity of the assumed distribution probability function. Reliable translocation predictions can be done by realistic distributions of chromosomes.

Moreover the distribution of centromeres in the cell nuclei was studied. While in phase G0 all centromeres of the 8 studied chromosomes were positioned at the nuclear rim, in the other interphase cell stages the position was partly in the interior. Hence the centromeres moved during the interphase.

Finally the occurrence of RNA and DNA was studied.

I. Einleitung

I.1. Thema der Arbeit

Im Vergleich zu den Kenntnissen der Molekularbiologie ist, was die größeren Strukturen in Zellkernen betrifft, noch wenig bekannt. Erst ab dem Jahre 1985 ist die Existenz von Chromosomenterritorien im Interphasenzellkern von Säugerzellen gesichert, als nämlich die Territorien mit Fluoreszens in Situ Hybridisierung (FISH) sichtbar gemacht werden konnten [Schardin 1985]. Bis zum Jahre 1998 gab es eine Reihe widersprüchlicher, qualitativer Befunde in 2D über die Chromosomenanordnung und die Anordnung subchromosomaler Bereiche. Ein Überblick über den Stand der Forschung bis 2001 befindet sich in [Cremer 2001a] und im Kapitel II.1 vorliegender Arbeit. Die in [v.Hase 1999, Croft 1999] geäußerte Vermutung, die Position der Chromosomen hingen von deren Aktivität ab, wurde in einer Arbeit aus dem Jahre 2001 bestätigt [Boyle 2001]. Darin wurde nämlich gezeigt, dass die Position des Chromosoms von der Gendichte abhinge. Dies bestätigt nun noch einmal vorliegende Arbeit, wobei Gegenstand dieser Arbeit die Interphasenzellkerne sind.

Besonders für den Interphasenzellkern ist es noch umstritten, wie er aufgebaut ist und funktionieren könnte. Das ICD- Modell sagt abwechselnde Bereiche mit Chromosomenterritorien mit aktiven Bereichen an deren Oberfläche und Zwischenräume, in denen sich Proteine befänden, die für die Genexpression wichtig sind, voraus. Dazu verweise ich auf die beiden Übersichtsartikel [Cremer 2000 und Cremer 2001b] oder auf das Kapitel II.1 dieser Arbeit. Andere Wissenschaftler wie T.A. Knoch glauben dagegen, dass in der Interphase die Chromosomenterritorien so weit dekondensiert sind, dass das Chromatin überall allein schon durch Diffusion erreichbar ist. (Der Zellkern als Reagenzglas, s. [Knoch 2002]).

Ganz am Anfang ist man noch bei der Erforschung der Formparameter der Chromosomen. Für das aktive und inaktive X ist bereits Literatur vorhanden,s. [Rinke 1995],[Edelmann 1996],[Eils 1996]. Die beiden homologen Geschlechts-chromosomen unterscheiden sich dabei sehr. Auch chromosomale Substrukturen sind noch weitgehend unerforscht. Zu diesen beiden Gebieten möchte vorliegende Arbeit ebenfalls neue Erkenntnisse liefern.

I.2. Biologische Einleitung

I.2.1. Die Zelle als Grundeinheit des Lebens

Aus alltäglicher Beobachtung von Lebewesen wird der Begriff Leben definiert als ein Organismus der reizbar ist, sich aktiv bewegt, Stoffwechsel betreibt, wächst und sich fortpflanzt [Czihak, Biologie, 1981,S.1]

Auf der molekularen Ebene betrachtet sind Lebewesen Naturkörper, die Nucleinsäuren und Proteine besitzen und imstande sind, solche Moleküle selbst zu synthetisieren. [Czihak, Biologie, 1981,S.1]

Kleinste Einheit des Lebens ist die Zelle. Zellen mit membranumgrenzten Organellen und insbesondere mit Zellkernen heißen eukariontisch und solche ohne Organellen Prokaryonten. Vielzeller bestehen ausschließlich aus spezialisierten Eukarionten. In der vorliegenden Arbeit wurden eukariontische Zellen von Vielzellern untersucht. In Wirbeltieren kommen hunderte verschiedener Zelltypen vor, gleichwohl ist eine Einteilung in 4 übergeordnete Typen möglich: Drüsenzellen, Neuronenzellen, Blutzellen und Gewebezellen. Untersucht wurden in vorliegender Arbeit die Zellkerne, die größten Organellen der Eukariontenzelle. Sie sind außer Mitochondrien alleiniger Ort, in dem die DNA liegt. Im DNA verschlüsselt, in einem Code aus vier "Buchstaben", liegt der Bauplan des Organismus. In Mitochondrien liegt die DNA vor, die den Bau der Mitochondrien selbst betrifft. Man glaubt, dass Mitochondrien, welche die Zelle energetisch d.h. mit ATP (Adesintriphosphat) versorgen, wie alle Organellen ursprünglich eigene Prokaryonten waren, die dann in einem Eukarionten integriert und vererbt wurden. Prokaryonten werden weiter in Bakterien und Archaebakterien unterteilt. Letztere leben anaerob. Eukarionten werden in tierische und in pflanzliche Zellen unterteilt. Letztere können unter Abgabe von Sauerstoff aus Sonnenlicht direkt ATP erzeugen (Photosynthese).

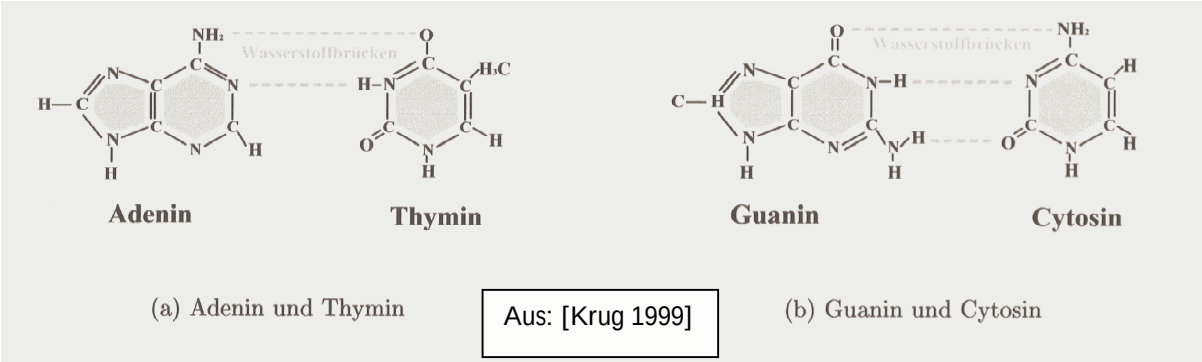

Aus: [Krug 1999]

Abb. I.1: 4 "Buchstaben", Grundbausteine der DNA sind möglich: A-T, T-A, G-C, oder C-G

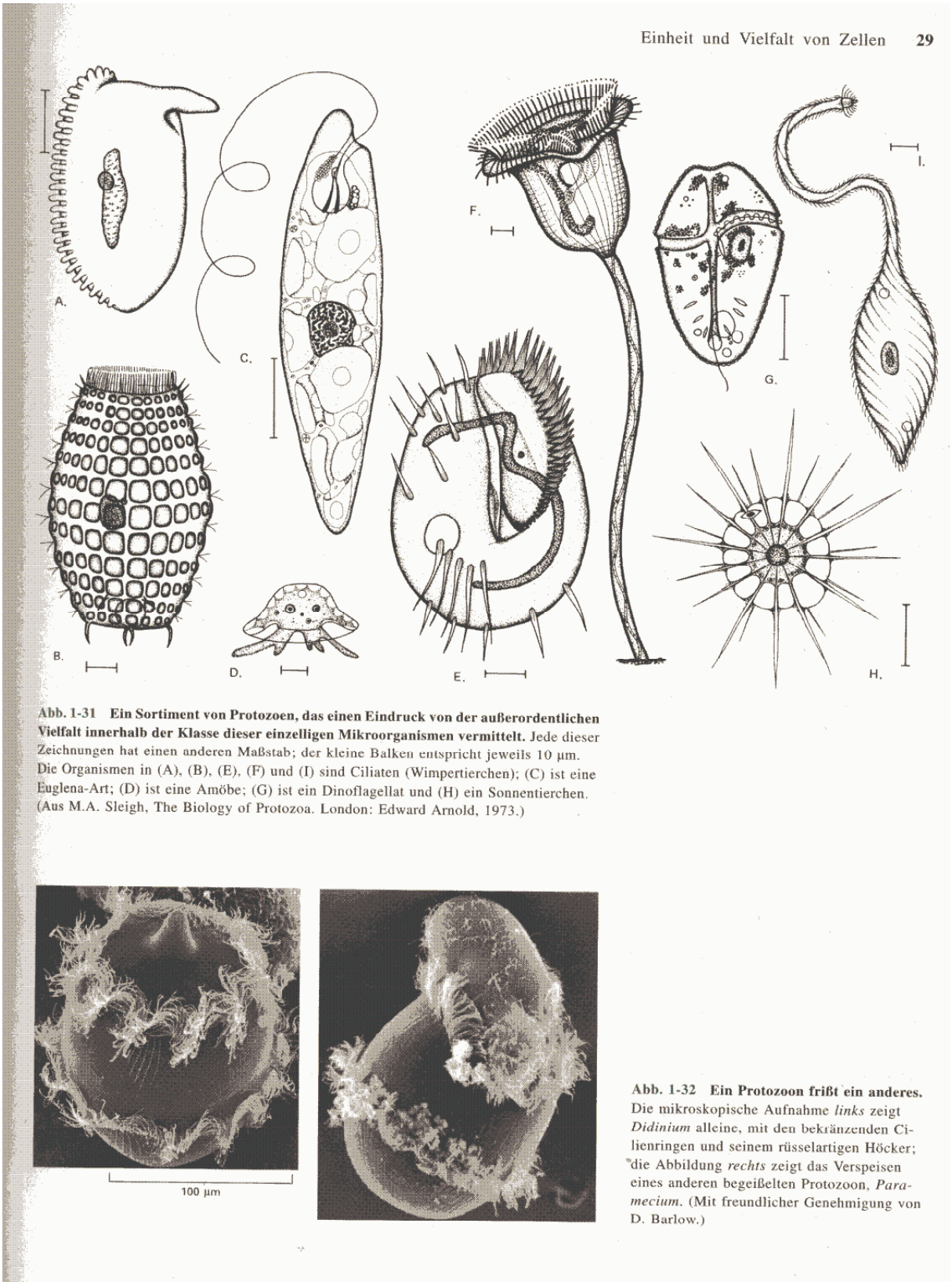

Abb. 1-31 Ein Sortiment von Protozoen, das einen Eindruck von der außerordentlichen Vielfalt innerhalb der Klasse dieser einzelligen Mikroorganismen vermittelt. Jede dieser Zeichnungen hat einen anderen Maßstab; der kleine Balken entspricht jeweils 10 µm. Die Organismen in (A), (B), (E), (F) und (I) sind Ciliaten (Wimpertierchen); (C) ist eine Euglena-Art; (D) ist eine Amöbe; (G) ist ein Dinoflagellat und (H) ein Sonnentierchen. (Aus M.A. Sleigh, The Biology of Protozoa. London: Edward Arnold, 1973.)

Abb. 1-32 Ein Protozoon frißt ein anderes. Die mikroskopische Aufnahme *links* zeigt *Didinium* alleine, mit den bekränzenden Cilienringen und seinem rüsselartigen Höcker; die Abbildung *rechts* zeigt das Verspeisen eines anderen begeißelten Protozoon, *Paramecium*. (Mit freundlicher Genehmigung von D. Barlow.)

Abb. I.2. aus [Alberts 1999] eine Abbildung über die Vielfalt an Protozoen, welche zu den einzelligen Eukarionten gehören.

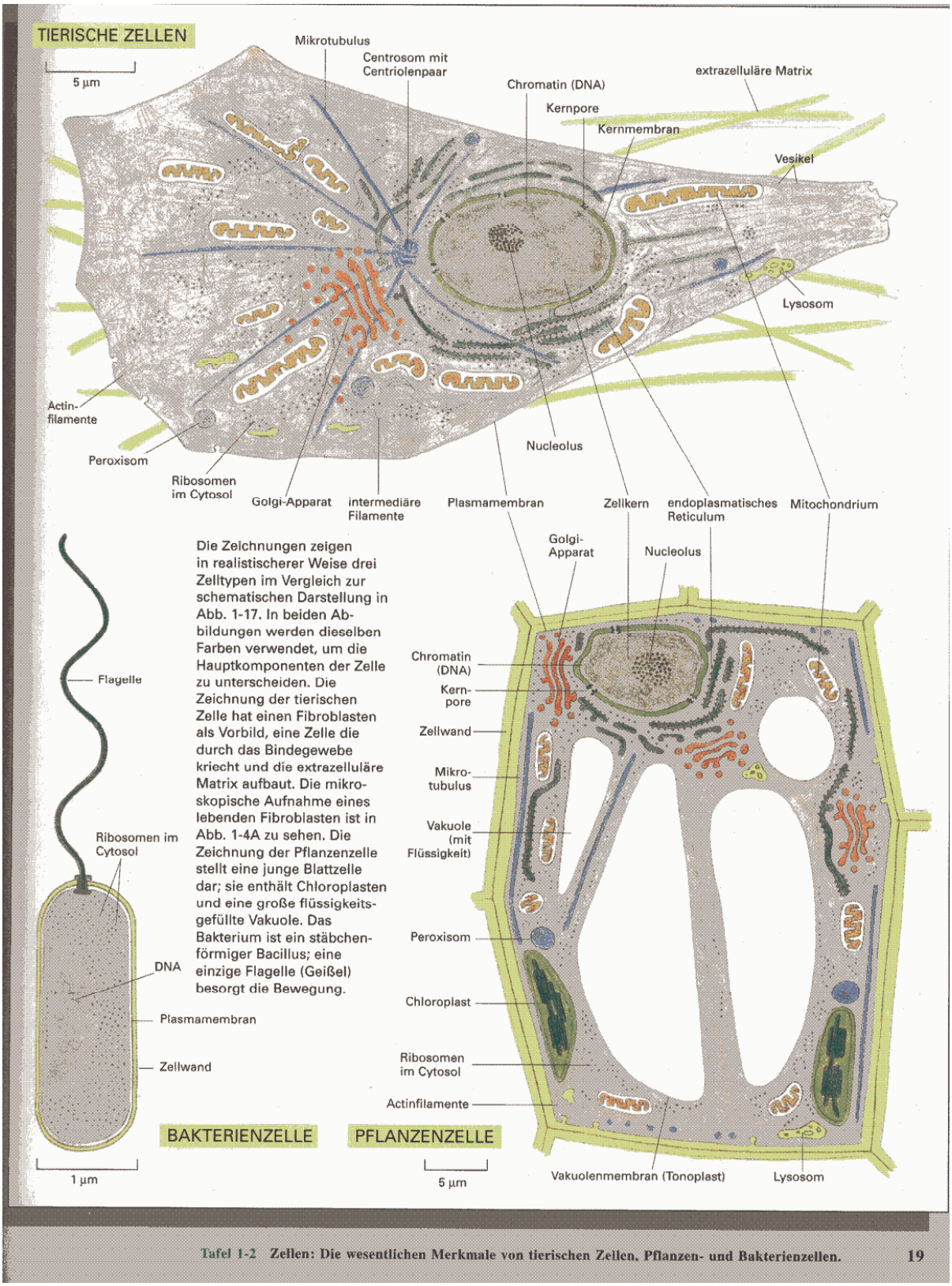

Abb. I.3. Schematische Ansicht einer tierischen, einer Pflanzen- und einer Bakterienzelle. Die ersten beiden sind Eukarionten, letztere ein Prokariont (aus [Alberts 1999])

I.2.2. Der Zellkern, Kompartiment des Chromatins, im Laufe des Zellzyklusses

Der Zellkern durchläuft im Laufe des Zellzyklus verschiedene Stadien. Wenn die Zelle sich praktisch nicht mehr teilt, weil das Wachstum des Organismus nachgelassen hat, befindet sich die Zelle in der G0-Phase. Sehr ähnlich der G0-Phase ist die G1-Phase der Zelle. Die G1 Phase während der die Zelle sich ernährt, wird von der S-Phase (Synthesephase) abgelöst. In der S-Phase wird dann im Zellkern die DNA dupliziert (Replikation). In der G2-Phase bereitet sich der Zellkern auf die Duplikation (Mitose), vor, die noch vor der eigentlichen Zellteilung (Cytose) stattfindet. In der G2-Phase wird die replizierte DNA auf Fehler überprüft. Fehler können während der S-Phase mit der Wahrscheinlichkeit von 10^{-7} pro Basenpaar auftreten, nach der Korrektur nur noch mit der Wahrscheinlichkeit von 10^{-9} pro Basenpaar. Wenn man das menschliche Genom mit $3x10^9$ Basen ansetzt und annimmt, dass nur 3% des Genoms also $9x10^7$ Basenpaare kodierend sind (das menschliche Genom weist etwa 30000-50000 Gene auf), ergibt sich für ca. jede 11te Zelle eine Mutation, die mehr oder weniger relevant sein kann. Bei Bakterien entfällt die Korrektur, höhere Mutationsraten sind daher zu erwarten.

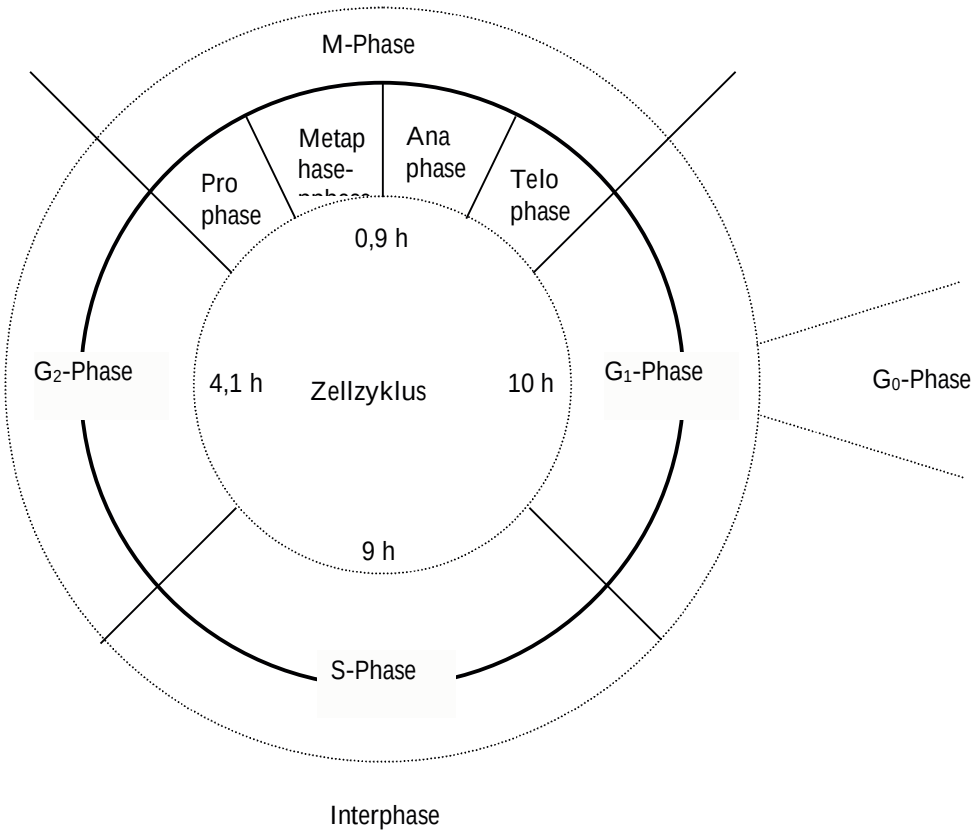

Abb. I.4. Schema eines Zellzyklus. (aus Kreth 1997).

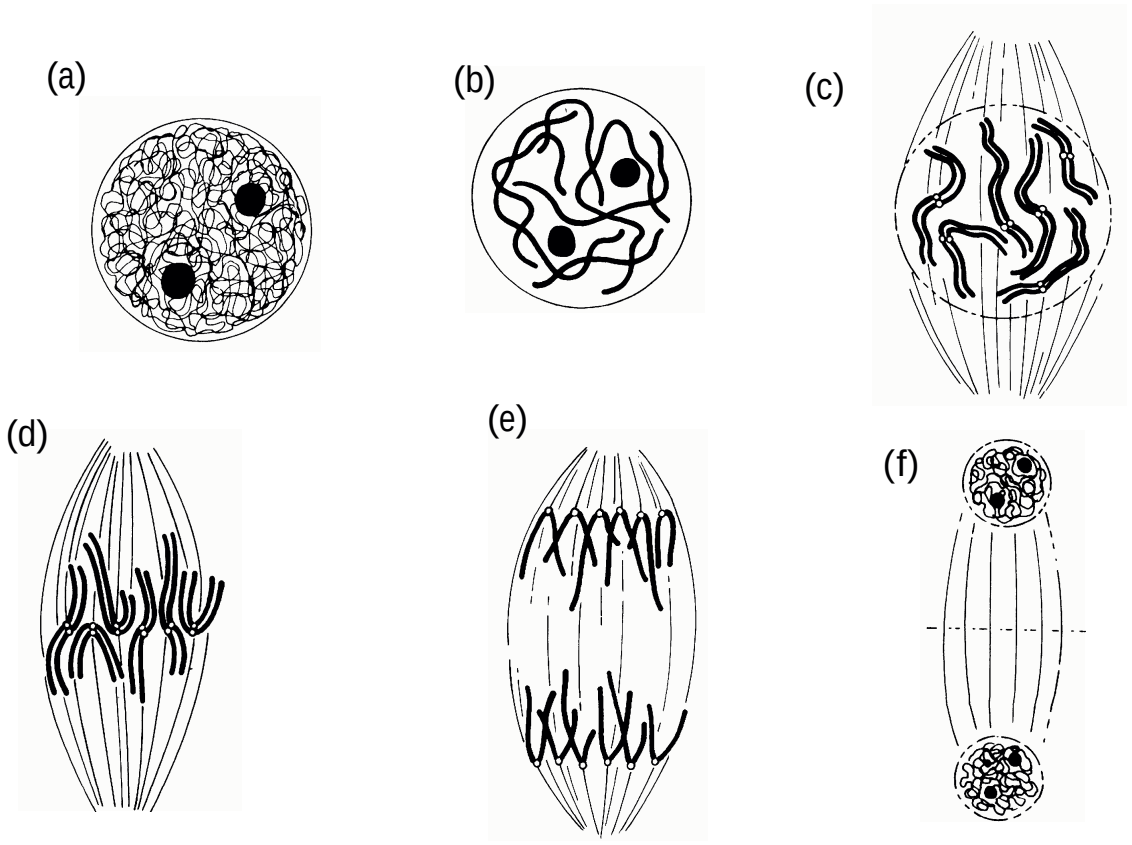

Abb. I.5. Aus Suzuki et al.(1986): Lehrbuchdarstellung der Mitose einer eukariontischen Zelle (b-f): (a): Interphase Kern mit lockerem aber schon repliziertem Chromatin (b) Prophase: das Chromatin beginnt zu dekondensieren. (c) Es bilden sich Spindeln von den Zellmembranen zu den Centromerregionen der Chromosomen. (d):Chromosomen bilden den Mitosering (e): Die beiden haploiden Chromosomensätze werden getrennt. (f): Es bilden sich zwei neue Kernmembranen und die alte löst sich auf.

I.2.3. Aufbau des Chromatins

In der Teilungsphase (M-Phase) liegt das Chromatin in kondensierten X-förmigen Stäbchen vor, und in allen anderen Phasen (G0, G1, S, und G2 bilden die Interphase) in dekondensierter Form. Seit den 80er Jahren des letzten Jahrhunderts weiß man aufgrund der Fluoreszenz in Situ Hybridisierung Methode (FISH), dass die Chromosomen in der Interphase zwar dekondensiert sind, jedoch immer noch in sich nicht überschneidende Territorien liegen. Weitere Einzelheiten siehe [Kreth 2001]

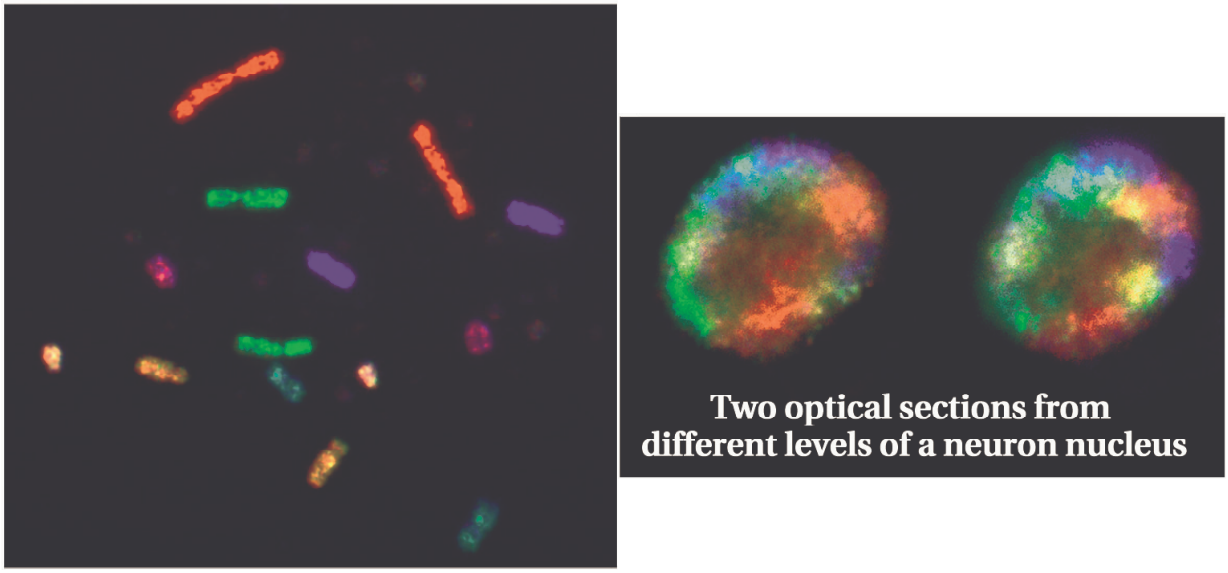

Abb I.6. gezeigt werden links experimentelle Metaphase Chromosomen und rechts Interphase Chromosomenterritorien in neuronalen Zellen aus einem 3D-Schnitt (Bilder von Felix Habermann)

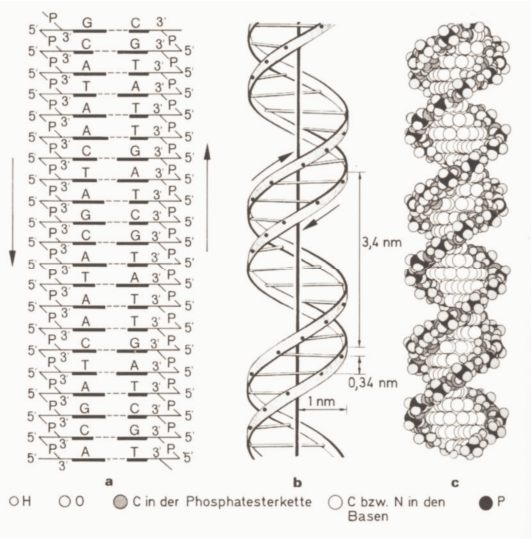

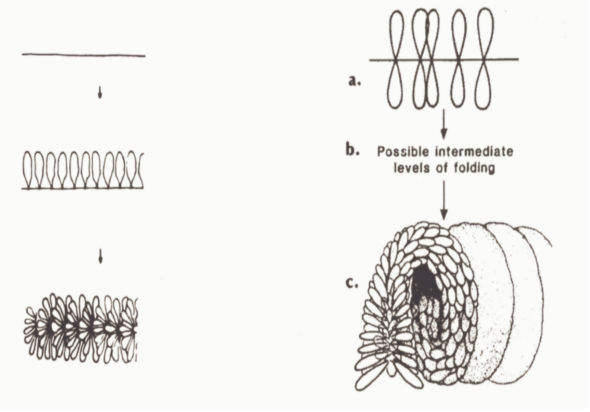

Abb I.7. links ist die DNA-Doppelhelix zu sehen,

rechts ist eine schematische Darstellung des *Radial loop/Scaffold* Modells zu sehen [Marsden & Laemmli 1979, Rattner & Lin 1985]. Danach wird die 30nm Chromatinfaser mithilfe nicht-histonischer Proteine zu 30-120 kbp großen Schleifen gebunden (links), welche entlang der Chromatidachse am Scaffold befestigt sind. In der Metaphaseanordnung wird zusätzlich eine helikale Struktur des Scaffolds angenommen. Entsprechend dem heute favorisierten Multi Loop Subcompartment (MLS) Model [Münkel & Langowski 1998] wird angenommen, daß etwa zehn 120 kbp große Schleifen (Kontourlänge ~1230 nm) zu einer Rosette verbunden sind. Diese Rosetten werden über einen Chromatinlinker der gleichen Größe miteinander verbunden. Während in der Metaphase dieser Linker eine weitere Schleife ausbildet, ist er in der Interphase geöffnet, woraus sich dann die gelockerte Struktur ergibt.

I.2.4. Das ICD Modell des Interphasenzellkernes (s. T.Cremer & C.Cremer 2001)

Das ICD Modell beschreibt eine funktionelle Trennung von Chromosomenterritorien (CT) und Interchromatindomänen (ICD), die zwischen den Chromosomen liegen oder in sie hineinragen. Im ICD Raum befinden sich nach der Modellvorstellung die Transkriptionsfaktoren. Daher besagt das Modell, dass aktives Chromatin an den Chromosomenrändern liegt, so dass es ohne geometrische Schwierigkeiten transkribiert werden kann, während Chromatin im Inneren des Territoriums inaktiv sein müsste, da es schlechter von den Transkriptionsfaktoren erreichbar sei. Die entstehende mRNA würde entlang der ICD Kanäle an die Zellkernmembran und weiter ins Cytosol gelangen.

Untersuchungen zur Kollokation von mRNA und DNA belegen aber lediglich eine Antikorrelation von -0,1 (s. Kap. Ergebnisse/RNA-DNA - Korrelation). Das würde aber bedeuten, dass die mRNA überall im Kern entstehen könne und damit der ICD-Raum ohne eine besondere Funktion wäre. Es müssten dann andere Faktoren die Aktivität der Gene kontrollieren. Man weiß jedoch, dass die Regionen am Zellkernrand oder am Nucleolusrand besonders inaktiv sind, dagegen sind solche im übrigen Zellkerninneren aktiv. Allerdings ist die optische Auflösung der hier zugrundegelegten konfokalen Laserscanningmikroskopie zu berücksichtigen; diese ist mit ca. 250nm in lateraler und 600nm in axialer Richtung (optische Achse) mit ca. 300 nm chromatischen Shifts nicht ausreichend, diese wichtige Frage abschließend zu beantworten.

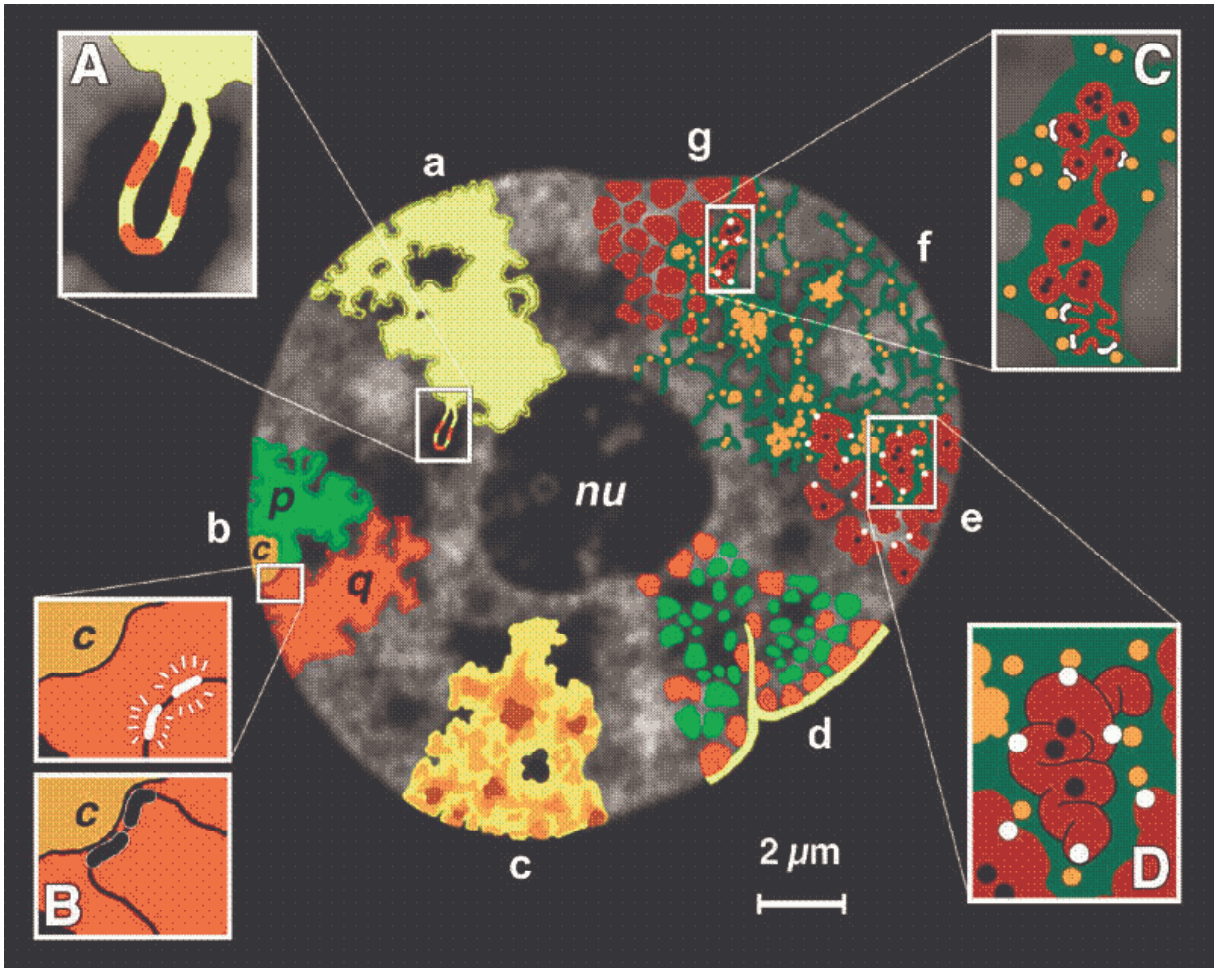

Abb.I.8: Modell einer funktionellen Zellkernarchitektur (Aus T.Cremer & C.Cremer, 2001) (a): Zur Aktivierung können Gene in den ICD-Raum ragen. (b): Gene (weiß) in einiger Entfernung der inaktiven Zentromerregion sind aktiv, in deren Nähe (schwarz) aber inaktiv. (c) Chromatin kann in unterschiedlicher Dichte vorliegen. (d): In rot dargestellt an der Kern- und der Nucleolushülle spät replizierende und genarme 1Mbp-Chromatin Domänen, dazwischen in grün genreiche Zonen. (e): feine Chromatinarme erzeugen eine große Oberfläche, an der Gene aktiviert oder inaktiviert sind je nach Abstand zum ICD-Raum. (f): der Interchromatinraum (grün) enthält Proteine zur Transkription, Splicing, DNA-Replikation und DNA-Reparatur. (g): Der ICD-Raum erstreckt sich sogar bis in 100 kbp Unterdomänen.

I.2.5. Bedeutung der Bestimmung der Kernstruktur

Durch die Untersuchung der Position und Form von Chromosomenterritorien konnte bestätigt werden, dass genreiche Chromosomen vorwiegend zentral liegen, während genarme Chromosomen eher am Zellkernrand zu finden sind [Boyle et al. 2001]. Dies wird im Verlauf der vorliegenden Arbeit für Lymphozyten bestätigt werden. Es wird im Verlauf dieser Arbeit gezeigt werden, dass diese Aussage sogar für Unterregionen der Chromosomenterritorien gilt. An Fibroblasten gab es eine etwas

abweichende Verteilung. Es zeichnet sich ab, dass aufgrund der Chromatinposition die Aktivität dieser Bereiche bestimmt werden kann.

I.3. Bewertung der verwendeten Methoden

I.3.1. FISH (Einführung s. [v. Hase 1999])

Bei der Fixierung der Zellen kann für Fibroblasten Formaldehyd verwendet werden. Dieses belässt die Position des Chromatin und sogar dessen Form, da es die Zelle nie austrocknen lässt [Zirbel et al. 1993]. Bei Lymphozyten musste Methanoleisessig verwendet werden: Dadurch schrumpfte der Kern aufgrund von Austrocknung, da die Umgebung des Kerns sehr salzig war (hypotonischer Schock) Es schrumpften auch die Chromosomen um den gleichen Faktor. Die relativen Positionen blieben dagegen erhalten [Popp et al. 1990].

I.3.2. Konfokale Mikroskopie

Beste Parameter bei der Mikroskopie waren die folgenden: Bildgröße 256x256xTiefe, das ist kleiner als die möglichen 512 x 512 Pixel. Es ging keine wesentliche Information verloren, und die Rechner (600 bis 800 MHz Taktfrequenz) konnten mit dieser Bildgröße um eine Größenordnung schneller umgehen. Als Voxelgröße war 66-100 nm ein guter Kompromiss zwischen theoretischer Auflösung und günstigem Signal zu Rausch Verhältnis. Anzustreben war zudem eine möglichst einheitliche Namengebung der Ausgabefiles.

I.3.3. 3D-Rekonstruktion von konfokalen Bildern

Die optische Auflösung am konfokalen Laser Scanning Mikroskop beträgt ca. 250x250x700 nm [J.v. Hase 1999]. Macht man eine 3D-Rekonstruktion, erschwert diese unterschiedliche Auflösung die richtige Vorstellung vom Objekt. Günstiger ist es nach Meinung des Autors manchmal, die bessere laterale Auflösung von 250nm auf den axialen Wert von 700 nm zu beschränken, um ein isotropes Bild zu erhalten. Diese Einschränkung der Bildauflösung wurde dabei durch vorhandene Tools der Bildverarbeitung erreicht, nicht aber durch Manipulation des Mikroskops.

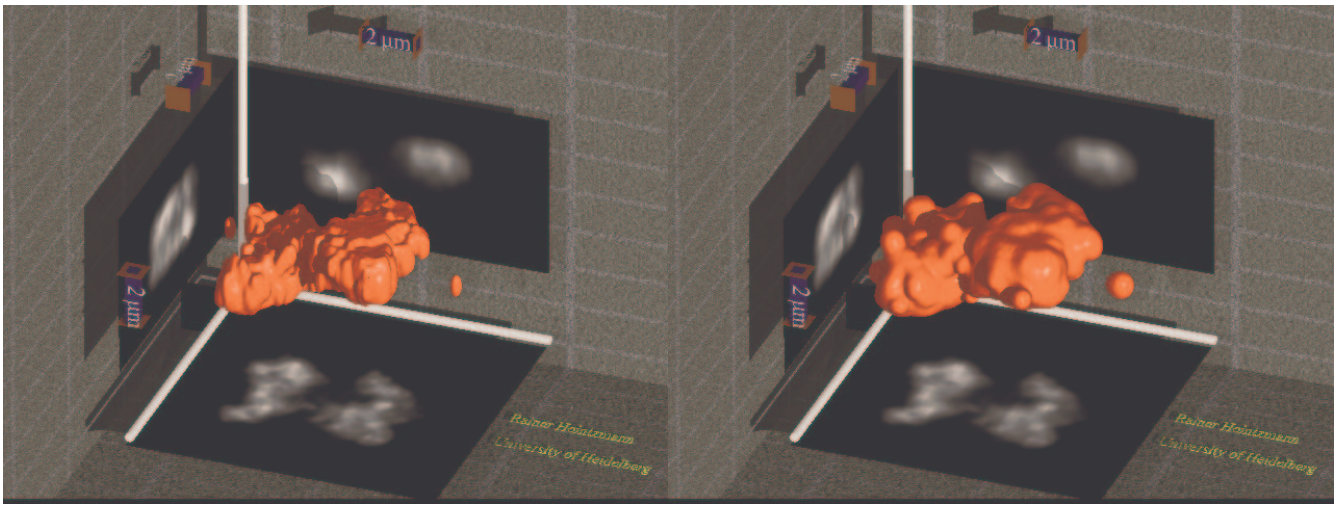

Abb. I.9: links ist Chr #18 aus einer Fibroblaste bei voller Auflösung, rechts bei verminderter dafür aber isotroper Auflösung.

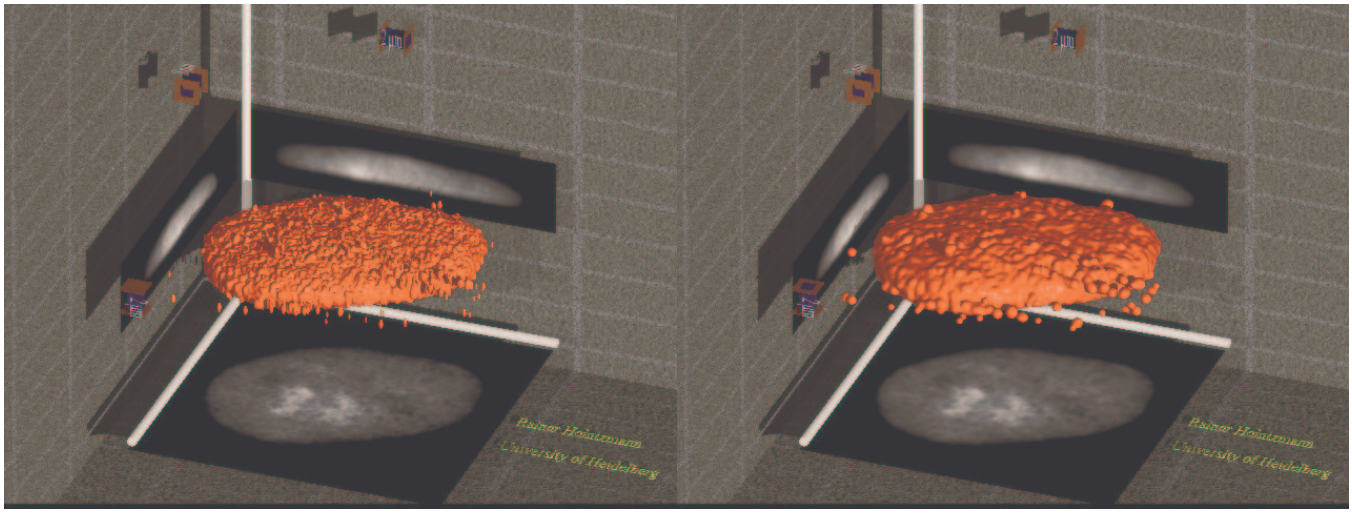

Abb. I.10: links ist ein Fibroblastenkern bei voller Auflösung, rechts bei verminderter, dafür aber isotroper Auflösung

I.4. Bildbearbeitungsmethoden

I.4.1. Automatische Schwellwertmethode

Um das Bild in Vordergrund und vernachlässigbarem Hintergrund aufzutrennen, wurde eine automatische Schwellwertmethode entwickelt, die mit dem Helligkeitshistogramm arbeitet. Bisherige Methoden nutzten es aus, wenn im Histogramm zwei oder mehr relative Maxima auftraten. Man konnte das niedrigere Maximum dem Hintergrund und das höhere dem interessierenden Objekt zuordnen. Wenn aber das Objekt oder die Objektgruppe klein gegenüber dem Gesamtbild waren, gab es keine zwei Maxima und das Verfahren funktionierte nicht.

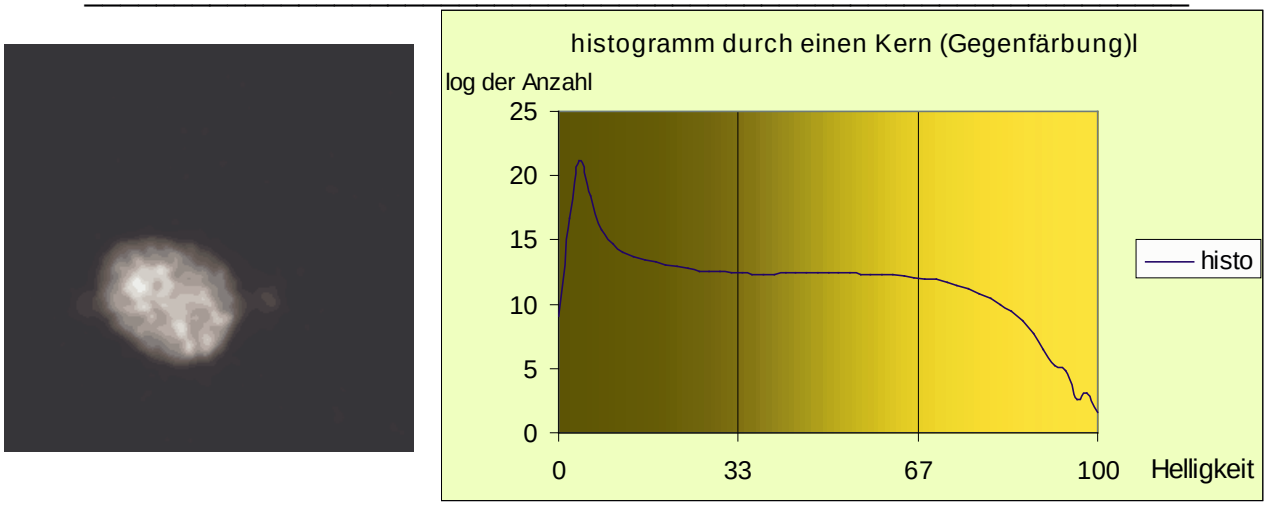

Abb. I.11. links im Bild ist ein Lymphozytenkern, rechts sein Histogramm, welches keine zwei relative Maxima aufweist. Ein guter Schwellwert läge bei 33, wie in der Abbildung weiter unten ermittelt wird.

Aufgrund des Bildes des Zellkerns weiß man aber, dass es einen Vordergrund und einen Hintergrund gibt, auch wenn das nicht aus dem Histogramm hervorgeht. Im Ergebnis wird der Schwellwert das Histogramm doch in eine obere und eine untere Hälfte teilen.

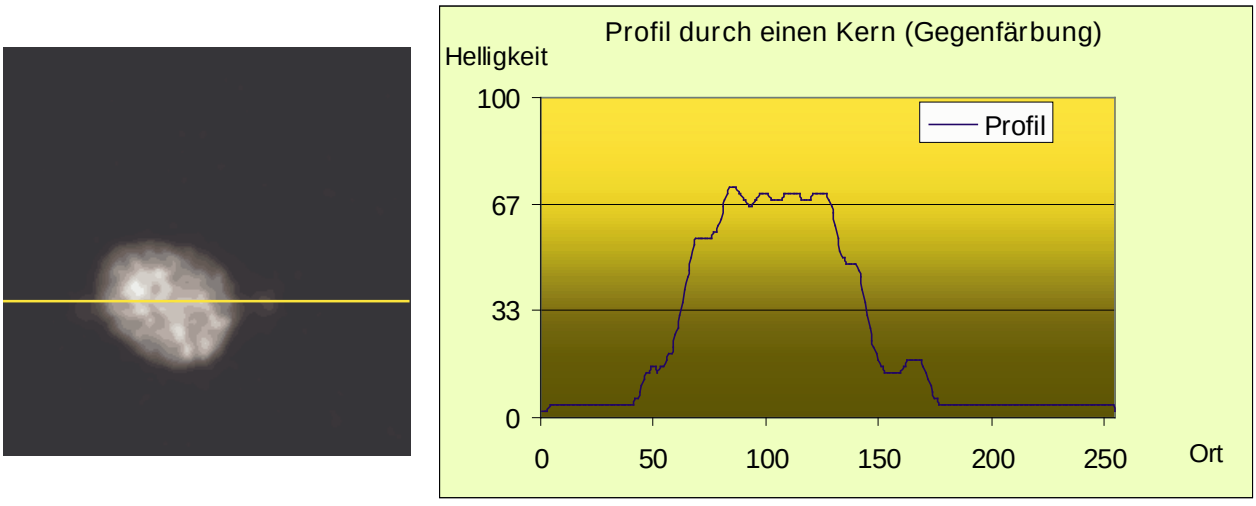

Abb.I.12.: Ein Helligkeitsprofil durch den gleichen Kern wie in Abb.I.11. Das Helligkeitsprofil deutet auf die Richtigkeit des Schwellwertes in Höhe von 33.

Man geht also so vor: als ersten Schätzwert T ("Threshold") nimmt man die Durchschnittshelligkeit aller Voxel. Dieser Wert liegt dann sicher innerhalb des Histogramms. Die Formel dafür lautet:

$$T = 1/N \times \sum_{i=1}^{N} h(i) \qquad (1.1)$$

Dabei ist N die Gesamtzahl der Voxel. Die Summe läuft über alle N Voxel.

Als nächsten Schritt berechnet man den Erwartungswert E1 als Durchschnittshelligkeit aller Voxel, die dunkler als die erste Schwelle T sind. Ebenso wird der Erwartungswert E2 als Durchschnittshelligkeit aller Voxel, die heller als die Schwelle T sind, berechnet. Die Werte E1 und E2 sollen dabei den im Histogramm nicht erkennbaren Erwartungswert für den Hintergrund und den Vordergrund darstellen. Daher ist es geschickt, einen Mittelwert zwischen E1 und E2 zu bilden, um so zu einem verbessertem Schwellwert zu kommen. Aus diesem errechnet sich E1 und E2 neu und es wird ein neuer Schwellwert aus dem neuen E1 und dem neuen E2 berechnet. Das Verfahren wird bis zur Konvergenz von T wiederholt (d.h. bis T sich nicht mehr ändert). Die Konvergenz ist bisher bei allen Kern- oder Territorienbildern eingetreten und kann als experimentell gesichert gelten; meistens werden nur 3 bis 7 Iterationsschritte benötigt.

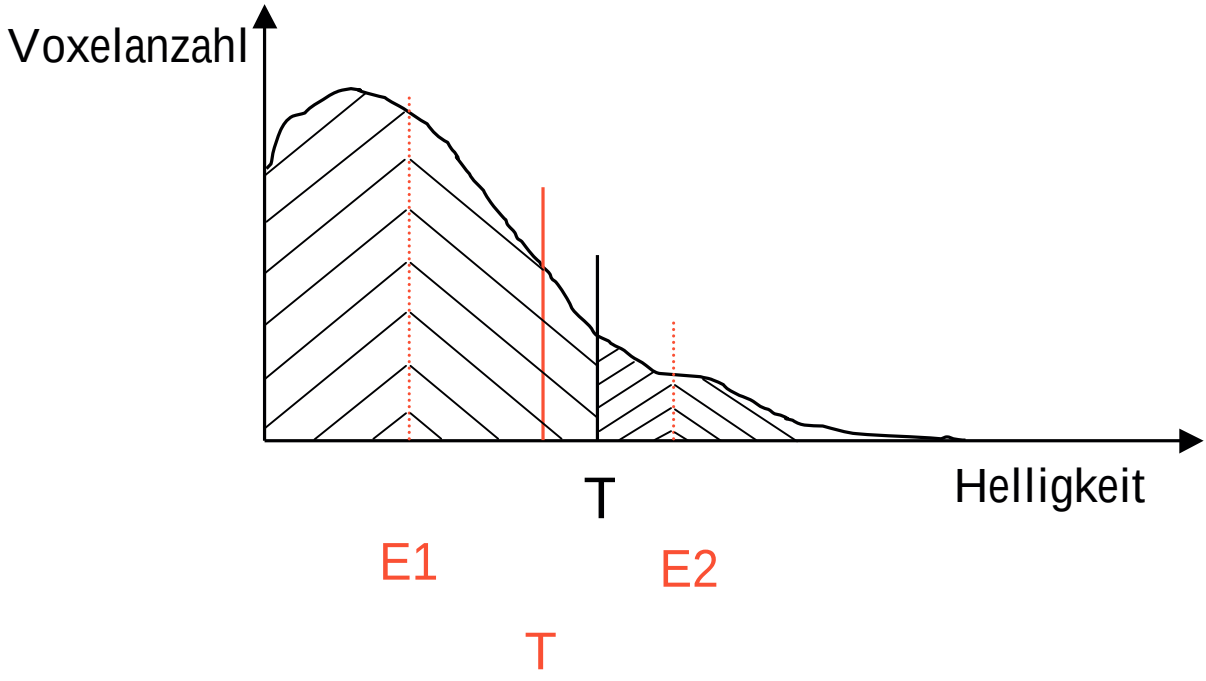

Abb. I.13.: Schema, nach welchem ein idealer Schwellwert gefunden wird, s.Text. Statt der Helligkeit könnte man auch andere Bildeigenschaften wie z.B. den Gradienten als Abszisse wählen. Dann würde ein Schwellwert dazu benutzt, besonders Kantenreiche oder Kantenarme Bereiche des Bildes zu erhalten.

Der Schwellwert kann interaktiv beeinflusst werden, indem die Gewichtung v der beiden Summanden E1 und E2 nach Gutdünken, d.h. interaktiv eingestellt wird:

$$T = v \cdot E1 + (1 - v) \cdot E2$$

Zumeist wird v zwischen 0.3 und 0.7 liegen, je nach Stärke des Hintergrunds oder Kondesnsation des Objekts. Für Bilder einer Serie genügt meist die Festlegung auf einer Gewichtung v für alle Bilder der Serie.

I.4.2. Segmentierung des Zellkerns

Um Objekte innerhalb des Zellkernes als solche zu erfassen, ist es nötig, die Ausdehnung des Zellkernes zu bestimmen. Also musste das Bild des Zellkernes vom Hintergrund hervorgehoben oder "segmentiert" werden. Dazu wurde zuerst anhand des Kanals der Gegenfärbung der Schwerpunkt bezüglich der Helligkeiten im Bild bestimmt. Die Absicht dabei war, einen Punkt um den Kernmittelpunkt zu finden. Das Bild wurde dergestalt geglättet, dass möglichst keine „Löcher“ im Bild waren. Dann wurde jeder Punkt auf Zugehörigkeit zum Kern einfach geprüft: konnte der Punkt mit einer geraden Strecke, die durch Punkte heller als der Schwellwert waren, mit dem Kernmittelpunkt verbunden werden, gehörte er zum Kern und wurde nicht verändert. Falls die Verbindungslinie aber durch Zonen mit Helligkeiten unter dem Schwellwert verlief, gehörte der Punkt nicht zum Zellkern und wurde auf Null gesetzt. Damit konnten elliptische und sogar sternförmige Kerne erkannt werden. Das reichte auch für die Praxis. Nicht ausreichend wäre es dagegen für einen stark sichelförmigen Kern. Den gab es aber zum Glück nicht. Auf Territorien hätte das Verfahren nicht angewandt werden können, da einige durchaus stark sichelförmig ausfallen konnten (z.B. Chr #17 in Lymphozyten)

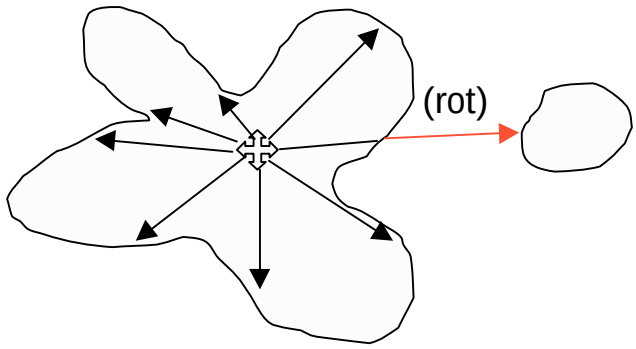

Abb.I.14.: Beispiel eines mathematisch sternförmigen Gebildes. Das Objekt rechts wird als nicht zum Kern gehörend identifiziert: Entlang der roten Linie liegen die Bildpixel unterhalb des Schwellwertes

I.4.3. Kartierung des Zellkernes

Um die Position von Chromosomenterritorien im Zellkern zu bestimmen, wird eine Kernkartierung benötigt. Hierbei wurde eine relative Angabe gefunden, bei der Orte an der Zellkernmembran den Wert 100 erhielten und am Zellkernmittelpunkt den

Wert 0. Der Zellkernmittelpunkt wurde neu berechnet als Schwerpunkt gleich heller Kernpunkte, d. h. ohne Intensitätswichtung der Voxel. Es wurde für alle Aufpunkte des Kernes das Längenverhältnis zwischen der Verbindung des Aufpunktes zum Kernmittelpunkt und der Verbindungsgeraden zwischen Kernmittelpunkt weiter durch den Aufpunkt bis zur Kerngrenze berechnet und mit 100 multipliziert. Daraus ergab sich die relative Radialkoordinate mit Werten zwischen 0 und 100, wie oben gesagt. Punkte mit der gleichen Radialkoordinate bildeten zur Kernhülle konzentrische Ringe in 2D und konzentrischen Schalen in 3D. Wegen der Beschaffenheit der Bilder aus endlich großen Voxel wurde eine Bestimmte Ring- oder Schalendicke erreicht.

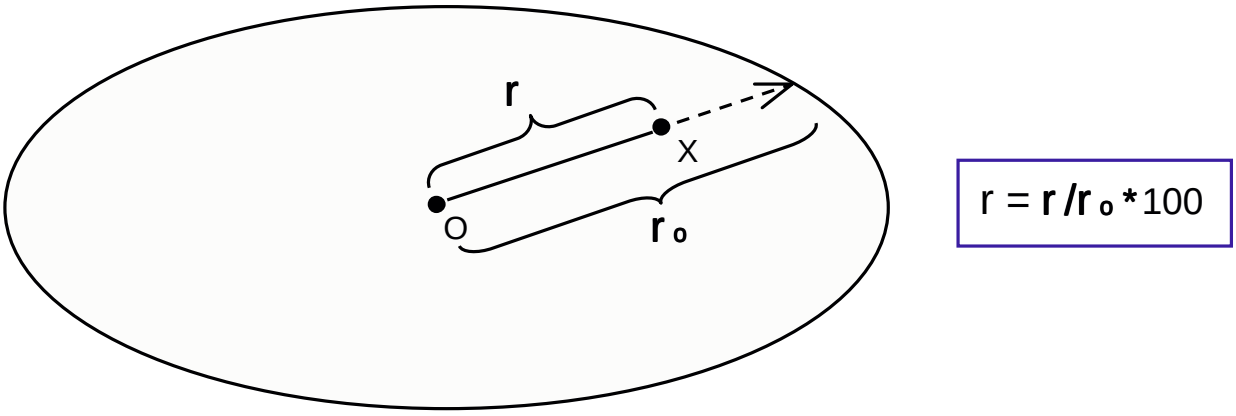

Abb.I.14. Erklärung der Radialkoordinate „r“. r beschreibt die Entfernung eines Punktes vom Kernmittelpunkt und von der Kernhülle. Näheres s. Text.

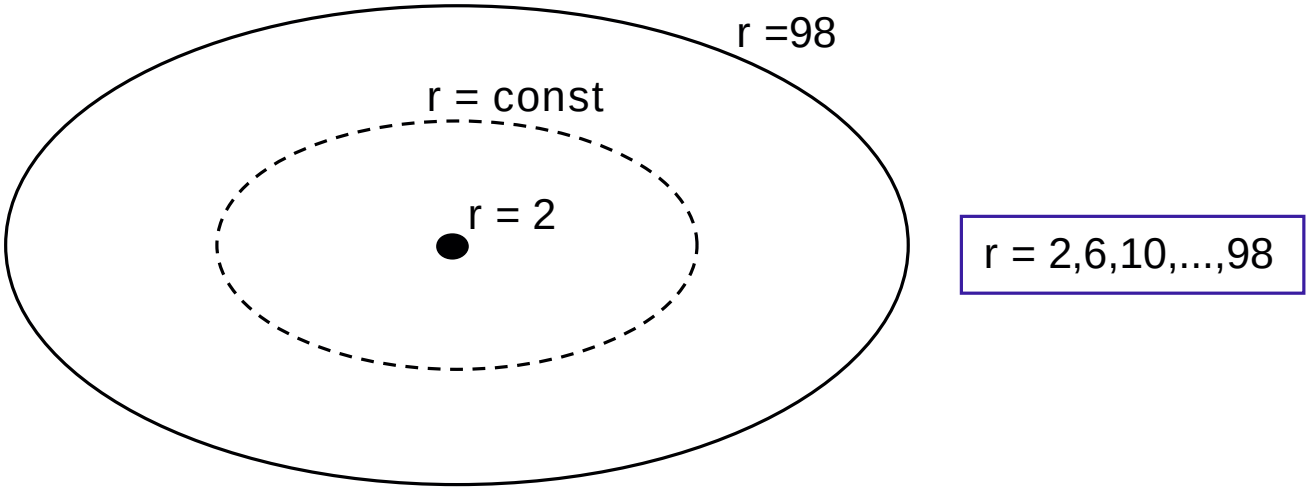

Abb. I. 15. In obiger Abbildung werden Punkte mit gleicher relativer Radialkoordinate gezeigt. Sie liegen auf konzentrischen Linien. Abb. I.16., unten, zeigt in 2D einen Ring, in 3D eine Schale mit diskreter Dicke

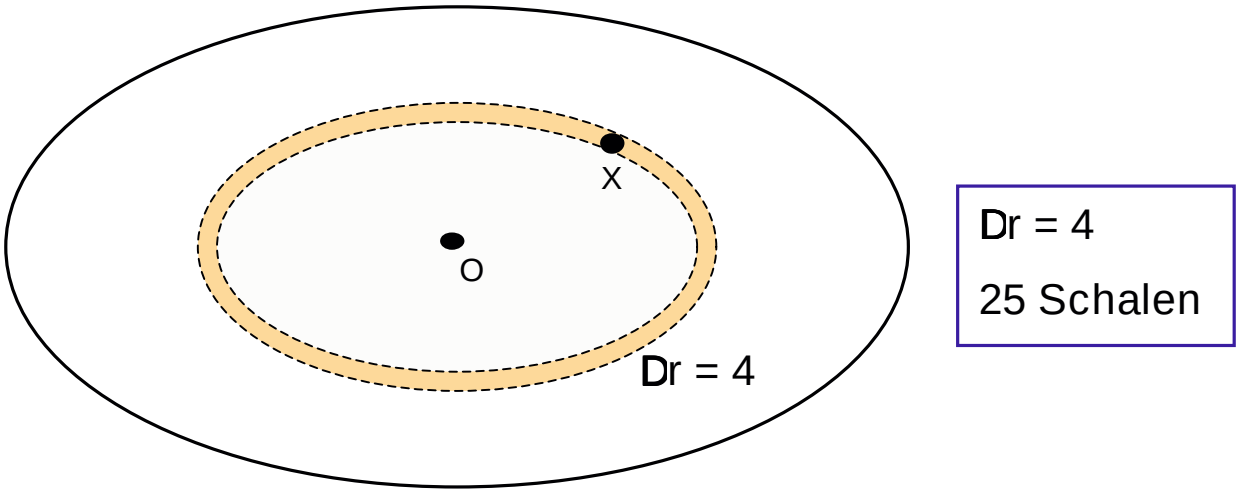

I.4.4. Von der DNA-Verteilung zum Graphen

In den verwendeten Diagrammen war auf der Abszisse die Schalennummer und auf der Ordinate der in der einzelnen Schale vorkommende DNA Gehalt angegeben. Der „DNA Gehalt“ wurde derart normiert, dass der integrierte Flächeninhalt unter dem Graphen 100 ergab. Alternativ wurden noch zwei weitere Normierungen durchgeführt: die eine stellte die DNA-Dichte dar und es wurde die vorkommende DNA Dichte (Gehalt pro Schalengröße) in Einheiten der durchschnittlichen DNA-Dichte im Kern angegeben. Die andere stellte die DNA Häufigkeit dar. Deren Norm war 1, falls mindestens ein DNA- Voxel in der Schale war und Null, falls kein DNA-

Voxel in der Schale vorkam. In der Arbeit werden aber nur "Gehalt" Kurven vorgestellt.

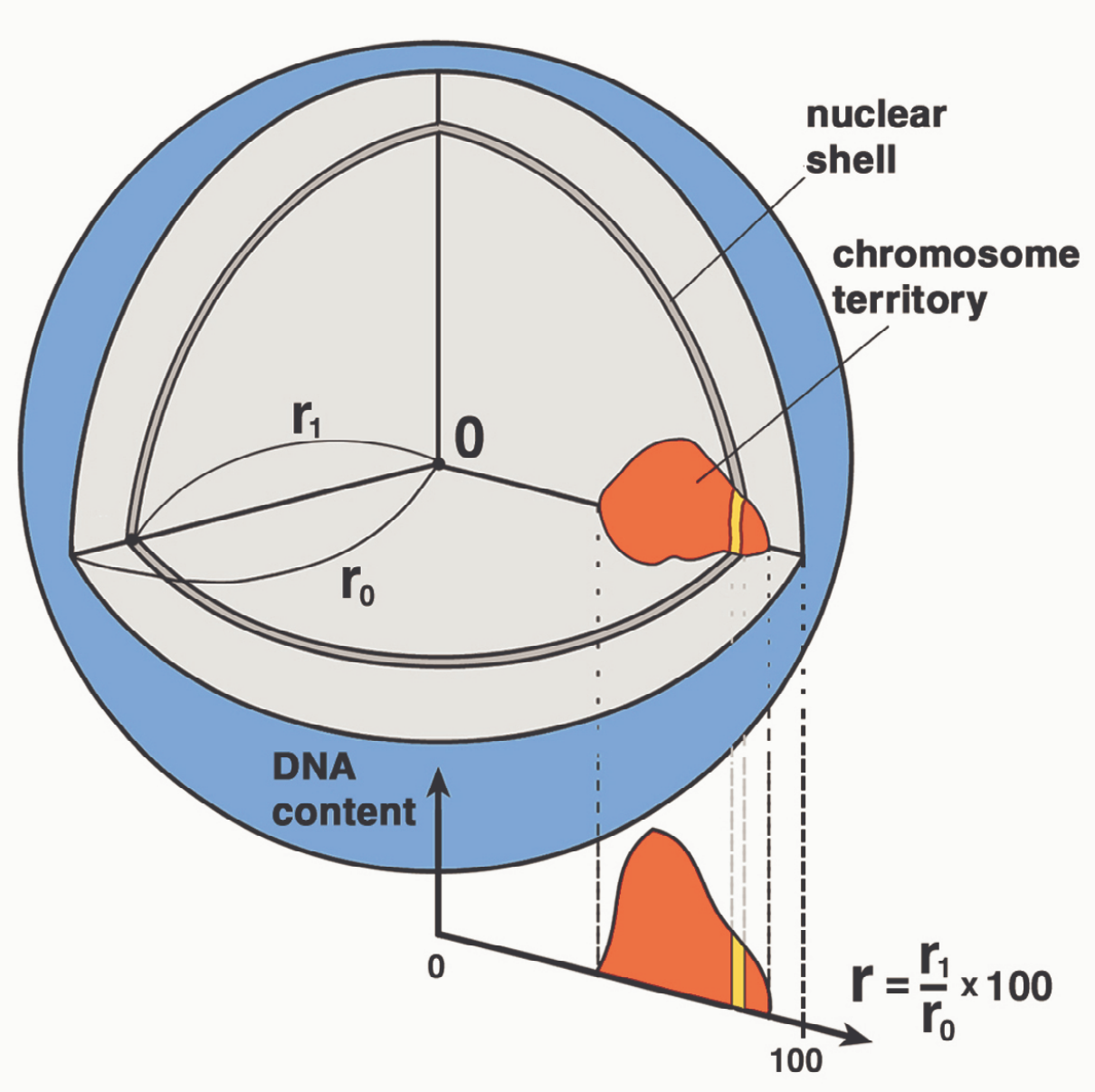

Abb. I.17. Obige Abbildung fasst noch einmal alle Arbeitsschritte von der Kernkartierung (r_1 und r_2) über die Erfassung des DNA-Territoriums in einem Graphen zusammen.

Es bleibt noch anzumerken, dass für alle Kerne einer Serie eine mittlere Kurve errechnet wurde.

I.4.5. 3D, 2D, oder 1D Auswertungen?

Fibroblasten sind eher flache Gebilde. Sie können also in erster Näherung als flache Zylinder aufgefasst werden. Sie haben hauptsächlich eine laterale Ausdehnung. Diese Zellkerne wurden auf eine Ebene projiziert, und nur die laterale Ausdehnung in die Kartierung eingebaut, so dass konzentrische Ringe als äquiradiale Mengen herauskamen. Eine Analyse der Verteilung in Abhängigkeit der Tiefe ergab keine

akzentuierte Verteilung, da die zur Verfügung stehende Höhe nur ca. 1,5 bis 2,5 des Durchmessers des Territoriums betrug.

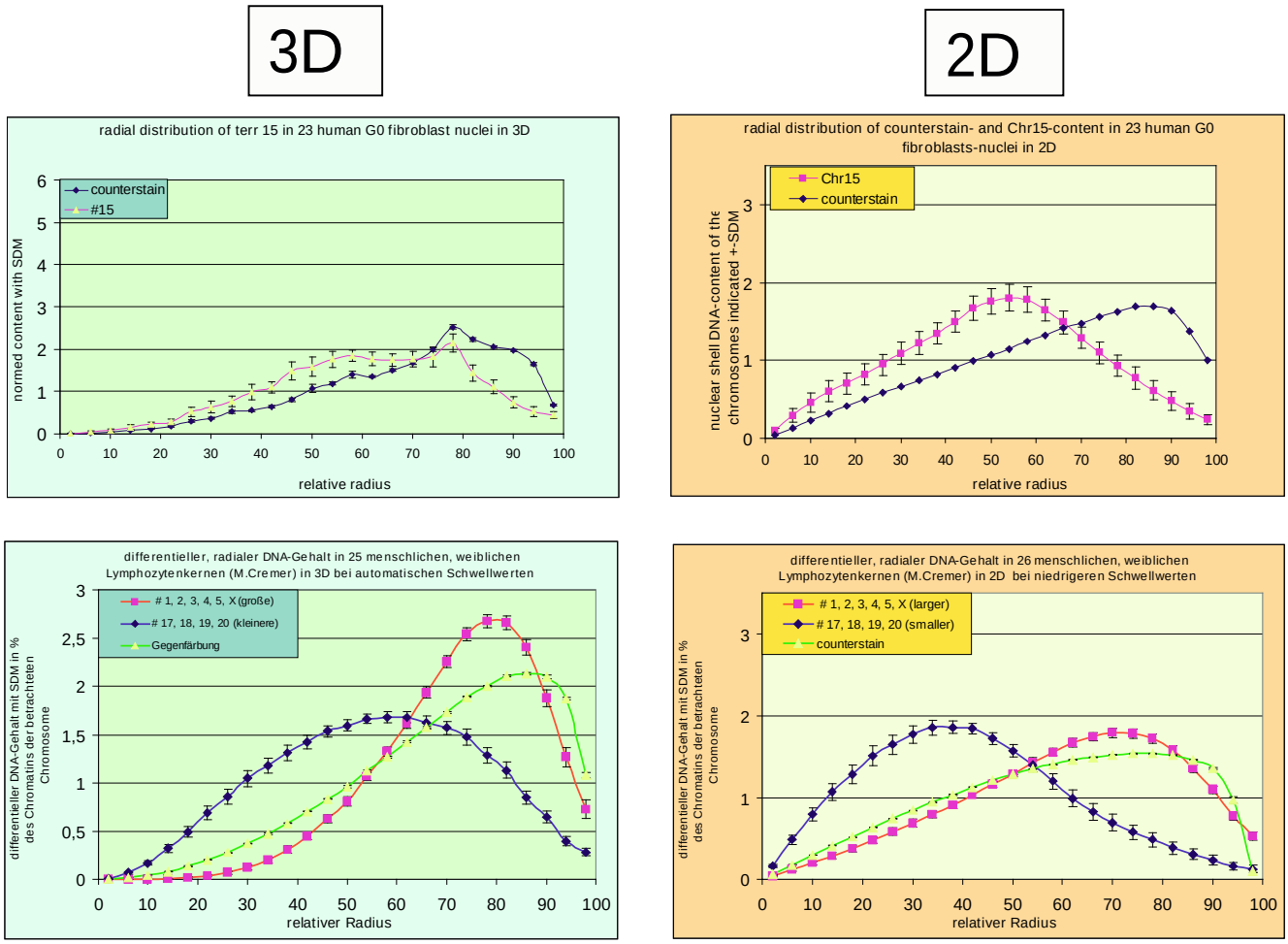

Abb. I.18. Der Vergleich 3D gegen 2D bei den flachen Fibroblasten (in der oberen Reihe) zeigt, dass nur bezüglich 2D eine zentralere radiale Verteilung des Chromosoms #15 existiert. Der Vergleich 3D gegen 2D bei den sphärischen Lymphozyten (in der unteren Reihe) zeigt, dass in der 3D-Darstellung besonders die kernrandnahe Verteilung (Graph in pink) existiert

I.5. Statistischer Vergleich von Kurven

Da kein funktionierender automatischer Kolmogorov-Smirnov Test zur Überprüfung der Übereinstimmung zweier Graphen zur Verfügung stand, wurden hier eigene Überlegungen entwickelt. Die Fehlerbalken an den Graphen in obiger Abbildung sind nur von begrenzter Aussagekraft, da diese Fehlerbalken in die Ordinaten- richtung gehen, wir aber die Kurven hinsichtlich ihrer radialen Richtung, d.h. entlang der Abszisse auf Übereinstimmung oder Verschiedenheit überprüfen wollten. Daraus ergaben sich zwei sich gegenseitig stützende Verfahren:

Als erstes war zu jedem Kern ein radialer Erwartungswert der Verteilung errechnet worden, so wie man in der Physik Schwerpunkte errechnet So erhielt man für jede Serie einen ganzen Satz von Erwartungswerten. Daraus wurde der mittlere Wert und dessen Standardabweichung errechnet. Nun konnten zwei Serien anhand ihres mittleren radialen Erwartungswertes verglichen werden. Eine effektive Varianz konnte anhand Gauß´scher Fehlerfortpflanzung errechnet werden:

$$< var >= \sqrt{(var\,1)^2 + (var\,2)^2}$$

Dieser Wert wurde durch die Differenz der beiden Mittelwerte dividiert. So hatte man die Differenz der beiden Mittelwerte in Einheiten der effektiven Standardabweichung s erhalten. So war für zwei gleiche Verteilungen mit 68% Sicherheit eine Differenz der Mittelwerte von 0 bis –1s zu erwarten und mit 95% Sicherheit eine Differenz von 0 bis –2s. Umgekehrt deutete die Differenz von 2s darauf hin, dass die beiden Verteilungen mit nur 5% Sicherheit gleich waren, also mit 95% Sicherheit verschieden. Gültig ist der Test bei etwa Gauß' scher Verteilung der radialen Erwartungswerte. Im Kapitel II.1b.2. sind vier Beispiele für eine Verteilung von Territorienschwerpunkten gegeben, was sehr ähnlich den radialen Erwartungswerten ist: In 3 von 4 Fällen war die Verteilung etwa glockenförmig. Für den Vergleich der ganzen Verteilungen war die Standardabweichung der Einzelwerte maßgeblich. Dieser Vergleich ist von der Anzahl der Kerne unabhängig. Zum Vergleich der Mittelwerte der Verteilungen wurde die Standardabweichung der Mittelwerte benutzt. Diese Ergebnisse wurden immer eindeutiger, die Trennung zwischen den Kurven immer deutlicher und die Zuverlässigkeit der berechneten mittleren Kurven immer höher, je größer die Stichprobe (~ÖN) war.

Eines musste jedoch beachtet werden: Mit Ausnahme von Chromosom Y waren die erhaltenen radialen Erwartungswerte jeweils der Mittelwert der Position von 2 Homologen, da mit Ausnahme von Chromosom Y immer 2 Homologen pro Kanal angefärbt waren. Die Standardabweichung der einzelnen Homologe erhielt man, indem man die gemessenen Mittelwerte von 2 Homologen mit ÖN = Ö2 multiplizierte.

Zweiter Ansatz um unterschiedliche radiale Positionen auf ihre Wahrscheinlichkeit, gleich zu sein, zu prüfen bestand darin, die von beiden Kurven gemeinsame Fläche als Maß der Übereinstimmung zu definieren. Dies machte deshalb Sinn, weil die Fläche der beiden Kurven gleich groß war (Normierung der

DNA-"Gehalt" Kurven). Damit hatte diese Methode Ähnlichkeit mit dem Kolmogorov-Smirnov Test. Mit einer Kalibrierung der Ergebnisse konnte eine Übereinstimmung mit dem ersten Verfahren erzielt werden. Diese Ergebnisse werden in dieser Arbeit jedoch nicht gezeigt.

II. Ergebnisse

II.1. Comparison between different cell types

II.1.1. Non-random radial higher order chromatin arrangements in nuclei of diploid human cells[1]

Marion Cremer[1], Johann von Hase[2], Tanja Volm[3,4], Alessandro Brero[1], Gregor Kreth[2], Joachim Walter[1], Christine Fischer[3], Irina Solovei[1], Christoph Cremer[2],and Thomas Cremer[1*]

[1] Institute of Anthropology and Human Genetics, University of Munich (LMU), Munich, Germany; Tel: (+49) 89 2180 6710; Fax: (+49) 89 2180 6719; E-mail: thomas.cremer@lrz.uni-muenchen.de; [2] Kirchhoff-Institute of Physics, University of Heidelberg, Heidelberg, Germany; [3] Institute of Human Genetics, University of Heidelberg, Heidelberg, Germany; [4] Present address: Dept. of Obsterics and Gynecology, University of Ulm, Ulm, Germany.

* Correspondence to T. Cremer

Key words: chromosome territory, chromosome topology, nuclear architecture, human interphase nuclei, 3D FISH.

[1] Published in: Chromosome Research 9, pp 541-567, 2001.

II.1.1.1. Abstract

A quantitative comparison of higher order chromatin arrangements was performed in human cell types with three-dimensionally preserved, differently shaped nuclei. These cell types included flat-ellipsoid nuclei of diploid amniotic fluid cells and fibroblasts and spherical nuclei of B and T lymphocytes from peripheral human blood. Fluorescence in situ hybridization (FISH) was performed with chromosome paint probes for large (#1-5) and small (# 17-20) autosomes, and for the two sex chromosomes. Other probes delineated heterochromatin blocks of numerous larger and smaller human chromosomes. Shape differences correlated with distinct differences in higher order chromatin arrangements: In the spherically shaped lymphocyte nuclei we noted the preferential positioning of the small, gene dense #17, 19 and 20 chromosome territories (CTs) in the 3D nuclear interior – typically without any apparent connection to the nuclear envelope. In contrast, CTs of the gene poor small chromosomes #18 and Y were apparently attached at the nuclear envelope. CTs of large chromosomes were also preferentially located towards the nuclear periphery. In the ellipsoid nuclei of amniotic fluid cells and fibroblasts all tested CTs showed attachments to the upper and/or lower part of the nuclear envelope: CTs of small chromosomes, including #18 and Y, were located towards the centre of the nuclear projection (CNP), while the large chromosomes were positioned towards the 2D nuclear rim. In contrast to these highly reproducible radial arrangements, 2D distances measured between heterochromatin blocks of homologous and heterologous CTs were strikingly variable. These results as well as CT painting let us conclude that nuclear functions in the studied cell types may not require reproducible side by side arrangements of specific homologous or non-homologous CTs. 3D-modeling of statistical arrangements of 46 human CTs in spherical nuclei was performed under the assumption of a linear correlation between DNA content of each chromosome and its CT volume. In a set of modeled nuclei we noted the preferential localization of smaller CTs towards the 3D periphery and of larger CTs towards the 3D centre. This distribution is in clear contrast to the experimentally observed distribution in lymphocyte nuclei. We conclude that presently unknown factors (other than topological constraints) may play a decisive role to enforce the different radial arrangements of large and small CTs observed in ellipsoid and spherical human cell nuclei.

II.1.1.2. Introduction

The question of an ordered chromatin arrangement in human diploid cell nuclei has been studied since the early sixties (for review see Comings (1968); Comings (1980); Hens et al.

(1982) and Wollenberg et al. (1982a). Extensive analyses of chromosome positions were performed in metaphase spreads under the assumption that an orderly arrangement of metaphase chromosomes should reflect aspects of an orderly interphase chromatin arrangement. Early studies of human lymphocyte metaphase spreads addressing peripheral and central positions of chromosomes in human cells yielded discordant results (reviewed in Comings (1968) and Wollenberg et al. (1982a), however, a general pattern emerged: Smaller chromosomes, containing mostly earlier replicating and gene dense chromatin were preferentially found near the centre of the metaphase spread, surrounded by larger chromosomes which finish their replication later during S-phase (Hens et al., 1982; Wollenberg et al., 1982a). Notably, the overall distribution patterns did not simply reflect chromosome size: While the gene dense chromosomes 17 (88 Mb; (Lander et al., 2001) and 19 (72 Mb) were observed in the more interior part, the gene poor and later replicating chromosomes 18 (86 Mb) and Y (51 Mb) were reproducibly observed in the periphery of the spreads. A size correlated positioning of chromosomes in interphase nuclei was reemphasized in studies of metaphase plates from human fibroblasts (Leitch et al., 1994; Mosgöller et al., 1991). Three-dimensional reconstructions of electron micrographs of 10 serially sectioned normal human male fibroblasts revealed that small chromosomes tended to be central in all metaphase plates, while large chromosomes were more peripheral. In contrast to the lymphocyte data mentioned above, the fibroblast data revealed a central location also for the 18 and Y chromosomes.

Other studies were based on the rationale that chromosomal rearrangements observed in metaphase spreads should be informative under certain suppositions for the problem of interphase chromosome arrangements (Hager et al., 1982; Vogel and Schroeder, 1974). In agreement with the analyses of metaphase spreads, the analysis of the frequencies of non-homologous interchanges in Trenimon-treated lymphocytes from a healthy female individual (46,XX) indicated a preferential distribution of smaller chromosomes towards the nuclear centre. Again a more central position was deduced for the gene dense #19 and a more peripheral for the gene poor #18.

Laser-UV-microirradiaton of a small part of the interphase nucleus yielded a more direct approach to study the potential relationship between interphase and metaphase chromosome arrangements (Cremer et al., 1982a; Cremer et al., 1982b; Zorn et al., 1979; Zorn et al., 1976). The evaluation of chromosome damage in the subsequent mitosis showed a significant correlation between the site of nuclear microirradiation and the location of damaged chromosomes in the resulting metaphase spread: microirradiation of either central or

peripheral parts of the flat-ellipsoid Chinese hamster cell nuclei corresponded with a central or peripheral location of damaged chromosomes in the metaphase spread (Cremer et al., 1984).

The results summarized above indicate differences in the distribution of large and small human chromosomes and support a relationship between chromosome positioning in the interphase nucleus and in the metaphase plate. These results, however, are not unambiguous. The extent to which the results of metaphase spread analyses were influenced by technical artefacts, e.g. by colcemid and hypotonic treatments, has remained doubtful. The evaluation of interchange frequencies was based on the disputable assumption that the observed frequencies for all pairs of non-homologous chromosomes depended solely or at least mainly on the frequency by which certain pairs were immediate neighbours during interphase. Approaches, such as electron microscopy and UV-microirradiation are tedious and only amenable to a small number of cells. In addition to technical limitations it is a major disadvantage of all these methods that only cycling cells can be analysed but not cells after exit from the cell cycle.

In the seventies the direct analysis of chromosome arrangements in the nucleus was restricted to a few special cases, including the nuclear position of the inactive X (Schwarzacher, 1976), of the heterochromatic Yq12 segment (Pearson et al., 1970) and of the paracentromeric heterochromatin block of chromosome 9 (Spaeter, 1975). In the eigthies advances of in situ hybridization in combination with the generation of chromosome specific DNA-probes resulted in a breakthrough: It became possible to visualize chromosomes (Manuelidis, 1985; Schardin et al., 1985) or chromosome segments - at first mostly specific heterochromatin targets (Cremer et al., 1986; Rappold et al., 1984) directly in the cell nucleus of both cycling and non-cycling cells. Chromosome painting has provided unequivocal evidence that the mammalian cell nucleus contains discrete chromosome territories (CT), composed of distinct chromosome arm and band domains (for reviews see Cremer and Cremer (2001); Cremer et al. (2000) and Cremer et al. (1993), for a review on chromatin organization including invertebrates, yeast and plants see (Leitch, 2000). In situ hybridization experiments with chromosome specific probes have opened the field for an extensive analysis on nuclear topology of subchromosomal target sequences and CTs and provided further evidence for a non-random distribution of target chromosomes in human lymphocyte and fibroblast nuclei (Emmerich et al., 1989; Höfers et al., 1993; Manuelidis, 1990; Popp et al., 1990; Rappold et al., 1984).

In spite of these advances the question to what extent CTs and CT-subregions, e.g. centromeres or telomeres, occupy specific nuclear positions in certain cell types and to what extent a given higher order chromatin architecture may be cell type specific and change reproducibly during cell cycle and cellular differentiation has not been satisfactorily answered to date (for review see Cremer and Cremer (2001). Views are still conflicting and range from a more or less complete lack of order to a rigidly maintained order. Nagele and coworkers have proposed a highly ordered positioning of chromosomes in prometaphase rosettes and a separation of paternal and maternal chromosome sets in human fibroblasts and Hela cells (Nagele et al., 1995; Nagele et al., 1998). They further reported the existence of an ordered interphase chromosome topology in quiescent fibroblasts for chromosomes 7, 8 and 16 (Nagele et al., 1999). Data contrary to the claim of a predetermined order were provided by Allison and Nestor (1999). For nuclei of unstimulated human lymphocytes Lesko et al. (1995) reported 3D positions of centromere-specific probes for chromosome 7, 11 and 17 in accordance with a random model distribution. In a study of human fibroblasts Sun et al. (2000) proposed a correlation between CT location and DNA content of chromosomes. In partial disagreement, Bickmore and co-workers (Boyle et al., 2001; Croft et al., 1999) provided evidence that gene content of a chromosome rather than DNA content may be a key determinant of CT positioning in human lymphocyte and fibroblast nuclei. The question whether non-random associations exist between homologous CTs in human cell nuclei is also controversially discussed. Nagele et al. (1999) reported a close association for homologues #8 and 11 CTs in quiescent human fibroblasts. Other examples of homologous associations were found for chromosomes 3, 7, 8, 13, 17, 21 and X in the majority of Sertoli cells but not in lymphocytes (Chandley et al., 1996). Evidence against homologous associations in dividing human fibroblasts was provided by Leitch et al. (1994) and in mammalian lymphocyte nuclei by Alcobia et al. (2000); Ferguson and Ward (1992) and Vourc'h et al. (1993).

It is difficult at present to assess to which extent biological and/or methodological factors account for this still inconsistent picture. The experiments of different groups involved different cell types and cell cycle stages, as well as different fixation conditions and pretreatments to achieve accessibility of denatured nuclear

target DNAs to probes employed for in situ hybridization. To achieve a reliable picture a comprehensive approach is required, which necessarily includes an evolutionary perspective. Based on generally accepted experimental procedures, which take critical notice of experimental artefacts, this approach must be applied to different cell types of human and other species, including cells at different stages of the cell cycle, as well as postmitotic cells during and after terminal differentiation. Such an approach, will form the indispensable basis to answer the question to which extent general and cell type specific nuclear functions depend on general and cell type specific motifs of an higher order chromatin architecture (see also Cremer and Cremer (2001).

Here, we have applied a 3D FISH approach that preserves the 3D topology of CTs and chromosomal subregions, down to the level of ~1 Mb chromatin domains (Solovei et al., 2001(in press). We address the question of chromosome positioning in three human cell types, including cultured amniotic fluid cells and fibroblasts, and non-stimulated T and B lymphocytes prepared as a single cell population from peripheral blood. First, we performed a 2D analysis of about 12.000 3D preserved human diploid amniotic fluid cell nuclei after two colour FISH. In these experiments we employed combinations of probes that delineate specifically constitutive heterochromatin of chromosomes #1, 3, 4, 7, 8, 15, 17, 18 and Y. 2D-distance measurements were carried out between heterochromatin targets and the centre of nuclear projection (CNP), as well as between homologous and heterologous targets. Second, entire CTs were visualized in 3D-preserved nuclei of human diploid fibroblasts, which are similar in shape to amniotic fluid cell nuclei, and in spherically shaped nuclei of lymphocytes. Following two-colour FISH with pools of whole chromosome paint probes for the large chromosomes #1-5 and X and the small chromosomes #17-20 and Y, light optical serial sections of nuclei were recorded with a confocal laser scanning microscope and used for 3D reconstruction and quantitative assessments. Third, the observed experimental distribution patterns of heterochromatin targets and CTs were compared with distributions obtained by computer simulations. The random, i.e. uniform and independent, distribution of points in spheres, ellipsoids or flat cylinders was used to model the random distribution of heterochromatin targets in spherical and flat - ellipsoid cell nuclei (Emmerich et al., 1989; Höfers et al., 1993; Rappold et al., 1984). While it seems reasonable to perform such a comparison in order to elucidate whether or not certain

target distributions reflect a random distribution of points, one should be aware that chromosomal subregions are part of a chromosome territory. Accordingly, topological constraints depending on CT volume, shape, rigidity and other factors may affect experimentally observed CT arrangements (Münkel et al., 1995). For this reason we performed a more complex modelling of CT arrangements in spherically shaped nuclei taking into account topological constraints that enforce a different 3D distribution of the gravity centres of small and and large CTs.

II.1.1.3. Materials and Methods

II.1.1.3.1. Cells, fixation procedure and FISH-pretreatments

Primary human fibroblasts (46, XX) were cultured on glass coverslips (26x76 mm, with a thickness of 0.17+/-0.01 mm) until confluency and fixed in 4% paraformaldehyde (PFA)/1 x PBS for 10 min. Amniotic fluid cells were established following diagnostic amniocentesis from normal male and female pregnancies during the 15^{th} to 17^{th} week of gestation. Cell clones were subcultured on microscopic slides, grown to subconfluency and fixed in 4% PFA/1 x PBS. For the identification of cells in S-phase, BrdU at a final concentration of 5mM was added to the culture medium for 30-60 min before fixation. T and B lymphocytes (G_0 cells) from peripheral blood were isolated by a Ficoll® gradient and resuspended in 50% FCS/RPMI medium at a concentration of approximately $1x10^6$ cells/ml. An aliquot of 300ml of this suspension was placed on a polylysine (1mg/ml) coated slide and cells were allowed to attach for 30 min at 37^0C. Prior to fixation with 4% PFA/0.3 x PBS, cells were incubated in 0.3 x PBS for 1min in order to prevent shrinkage of the nucleus. Permeabilization steps for all cells included treatment in 0.5% Triton-X-100 (20min), 20% glycerol in PBS (30min), repeated freezing/thawing in liquid nitrogene, and incubation in 0.1M HCl (5min) or pepsin (1mg/ml in 0.01 M HCl (described in detail in Solovei et al. (2001) in press). Slides were kept at 4°C in 50% formamide/2 x SSC until hybridization.

II.1.1.3.2. DNA probes

The following chromosome specific alphoid or satellite sequences cloned from the centromeric or paracentromeric regions of human chromosomes were used: 1q12 (pUC1.77, (Cooke and Hindley, 1979)), 2c (Dunham et al., 1992), 3c (pa3.5, (Willard and Waye, 1987), 4c (pYAM11-39, (Hulsebos et al., 1988), 7c (p7t1, (Waye et al., 1987), 8c ((Dunham et al., 1992), 12c (BR12, (Rocchi et al., 1989)), 15p/c (D15Z1, (Higgins et al., 1985), 16q12 (pHUR-195, (Moyzis et al., 1987), 17c (p17H8, (Willard et al., 1986), 18c (L1.84, (Devilee et

al., 1986), Xc (pXBR, (Willard and Waye, 1987), and Yq11 (pYH2.1, (Cooke et al., 1982). Probes were labelled by nick-translation according to standard protocols.

Human chromosome paint probes, produced by DOP-PCR from sorted chromosomes, were kindly provided by M. Ferguson-Smith (University of Cambridge, UK). Paint probes were re-amplified by DOP-PCR, depleted from repetitive sequences as described (Bolzer et al., 1999; Craig et al., 1997), and used without Cot1-DNA in the hybridization mix. Pools of chromosome paints were prepared for large and small sized chromosomes. The pool for the large chromosomes contained chromosomes #1 - 5 and X; pools for the small chromosomes included either #17 - 20, or #17, 19, 20. Labelling of single chromosome paints #18, 19 and Y or of paint pools was done by DOP-PCR as described (Schermelleh et al., 1999) using biotin-dUTP or digoxigenin-dUTP.

II.1.1.3.3. FISH and probe detection

FISH was performed in 50% formamide/10% dextran sulfate/1 x SSC at 37°C over 1 - 3 days. Posthybridization washings included 2xSSC at 37° and 0.1 x SSC at 60°. Detection of biotin was done by one to three layers using either avidin-Cy3 or avidin-Alexa-488 followed by goat-anti-avidin-FITC or avidin-Cy5, followed by biotinylated goat-anti-avidin and avidin-Cy5. Detection of digoxigenin was done by one or two layers of specific antibodies, using either Cy3-conjugated mouse-anti-digoxigenin or rabbit-anti-digoxigenin followed by Cy3-conjugated goat-anti-rabbit. For counterstaining of nuclei, 4',6-diamidino-2-phenylindole (DAPI), propidium iodide (PI), or YOYO-1 (Molecular Probes, USA) were used, depending on microscopy and fluorochromes chosen for the detection.

II.1.1.3.4. 2D evaluation of amniotic fluid nuclei

Nuclei were viewed with a conventional epifluorescence microscope (Zeiss) and two dimensional analysis of heterochromatin target distributions was performed as described

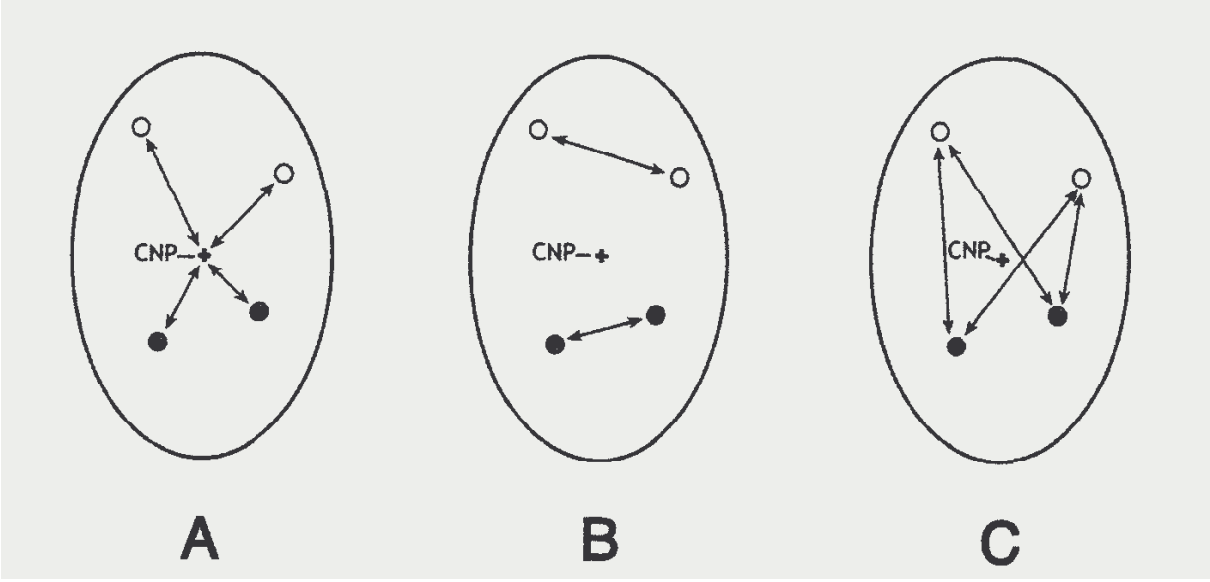

(Emmerich et al., 1989). Only nuclei with regular shape showing complete and specific hybridization were included. Nuclei showing only a single hybridization signal were excluded in cases where the second signal was possibly missing due to incomplete hybridization, while nuclei where size and shape of a given signal indicated an overlap of the signals from two homologues were included. These selection criteria provide a bias against nuclei with homologous target association. The percentage of evaluated nuclei was > 90% in all experiments. An ellipse was adapted to each nucleus and their major and minor axis was measured. Distances were measured between each target and the centre of the 2D nuclear projection (CNP) (Figure 1A), between two homologous targets (Figure 1B), and between heterologous targets (Figure 1C).

Figure 1. Scheme of 2D distance measurements performed in amniotic fluid cell nuclei. (A) Distances between chromosome targets and the centre of the nuclear projection (CNP). (B) Distances between homologous chromosomes. (C) Target-target distances between heterologous chromosomes.

II.1.1.4. Modelled heterochromatin target distributions and comparison with experimental data

As models for the random distribution of the heterochromatin targets in the nucleus 3D uniform distributions of points in ellipsoids and elliptic cylinders were considered. The orthogonal projections of random 3D distances onto the x,y-plane were used for the calculation of 2D model distances. The resulting 2D-model distribution functions were independent from the height z of the model nuclei. For each experiment model distribution functions were determined by means of Monte Carlo simulations for 10.000 ellipsoids and cylinders, respectively, using the diameters measured in the respective set of experimental nuclei. On the basis of the graphically presented experimental and model distribution curves, we calculated p-values of the Kolmogorov-Smirnov test (Knuth, 1981). To test for deviations between experimental and model distance distributions the Kolmogorov-Smirnov one-sample test was used. The Kolmogorov-Smirnov two-sample test was chosen to test for significant differences of the distribution functions of distances obtained for two chromosome specific heterochromatin targets in two colour FISH experiments. The analyses were not adjusted for multiple comparisons and all p-values are considered descriptive. In double hybridization experiments four target-CNP distances, two homologous target-target distances and four heterologous target-target distances were determined in each experimental and model nucleus. These distances were used to determine cumulative experimental and model distribution functions. The distances determined per nucleus could not be considered to be independent

from each other, at least in the case of the four heterologous target-target distances. To account for this fact, only two degrees of freedom per nucleus were assumed when calculating the test statistics.

II.1.1.5. Laser scanning confocal microscopy (LSCM)

Stacks of optical sections of fibroblast and lymphocyte nuclei were collected after FISH with probes containing pools for the large and small chromosomes or probes containing chromosomes #18,19 or Y. Optical sections with an axial distance of 250 nm were recorded using a three channel LSCM (Zeiss LSM 410) or Leica TCS SP equipped with a Plan Apo 63x/1.4 oil immersion objectives. For each optical section, images were collected sequentially for all three fluorochromes. Stacks of 8-bit gray-scale 2D-images were obtained with a pixel size of 50 nm in x,y direction. Maximum intensity projections of image stacks were done using Zeiss or Leica operating software. Displayed overlays of confocal images were done and processed with Adobe Photoshop. 3D reconstructions of image stacks were performed using Amira 2.0, Template Graphics software, USA.

II.1.1.6. Quantitative assessment of 3D radial distributions of painted chromosome territories in lymphocyte nuclei[2]

Data from lymphocyte nuclei were analyzed by quantitative 3D evaluation. For the evaluation of the digitized data stack obtained from each painted nucleus, a voxel (volume element) based algorithm was applied. As the first step, nuclear volume segmentation was performed using counterstain fluorescence and its 3D nuclear centre was determined. To separate the nuclear volume from background noise, the 3D data stack of the counterstain image was smoothed in 4 steps by an isotropic gaussian (1 4 6 4 1) 2D filtering (corresponding to a 61 x 61 x 1 gaussian mask) and normalized to a maximum intensity value of 255. All voxel intensities below an automatically (see below) set threshold were set to zero. For the segmentation of the nuclear border, a straight line was drawn from the gravity centre of the 3D data stack towards the voxel considered. For all the voxels on the straight line, the 3 x 3 environment was tested. If in this environment 5 or more voxels set to zero were found, it was concluded that the voxel considered was likely located outside the nuclear boundary and removed, i.e. its intensity was set to zero. This segmentation procedure was applied to all voxels with intensities above the threshold. The resulting image represented the segmented nuclear volume. As the next step, segmentation of CTs was performed in each 3D stack

[2] The evaluation algorythm has been simplified yet, s. Chapter "Einleitung"

representing the colour channel for the recording of the respective painted CTs. Image stacks were smoothed in three steps by a gaussian 2D filtering (corresponding to a 29x29x1 gaussian mask) and normalized to a maximum intensity value of 255. All voxel intensities below an automatically set threshold (see below), as well as occasional background voxel intensities in the CT stacks outside the segmented nuclear volume were set to zero. Using an iterative procedure, a threshold value was estimated for each 3D data set for nuclear and CT thresholding. For this purpose an intensity value (I) histogram (frequency of intensity values 1 – 255; highest intensity at 255) was established for each 3D stack. After the smoothing of the intensity histogram thus obtained by a gaussian 1D-filtering (omitting intensity value 0), the histogram was divided in a lower and a higher part by choosing a threshold of T = 100 as a first guess. The expectation value of the lower part, called E_1, and the expectation value E_2 of the upper part were calculated. The mean value of both became the new estimate of the threshold T. The expectation values E_1 and E_2 are given by:

$$E_1 = \frac{\int_1^T I_1 \, h(I_1)dI_1}{\int_1^T h(I_1)dI_1}, \quad E_2 = \frac{\int_T^{255} I_2 \cdot h(I_2)dI_2}{\int_T^{255} h(I_2)dI_2}, \quad I_1, I_2 \in [1,255]$$

I_1, I_2 denote the intensity values in the lower (I_1) and the upper (I_2) part of the histogram; $h(I_1)$, $h(I_2)$ describe the frequencies with which the intensities I_1, I_2 occur in the respective parts of the histogram. In the next step, applying this estimate of T, E_1 and E_2 were calculated again and the next T was determined. The procedure was repeated, until the estimated T was equal to the previous estimation of T. As the third step, the segmented nuclear space was divided into 25 equidistant shells with a thickness of Dr as a fraction of the radius from the nuclear centre to the nuclear border. For each voxel X located in the nuclear interior or at its border the relative distance r from the nuclear centre was calculated. $r = (r_1 / r_0) \times 100$; also see chapter I

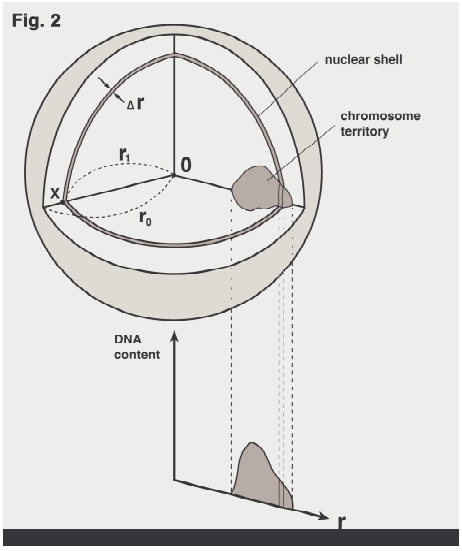

Figure 2: Scheme of 3D evaluation of the chromosome territories arrangements in spherical nuclei. The geometrical centre of the nucleus (0) was defined and the position of each voxel was expressed as relative radius, $r = r_1/r_0 \times 100$. The volume of the sphere was divided into 25 equidistant shells. DNA content of each shell was determined by summing up the voxel

A shell at a given r contains all nuclear voxels having a distance between r - Dr/2 and r + Dr/2. For each shell all voxels with signal intensities above an applied CT-threshold were identified and the fluorescence intensities derived from the emission spectrum of a given fluorochrome were summed up. For each evaluated nucleus this procedure yielded the individual DNA-shell contents for painted CTs as well as the overall DNA content reflected by the DNA counterstainintensities within this shell.

. Finally, the sum of the voxel intensities measured in the evaluated set of nuclei was set to 100% for each fluorochrome. Using this normalization, the average relative DNA content in nuclear shells as a function of the relative distance r from the 3D centre represents the average distribution of painted CTs or overall DNA in the entire set of evaluated nuclei. As an estimate for the variation obtained for each relative distance r, the standard deviation of the mean DNA shell content was calculated.

Using this method of evaluation, a homogeneous counterstain was expected to result in a parabola like increase with r. In case of a preferential positioning of painted CTs in the evaluated set of nuclei, the average relative DNA content in nuclear shells was expected to deviate significantly from the measured counterstain curve. A decline of the DNA shell content curves was noted in the nuclear periphery (r ‡ 90%) resulting from the smoothing of

the data as shown by computer simulations and partly also from irregularities of the nuclear shape.

II.1.1.7. Quantitative assessment of 2D radial distributions of painted chromosome territories in fibroblast nuclei

For the elliptically shaped and rather flat fibroblast nuclei in G_0 a 2D evaluation procedure was used. The axial projections of light optical serial sections from individual nuclei were used separately for the different colour channels. For the segmentation of the projected nuclear area, and the determination of 2D radial distributions of painted CTs and counterstained DNA, respectively, the procedure described above for the 3D evaluation of spherically shaped lymphocyte nuclei was modified as follows: pixels contained in 25 concentrical elliptical shells of thickness Dr were evaluated (instead of voxels in shells in the 3D case). The relative 2D distance r of a shell was calculated as $r = (r_1/ r_0) \times 100$; r_1 represents the 2D distance from the centre of the nuclear projection to X, i.e. the pixel in question; r_0 denotes the distance between the 2D nuclear centre and the border of the nuclear projection (nuclear rim) drawing a line through X. A shell at a given r contains all pixels of the nuclear projection with a distance between r - Dr/2 and r + Dr/2. Accordingly, the average relative 3D DNA content obtained in nuclear 3D shells was replaced by the average relative 2D DNA content in 2D shells.

II.1.1.8. Computer simulations of CT arrangements in spherical human model cell nuclei

The experimentally determined 3D-distribution of given groups of CTs in lymphocytes was compared with a statistical distribution of simulated CTs in spherical nuclei applying the "spherical 1-Mb chromatin domain (SCD)" model ("statistical SCD-model") (Cremer et al., 2000; Kreth et al., 2001(in press)). Based on evidence for a compartmentalization of CTs into 300-800 nm sized ~1 Mb chromatin domains, the SCD model assumes a chain of spherical chromatin domains with 500 nm diameter for each chromosome connected by flexible chromatin linkers. Chromatin linkers were modeled by a spring potential (with a thermodynamic equilibrium distance of about 600 nm between the centres of connected chromatin domains at 37°C). Between different domains, repulsive forces (modeled by an increasing potential with a half width of ~250nm) were assumed. This way of modeling ~1 Mb chromatin domains allowed for slight volume overlaps between neighboring domains. In addition, a weak spherical energy barrier was applied around each territory with a size corresponding to its DNA-content. This energy barrier is essential to maintain the

compactness of the modeled chromosome chains in territories. The potential accounts in a drastically simplified way for forces, which in real nuclei may arise from a combination of parameters, including the rigidity of higher order chromatin segments and the effects of CT anchoring proteins.

As a start configuration the ~ 1 Mb domains were assumed to be compressed into 46 statistically distributed "start cylinders" in a spherical nuclear volume (10mm in diameter). These start cylinders represent the chromatids of the diploid human chromosome set in anaphase/telophase. The number of the ~ 1 Mb domains assumed for a given start cylinder was equal to the DNA content (Mb) of the modeled chromosome. Start cylinders were allowed to relax according to the "Metropolis Importance Sampling Monte Carlo" method to sample thermodynamic equilibrium configurations (Metropolis et al., 1953). For the relaxation of a whole nucleus, about 400.000 Monte Carlo cycles were used. As a consequence the "decondensation" of start cylinders into model chromatid territories was compatible with the topological constraints defined above. Accordingly, deviations from a random, i.e. uniform and independent, distribution of points in a sphere, reflect these topological constraints. Virtual microscopy image data stacks were calculated from the simulated cell nuclei (Cremer et al., 2000). For this purpose, two virtual territory colour channels were obtained by digitizing the respective simulated CTs of each channel employing a three dimensional grid (voxel spacing in xy: 50 nm, z: 250 nm). To account for the limited resolution of a confocal laser scanning microscope and the smoothing of the experimental data stacks (see above), the virtual image data stacks were smoothed with an anisotropic gaussian filter corresponding to 400 x 400 x 700 nm.

II.1.1.9. Results

II.1.1.9.1. Differences in the 2D-positioning of chromosome specific constitutive heterochromatin in amniotic fluid cell nuclei correlate with chromosome size

Non-synchronized, first passage amniotic fluid cell cultures with normal diploid karyotypes (46,XX and 46,XY) were established after diagnostic amniocentesis from 40 pregnancies of healthy women. These cultures were established from epithelial cells of the fetal urogenital tract and showed three types of cellular morphology: E-type (epithelial-like), F-type (fibroblast-like) and intermediate (AF-type) morphology (Ochs et al., 1983). Fourteen single and 33 double colour 2D-FISH experiments with chromosome specific, repetitive DNA probes were performed (Table 1). In each experiment 2D projections of at least 200 nuclei were evaluated: distances between hybridized chromatin targets and the centre of the 2D

nuclear projection (CNP) as well as distances between homologous and (in double colour FISH experiments) also non-homologous targets (referred to as 2D homologous and heterologous target-target distances) were measured as shown in Figure 1. In single colour experiments the experimentally derived distribution of distances was compared with two model distributions of 2D-distances based on the independent and uniform distribution of points (reflecting chromosomal targets) either in ellipsoids or in flat cylinders (see Material and Methods). Figure 3 shows typical examples of cumulative frequency distribution curves obtained in three FISH experiments performed with probe combinations for the following targets: (A-C) 1q12 and 3c; (D-F) 16q12 and 17c; (G-I) 3c and 17c.

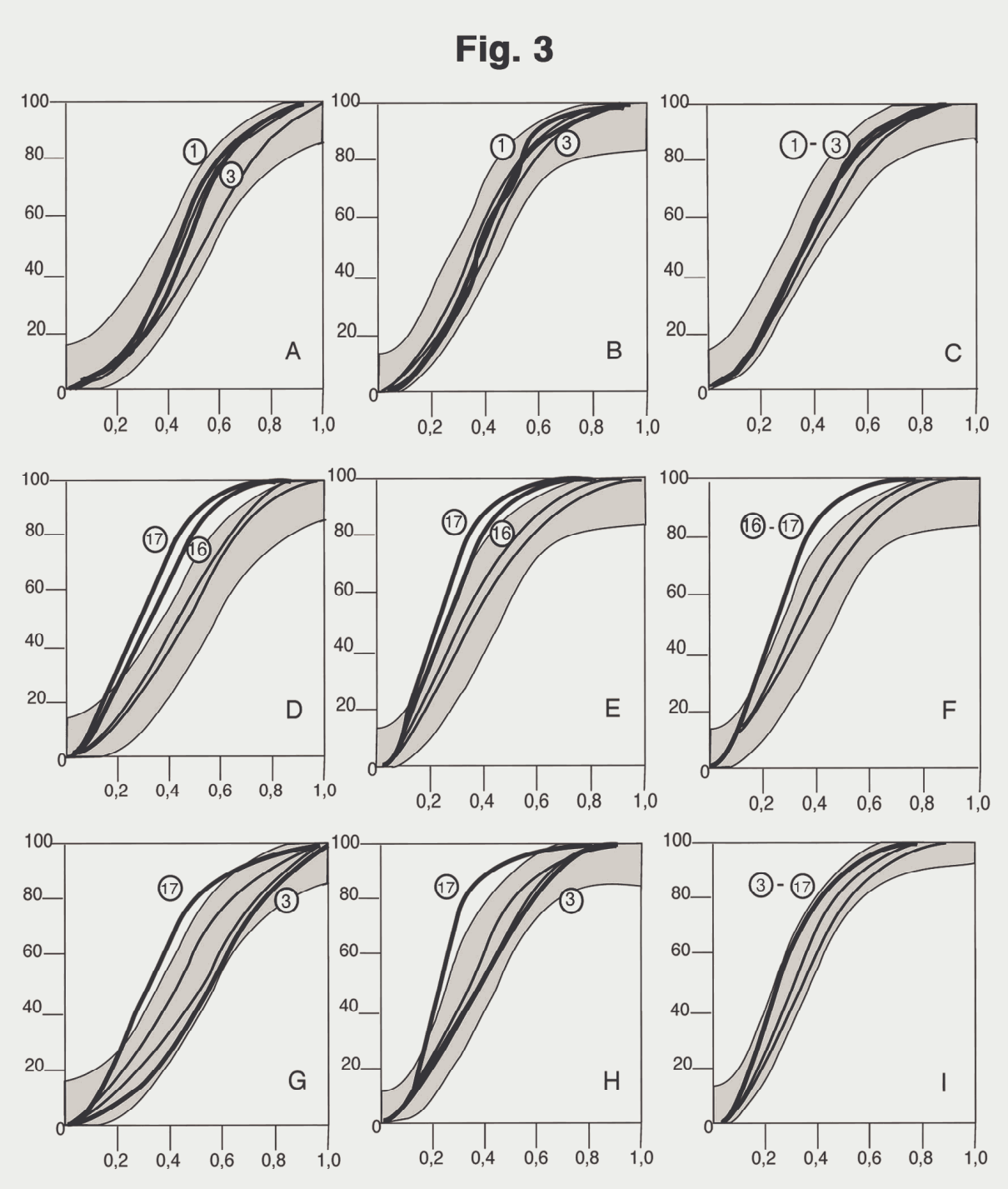

Figure 3. Cumulative frequency distribution curves obtained in amniotic fluid cell nuclei after two colour FISH experiments with probe combinations for the following targets: (A-C) 1q12 and 3c; (D-F) 16q12 and 17c; (G-I) 3c and 17c. (A, D, G) target-CNP distances; (B, E, H) homologous target-target distances; (C, F, I) heterologous target-target distances. Abscissa: Normalized 2D distances. Ordinate: Percentage of nuclei with a normalized distance equal to or smaller than the corresponding distance on the abscissa. Shaded areas show the low 99% confidence limits of the one-sample Kolmogorov-Smirnov test for the ellipsoid model (left borderline) and the upper 99% confidence for the cylinder model (right borderline). Thin lines

represent the cumulative model distributions. Bold lines represent the cumulative experimental distance distributions. Those located between the two confidence limits were considered as not significantly different from the random distributions defined by the two models. Accordingly, the 1q12-3c targets (A - C) were distributed within the range defined for random target distributions, while 16q12 - 17c targets (D - F) were distributed significantly closer to CNP and to each other. The comparison between 3c-17q targets (G - I) confirms the different distance distribution.

The targets for chromosome 1 and 3 were distributed within the range defined for random target distributions, while 17c and 16q12 were distributed significantly closer both to CNP and to each other. A significant deviation of the distribution of chromosome specific heterochromatin targets was assumed, if the deviation was significant for both models at $p<0.01$ by the Kolmogorov-Smirnov one-sample test. According to this criterium, centromeres of the larger CTs (#1, 2, 3, 4, 7, 8, 12 and X) did not show a significant deviation in contrast to the centromeres of smaller CTs (#15, 16, 17, 18 and Y) (Table 1). In two colour FISH experiments the two-sample Kolmogorov-Smirnov test was used to test for a significant difference ($p<0.01$) between the centromere-CNP and centromere - centromere distances from two non-homologous chromosome types. This test revealed significant differences in all comparisons of the positions of a larger CT with a smaller one (#1-15, 1-16, 1-17, 1-18, 1-Y, 3-17, 3-18, 4-17, 4-18, 7-15, 7-16, 7-17, 7-18, 7-Y, 8-18, 12-18, 18-X, X-Y) (Table 1).

Exp. No.	combination of chromo-some targets a; b	sex	number of cells	ratio of major/minor axis – SD	deviation of experimental target-CNP and target-target distances from model distribution curves					difference between two experimental distribution curves	
					a-CNP	b-CNP	a-a	b-b	a-b	a-CNP vs b-CNP	a-a vs b-b
1	1q12 only	m	200	0.55 – 0.13	ns	---	ns	---	---	---	---
2	1q12; 3c	f	250	0.64 – 0.12	ns	ns	ns	ns	ns	ns	ns
3	1q12; 4c	m	250	0.62 – 0.10	ns	ns	ns	ns	ns	ns	ns
4	1q12; 7c	f	250	0.60 – 0.11	ns	ns	ns	ns	ns	ns	ns
5	1q12; 8c	m	250	0.59 – 0.10	ns	ns	ns	ns	ns	ns	ns
6	1q12; 12c	f	250	0.52 – 0.09	ns	ns	ns	ns	ns	ns	ns
7	1q12; 15p	m	250	0.69 – 0.10	ns	***	ns	***	***	***15p	***15p
8	1q12; 16q12	f	250	0.69 – 0.10	ns	***	ns	***	***	***16q12	***16q12
9	1q12; 17c	m	250	0.63 – 0.10	ns	***	ns	***	*	***17c	***17c
10	1q12; 18c	f	250	0.63 – 0.11	ns	***	ns	***	*	***18c	***18c
11	1q12; Xc	f	250	0.50 – 0.09	ns	ns	ns	ns	ns	ns	ns
12	1q12; Yq12	m	250	0.68 – 0.11	ns	***	ns	---	***	***Yq12	---
13	2c only	f	200	0.59 – 0.11	ns	---	ns	---	---	---	---
14	3c only	m	200	0.53 – 0.13	ns	---	ns	---	---	---	---
15	3c; 17c	m	250	0.55 – 0.13	ns	***	ns	***	*	***17c	***17c
16	3c; 18c	f	250	0.56 – 0.14	ns	***	ns	***	**	***18c	***18c
17	4c only	f	200	0.62 – 0.09	ns	---	ns	---	---	---	---
18	4c; 17c	m	250	0.65 – 0.10	ns	***	ns	***	***	***17c	***17c
19	4c; 18c	f	250	0.70 – 0.11	ns	***	ns	***	***	***18c	***18c
20	7c only	f	200	0.58 – 0.12	ns	---	ns	---	---	---	---
21	7c; 18c	f	250	0.62 – 0.10	ns	***	ns	***	***	***18c	***18c
22	7c; 15p	f	250	0.61 – 0.08	ns	***	ns	***	***	***15p	***15p
23	7c; 16q12	f	250	0.62 – 0.11	ns	***	ns	***	**	***16q12	***16q12
24	7c; 17c	f	250	0.68 – 0.10	ns	***	ns	***	**	***17c	***17c
25	7c; 18c	f	250	0.69 – 0.11	ns	***	ns	***	***	***18c	***18c
26	7c; Yq12	m	250	0.65 – 0.10	ns	***	ns	---	***	***Yq12	---
27	8c only	f	200	0.69 – 0.13	ns	---	ns	---	---	---	---
28	8c; 18c	f	250	066 – 0.10	ns	***	ns	***	*	***18c	***18c
29	12c only	f	200	0.51 – 0.09	ns	---	ns	---	---	---	---
30	12c; 18c	f	250	0.52 – 0.10	ns	***	ns	***	*	***18c	***18c
31	12c; Xc	f	250	0.52 – 0.10	ns	ns	ns	ns	ns	ns	ns
32	15p only	f	200	0.60 – 0.11	***	---	***	---	---	---	---
33	15p; 16ql2	f	250	0.63 – 0.11	***	***	***	***	***	**15p	**15p

Tabelle 1 Fortsetzung

Exp. No.	combination of chromo-some targets a; b	sex	number of cells	ratio of major/minor axis – SD	deviation of experimental target-CNP and target-target distances from model distribution curves					difference between two experimental distribution curves	
					a-CNP	b-CNP	a-a	b-b	a-b	a-CNP vs b-CNP	a-a vs b-b
34	15p; 18c	f	250	0.66 – 0.10	***	***	***	***	***	**15p	**15p
35	16ql2 only	f	200	0.68 – 0.11	***	---	***	---	---	---	---
36	16ql2; 17c	f	250	0.60 – 0.10	***	***	***	***	***	ns	ns
37	16ql2; 18c	f	250	0.68 – 0.10	***	***	***	***	***	*18c	ns
38	17c only	m	200	0.56 – 0.12	***	---	***	---	---	---	---
39	17c; 18c	m	250	0.57 – 0.12	**	***	*	*	***	ns	ns
40	17c; Yq12	m	250	0.65 – 0.09	***	***	***	---	***	***18c	---
41	18c only	m	200	0.55 – 0.13	**	---	***	---	---	---	---
42	18c; Xc	f	250	0.54 – 0.10	***	ns	***	ns	*	***18c	***18c
43	18c; Yq12	m	250	0.65 – 0.10	***	***	***	---	***	***Yq12	---
44	Xc only	f	200	0.69 – 0.11	ns	---	ns	---	---	---	---
45	Xc only	m	200	0.67 – 0.11	ns	---	ns	---	---	---	---
46	Xc; Yq12	m	250	0.65 – 0.11	ns	***	ns	---	***	***Yq12	---
47	Yq12 only	m	200	0.58 – 0.11	***	---	---	---		---	---

Table 1. FISH with chromosome specific repetitive DNA probes (for probes see material and methods) to nuclei of male and female amniotic fluid cell cultures. The major and minor axis of an ellipse adapted to each nucleus was measured yielding similar ratios in all cultures. The deviation of experimental from model frequency distribution curves for target-CNP distances (a-CNP and b-CNP), homologous target-target distances (a-a and b-b) and heterologous target-target distances (a-b) was tested by the Kolmogorov-Smirnov one-sample test. ns: deviation not significant; *: deviation significant at P<0.01; **: P<0.001: ***: P<0.0001. Significant deviations of experimental from model distances were only observed in the direction of smaller values (for examples compare with Figures 3-5). The two sample Kolmogorov-Smirnov test was applied to test for differences between the two experimental curves, i.e. two target-CNP frequency distribution curves (a-CNP vs. b-CNP) and two homologous target-target frequency distribution curves (a-a vs b-b) obtained for each indicated target combination a;b. In case of a significant difference, the target which is distributed to the left (compare with Figure 3) is indicated.

Significant differences in the positioning of two non-homologous targets with regard to each other and to CNP reflect only mean differences. In all experiments a pronounced internuclear variability of individual target positions was observed both with regard to CNP and relative to other targets. Thus the positioning of the various chromosome targets cannot be described by a deterministic order. The same results were obtained with amniotic fluid cells fixed after the first passage or after a few additional passages (data not shown). Distributions of autosome specific targets were the same in male and female amniotic fluid cell cultures (Table 1). Furthermore, distributions were the same in nuclei of amniotic fluid cells with E-type, F-type or AF-type morphology (data not shown).

Figure 4 shows the median target-CNP (A, B) and target - target distances (C,D) with 95% confidence intervals under the assumption of normality (Hartung, 1991). The distances measured between homologous peri- or paracentric heterochromatic regions of the larger chromosomes 1, 2, 3, 4, 7, 8, 12 and X and the distances between these regions and CNP fit the random model distribution in all experiments. In contrast, the median homologous target-target and target-CNP distances of the heterochromatic regions of the smaller chromosomes 15, 16, 17, 18 showed a significant predominance of smaller distances (one-sample Kolmogorov-Smirnov test; $p<0.01$ - $p<0.0001$). The smallest median target-CNP distance was observed for the Yq12 heterochromatin. In agreement with the above results, the median distances between the heterologous targets of larger chromosomes again fit the random distribution, while significantly smaller median target-target distances were observed between non-homologous targets from all tested smaller chromosomes, as well as between the heterochromatic targets of smaller and larger chromosomes (Table 1).

Figure 4. Median target-CNP distances for constitutive heterochromatin targets of larger chromosomes, 1q12, 2c, 3c, 4c, 7c, 8c, 12c, Xc (A) and of smaller chromosomes, 15q12, 16q12, 17c, 18c, Yq12 (B). The median homologous target-target distances of the respective targets for the larger chromosomes (C) and for the smaller chromosomes (D). Ordinate: normalized target-CNP distances (A, B) and homologous target-target distances (C, D). Horizontal bars indicate the median distances with 95% confidence intervals estimated under the assumption of normality to judge the magnitude of deviation from random model distributions. The gray-shaded area indicates the border of the confidence bands for the model distributions (see the legend for Figure 3). These medians differ from experiment to experiment according to the variations of the diameters of the ellipses adapted to different sets of nuclei. Note that all median target-CNP distances obtained for the larger chromosomes are

found within the corresponding 99% confidence band, while all median target-CNP distances measured for smaller chromosomes are found below this range. For the statistical analysis by the Kolmogorov-Smirnov test see Table 1. Homologous target-target distances obtained for the larger chromosomes fit to a random model distributions, whereas target-target distances for smaller chromosomes show a highly significant predominance of smaller values.

Fig. 4

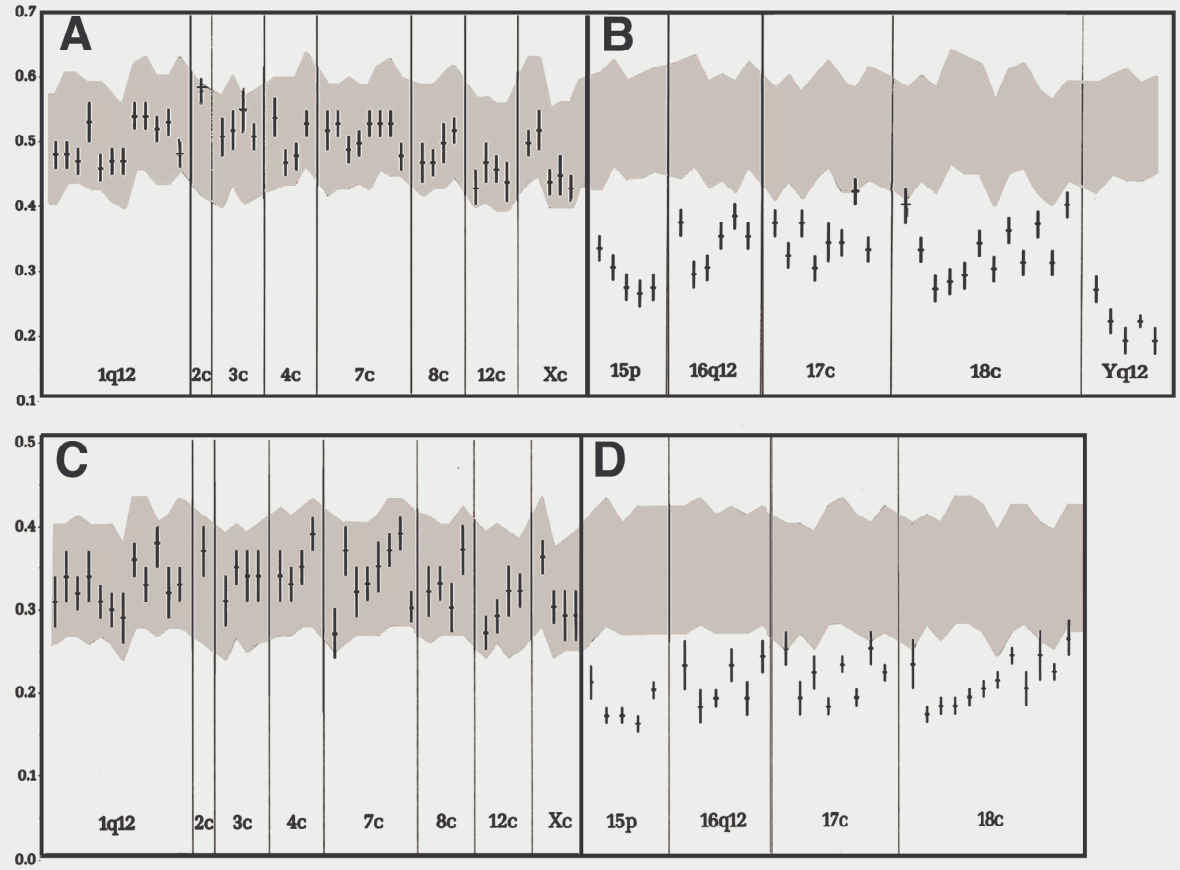

II.1.1.9.2. Differences in the 2D positioning of heterochromatin targets from large and small chromosomes are maintained during interphase

Cultures of growing amniotic fluid cells contained 5–10% of the cells in S-phase identified by BrdU pulse labelling (data not shown). To evaluate a potential influence of the cell cycle on the distribution of heterochromatic targets, FISH with biotinylated probes for 1q12 and 18c after BrdU pulse labelling was performed. The distribution of each target region was evaluated in 200 BrdU-positive and 200 BrdU-negative nuclei. (Figure 5). Target - CNP distributions were identical for a given target in both BrdU positive (Figure 5A and C) and BrdU negative nuclei. In agreement with 1q12 and 18c target distributions in nuclei evaluated

at random in non-synchronized cultures, the median 18c - CNP distance was significantly smaller than the median 1q12 - CNP distance. In conclusion, these data do not support a cell cycle dependent difference in the distribution of these targets.

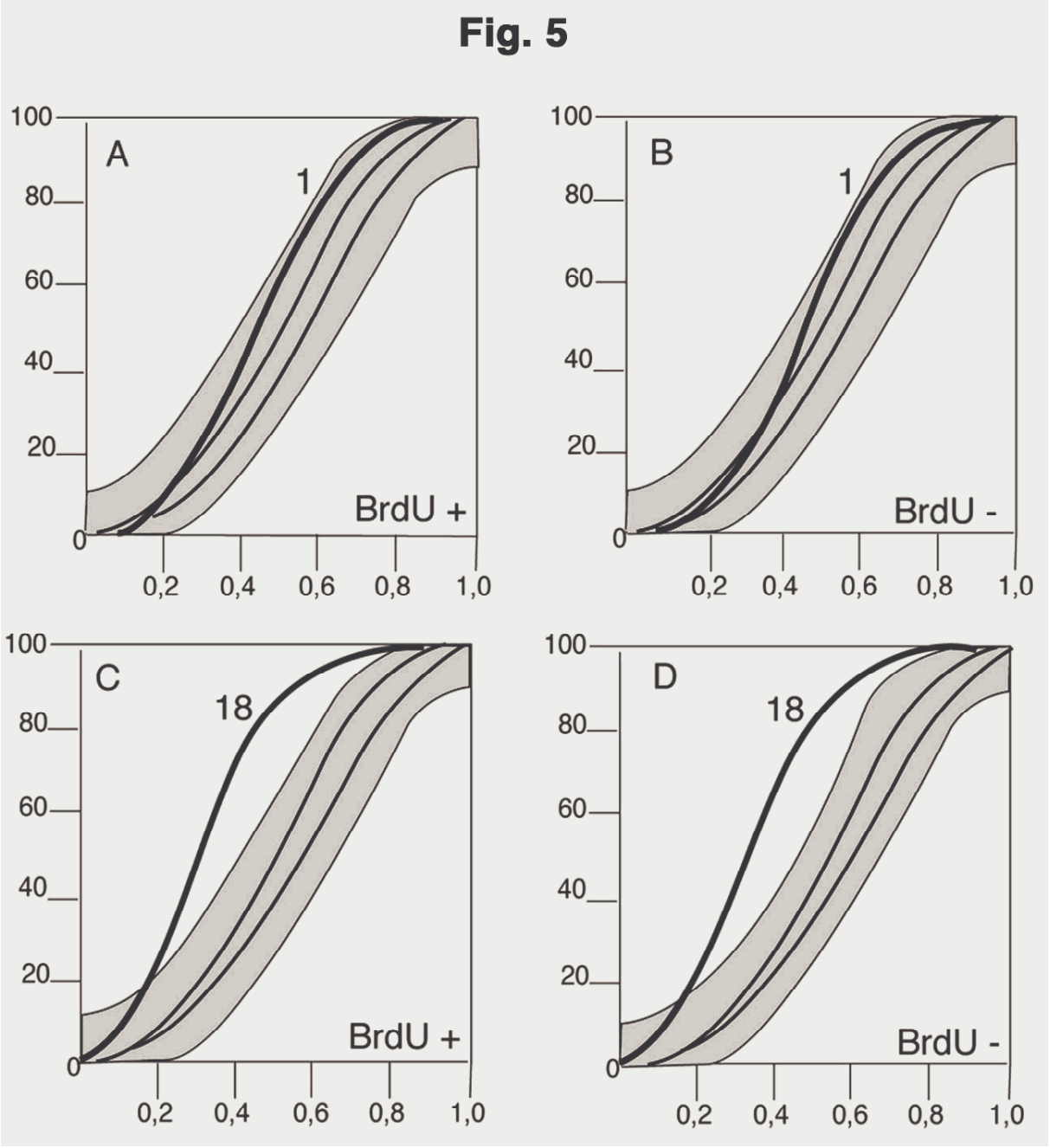

Figure 5: Cumulative frequency distribution curves for 1q12-CNP distances (A, B) and 18c-CNP distances (C, D) obtained in amniotic fluid cell nuclei after pulse-labelling with BrdU. Abscissa: normalized 2D distances. Ordinate: percentage of nuclei with a normalized distance equal to or smaller than the corresponding distance on the abscissa. While target-CNP distance distributions obtained for the two different chromosomes confirm their different distribution (compare A and C), no difference could be detected with regard to the cell cycle stages: curves for cells in S phase and for nuclei without chromatin replication are similar for both chromosome 1 (compare A and B), and for chromosome 18 (compare C and D).

II.1.1.9.3. Different 2D radial arrangements of CTs of large and small chromosomes in fibroblast nuclei

In further experiments we studied the 2D-positions of territories of large chromosomes, (comprising #1-5 and X) and of small chromosomes (comprising #17-20) in human fibroblast nuclei (Figure 6). For this purpose, primary human diploid fibroblast cultures were maintained in a confluent state for three days prior to fixation, resulting in less than 1% of cells being identified in S phase by BrdU incorporation (data not shown). Pools of differently labelled paint probes for large and small chromosomes, comprising approximately 40% and 10% of the human genome, respectively (Morton, 1991), were hybridized to 3D preserved nuclei, which were rather flat with a z-extension in the order of 3 to 4 µm. Light optical serial sections were obtained from 67 fibroblast nuclei. For example, Figure 6C shows the maximum intensity 2D projection and Figure 6D four single light optical sections from a typical nucleus. The painted CT-pools were typically observed side by side and did not overlap (compare Figures 6C and 6D). The set of larger CTs was found predominantly towards the 2D nuclear rim in contrast to the set of smaller CTs, which was observed closer to the 2D nuclear centre. Two-dimensional projections of serial sections (Figure 8A) from 67 nuclei were quantitatively evaluated. The peak content of DNA from the small chromosome pool was found at a relative radius of 42%, while the maximum content from the large chromosome pool was observed at 75% of the relative radius. Evaluations from nuclear mid-plane sections gave almost identical results (data not shown). These results are consistent with the different localization of (para)centromeric heterochromatin of small and large chromosomes in amniotic fluid cell nuclei.

Within the set of the small human chromosomes #17 – 20 and Y chromosomes #17,19 and 20 are mostly early replicating and gene dense, with #19 being the most gene dense. Chromosome #18 and Y on the other hand are mostly later replicating and gene poor, (Craig and Bickmore, 1994); Deloukas et al., 1998; Lander et al., 2001).the latter carries only relatively few although important genes on its short arm and on Yq11, while Yq12 is comprised by a large block of late replicating repetitive sequences.

Irrespective of these differences the hybridization for each of the territories of chromosomes #18, 19 and Y revealed a similar distribution pattern predominantly found in the centre of the 2D nuclear projection as shown for #18 and 19 in Fig. 6E. [3]

[3] An evaluation of chromosome #15 in interphase fibroblasts has been performed yet

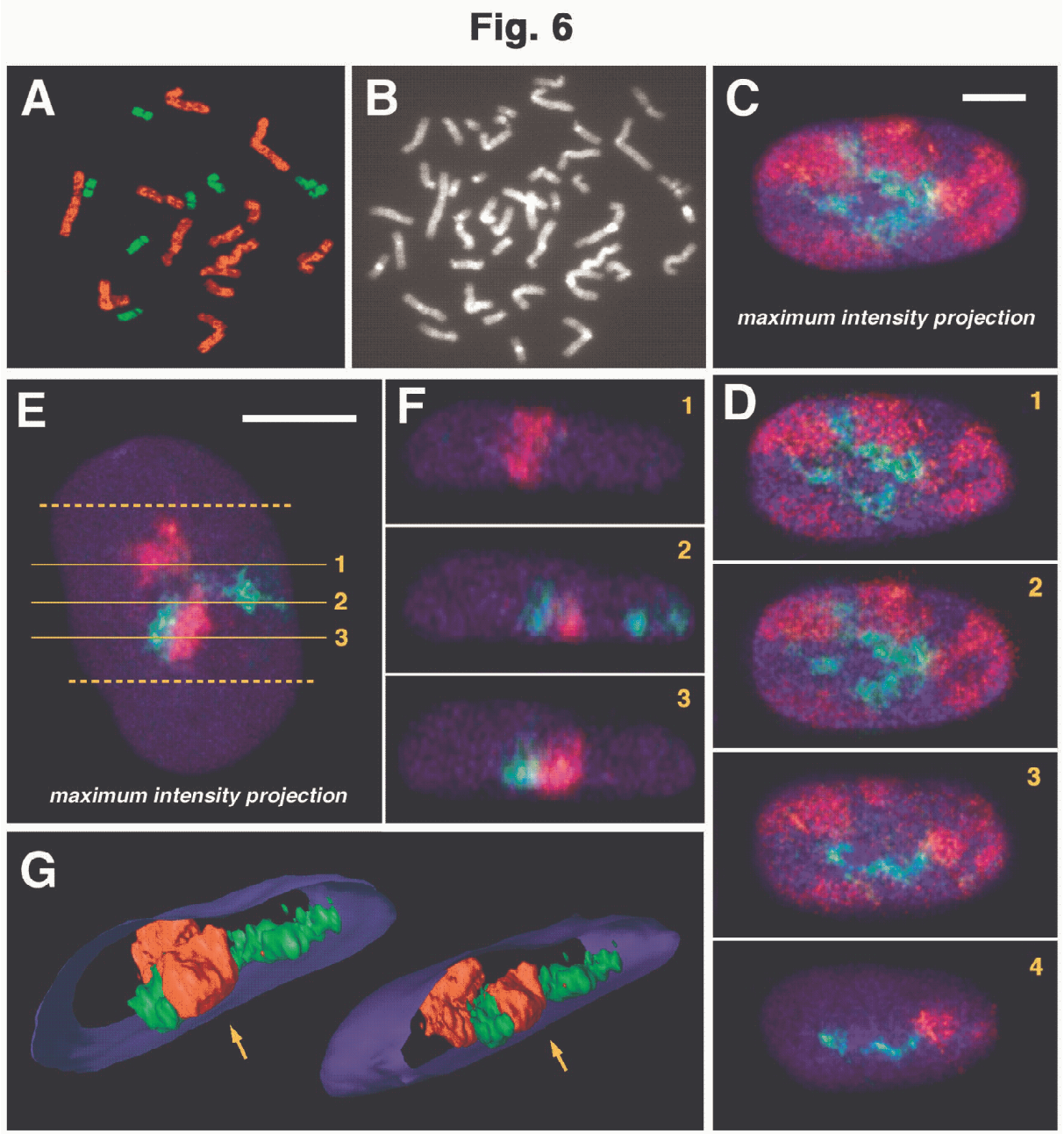

Figure 6. Distribution of small and large CTs in the flat nuclei of primary human fibroblasts. (A) FISH on metaphase spread with two probe pools for the large chromosomes (1-5 and X, red) and for the small chromosomes (17-20, green). (B) The same metaphase after DAPI staining. (C) Maximum intensity projection of a series of confocal sections through a fibroblast nucleus after 3D-FISH with the same two probe pools as shown on A. The nucleus shows the typical distribution pattern of CTs: large CTs (red) occupy peripheral positions, while small CTs (green) are situated more centrally. Counterstaining (PI) is shown in blue. (D) Four optical sections, out of a total of 16, from the bottom (section #1) to the top (section #4) of the same nucleus as shown on (C). The distance between optical sections is 0.75mm. Fibroblasts are strongly flattened - only 3 - 4 mm thick in the central part - and the majority of

painted chromosome territories extend from the bottom to the top of the nucleus. Therefore, projection sufficiently represents the distribution of chromosomes in the whole nucleus (compare the projection on C and individual sections on D). (E-G) Spatial arrangement of CTs #18 (red) and #19 (green) in a fibroblast nucleus counterstained with PI (blue). (E) Maximum intensity projection; all four chromosome territories are found in the central area of the 2D projection. Lines 1-3 mark the positions of sections in x,z plane reconstructed using Amira software and shown on (F) (1-3, respectively). (G) 3D reconstruction (surface rendering) shown at two different tilting angles (rotation both around x and z axes). Surface of the nucleus is shown in blue, levels at which parts of the nucleus were cut off to show its interior are marked on E with dotted lines. Arrows point to the bottom of the nucleus. Note that both CTs # 18,19 lie close to the nuclear border. In this particular nucleus both homologues of the #19 lie closer to the bottom (G, F2,3). One of the #18 homologues is also located on the bottom (G, right, F2,3), while the other one is stretched between the top and bottom walls (G, right, F1). Bars = 5µm.

The visual inspection of z,y sections and rotation of 3D reconstructions allowed to show that #18, 19 and Y CTs were attached either to the nuclear top or to the nuclear bottom, and in few cases of #18 and 19 CTs expand from top to bottom (Figure 6F, G). A quantitative 2D analysis from nuclear projections resulted in similar distribution curves for #18, #19 and Y territories (Figure 8E, G) as well as for the pool of small chromosomes #17-20 (Figure 8A) with a content maximum for each around 30% to 40% of the relative radius, respectively; standard deviations argue against any significant difference. In agreement with our 2D - data for the positioning of 17c, 18c and Yq11 target sequences in amniotic fluid cell nuclei chromosome painting of the respective chromosome territories confirmed their positioning close to the CNP.

II.1.1.9.4. 3D evaluation of CT positions in human lymphocyte nuclei

Two colour FISH with the probe pools for large and small chromosomes as described above was also performed on unstimulated human lymphocytes. Nuclei of lymphocytes have a nearly spherical shape with a diameter of approximately 9-10 µm and therefore required a 3D evaluation of CT positions. Optical serial sections from 62 nuclei were recorded. Small chromosomes typically were clustered in the 3D nuclear interior, though some small CTs were found also at the nuclear periphery (see below). Territories of large chromosomes were preferentially located at the nuclear periphery (Figure 7A, B). The results of the quantitative

3D evaluation are shown in Figure 8B. For the pool of small chromosomes the maximal DNA content was observed in a relatively broad range, between 50% and 70% of the relative radius, while a peak content for territories of the large chromosomes was found at 80%. For comparison, 2D evaluation was performed from a subset of nuclei employing mid plane sections as well as 2D projections of light optical serial sections. In both 2D evaluations the relative radii of the maximum DNA content for smaller CTs were significantly smaller (26% and 36% respectively, data not shown) compared to the 3D evaluation. This substantiates the necessity of 3D evaluation for the spherical lymphocyte nuclei.

In 28 lymphocyte nuclei we analyzed the 3D positioning of the chromosome Y territories and in 37 nuclei the 3D positioning of the #18 CTs in comparison to the #19 territories (Figure 7C – E). In a set of 11 nuclei we also compared the 3D positioning of #18 CTs with #17, 19 and 20 territories. Optical serial sections revealed striking distribution differences between CTs of small chromosomes. Chromosome #19 territory was typically located around the nuclear centre, frequently in a very close association to each other making the identification of two distinct territories impossible. A similar distribution was found for chromosomes #17 and 20. The territories of the Y chromosome and of chromosomes #18, in contrast, were found in almost all cases at the nuclear periphery, both #18 territories often were situated quite apart from each other, as exemplified in Figure 7C-E. The 3D evaluation showed a maximum content for CT #19 around 40% (Fig. 8D) and of pooled chromosomes #17,19,20 around 45% of the relative radius (Fig. 8C). For CT #18 the maximum content was at 80-85% of the relative radius in both experiments (Figure 8C, D) and coincided with the maximum for the large chromosomes (Figure 8B). A similar peripheral distribution was found for the Y chromosome with a maximum content at about 82% of the relative radius (Fig. 8F).

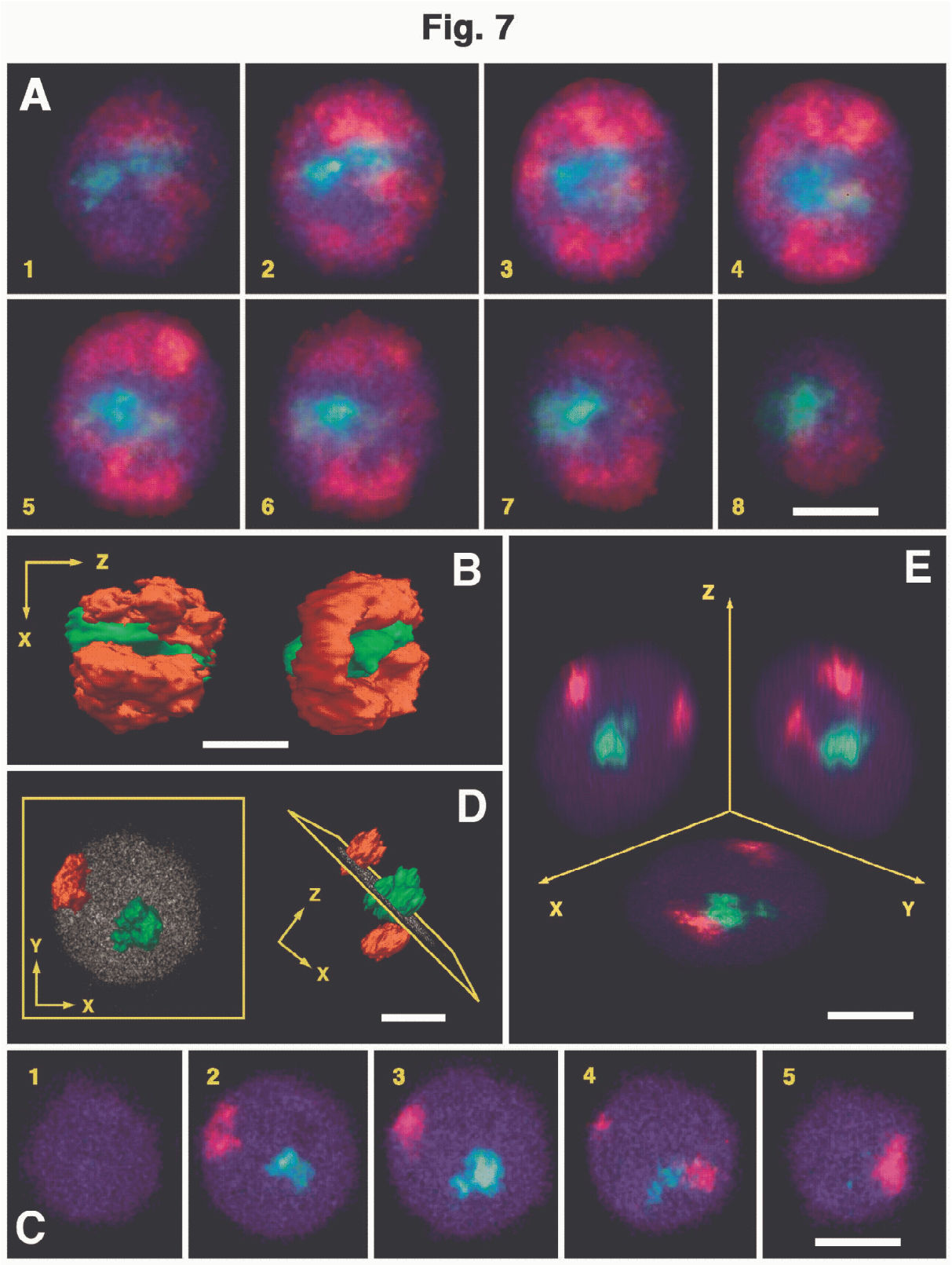

Figure 7. Distribution of small and large CTs in the spherical nuclei of human lymphocytes. (A) Gallery of optical sections through a lymphocyte nucleus after FISH with two probe pools: for large CTs (1-5 and X, red) and for small CTs (17-20, green); the nucleus was counterstained with YOYO-1 (blue). The distance between sections is 1mm. Large CTs are

located preferentially on the periphery of the nucleus; small CTs are situated mainly in the central area of the nucleus. (B) 3D reconstruction (surface rendering) of the same nucleus shown at two different angles. (C-E) Spatial arrangement of CTs #18 (red) and #19 (green) in lymphocyte nucleus; the nucleus was counterstained with PI (blue). (C) Gallery of optical sections; the distance between sections is 1.25 mm. (D) 3D reconstructions of CTs combined with a mid plane section of the counterstained nucleus (shown in gray). Reconstruction viewed along z axis (left) and along y axis (right). (E) Maximum intensity projections in three planes. Note that both homologs #18 are located at the nuclear periphery, while two homologs of #19 have a central localization typical of small chromosomes. Bars = 5µm.

Figure 8.[4] Quantitative evaluation of 2D-radial arrangements of CTs in fibroblast nuclei (A, E) and 3D-radial arrangements of CTs in lymphocyte nuclei (B-D, F). For a detailed description of the mapping of radial CT arrangements see Materials and Methods and Figure 2. The abscissa denotes the relative radius r of the 25 nuclear areas, used for 2D evaluations and 25 nuclear shells, used for 3D evaluations. The ordinate represents the normalized, relative DNA content of painted CTs in a given area or shell. For this purpose all pixel/voxel intensities of the fluorochrome employed for CT painting were summed up within a given area/shell. For normalization the total relative DNA content for CTs painted with a given fluorochrome or for counterstained nuclear DNA was summed up over all 25 areas/ shells and was set to 100. Bars represent standard deviations of the mean.

[4] Please see the Graphs in the chapter "Ergänzungen" of this chapter (II.1b.). There are more graphs and based on better cell nuclei series.

Fig. 8

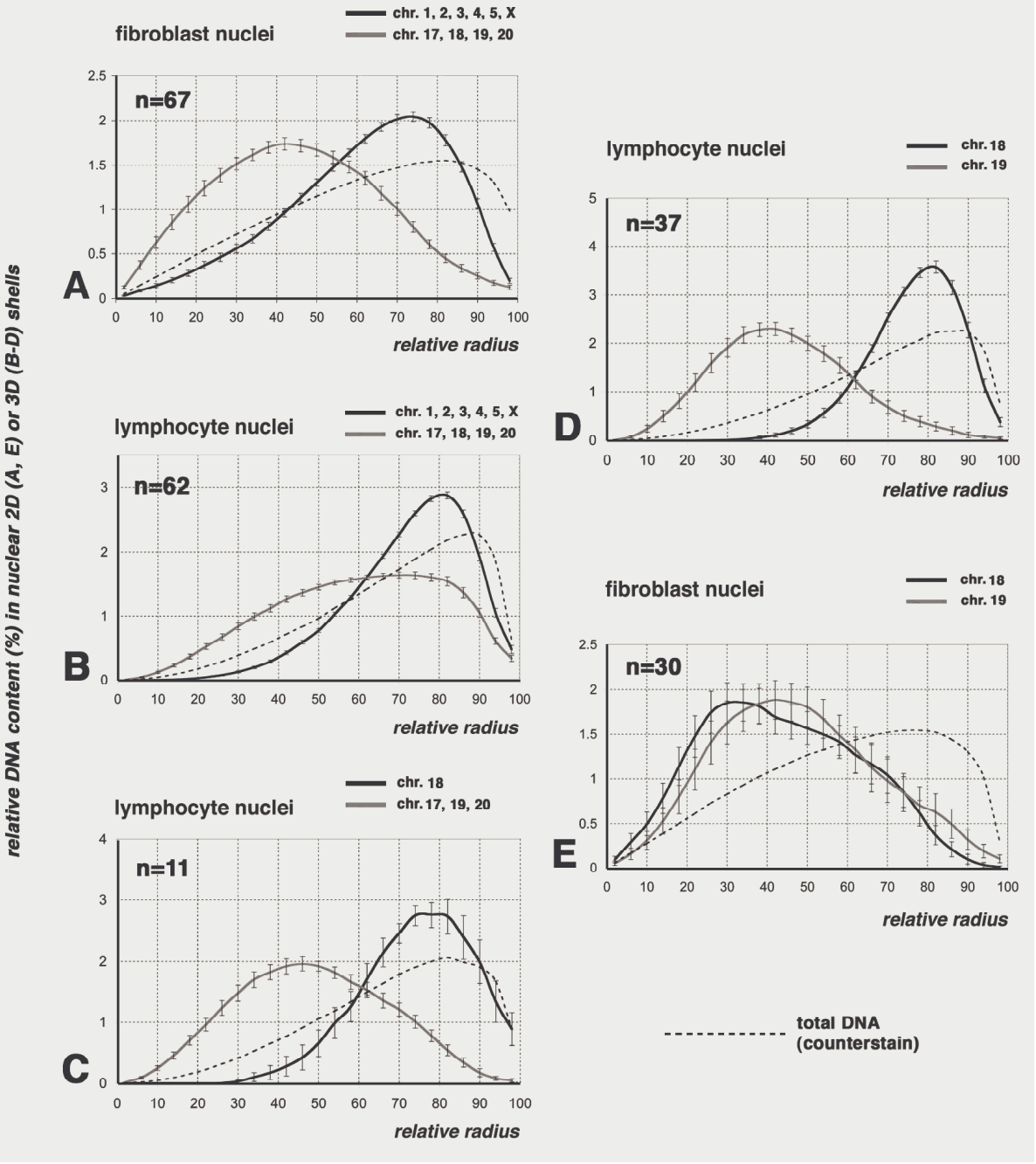
fibroblast nuclei
chr. 1, 2, 3, 4, 5, X
chr. 17, 18, 19, 20
n=67
A
relative radius
lymphocyte nuclei
chr. 18
chr. 19
n=37
D
relative radius
lymphocyte nuclei
chr. 1, 2, 3, 4, 5, X
chr. 17, 18, 19, 20
n=62
B
relative radius
fibroblast nuclei
chr. 18
chr. 19
n=30
E
relative radius
lymphocyte nuclei
chr. 18
chr. 17, 19, 20
n=11
C
relative radius
relative DNA content (%) in nuclear 2D (A, E) or 3D (B-D) shells
total DNA
(counterstain)

II.1.1.9.5. 3D modeling of spherical human cell nuclei with 46 statistically distributed CTs

For the comparison of the 3D positions of chromosome territories in human lymphocyte nuclei with computer simulations according to the "statistical SCD-model" (see M&M) we analyzed 50 simulated spherical nuclei with a statistical distribution of the human CTs. The 3D evaluation of these simulated configurations was executed in the same way as the experimental data stacks. In the first experiment, distribution of all 46 CTs was modeled and distances between gravity centres of simulated CTs to the nuclear centre were measured. Fig. 9E shows that gravity centres of large chromosomes were slightly shifted to the nuclear centre in comparison to the small sized chromosomes. In the second simulation, model data stacks representing nuclei with painted large (#1, 2, 3, 4, 5 and X) and small CTs (#17, 18, 19, 20) were calculated from configurations simulating the statistical distribution of all 46 human CTs. Figure 9A shows the 3D reconstruction of a typical model nucleus, and Figures 9B and 9C show virtual nuclear mid plane sections of two different modeled nuclei, calculated under conditions that reflect the limited resolution of a confocal scanning microscope. The distributions of both simulated chromosome groups were similar (Figure 9D) although a small shift of the larger CTs towards the centre of the model nuclei was notable in agreement with the data shown in Fig. 9E. In conclusion, a statistical distribution of small and large CTs in model nuclei produced results not consistent with observations described above for CT positions in human lymphocyte nuclei (compare Figures 8B and 9D).

Figure 9. Arrangements of large (#1, 2, 3, 4, 5 and X) and small (#17, 18, 19, 20) CTs in spherical human model nuclei containing 46 statistically distributed CTs. The SCD (spherical 1-Mb chromatin domain) model was applied assuming that each chromosome is built up by a number of 1 Mb-chromatin domains that reflects the DNA content of the respective chromosome (for details see Material and Methods). (A) 3D reconstruction of a calculated virtual stack of a spherical human model nucleus with virtually painted large (red) and small (green) CTs. Visualization was done with Persistence of Vision Raytracer (TM) Povray (TM). (B) and (C) show mid sections of the virtual data stacks of two different model nuclei. The virtual counterstain (blue) represents a smoothed image of all 46 simulated CTs after convolution. (D) 3D radial arrangements of the large and small CTs in 50 simulated spherical

model nuclei. The evaluation method was the same as for the mapping of 3D-radial CTs arrangements in human lymphocyte nuclei (compare with Figure 8B). (E) Mean 3D distances between the gravity centres of virtual CTs and the virtual nuclear centre in 50 simulated spherical nuclei are shown as a function of DNA content reflecting the size of modeled CTs. The distributions of both simulated CT groups show - in spite of a large internuclear variability - the slightly preferential location of small CTs at the nuclear periphery and of large CTs in the nuclear interior. This result is in stark contrast to the 3D radial CT arrangements observed in real lymphocyte nuclei.

Fig. 9

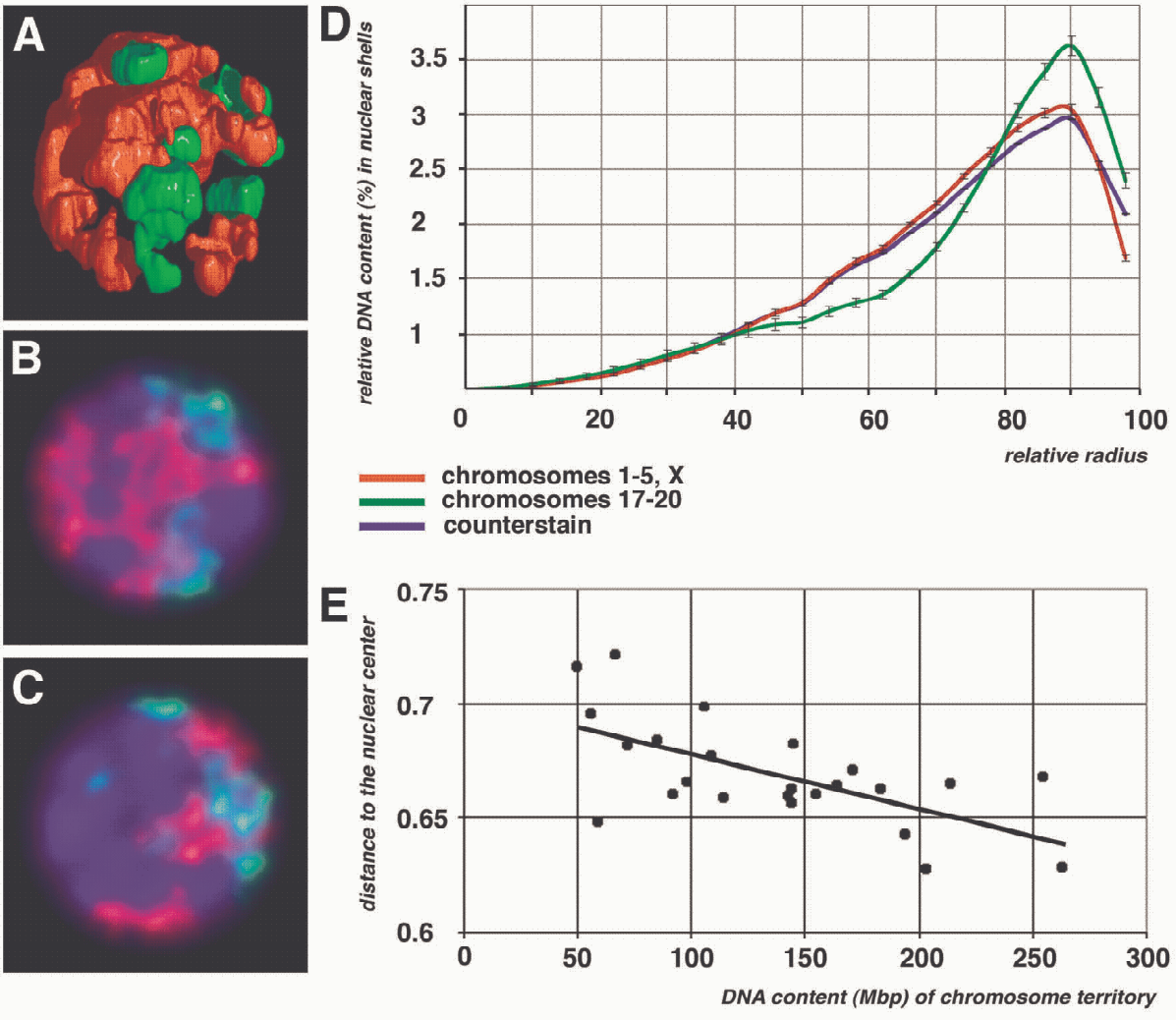

II.1.1.10. Discussion

In this study we observed non-random radial nuclear positions of human chromosome specific constitutive heterochromatin and entire CTs. In contrast,

we found that side by side arrangements of specific homologous and non-homologous targets were highly variable. Our findings expand previous studies from our and other groups (see introduction) and shed new light (1) on the controversy regarding random or non-random chromosome arrangements in human cell nuclei and (2) on the question, whether CT arrangements differ in nuclei with different shapes such as ellipsoid nuclei of fibroblasts or amniotic fluid cells and spherical lymphocyte nuclei.

In amniotic fluid cell nuclei we noted non-random 2D-radial arrangements of constitutive heterochromatin. Targets from a group of smaller chromosomes (#15, 16, 17, 18 and Y) were distributed significantly closer to CNP (centre of the 2D-nuclear projection), the Y target being the closest, while targets of larger chromosomes (#1, 3, 4, 7, 8, 12 and X) were preferably located towards the periphery of the 2D nuclear projection, i.e. the nuclear rim. Similar 2D-radial arrangements were observed both in S-phase and non-S-phase cells. Although this finding argues against drastic changes of 2D target arrangements during the cell cycle, it does not exclude cell cycle specific positional changes in the third dimension, resulting, e.g. in different association frequencies of centromeric heterochromatin with the top or bottom nuclear envelope at different stages of the cell cycle (our unpublished data).

In contrast to these specific 2D radial arrangements, we observed highly variable side by side arrangements of heterologous and homologous heterochromatin blocks with respect to each other as demonstrated by the pronounced cell to cell variability of the 2D-distances measured between these targets. Taking into account that the difference between 2D–distances and true 3D–distances is small in the rather flat – ellipsoid amniotic fluid cell nuclei, these 2D results indicate variable 3D side by side arrangements of heterochromatin targets as well.

In agreement with the non-random radial arrangements of larger and smaller CTs in fibroblast nuclei discussed below, 2D target-target distances between heterochromatin targets of smaller homologous and heterologous autosomes were significantly smaller than the respective distances measured between heterochromatin targets of larger chromosomes. Notably, these smaller target-target distances are compatible with the hypothesis of a random side by side distribution of smaller chromosomes in the nuclear interior.

Presently, we have no positive evidence for non-random associations, not to mention somatic pairing, of any pair of homologous chromosomes in the studied cell types. Our results are in agreement with previous data arguing against an association of homologues in nuclei of fibroblasts and lymphocytes provided by Chandley et al. (1996); Emmerich et al. (1989); Ferguson and Ward (1992); Leitch et al. (1994); Lesko et al. (1995); Popp et al. (1990); Vourc'h et al. (1993), and Alcobia et al. (2000). The latter however found non-random spatial associations of certain heterologous centromeres which were not restricted to acrocentric chromosomes. These results are hardly compatible with a precise circular arrangement of chromosomes in prometaphase rosettes of fibroblasts described by Nagele et al. (1995). It seems unlikely that side by side arrangements of chromosomes in mitosis, i.e. at a time when chromosomes are transcriptionally inactive, should be much more precise than during interphase.

Observations of painted CTs in 3D-preserved fibroblast nuclei showed a distribution of large and small CTs consistent with the observed non-random radial arrangements of heterochromatin targets in amniotic fluid cell nuclei. Following two-colour FISH with probes for large and small chromosomes, analysis of mid-plane sections and projections of entire stacks of serial sections demonstrated that large CTs were located preferentially towards the 2D nuclear rim. CTs of small chromosomes (#17 – 20 and Y) were located close to CNP with a similar distribution for each of the separately tested territories (#18, #19 and Y). Apparently, these territories were directly associated with the top or bottom part of the nuclear envelope top or bottom as shown by DNA counterstaining.

Preliminary evidence for a size correlated arrangement of CTs in interphase nuclei of fibroblasts and amniotic fluid cells have been reported by (Emmerich et al. (1989); Höfers et al. (1993); Popp et al. (1990). These studies were based on FISH experiments with probes specific for the centromeric regions of chromosome #1 and #15, X and #18, #7 and #15, respectively. Recently, Sun et al. (2000) presented further evidence for a size-dependent positioning of CTs in human fibroblast nuclei. These authors analysed the positioning of nine different subtelomeric q-arm probes and found the q-arm ends of large chromosomes more towards the nuclear rim than those of small

chromosomes. In a study of proliferating fibroblasts Bickmore and coworkers did not find a constant relationship between chromosome size and nuclear position but rather with gene content (Boyle et al., 2001). The distribution of the similarly sized human CTs 18 and 19 provides a striking example: In proliferating fibroblast nuclei Croft et al. (1999) reported the preferential localization of the gene-dense #19 CTs towards the 2D nuclear centre and of the gene-poor #18 CT towards the nuclear edge. The latter observation is in disagreement with our observations in both proliferating amniotic fluid cells (Figure 5C) and proliferating fibroblasts (our unpublished data). In both cell types we found #18 territories towards CNP. In agreement with our own observations Bridger et al. (2000) reported the central location of #18 territories in nuclei of Go fibroblasts. These authors claim that #18 CTs move from a more peripheral to a more central position when fibroblasts exit the cell cycle.

In the spherical lymphocyte nuclei the territories of the large chromosomes #1 – 5, X were found predominantly towards the 3D nuclear periphery. Compared to our findings in the ellipsoid nuclei of fibroblasts and amniotic fluid cells, however, the distribution pattern of small CTs was strikingly different. The gene-dense #17, 19 and 20 were clustered in the 3D-nuclear interior often without any recognizable attachment to the nuclear envelope (note: we cannot exclude the possibility of nuclear envelope invaginations). In contrast, the territories of the gene poor chromosomes #18 and of the Y chromosome were always observed towards the nuclear periphery, apparently abutting the nuclear envelope.

Our results obtained from unstimulated lymphocytes are in agreement with data on PHA stimulated lymphocytes and lymphoblastoid cells, recently published by Croft et al. (1999). These authors first described the preferential localization of the gene poor #18 CTs towards the nuclear periphery and of the gene dense #19 CTs towards the nuclear centre.

These differences in the distribution of gene poor and gene dense territories from chromosomes with similar DNA contents supports the hypothesis that in lymphocyte nuclei gene density of CTs may indeed be an important parameter with regard to 3D-radial arrangements. Further support for this claim was recently provided by the Bickmore group in a study of 2D-radial arrangements of all human CTs in nuclei of lymphoblastoid cells (Boyle et al., 2001). More gene-dense CTs were preferentially located towards the nuclear centre, while gene-poor CTs were observed at the nuclear edge. Interestingly, the Y chromosome, which is by far the chromosome with the lowest gene density, occupied an intermediate position in their investigation. In contrast, we found a distinctly peripheral position of the Y in

Go lymphocyte nuclei as well as in lymphoblastoid cells. (data not shown). Different protocols employed in our laboratory and in the Bickmore laboratory should be taken into consideration. In our experiments, lymphocytes were first attached to polylysine coated slides, then fixed with buffered paraformaldehyde and further treated in a way that preserved their spherical shape as best as possible during FISH. In particular, the cells were never air dried throughout the entire procedure. Data obtained in the study of Boyle et al. (2001) were obtained from lymphocytes subjected to hypotonic solution, fixed with methanol/acetic acid and air dried prior to FISH. This procedure results in severely flattened nuclei and affects interior and peripheral CT arrangements to an unknown extent.

Zink and coworkers have demonstrated a polarized arrangement of CTs (Sadoni et al., 1999). In agreement with previous studies (for references see Sadoni et al. (1999) gene poor, mid-late replicating chromatin was preferentially observed at the nuclear periphery and around the nucleoli, while gene dense, early replicating and transcriptionally active chromatin was noted in the interior nuclear compartment that expands between the peripheral and perinucleolar compartments. This distinct radial distribution of early and mid-late replicating chromatin was observed in nuclei of normal, as well as malignant cell types with highly rearranged chromosomes. The polarized arrangements of gene dense and gene poor chromatin were noted not only in all cell types from man and other mammals so far but also in chicken (see (Habermann et al. (2001), this issue) for a thorough discussion of conserved motifs of higher order chromatin architecture detected in various cell types from human and chicken). These findings let us conclude that evolutionary conserved motifs of higher order chromatin arrangements exist. The observed differences in the radial distribution of #18, 19 and Y CTs as well as available evidence from the literature (Koutna et al., 2000; Skalnikova et al., 2000), are also suggestive for functionally important radial chromatin arrangements. Comparing the centromere distribution from human chromosomes 8, 9, 14 and 22 these authors found the preferential positioning of these centromeres towards the nuclear periphery, while gene loci were located significantly closer to the nuclear centre suggesting an orientation of chromosome arms towards the nuclear interior. Possible functional implications of different radial CT arrangements noted in different cell types still remain obscure. Sadoni et al. (1999) have suggested that neighbouring CTs build up genetically active and inactive higher order nuclear compartments in the cell nucleus. While the formation of these compartments requires contributions from similarly “polarized“

neighbouring CTs, it is fully compatible with the high variability of side by side CT arrangements observed in all cell types studied so far by us and others.

This variability should also be considered in the context of chromosome reshuffling that has occurred during evolution. For example, a minimum number of 160 rearrangements distinguishes the mouse from the human karyotype (O'Brien et al., 1999). If a functional nuclear architecture required strict side by side arrangements of entire sets of CTs, balanced reciprocal translocations should often lead to failures of development. This is apparently not the case. This argument, however, does not exclude special instances where the neighbourhood of specific chromosome segments is required for functional reasons (Nikiforova et al., 2000).

As models for a random distribution of heterochromatic regions in amniotic fluid cell nuclei we simulated randomly distributed points in ellipsoids and flat cylinders, respectively. The 2D target-target distances experimentally measured between homologous and heterologous heterochromatin targets of the larger chromosomes fit the random expectation, while the distances between the respective targets of smaller chromosomes were highly significantly smaller. The effects of topological constraints which result from the fact that heterochromatin targets are structural parts of entire CTs are apparently small (see Introduction). The simulation of point like targets that do or do not belong to model CTs gave similar 2D-target-target distances (C. Münkel, personal information). Thus we believe that the simplified way of modelling 2D distances was sufficiently accurate for comparison with 2D distances experimentally measured in amniotic fluid cell nuclei .

The development of improved computer models to generate model CT distributions is an important but demanding task. The size differences of chromosomes in the human and even much more pronounced in the chicken karyotype (see Habermann et al., (2001) this issue) may result in topological constraints that affect the distribution of large and small CTs considerably. If so, a significant difference between a random, i.e. uniform and independent 3D distribution of points within a set of geometrical bodies (spheres, ellipsoids, flat cylinders etc.) and the experimentally observed 3D distribution of CTs or subchromosomal regions in a set of nuclei with a comparable geometrical configuration, may simply mean that the topological constraints imposed on objects with different sizes and complex shapes enforce a distribution which is different from the random distribution of points – a trivial finding. In an attempt to model the statistical distribution of all 46 human CTs within nuclei, the spherical 1-Mb chromatin domain (SCD) was developed. For simplicity, we considered only model

nuclei with spherical shapes and assumed that the volume of each territory is strictly related to its DNA content (although it is possible that CTs with a high density of active genes show different shapes and volumes as compared to CTs with low gene densities and mostly inactive genes). The distribution of large and small CTs in these spherical model nuclei differed from our observations in real lymphocyte nuclei. In particular, our present 3D modelling of CT arrangement did not predict the distinct differences in the distribution of #18 and #19 CTs. One should note, however, that several parameters that could influence the distribution patterns of CTs, such as possible differences in size, shape and structural rigidity, have not been systematically studied so far.

II.1.1.11. Acknowledgements

We thank R. Heintzmann and B. Schaedler for their help in image analysis procedures. This work was supported by grants from the Deutsche Forschungsgemeinschaft to T.C. (Cr 59/19-1 and Cr 59/20-1) and from the European Union to C.C. (FIGH-CT1999-00011). G.K. received a grant from the Deutsche Forschungsgemeinschaft for graduate students "modeling and scientific computing".

II.1b. Ergänzungen des Vergleiches zwischen Fibroblasten und Lymphozyten[5]

II.1b.1. Morphologische Parameter[6]

Nicht nur die Lage von subnuklearen Strukturen waren von Interesse, sondern auch deren Form. Als zusammenhängende Objekte wurden Gesamtheiten von Voxel angesehen, die heller als ein Schwellwert waren und mindestens über eine 3D- Ecke zusammenhingen (sog. 3D Nachbarschaften) .Als Formparameter wurden untersucht: die Volumina, die Oberflächen, die Roundness und die Smoothness. Die Roundness wird proportional dem Quotient zwischen dem Quadrat des Volumens und dem Kubus der Oberfläche definiert. Diese Größe hängt stark von der Rauheit der Oberfläche des Objektes ab. Dabei konnten die Werte der Roundness aufgrund der Digitalisierung und der so vergrößerten Oberfläche nur Werte zwischen 0 und 0,34 erreichen, statt zwischen 0 und 1.

$$\text{Roundness} = 36 \cdot \pi \cdot \frac{Vol^2}{Ob^3} \qquad \text{(II.1b.1)}$$

Die Smoothness hing dagegen Hauptsächlich von der Form im Großen ab. Im Zähler steht die Summe aller Abstände im Quadrat aller Punkte einer Kugel zu dessen Schwerpunkt. Dabei soll das Volumen der Kugel gleich groß wie das des Territoriums sein. Im Nenner steht die Summe aller Abstände im Quadrat aller Punkte des Territoriums zu dessen Schwerpunkt.

$$\text{Smoothness} = \frac{\int_{Kugel} [(x - xs)^2 + (y - ys)^2 + (z - zs)^2] dxdydz}{\int_{Territorium} [(x - xs)^2 + (y - ys)^2 + (z - zs)^2] dxdydz} \qquad \text{(II.1b.2)}$$

Hierbei wurden auch in der digitalen Praxis Werte zwischen 0 und 1 erreicht.

[5] In Kapitel II.3.1. können noch Graphen von Hühnerneuronen eingesehen werden.
[6] Siehe [Edelmann 1996]

II.1b.1.1. Territorienbilder

Fibroblasten (I.Solovei)

Chr #18 Chr #19

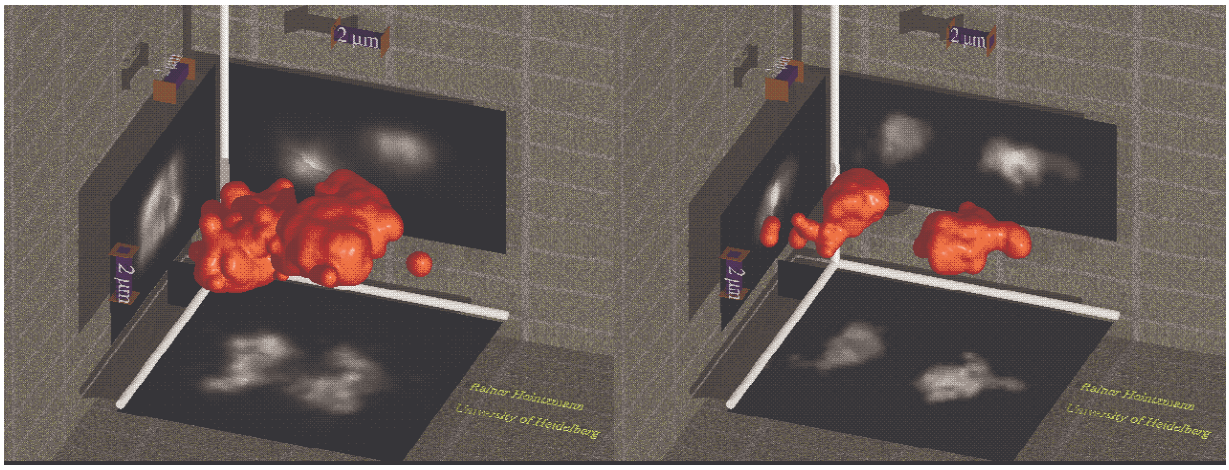

Lymphozyten (M. Hofbauer)

Chr #18 Chr #19

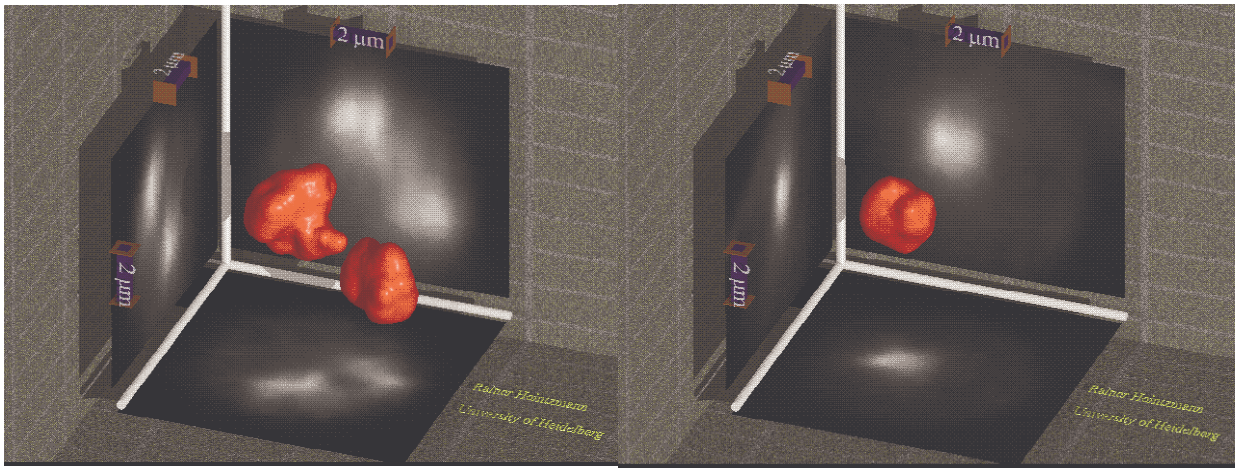

Abb.II.1b.1.Hier scheint es, dass in Lymphozyten die Chromosomen runder sind als in Fibroblasten. Das könnte an der unterschiedlichen Fixierung der Zellen liegen: wie bereits in der Einleitung diskutiert wurde, durchlaufen Lymphozyten zuerst eine Schrumpfung durch Austrocknung und dann wieder eine Aufblähung. Die Form könnte dabei sich ändern und kugelförmiger werden.

Aufgrund der unterschiedlichen Fixierungen lassen sich die Formen von Fibroblast- und Lymphozytenkernen nicht vergleichen. Es konnten aber noch die Formparameter verschiedener Chromosomenterritorien der Fibroblasten bestimmt werden.

II.1b.1.2. Formparametergraphen

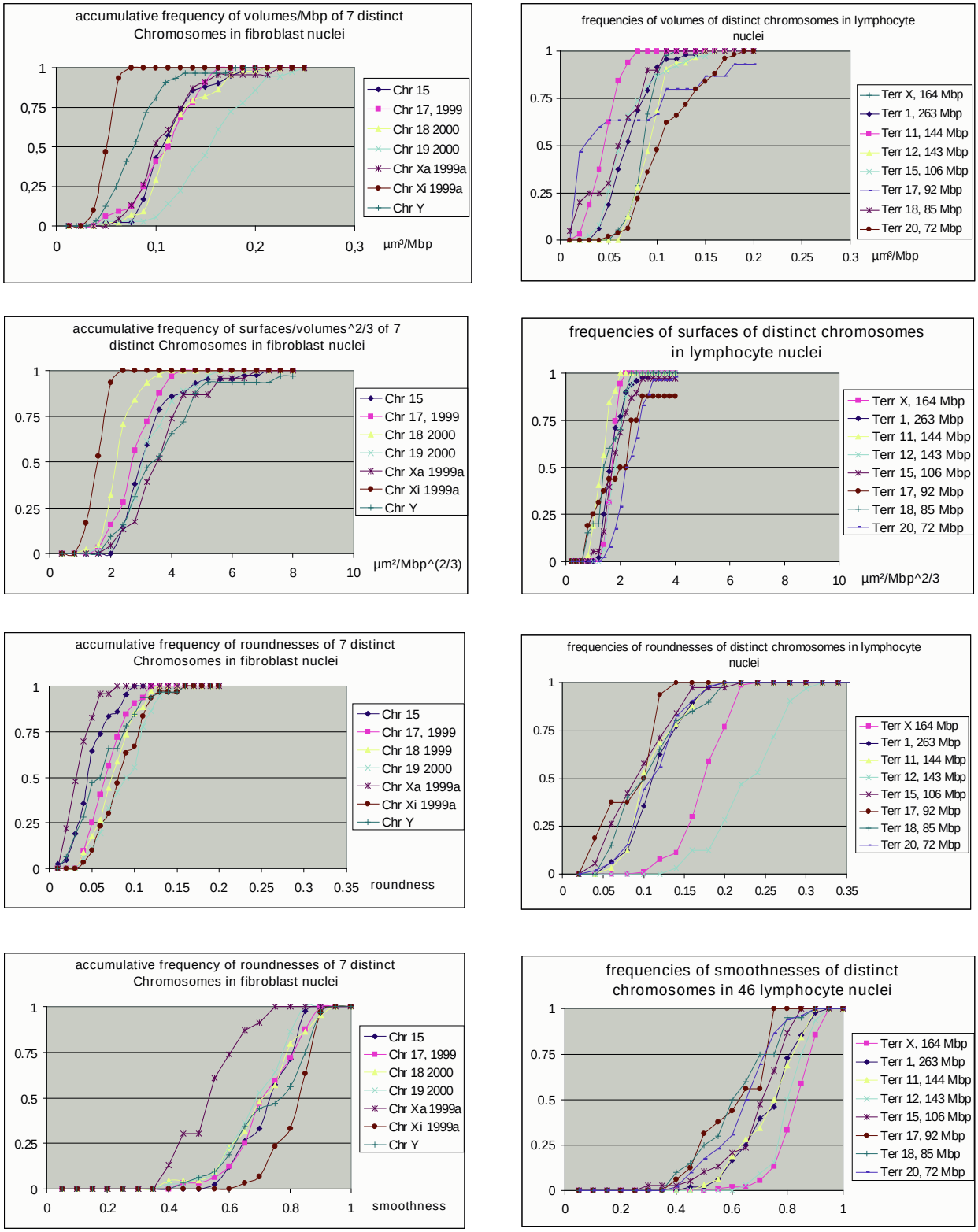

Abb.II.1b.2.In Fibroblasten gibt es eine hohe Variation in der Dichte (Vol/Mbp). Besonders das inaktive X-Chromosom ist doppelt so stark verpackt wie die anderen Territorien (s. erste Reihe). Bei der Oberfläche und der Roundness ist der Unterschied zwischen Fibroblasten und Lymphozyten besonders groß (2. und 3. Reihe). Interessanterweise ist der Unterschied in der

Variationsbreite zwischen Fibroblasten und Lymphozyten in der Smoothness aber weniger ausgeprägt. Die beiden Homologen des X-Chromosoms in Fibroblasten unterscheiden sich stark, auch in der Smoothness. Die X-Homologen in den weiblichen Lymphozyten wiesen dagegen eine geringe Variation auf.

II.1b.2. Übersicht über alle radialen Auswertungen

Zusätzlich zu den bisher gezeigten Ergebnissen wurden weitere radiale Auswertungen gemacht. Zum einen betrifft es das Chromosom #15, sodann bei den Lymphozyten die Chromosomen # 1, #11, #12, # 17, #20 sowie X. Hier wurde zwischen der Position der Chromosomen und der Centromere in den Lymphozyten verglichen, sowie bei den Fibroblasten von allen Territorien die Lage der Chromosomenschwerpunkte ausgewertet und graphisch aufbereitet (vgl. im Anhang S. 3,4 mit S.16,17)

II.1b.2.1. Multi FISH Bilder

Es wurden an 43 Fibroblasten mit einem 7 Multicolor – FISH Verfahren alle Territorien in der Zelle mit einem kombinatorischen Färbeverfahren hybridisiert. (Einzelheiten s. z.B. in [J.v.Hase 1999], sowie [A.Bolzer 2002]).

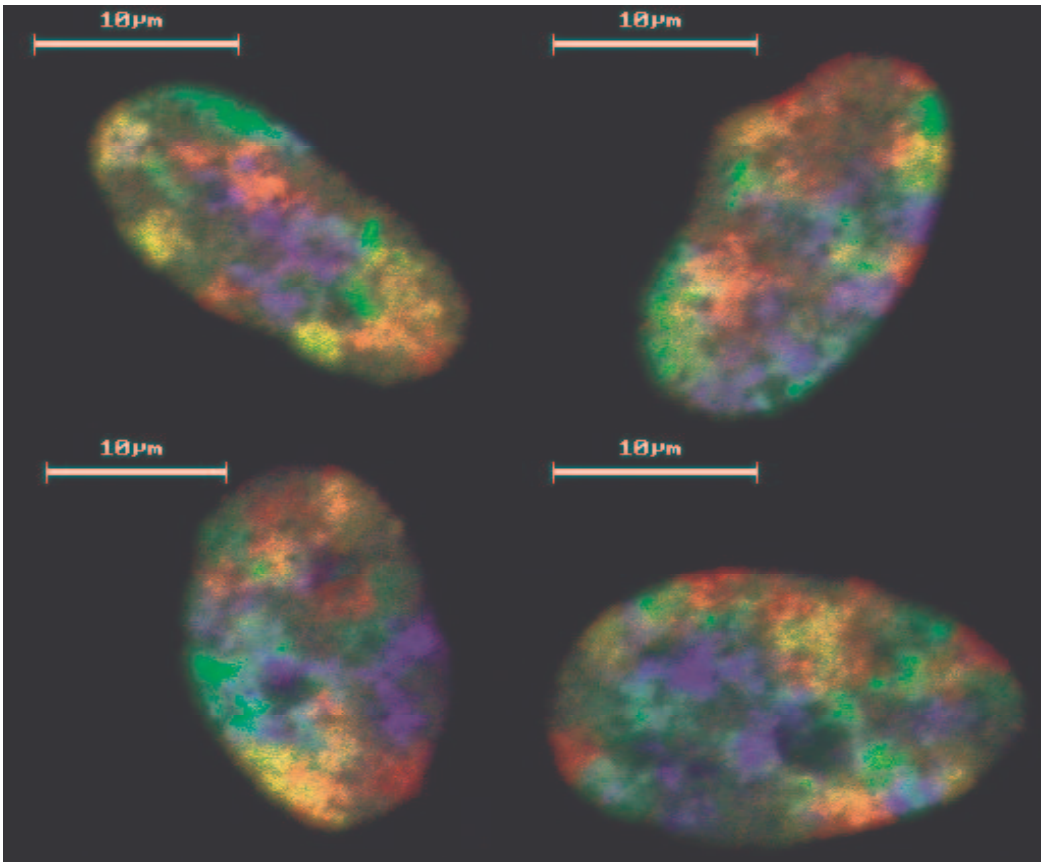

Abb.II.1b.3. In obiger Abbildung sind 4 Beispiele für eine rot-grün-blaue Anfärbung.

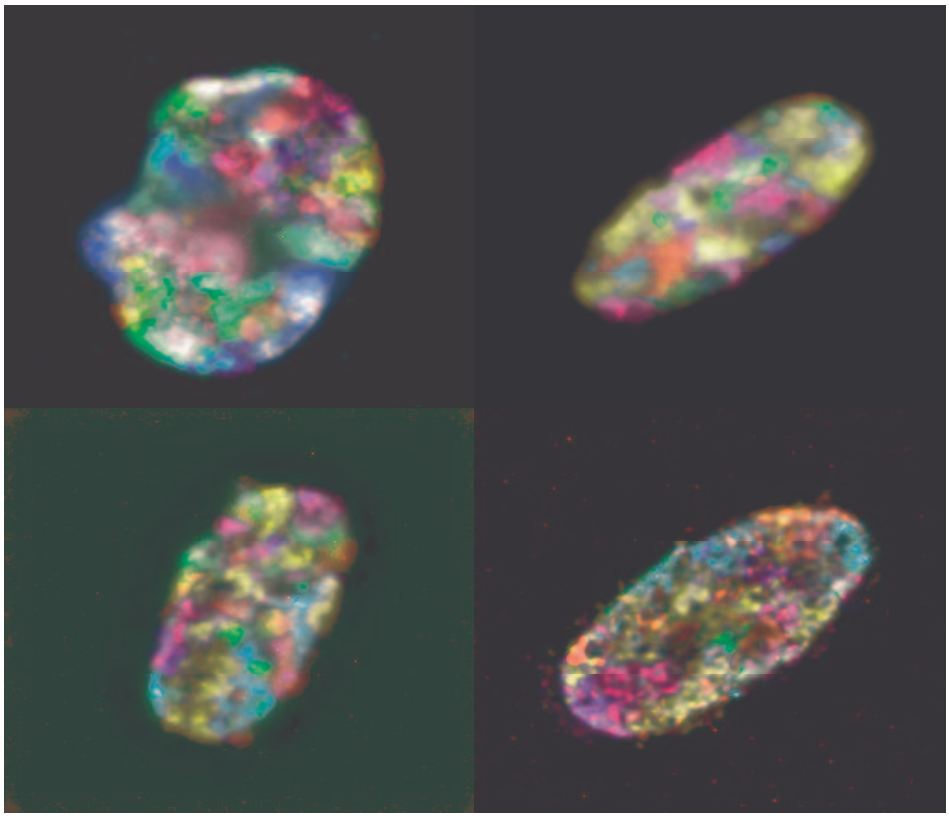

Abb.II.1b.4. In obiger Abbildung sind 4 Beispiele für Multicolor FISH mit 7 Grundfarben

Von allen Territorien wurde der Schwerpunkt ermittelt. Dann wurde mit Zuhilfenahme der Gegenfärbung eine Kernkartierung (Erklärung s. Einleitung, Kap I.2.) mit nur 10 Schalen erstellt. Zusammen mit den Koordinaten der Schwerpunkte wurden die radialen Werte der Schwerpunkte ermittelt und davon eine Häufigkeitsverteilung und eine kumulative Häufigkeit erstellt.

II.1b.2.2. Graphen zur Chromosomenposition in Fibroblasten und Lymphozyten

Die Diagramme die Fibroblasten betreffend werden in der kumulativen Form gezeigt, da die gewöhnlichen Häufigkeitsverteilungen trotz der guten Statistik sehr „wellig“ waren und somit die Darstellung mehrerer Kurven in einem Diagramm unübersichtlich gewesen wäre. Die Welligkeit rührt daher, dass nicht ganze Territorien, sondern nur die Territorienschwerpunkte in die Auswertung eingingen. Die Diagramme der kumulativen Häufigkeiten stehen im Anhang (S 3,4). Dabei sieht man Kurven rechts und links von der kumulativen Kurve der Gegenfärbung. Die Kurven rechts von der Gegenfärbung sind periphere Chromosomen, die links davon zentrale Chromosomen.

Es folgt eine Übersicht über den Vergleich zwischen Fibroblasten und Lymphozyten:

Fibroblasten

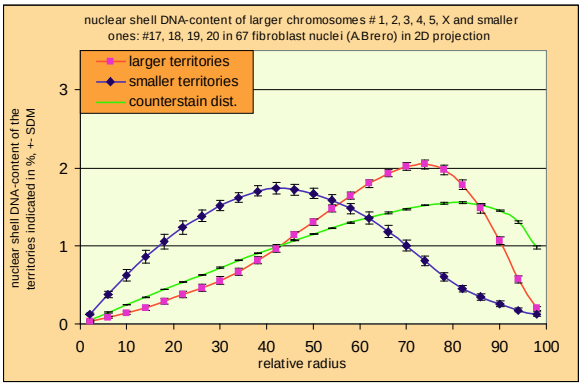

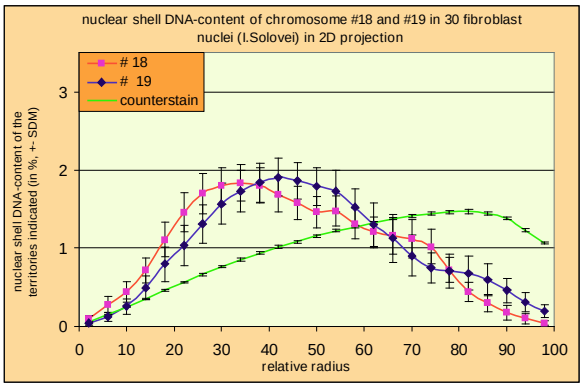

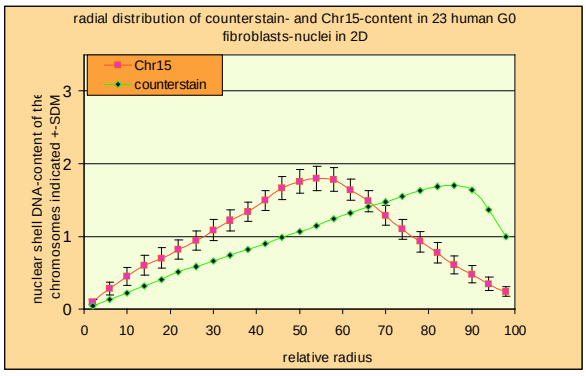

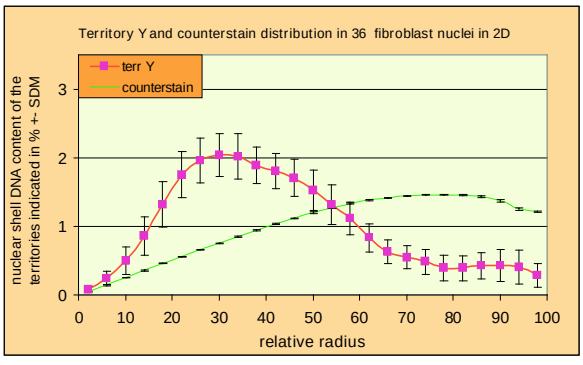

Lymphozyten

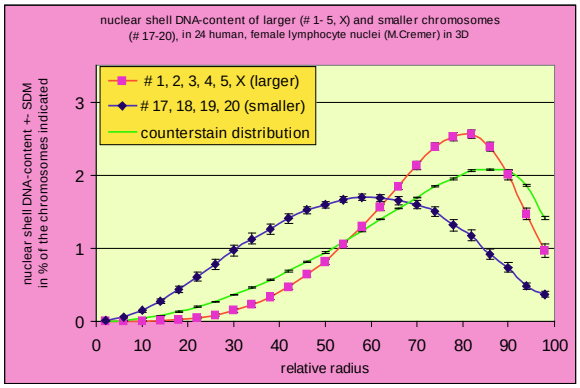

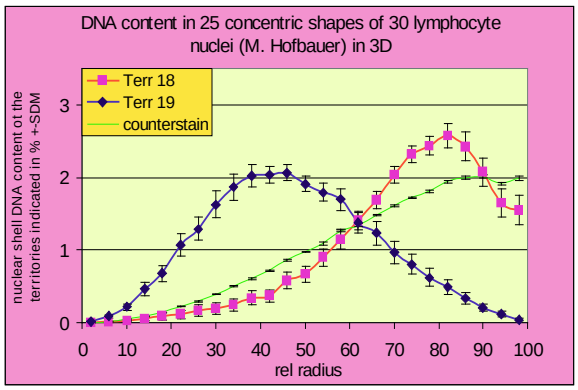

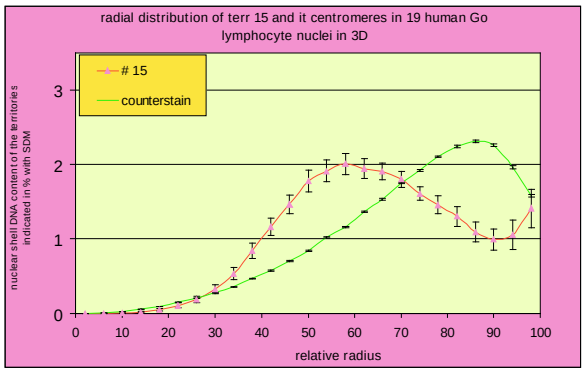

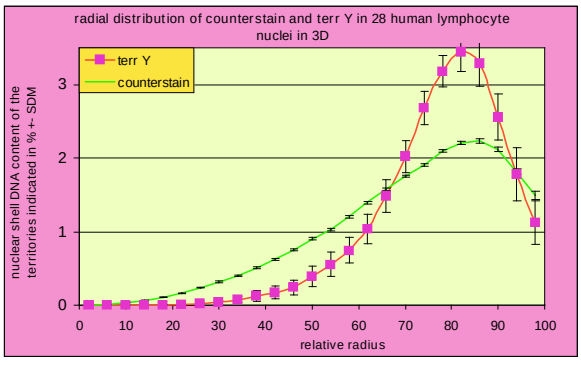

Abb.II.1b.5.Im direkten Vergleich zwischen Fibroblasten und Lymphozyten weichen Chromosom #18 und Chromosom Y in ihrer Position voneinander ab. Anders als in Kap. II.1.

wurde bei der Serie gr/kl Lymphozytenkerne eine Serie ausgelassen, bei der die Signale der Territorien teilweise über den Kernrand hinausgingen, und daher meiner Meinung nach falsch waren. In der vernachlässigten Serie hatten die kleinen Territorien ein nur 30% kleineres Volumen als die großen Territorien, was auch nicht stimmen kann.

Es folgt nun ein Beispiel zur Darstellung der Verteilung der Schwerpunkte der Chromosomen #21, #22, X und Y in 43 Fibroblasten.

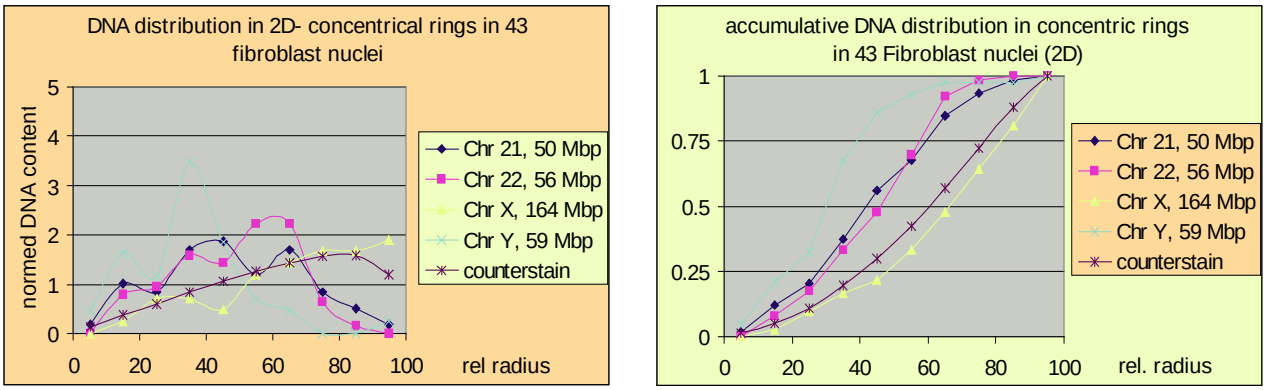

Abb.II.1b.6.Mit obigem Beispiel soll gezeigt werden, dass die kumulative Darstellung (rechts) von komplizierteren Verteilungen (links) übersichtlicher wird. Darin erscheint Chromosom Y extrem zentral gelegen und X eher an der Zellkernperipherie.

II.1b.2.3. Statistik der Lage der Chromosomen zu je einem Zelltypus

II.1b.2.3.1Fibroblasten

	<r terr>	SDkorr	SDMkorr	N
1) A.B. Chr 1-5, X in human fibroblasts	62,4	8,20	1,00	67
2) A.B. Chr 17-20 in human fibroblasts	45,3	11,74	1,43	67
3) I.S. Chr 15 in human fibroblasts	51,4	14,57	3,04	23
4) I.S. Chr 18 in human fibroblasts	44,8	18,38	3,36	30
5) I.S. Chr 19 in human fibroblasts	48,7	21,78	3,98	30
6) A.B. Chr Y in human fibroblasts	42,9	19,3	3,22	36

Verschiedenheit der Verteilungen in Standardabweichungen

	1)	2)	3)	4)	5)	6)
1)	0,00	1,19	0,66	0,87	0,59	0,93
2)	1,19	0,00	0,33	0,02	0,14	0,11
3)	0,66	0,33	0,00	0,28	0,10	0,35
4)	0,87	0,02	0,28	0,00	0,14	0,07
5)	0,59	0,14	0,10	0,14	0,00	0,20
6)	0,93	0,11	0,35	0,07	0,20	0,00

Tab.II.1b.1. In obigen Tabellen findet sich die Statistik zu den 6 verglichenen Territorien und Territoriengruppen in Fibroblasten. Man erkennt besonders zwischen „1)“ und „2)“ eine

Verteilung ausserhalb der Fehlergrenzen, die aber noch nicht signifikant ist. Alle anderen Verteilungen stimmen innerhalb der Fehlergrenzen überein.

Unterscheidung der Mittelwerte untereinander in Standardabweichungen

	1)	2)	3)	4)	5)	6)
1)	0,00	9,77	3,44	5,02	3,34	5,79
2)	9,77	0,00	1,82	0,14	0,80	0,68
3)	3,44	1,82	0,00	1,46	0,54	1,92
4)	5,02	0,14	1,46	0,00	0,75	0,41
5)	3,34	0,80	0,54	0,75	0,00	1,13
6)	5,79	0,68	1,92	0,41	1,13	0,00

Tab.II.1b.2. In Einheiten von Standardabweichungen ist die Wahrscheinlichkeit für die Übereinstimmung der Mittelwerte aufgetragen. In Blau: p £ 0,3% . Rot und Gelb haben die gleiche Bedeutung wie in der darüberliegenden Abbildung. Besonders die großen Chromosomen weichen von den übrigen Territorien, den kleinen, ab.

II.1b.2.3.2. Lymphozyten:

	<r terr>	SD korr	SDM korr	N
1) M.C. Chr 1-5,X in human lymphocytes	72,9	3,68	0,75	24
2) M.C. Chr 17-20 in human lymphocytes	56,9	6,93	1,41	24
3) C.W. Chr 15 in human lymphocytes	65,1	9,05	1,85	19
4) M.H. Chr 18 in human lymphocytes	73,6	13,58	2,77	30
5) M.H. Chr 19 in human lymphocytes	47,3	14,57	2,97	30
6) M.C. Chr Y in human lymphocytes	77,8	8,8	1,80	28

Verschiedenheit der Verteilungen in Standardabweichungen

	1)	2)	3)	4)	5)	6)
1)	0,00	2,04	0,80	0,05	1,70	0,51
2)	2,04	0,00	0,72	1,10	0,60	1,87
3)	0,80	0,72	0,00	0,52	1,04	1,01
4)	0,05	1,10	0,52	0,00	1,32	0,26
5)	1,70	0,60	1,04	1,32	0,00	1,79
6)	0,51	1,87	1,01	0,26	1,79	0,00

Tab.II.1b.3.In obigen Tabellen findet sich die Statistik zu den 6 verglichenen Territorien und Territoriengruppen in Lymphozyten. Man erkennt, in rot unterlegt, Verteilungen, die sich signifikant unterscheiden (p‡95% für Verschiedenheit), in gelb Verteilungen, die sich noch nicht signifikant unterscheiden (95% ‡ p ‡ 68%). Alle anderen, ohne Farbe, stimmen innerhalb der Fehlergrenzen der Verteilung (nicht der Fehler der Mittelwerte) überein. "SD korr" ist ein um den Faktor Ö2 vergrößerter Wert gegenüber dem gemessenen. Dieser Faktor ergibt sich daraus, dass immer der Mittelwert von 2 Homologen gemessen wurde (Vgl. Kap I.5.)

Unterscheidung der Mittelwerte in Standardabweichungen

	1)	2)	3)	4)	5)	6)
1)	0,00	10,02	3,91	0,24	8,36	2,52
2)	9,99	0,00	3,52	5,37	2,92	9,14
3)	3,91	3,53	0,00	2,55	5,09	4,93
4)	0,24	5,37	2,55	0,00	6,47	1,27
5)	8,35	2,92	5,08	6,47	0,00	8,78
6)	2,52	9,15	4,93	1,27	8,79	0,00

Tab.II.1b.4. In obiger Tabelle konnte die Statistik nur die Mittelwerte von „1)“ und „4)“, sowie „4)“ und „6)“ nicht ganz sicher unterscheiden

Insgesamt deutet diese statistische Analyse darauf hin, dass die radialen Bereiche, in denen die Territorien vorkommen, vor allem bei den Fibroblasten, sich überlappen.

II.1b.3. Untersuchung der Histogramme von Chromosomen unterschiedlicher genetischer Aktivität

Das X- Chromosom ist mit seinen aktiven und inaktiven Homologen ein gutes Beispiel für Territorien, die unterschiedlich aussehen, s. Bild:

Abb.II.1b.7. links ist das aktive und rechts das inaktive Chromosom X aus dem gleichen Fibroblastenkern aufgenommen. Das inaktive Chromosom X erscheint eher kondensiert. Man erkennt beim aktiven X mehr Feinstruktur, d.h. mehr Gradienten. Das aktive Chromosom X kann aufgrund seiner Aufgelockertheit möglicherweise leichter von größeren biomolekularen Maschinen wie den Transkriptionsfaktorkomplexen erreicht werden.

Die Bilder mit den einzelnen Homologen wurden so geteilt, dass in jeder Bildhälfte ein Homolog lag. Davon wurde dann jeweils ein Helligkeitshistogramm gemacht. Das Bild wurde vorher mit einem [1 4 6 4 1] - Gauß Filter in beide lateralen Richtungen geglättet, um Streuungen der Helligkeit aufgrund von Bildrauschen zu verhindern. Für das Histogramm bedeutet dies weniger Streuung um Hauptwerte der Abszisse,

was einer besseren Auflösung entspricht. Das Bild wurde außerdem von 255 auf 50 normiert, auch um die Statistik zu den einzelnen Histogrammargumenten zu verbessern und so das Histogramm glatter werden zu lassen. Zusätzlich wurde das Histogramm geglättet. Ein Schwellwert wirkt sich auf ein Histogramm wie ein Abschneiden der ersten Helligkeitsargumente aus. Bei unterschiedlichen Schwellwerten im Laufe der Serie erhält man dann Histogramme unterschiedlich großer Bereiche. Das würde die Berechnung eines mittleren Histogramms erschweren. Daher wurde auf eine Schwellwertsetzung verzichtet. Da die Histogramme häufig über sehr große Intensitätsbereiche gehen, wurde das Argument der Ordinate, das die Anzahl der Voxel angibt, logarithmiert.

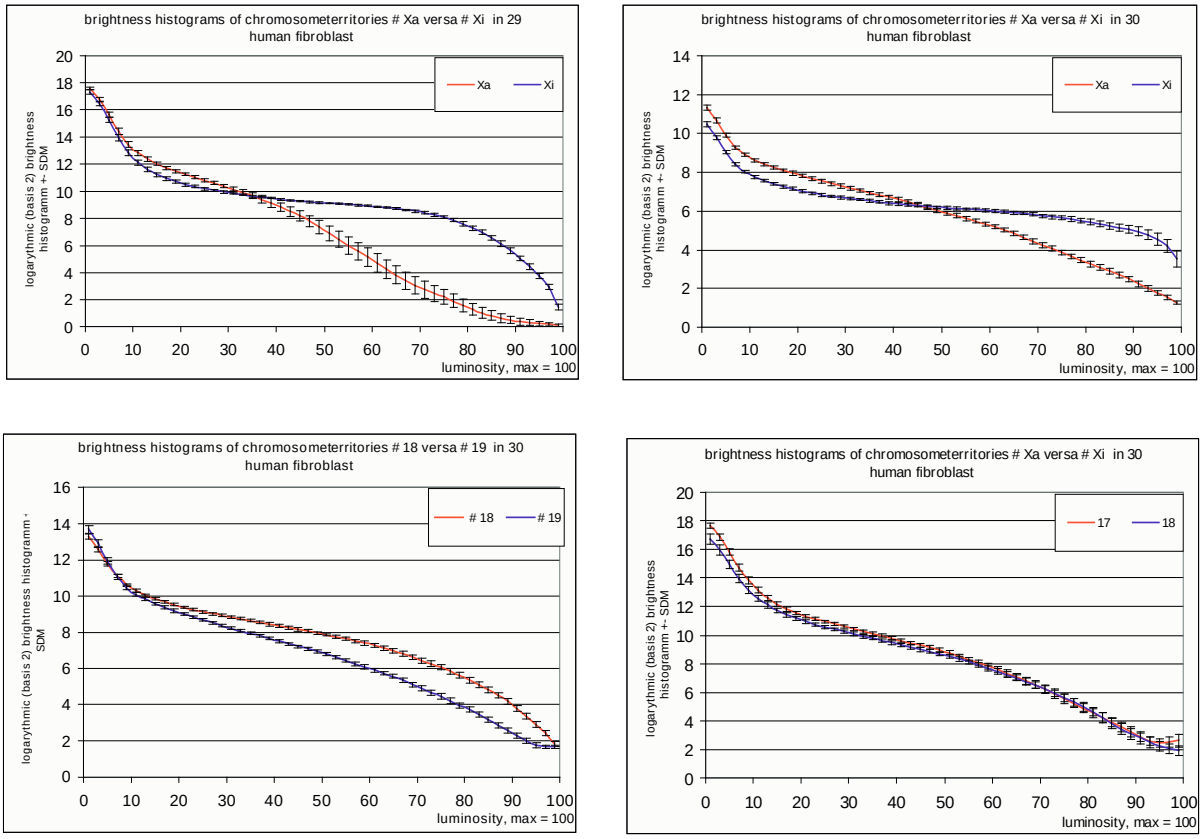

Abb.II.1b.8 die Histogramme der Chromosomen Xa und Xi werden links in einer Serie aus dem Jahr 2000 und rechts in einer Serie aus dem Jahr 1998 ausgewertet. In den beiden unteren Diagrammen werden links die Chromosomen #18 und #19 und rechts die Chromosomen #17 und #18 ausgewertet. Man erkennt in den Diagrammen links den Anstieg für den Hintergrund der nicht weiter stört. Besonders zwischen Xi und Xa und da besonders in der qualitativ hochwertigen Serie aus dem Jahr 2000 sieht man, dass die Kurve des inaktiven Chromosoms X bedeutend konvexer als diejenige des aktiven X ist.

Hinsichtlich der Untersuchung der Histogramme unterscheiden sich besonders die aktiven X von den inaktiven X Chromosomen in Fibroblasten. Besonders das inaktive X ragt heraus.

II.2. Radial arrangement of chromosome territories in human cell nuclei: a computer model approach regarding the gene density (article in preparation)

G Kreth[a,7], J Finsterle[a], J v Hase[a], M Cremer[b], C Cremer[a]

[a]Kirchhoff Institute for Physics, University of Heidelberg, Germany

[b]Institute of Anthropology and Human Genetics, University of Munich, Germany

II.2.1. Abstract

In the last years Fluorescence in situ-hybridization (FISH) techniques has been raised to one of the most powerful tools to investigate the chromosomal organization. Recent experiments, concerning the positioning of chromosomes in the nuclear volume suggest a close relationship between the gene density of a Chromosome Territory (CT) and its distance to the nuclear center. To relate chromosome positioning and gene density in a quantitative way, on the basis of the Spherical 1-Mbp Chromatin Domain (SCD) model (s. Appendix p.6), computer simulations of whole cell nuclei were performed weighting the distance of each CT to the nuclear center with a gene density correlated probability function. A comparison of the radial distributions of simulated and experimental data showed for certain CTs a quite good agreement (e.g. #18,#19) applying the same quantitative mapping procedure. For other CTs a deviation was observed (e.g. #15, #20). In contrast to these findings simulated nuclei with a statistical arrangement of CTs in the nuclear volume show a clear deviation for all CTs in relation to the experiments. Such Computermodells can be used e.g. for better translocation rate predictions in radiology.

II.2.2. Introduction

Until today the spatial organization of different compartments in nuclei of mammalian cells is still poorly understood. The compartmentalization of the nucleus in several well-defined sub-regions like nucleoli, Chromosome Territories (CTs) and the higher compartmentalization levels of CTs and the spatial arrangements of these compartments seems to have a profound influence on functional processes inside the nucleus [1-4]. E.g. it has been shown that territories are compartmentalized in domains of early and late replicating chromatin, representing R and G bands on

[7] gkreth@kip.uni-heidelberg.de, INF 227, 69120 Heidelberg, Fax: +49-6221-549275

metaphase chromosomes [5,6]. While R-band domains are found to be distributed more or less randomly in the whole nuclear volume, for late replicating G-band domains a preferential localization near to the nuclear envelope and close to the nucleoli was observed [7]. This specific arrangement of early/late chromatin may mirror the results of recent investigations, regarding the positioning of whole CTs inside the nuclear volume. Chromosome painting experiments of single CTs and groups of CTs in different species suggest a relationship between the gene density of a chromosome and its positioning in the nuclear volume. [8-11]. E.g. a 3D evaluation of human lymphocyte nuclei revealed the preferential positioning of the gene dense #17, 19 and 20 CTs in the 3D nuclear interior, while the gene poor #18 CTs, and the CTs of larger chromosomes (#1, 2, 3, 4, 5, X) were located at the 3D nuclear periphery [9]. Additionally it could be shown that the specific localization of the gene poor #18CTs and the gene rich #19CTs was maintained during the evolution of primates [12]. A 2D analysis of every human chromosome in diploid lymphoblasts and primary fibroblasts suggest a close correlation between the gene density of a chromosome and its distance to the nuclear center/border [11].

In contrast to these highly consistent radial arrangements, for calculated CT distributions, assuming a linear correlation between CT volume and DNA content (according to the "Spherical 1-Mbp Chromatin Domain (SCD)" model [13,14]), a similar distribution of both large and small chromosomes was found [9]. The assumed geometrical constraints alone are therefore not sufficient to explain the observed radial arrangements. In the present contribution the SCD model was extended to regard also the influence of the gene density as an additional geometrical constraint. The 3D mapping of CTs in human lymphocytes performed in [9] was used as a experimental basis for the comparison with the radial arrangements of CTs assuming a simulated gene density correlated distribution inside the nuclear volume.

II.2.3. Results

In the present study the simulated distributions of CTs were compared with the evaluations of chromosome painting experiments of human lymphocytes described in [9]. Here, the radial distributions of groups of larger (#1-5,X) and smaller chromosomes (#17-20) were investigated. To compare the radial arrangements of CTs with nearly the same DNA content but a different gene density, also the CTs #18 and #19 were labeled separately. Applying the virtual microscopy approach (see Material and Methods), the virtual painting of these CTs was performed respectively,

applying the simulated gene density correlated distribution and the simulated statistical distribution of CTs in human cell nuclei according to the SCD model (see Material and Methods) (for a 3D visualization see Fig. 1). Applying the 3D mapping procedure (Material and Methods), in Fig. 2,3 the radial distributions for the respective CTs of the simulated nuclei are compared with the experimental evaluations performed in [9]. For the mapping, a division of the nuclei in 25 concentrical shells was performed. In this way a shell with relative radius 0 is located in the center of the nucleus and the shell with radius 100 at the nuclear border. The normalization of the voxel intensities of a given distribution was made in such a way, that the intensities of all shells together amounted to 100.

Regarding the comparison of the experimental data with the simulated gene density correlated distribution (see Fig. 2), the comparison shows that the radial distribution curves for the chromosome group #1-5,X agree quite well both in simulation and experiment, while for the group #17-20 a significant difference is observed. The separate evaluation of the #18 and #19 CTs show again a good agreement between simulation and experiment. Here, the gene richest CTs #19 are localized in the interior while the more inactive #18 CTs are arranged near to the nuclear envelope. A more detailed analysis indicated that the observed difference between simulation and experiment regarding the arrangement of the group #17-20 results from the localization of the #20 CTs. In the simulation, these CTs are located more in the periphery while in the experiment a preferential positioning in the middle of the nucleus is observed (compare the inserts of Fig. 2). In contrast to this findings regarding the comparison with the simulated statistical distribution, a clear deviation for all CTs is observed (see Fig. 2). Regarding the groups of larger CTs in comparison to the group of smaller CTs, in the simulation the larger CTs are located even more in the interior and the smaller ones more in the periphery. This is the geometrical effect of the higher volumes of larger CTs which are located therefore more in the interior (see also [9]). Comparing the positioning of the CTs #18 and #19 in the simulation, here because of the similar volumes of both CTs, they are located quite similar also (compare Fig. 2).

II.2.4. Discussion

In the present study we applied the SCD computer model for human cell nuclei to interpret the experimentally observed specific arrangement pattern of CTs in the

nuclear volume. Chromosome painting experiments have suggested a close relationship between the localization of CTs in the nuclear volume and their gene densities. To relate gene density and CT positioning, the distances of simulated CTs to the nuclear center were weighted with the respective gene densities (derived from sequence data) applying the SCD model. Using a quantitative 3D mapping algorithm for experimental and simulated data, the calculated radial distributions of CTs #1-5, X and #18,19 in experiment and simulation are in quite good agreement. An exception are the CTs #20. With this first approach, the possible influence of the gene density of a chromosome on its spatial positioning in the nuclear volume could be verified by computer simulations. For this purpose, only sequence data (number of bp per chromosome, number of genes) were taken into account as parameters. However, also other constraints (not yet realized in the present simulations) have to be regarded, like the specific arrangement of nucleoli CTs around the nucleoli and other still unknown factors. The simulations presented here may help to determine the influence of such constraints on the arrangement of CTs in the nucleus and may provide a model system for further experimental investigations.

II.2.5. Material & Methods

II.2.5.1. Lymphocytes preparation, fixation procedure and Fluorescence in-situ hybridization

Chromosome painting experiments used for the comparison with simulated nuclei in the present contribution were executed in [9]. For a better understanding in the following a short summarization is given.

Lymphocytes are prepared as described previously [9]. After isolation from human blood by a Ficoll gradient the chromosomes were fixed on a polylysine coated slide with 4%PFA/0.3xPBS. Pools of chromosome paints were prepared for large and small-sized chromosomes. Human chromosome paint probes were produced by DOP-PCR from sorted chromosomes and re-amplified by DOP-PCR as described[15,16]. The pool of the large chromosomes contained chromosomes 1-5 and X; pools for the small chromosomes included the chromosomes 17-20, single chromosome paints 18 and 19 and of paint pools was done as described before [17]. FISH was performed in 50% formamide/10% dextran sulphate/1xSSC at 37℃ over 1-3 days. Posthybridization washings included 2xSSC at 37℃ and 0.1 x SSC at 60℃. Detection of biotin was done by one to three layers using either avidin-Cy3 or

avidin-Alexa-488 followed by goat-anti-avidin-FITC or avidin-Cy5, followed by biotinylated goat-anti-avidin and avidin-Cy5. Detection of digoxigenin was done by one or two layers of specific antibodies, using eithervCy3-conjugated mouse-anti-digoxigenin or rabbit-anti-digoxigenin followed by Cy3-conjugated goat-anti-rabbit. For determination/detection of the complete distribution of all chromosomes, the data from the counterstaining with YOYO-1 (Molecular probes, USA) are used.
For a more detailed procedure see [9].

II.2.5.2. Virtual microscopy and 3D Mapping algorithm

For a compatible comparison between the experimentally observed and the simulated gene density correlated and statistical distributions of CTs inside the nuclear volume, the same 3D mapping algorithm was applied. For this purpose from the simulated nuclear configurations virtual image data stacks were calculated. This virtual microscopy approach consists of a digitization of the spherical domains with diameters of 500nm by a grid of 80x80x250nm voxel spacing and a convolution of the digitized stacks with a measured confocal point spread function (with a Full Width at Half Maximum (FWHM): FWHMx=279nm, FWHMy=254nm, FWHMz=642nm; compare [18]). For the mapping algorithm the segmented nuclear volumes of experimental and simulated stacks were divided in 25 concentrical shells. The normalization of the voxel intensities was made in such a way, that the intensities of all shells together amounted to 100. For this purpose, for each voxel located in the nuclear interior or at its border the relative distance r was calculated. All voxels intensities below an automatically set threshold were set to zero. A shell at a given r contains all nuclear voxels having distances within a certain range □r. With a semi automatic thresholding procedure, the labeled chromosomes were segmented and the respective voxel intensities in the shells were summed up [9].

II.2.5.3. Simulation of human cell nuclei regarding a gene density correlated chromosome distribution

For a simulation of the overall structure of CTs in human cell nuclei, the SCD model was applied [13,14]. According to this model each chromosome of the diploid human genome is approximated by a linear chain of spherical 1-Mbp sized domains (with a diameter of 500nm each), which are linked together by an entropic spring potential. Different domains interact with each other by a repulsive increasing potential, taking into account the presence of fiber like structures inside these domains. The number of domains is given by the respective DNA content (compare [19]) for a specific chromosome. To maintain the compaction of the simulated chains in distinct

regions/territories, a weak enveloping potential barrier around each chain was assumed to exist. To obtain thermodynamic equilibrium configurations with respect to the energies, the Metropolis Monte Carlo method was applied. For this purpose, in a first start configuration the spherical domains of each simulated chromosome were placed site by site in a mitosis like arrangement (start cylinders). Random displacements of the domains results in relaxed interphase-like configurations using the Importance Sampling Monte Carlo procedure. About 400000 Monte Carlo Steps (displacements) for the relaxation of each start configurations were used. Because of the low local mobility of the simulated chromosomes during the relaxation process, the positioning of a chromosome depends mainly from the localization at the starting point.

The arrangement of the start cylinders was made statistically and gene density correlated. For both cases also two nucleoli were inserted, simulated as additional CTs with a DNA content of 80Mbp. The midpoints of the nucleoli in the start configuration are considered to maintain a minimal distance of 1.75mm to the nuclear envelope and a minimal distance of 3.75mm from each other. The start cylinders are located first in so called "initial" CT spheres with a volume (relative to the nuclear volume) proportional to the DNA content of the respective chromosome. In the case of the statistical distribution of the CTs (compare [9]) the "initial" spheres were positioned randomly in the nuclear volume with the condition that overlapping with still existing "initial" spheres is forbidden. In the case of the gene density correlated distribution the "initial" spheres were put in the nuclear volume according to the order of the gene density. It was started with the nucleoli and then the order: #19, 17, 22, 11, 1, 15, 14, 12, 20, 6, 10, 3, 7, 9, 5, 21, 8, 4, 13, 18, X, Y was chosen. Besides the condition that overlapping with still existing "initial" spheres is forbidden also the distance from the center of the "initial" sphere to the nuclear center was weighted with a exponential probability density function which depends on the gene density (derived from sequence data compare [11]) of a given chromosome i:

$$P(d)_i = \exp\left(d \times \frac{\text{density}(i)}{\text{density}(\#19)} \right) \times a$$

Here d determines the distance of the "initial" sphere to the nuclear center in units of the nuclear radius. The actual position is confirmed when a random number [0;1[‡P(d), according to the Monte Carlo procedure. In Fig. 4 for some CTs the probability function P(d) in dependence of d is plotted. This is a required acceptance factor to ensure the convergence of the algorithm.

Also in both cases the volumes of the "initial" spheres have to be reduced with a common factor to let the algorithm convergence. When the start configuration with the "initial" spheres of the diploid human chromosome set (22,X,Y) and the two nucleoli is created, the start cylinders were placed inside these spheres. In the next step for the relaxation process of the start cylinders in a equilibrium state the "initial" spheres disappear and play no further role in the relaxation process. For both cases 50 nuclei each were simulated.

II.2.6. Acknowledgements

For stimulating discussions we thank T. Cremer and M. Hausmann. The chromosome painting experiments used for the comparison with simulated data were performed in the group of T. Cremer. Special thanks to I. Solovei and A. Brero. The present studies were supported financially from the Deutsche Forschungsgemeinschaft (Grant CR 60/19-1) and the European commission (Grant FIGH-CT1999-00011).

II.2.7. References

[1] A.S. Belmont, S. Dietzel, A.C. Nye, Y.G. Strukov, T. Tumbar “Large-scale chromatin structure and function”, Current Opinion in Cell Biology, 11, pp 307-311, 1999

[2] T. Cremer, G. Kreth, H. Koester, R.H.A. Fink, R. Heintzmann, M. Cremer, I. Solovei, D. Zink, C. Cremer "Chromosome territories, interchromatin domain compartment and nuclear matrix: An integrated view of the functional nuclear architecture", Crit. Rev. Eukaryotic Gene Expression, 12, pp. 179-212, 2000

[3] A.E. Visser, F. Jaunin, S. Fakan, J.A. Aten “ High resolution analysis of interpase chromosome domains”, J. of cell Science, 113, pp 2585-2593, 2000

[4] J. Ferreira, G. Paolella, C. Ramos, A.I. Lamond “ Spatial organisation of large-scale chromatin domains in the nucleus: A magnified view of single chromosome territories”, J. of cell biology, 139, pp 1597-1610, 1997

[5] A.E. Visser, R. Eils, A. Jauch, G. Little, P.J.M. Bakker, T. Cremer, J.A. Aten "Spatial distribution of early and late replicating chromatin in interphase chromosome territories", Exp. Cell Res., 243, pp. 398-407, 1998

[6] D. Zink, H. Bornfleth, A.E. Visser, C. Cremer, T. Cremer "Organization of early and late replicating DNA in human chromosome territories", Exp. Cell Res., 247, pp. 176-188, 1999

[7] N. Sadoni, S. Langer, C. Fauth, G. Bernardi, T. Cremer, B.M. Turner, D. Zink "Nuclear organization of mammalian genomes. Polar chromosome territories build

up functionally distinct higher order compartments", J. Cell Biol., 146, pp. 1211-1226, 1999

[8] F.A. Habermann, M. Cremer, J. Walter, G. Kreth, J.v. Hase, K. Bauer, J. Wienberg, C. Cremer, T. Cremer, I. Solovei "Arrangements of macro- and microchromosomes in chicken cells", Chrom. Res. 9, pp 569-584, 2001.

[9] M. Cremer, J.v. Hase, T. Volm, A. Brero, G. Kreth, J. Walter, C. Fischer, I. Solovei, C. Cremer, T. Cremer "Non-random radial higher-order chromatin arrangements in nuclei of diploid human cells", Chrom. Res. 9, pp 541-567, 2001

[10] J.A. Croft, J.M.Bridger, S. Boyle, P. Perry, P. Teague, W.A. Bickmore " Differences in the localisation and morphology of chromosomes in the human nucleus", J. of Cell biology, 145, pp 1119-1131, 1999

[11] S. Boyle, S. Gilchrist, J.M. Bridger et al. "The spatial organization of human chromosomes within the nuclei of normal and emerin-mutant cells", Hum. Mol. Genet. 10, pp 211-219, 2001

[12] H. Tanabe, St. Müller, M. Neusser et al. "Evolutionary conservation of chromosome territory arrangements in cell nuclei from higher primates", Proceedings of National Academy of Science, 99 (7), pp. 4424-4429, 2002

[13] T. Cremer, G. Kreth, H. Koester et al. "Chromosome territories, interchromatin domain compartment and nuclear matrix: An integrated view of the functional nuclear architecture", Crit. Rev. Eukaryotic Gene Expression 12, 179-212, 2000

[14] G. Kreth, P. Edelmann & C. Cremer "Towards a dynamical approach for the simulation of large scale, cancer correlated chromatin structures", It. J. Anat. Embryol. (eds. P.M. Motta, G. Macchiarelli, S.A. Nottola) 106(2), pp 21-30, 2001

[15] J.M. Craig, J. Kraus, T. Cremer, " Removal of repetitive sequences from FISH probes using PCR-assisted affinitiy chromatography", Hum Genet, 100, pp 472-476, 1997

[16] A. Bolzer, J.M. Craig, T. Cremer, M.R. Speicher, " A complete set of repeat-depleted, PCR-amplifiable, human chromosome-specific painting probes", Cytogent Cell Genet, 84, pp 233-240, 1999

[17] L. Schermelleh, S. Thalhammer, W. Heckl et al., " Laser microdissection and laser pressure catapulting for the generation of chromosome-specific paint probes", Biotechniques, 27, pp 362-267, 19991

[18] G. Kreth, P. Edelmann, Ch. Münkel et al. "Translocation frequencies for X and Y chromosomes predicted by computer simulations of nuclear structure", Some Aspects of Chromosome Structure and Functions, Edts. R.C. Sobti, G. Obe, R.S.

Athwal, pp 57-71, 2002.

[19] International Human Genome Sequencing Consortium "Initial sequencing and analysis of the human genome", Nature 409, pp 860-921, 2001.

II.2.8. Legends

Fig. 1: see Appendix, p. 6,7. Visualization of reconstructed CTs of a simulated human cell nucleus (a,b) and a human lymphocyte cell nucleus (c,d). For the simulated virtual image data stack the SCD model regarding the gene density correlated distribution of CTs was applied. In both cases, left: CTs #1-5, X are visualized in red and CTs #17-20 are visualized in green. Right: CTs #18 are visualized in red and simulated CTs #19 in green. The visualization tool was kindly provided by Dr. R. Heintzmann, MPI Göttingen, Germany.

Fig. 2: see Appendix, p. 8,9. Radial distribution curves of experimental (compare [9]) and virtual chromosome painting experiments applying a 3D mapping algorithm (see Material and Methods). The radial arrangements were evaluated for CTs 1-5,X and #17-20 (left column) and CTs #18, #19 (right column). For the comparison of theThe counterstain distribution results from the mapping of all chromosomes. In upper both roughs The relative radius determines the relative position of a shell with respect to the nuclear border. E.g. a shell at the relative radius 0 is located in the nuclear center, while the shell 98 is positioned at the nuclear envelope

Classification: Biological Sciences, Evolution

II.3. Evolutionary conservation of chromosome territory arrangements in cell nuclei from higher primates[8]

Hideyuki Tanabe[*†], Stefan Müller[*], Michaela Neusser[*], Johann von Hase[‡], Enzo Calcagno[‡], Marion Cremer[*], Irina Solovei[*], Christoph Cremer[‡], and Thomas Cremer[*§]

[*]Department of Biology II – Human Genetics, University of Munich, Richard Wagner Str. 10, 80333, München, Germany

†Cell Bank Laboratory, Division of Genetics and Mutagenesis, National Institute of Health Sciences, 1-18-1, Kamiyoga, Setagaya-ku, Tokyo 158-8501, Japan

‡Kirchhoff Institute of Physics, University of Heidelberg, INF 227, 69120, Heidelberg, Germany

§Corresponding author: Thomas Cremer

address: Department of Biology II – Human Genetics, University of Munich, Richard Wagner Str. 10, 80333, Munich, Germany

phone: +49-89-2180-6709 fax: +49-89-2180-6719

e-mail: Thomas.Cremer@lrz.uni-muenchen.de

Abbreviations footnote

CTs; chromosome territories. HSA; Homo sapiens

3D-FISH; three dimensional-fluorescence in situ hybridization

[8] Published in: Proceedings of National Academy of Sciences, Vol 99 No 7 pp.4424-4429, 2002.
Comunicated by Günther Blobel.

II.3.1. Abstract

We demonstrate that the nuclear topological arrangement of chromosome territories (CTs) has been conserved during primate evolution over a period of about 30 million of years. Recent evidence shows that the positioning of chromatin in human lymphocyte nuclei is correlated with gene density. For example, human chromosome 19 territories which contain mainly gene dense, early replicating chromatin, are located towards the nuclear center, while chromosome 18 which consists mainly of gene-poor and later replicating chromatin, is located close to the nuclear border. In this study, we subjected seven different primate species to comparative analysis of the radial distribution pattern of human chromosome 18 and 19 homologous chromatin by three-dimensional fluorescence in situ hybridization (3D-FISH). Our data demonstrate for the first time that gene density-correlated radial chromatin arrangements were conserved during higher primate genome evolution, irrespective of the major karyotypic rearrangements that occurred in different phylogenetic lineages. The evolutionary conserved positioning of homologous chromosomes or chromosome segments in related species support evidence for a functionally relevant higher order chromatin arrangement that is correlated with gene-density.

II.3.1. Introduction

The chromatin of individual chromosomes is organized in chromosome territories (CTs) that are essential components of the higher order chromatin architecture of the vertebrate cell nucleus (reviewed in refs. (1-5)). Recently, the extent to which evolutionary conserved, cell type, cell cycle and species specific motifs of chromatin arrangements may exist, has become the focus of intense studies (6-9). In mammals two principal components of mitotic chromosomes can be distinguished: G-light bands (also called R-bands) replicate early during S-phase and contain most of the housekeeping but relatively few tissue specific genes. G-dark bands replicate later, are gene poor and contain tissue specific genes (10). Recently it has been demonstrated that these chromosome bands are maintained in interphase nuclei as focal chromatin aggregations (11) built up by a number of chromatin domains in the order of ~1 Mb. These domains apparently persist through all interphase stages, show distinct nuclear localization patterns and may provide an important component of the higher order nuclear architecture (11-14), for review see ref. 2. The nuclear location of human (Homo sapiens, HSA) chromosomes 18 and 19 CTs (further referred to as HSA18 and HSA19) has become of special interest in this respect. These chromosomes are of similar DNA content (86 Mb and 72 Mb, respectively (15)) but differ strongly in their gene content and replication timing: most of HSA19 chromatin belongs to G-light bands, is gene-dense (20.5 genes/Mbp), while most of HSA18 chromatin represents G-dark bands and consists mainly of gene-poor chromatin (4.3 genes/Mbp; http://www.ensembl.org/Homo_sapiens/, (10)). In human lymphocyte nuclei, which exhibit an almost spherical shape, HSA19 CTs are consistently localized towards the nuclear center without any detectable attachment to the nuclear envelope while the HSA18 CTs are positioned close to the nuclear border (7, 8). In this study we demonstrate the evolutionary conservation of radial nuclear arrangements for chromosomes or chromosome segments homologous to HSA18 and 19 in seven higher primate species. The last common ancestor of these species dates back approximately 30 to 40 million years ago. This evolutionary conservation argues for a still

unknown functional significance of distinct radial higher order chromatin arrangements.

II.3.2. Material and Methods

II.3.2.1. Cell Lines and Slide Preparation.

Epstein Barr virus-transformed lymphoblastoid cell lines were obtained from human (Homo sapiens, HSA; LB-3), chimpanzee (Pan troglodytes, PTR; EB176 (JC), ECACC No.89072704), gorilla (Gorilla gorilla, GGO; EB (JC), ECACC No.89072703), orangutan (Pongo pygmaeus, PPY; EB185 (JC), ECACC No.89072705), white-handed gibbon (Hylobates lar, HLA), cotton-top tamarin (Saguinus oedipus, SOE; B95-8, ECACC No.85011419), common marmoset (Callithrix jacchus, CJA) (kindly provided by M. Rocchi) and squirrel monkey (Saimiri sciureus, SSC). All cell lines were karyotypically normal, except for cell line B95-8, derived from Saguinus oedipus, which exhibited five marker chromosomes (16, 17) of which none involved chromosomes relevant for this study. For S-phase detection cells were pulse-labeled with 5-bromo-deoxyuridine (BrdU) for 1hr prior to fixation. For preparing three-dimensionally preserved cell nuclei, cells were seeded onto polylysine coated slides and fixed in 4% paraformaldehyde in 0.3 x PBS. Permeabilization steps included treatment of cells in 0.5% Triton X-100 / 0.5% saponin in PBS, 20% glycerol in PBS, repeated freezing/thawing in liquid nitrogen, and incubation in 0.1M HCl as described in detail elsewhere (18).

II.3.2.2. Probe Preparation, 3D-FISH and Fluorescent Detection.

For each target primate species painting probes for the delineation of chromosomes or chromosome segments homologous to HSA18, HSA19 and HSA1q32→qter were generated by DOP-PCR (19) from flow sorted chromosomes. Since human paint probes were not found appropriate to achieve intensely painted CTs useful for light optical sectioning and 3D reconstruction in distantly related primate species, for any given target primate species we used HSA18 and HSA19 homologous probes that were established from a close related primate species (Table 1, Fig. 2a-c).

Table 1: DNA probes used for the respective target species (see text for details). For the delineation of the indicated target chromatin in the respective species, chromosome specific painting probes derived from human (HSA), gorilla (GGO), orangutan (PPY) and the New World monkeys tamarin (SOE) and wooly monkey (Lagothrix lagothricha, LLA) were used.

Target species	Paint probes used for the delineation of homologous chromosomal regions to		
	HSA18	HSA19	HSA1q32→qter
Human (HSA)	GGO16	PPY20	-
Chimpanzee (PTR)	GGO16	PPY20	-
Gorilla (GGO)	HSA18	PPY20	-
Orangutan (PPY)	GGO16	HSA19	-
Gibbon (HLA)	GGO16	PPY20	-
Marmoset (CJA)	LLA4*	SOE5*	LLA25*
Tamarin (SOE)	LLA4*	LLA13*	LLA25*
Squirrel monkey (SSC)	LLA4*	SOE5*	LLA25*

* LLA4 is homologous to HSA18 and HSA8p, LLA13/SOE 5 to HSA19 and LLA25 to HSA1q32→qter, respectively.

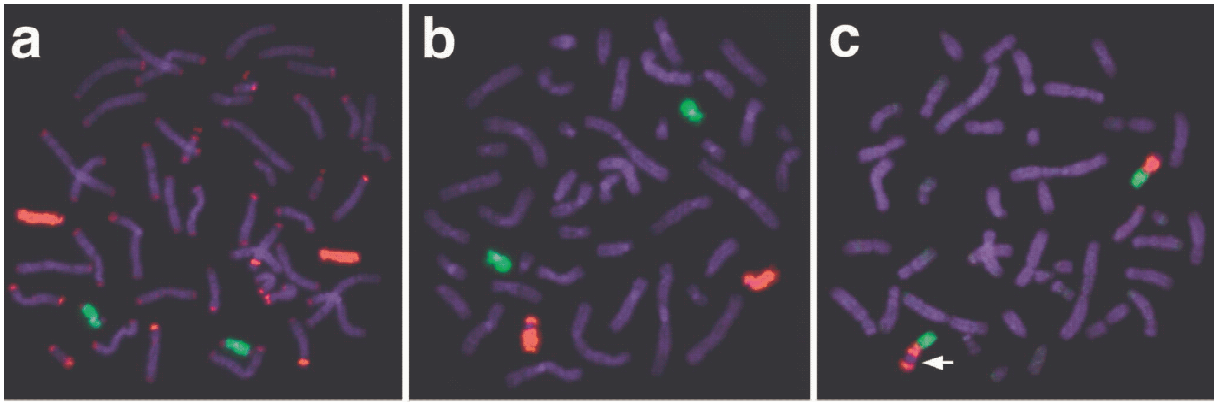

a and b, Hybridization of GGO16 (red) and PPY20 (green) to gorilla and human metaphase preparations. a, In the gorilla extensive cross hybridization of subtelomeric heterochromatin was observed when employing a gorilla paint (red), whereas the orangutan paint (green) yielded no cross hybridization. b, In human both probes produced highly specific hybridization signals. These experiments demonstrate the necessity to use probes derived from evolutionary closely related, but different species than the target species for the unequivocal and exclusive delineation of homologous chromatin in subsequent 3D-FISH experiments (see Materials and Methods for details). c, In the squirrel monkey, SOE5 (green) and LLA25 (red) visualize syntenic association of HSA19 (green) and HSA1q32→qter (red) homologous material. The polymorphic heterochromatin block is highlighted by an arrow (see also Fig. 1 and Discussion for details).

Further, it was previously reported for human chromosomes that painting probes derived from close related non-human primates yield equal signal intensities compared to human probes, but superior specificity even in the absence of suppression with Cot1-DNA, since repeat sequences that cause cross hybridization show a higher rate of evolutionary divergence compared to euchromatic DNA (17). We therefore avoided the hybridisation of paint probes to target nuclei from the same species (see Table 1). Employing this approach, an excellent specificity and signal to noise ratio was obtained in all cross species 3D FISH experiments. All primate paint probes were previously characterized by reverse painting to human metaphases (16, 17, 20, 21). 3D-FISH, detection of labeled probes and of incorporated BrdU and DNA counterstaining was performed according to the protocols described elsewhere (9, 18). Only BrdU positive nuclei indicating their S-phase stage were selected for further evaluation.

II.3.2.3. Confocal Microscopy.

Nuclei were scanned with an axial distance of 200 nm using a three-channel laser scanning confocal microscope (Zeiss LSM 410). For each optical section images were collected sequentially for all three fluorochromes. Stacks of 8-bit gray scale 2D images were obtained with a pixel size of 66 nm. Displayed overlays of confocal images were processed with Adobe Photoshop 5.5. 3D

reconstructions of CT image stacks were performed using Amira 2.2 TGS (http://www.amiravis.com/). The nuclear periphery was reconstructed from thresholded images of the DNA counterstain.

II.3.2.4. Quantitative Evaluation of the 3D Positioning of Painted Territories.[9]

A detailed description of the quantitative 3D evaluation of light optical serial sections was published elsewhere (7). Briefly, a voxel (volume element) based algorithm was applied (Fig. 4). As a first step, the center and the border of the nucleus were determined using the 3D data set of the DNA-counterstain fluorescence in the following way: First, the fluorescence intensity gravity center of the counterstain voxels after automatic thresholding was calculated. For the interactive segmentation of the nuclear border, a straight line was drawn from the gravity center towards each voxel considered and the nuclear center was then determined as the geometrical center of the segmented voxels. In the second step, segmentation of CTs was performed in each 3D stack representing the color channels for the respective painted CTs. The segmented nuclear space was divided into 25 equidistant shells with a thickness of $Dr = 1/25\ r_0$. For comparison of nuclei with different shape and size, the distance between the nuclear center and any point on the segmented nuclear border along the straight lines mentioned above, was given as $r_0 = 100$. For each voxel located in the nuclear interior the relative distance r from the nuclear center was calculated as a fraction of r_0. A shell at a given r contains all nuclear voxels with a distance between $r - Dr/2$ and $r + Dr/2$. For each shell all voxels assigned to a given CT were identified and the fluorescence intensities derived from the respective emission spectrum were summed up. This procedure yielded the individual DNA-shell contents for painted CTs as well as the overall DNA content reflected by the DNA counterstain. For better comparison of different nuclei, the sum of the voxel intensities measured in each nucleus was set to 100% for each fluorochrome. Using this normalization, the average relative DNA content in nuclear shells as a function of the relative distance r from the 3D center represents the average radial distribution of the DNA representing the painted CTs or of the overall DNA in the entire set of evaluated nuclei. As an

[9] for figures see Chapter "Einleitung"

estimate for the variation obtained for each relative distance r, the standard deviation of the mean DNA shell content was calculated. The data collected for each species were plotted as graphs.

II.3.3. Results

II.3.3.1. Delineation of Human Chromosome 18 and 19 Homologous Territories in Primates.

We chose lymphoblastoid cell lines from human and from seven other higher primate species which exhibit distinct differences in their pattern of karyotype evolution (22): three great apes (chimpanzee, gorilla, orangutan), the white-handed gibbon and three New World monkeys (cotton-top tamarin; common marmoset, squirrel monkey). In comparison to the human karyotype, great ape chromosomes are strongly conserved and differ from human mainly by intra-chromosomal rearrangements (23), whereas gibbon karyotypes show a high degree of chromosome reshuffling (24). Compared to gibbons, New World monkeys show a moderate rate of chromosomal changes, mainly Robertsonian type or tandem rearrangements (21). Fig. 1 shows individual higher primate chromosomes and chromosomal segments homologous to HSA18 and HSA19, respectively, as well as chromosomal material homologous to HSA1q32→qter and HSA8p (see below).

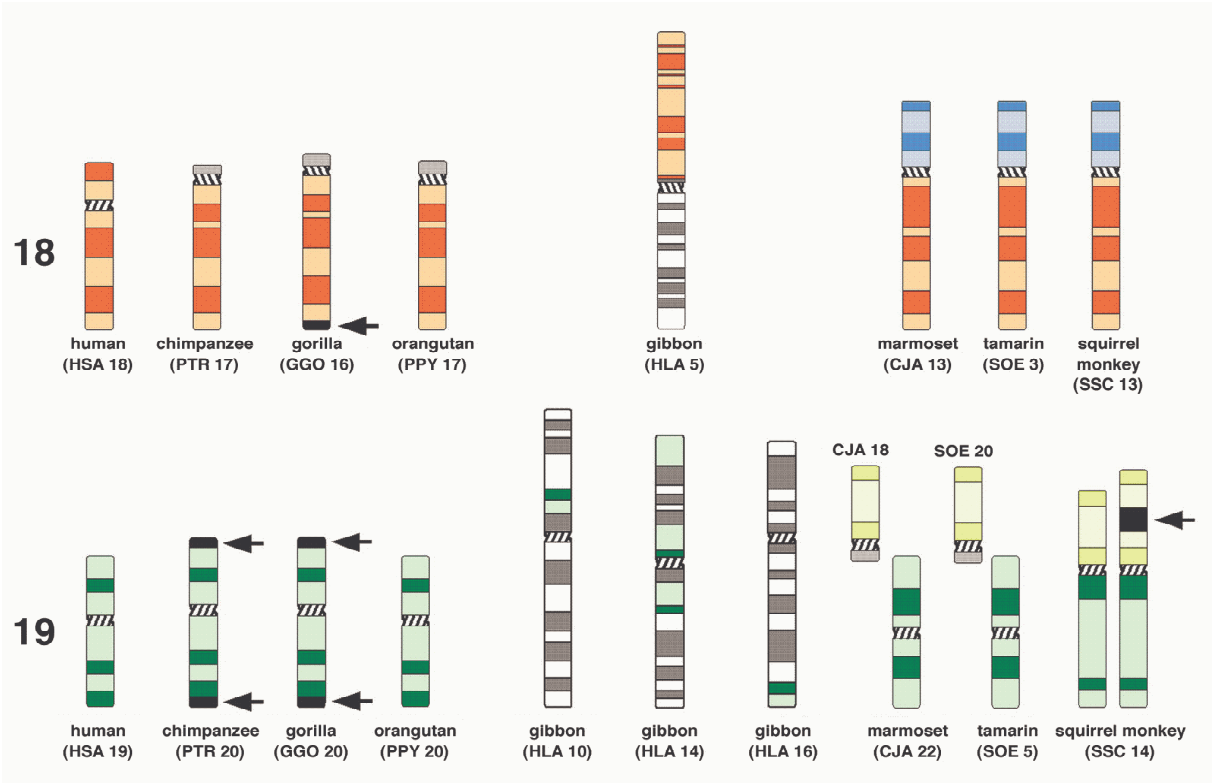

Figure 1. Idiogramatic illustration of G-banded primate chromosomes or chromosomal subregions homolgous to human chromosome 18 (red; top) or 19 (green; bottom). Arrows indicate heterochromatin blocks not present in the human and orangutan chromosomes. P-arms of CJA13, SOE 3 and SSC 13 (highlighted light-blue) are homologous to HSA8p. SSC14p, CJA18 and SOE20 (highlighted yellow) are homologous to HSA1q32→qter. The investigated squirrel monkey individual showed an interstitial repeat heteromorphism in SSC14p (arrow). Chromosome nomenclature was followed by refs. (16, 20, 21, 24).

Employing two color FISH, we delineated CTs and chromosomal segments, respectively, homologous to HSA18 or HSA19 in 3D preserved lymphoblastoid cell nuclei from all the primate species mentioned above. As the extent to which radial chromosome territory arrangements in these nuclei may change during the cell cycle is not clear at present, all analyses described below were restricted to cells at a clearly identifiable stage of the cell cycle, namely S-phase. 3D preserved cell nuclei were then hybridized with differentially labeled painting probes specific for HSA18 or HSA19 or their primate homologues (Table 1). Four different fluorochromes were employed for the visualization of painted CTs, BrdU labeled DNA and overall nuclear DNA. Light optical serial sections were recorded from BrdU positive nuclei with a laser scanning confocal microscope. As an example, Fig. 2d shows an image gallery from a marmoset lymphoblastoid cell nucleus demonstrating the interior location of HSA19 homologous CTs and the peripheral location of the HSA18 homologous chromosome segments. Fig. 2e shows representative 3D reconstructions of this nucleus. Figs. 2f-g and 3a-f indicate the same radial arrangement of HSA18 and HSA19 homologous chromatin in lymphoblastoid cell nuclei in all species.

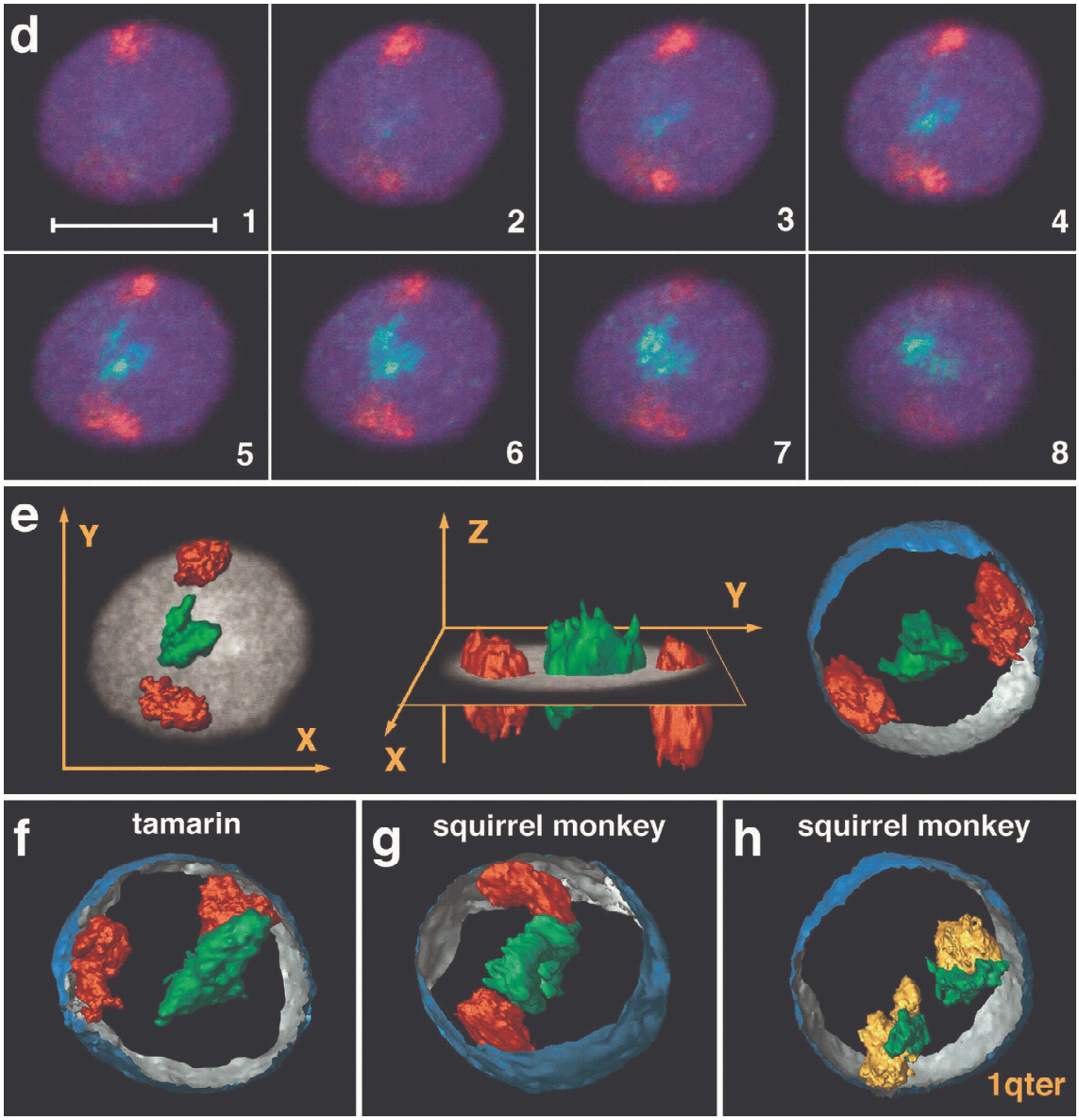

d, Gallery of 200 nm serial light optical sections (every third section shown) through a marmoset lymphoblastoid cell nucleus after painting of HSA18 (red) and HSA19 (green) homologous chromosome material, DNA counterstain shown in blue (Scale bar 10 µm). e, 3D reconstructions of painted CTs presented in a. In the X, Y view (left) and X, Z view (middle) the mid plane section of the counterstained nucleus is added as a gray shade. The right panel shows CTs together with a partial 3D reconstruction of the DNA-counterstained nuclear border (outside: blue, inside: silver-grey). f-g, 3D reconstruction of chromosome material homologous to HSA18 and HSA19 in a tamarin and squirrel monkey nucleus. h, 3D reconstruction of the two SSC 14 territories in a squirrel monkey nucleus following two color FISH of SSC14q (green; homologous to

HSA19) and SSC14p (orange; homologous to HSA1q32→qter (compare Fig. 1)). The origin of paint probes used for each species is described in Table 1.

II.3.3.2. Quantitative 3D Evaluation of primate homologous CTs.

For each species this positioning was quantitatively evaluated in a set of nuclei (31 to 43 nuclei per species) after defining the geometrical center and border of each nucleus and dividing its space into 25 radial concentric shells (Fig. 4)[10]. The relative contribution of each painted CT to each of these shells was calculated as described in Methods. For comparison, the relative contribution of nuclear DNA was also recorded in each shell. The resulting data are graphically presented in Figs. 5 and 6.

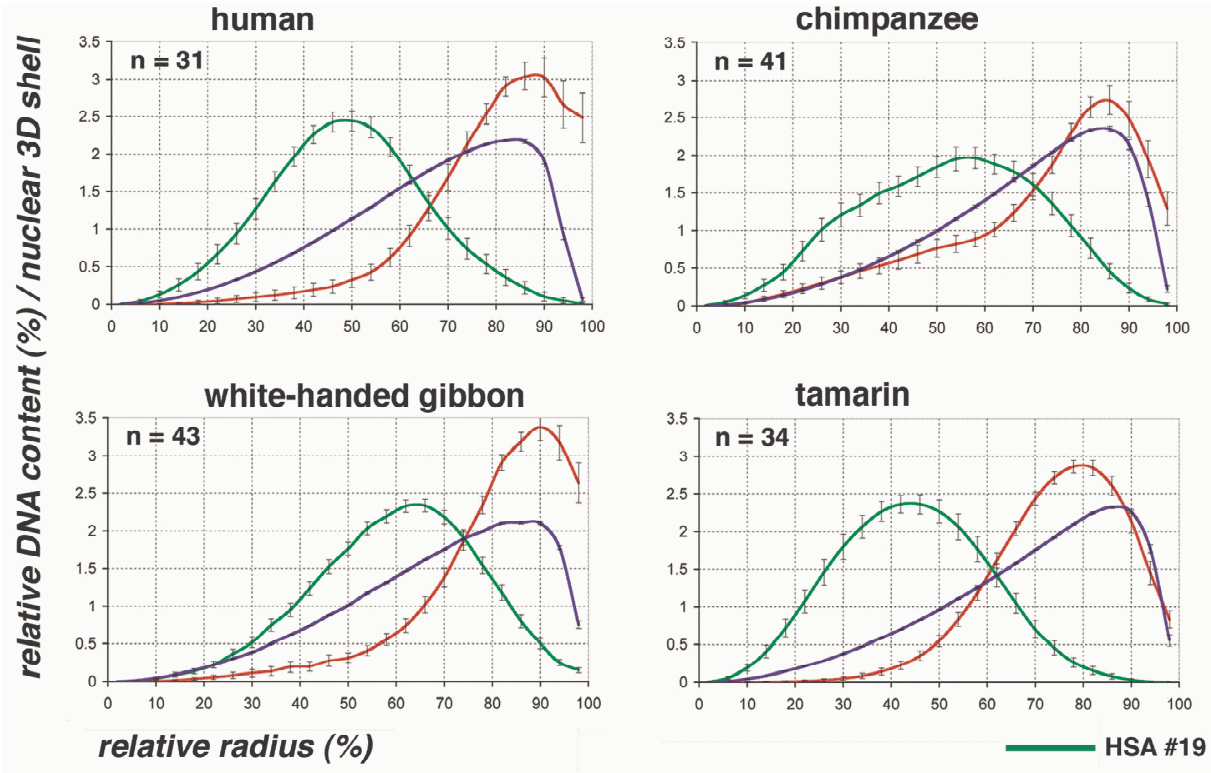

[10] for figures see Chapter I, "Einleitung"

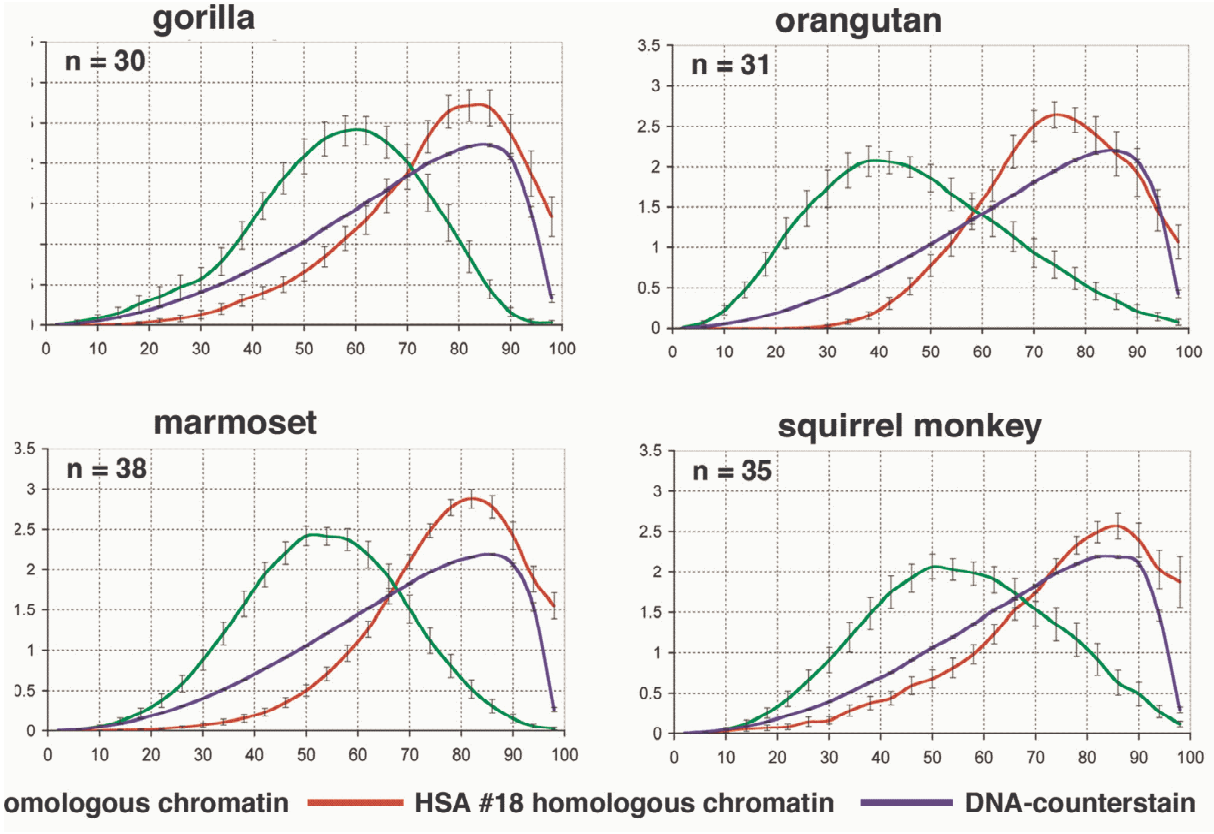

Figure 5. Quantitative 3D evaluation of radial chromatin arrangements in primate cell nuclei with HSA18 and HSA19 homologues. Radial chromatin arrangements observed after painting with HSA18 and HSA19 homologous probes evaluated in 25 radial concentric nuclear shells (compare Fig. 4). The ordinate denotes the relative radius r of the nuclear shells, the abscissa denotes the normalized sum of the intensities in the voxels for a respective fluorochrome belonging to a given shell. For normalization, the area underlying the curve for each color (total relative DNA content) was set to 100. Primate cell nuclei; n = number of 3D evaluated nuclei. In all species a highly significant difference ($p<0.001$) was noted between the radial positioning of HSA18 (red) and HSA19 (green) homologous chromatin. HSA18 homologous chromosome material is consistently distributed closer to the nuclear border, while HSA19 homologous material is distributed towards the nuclear interior. Bars indicate standard deviations of the mean for each shell. Blue curves represent counterstained DNA.

In cell nuclei from human and great apes we observed homologous HSA18 chromatin at the nuclear periphery with a maximum DNA content between 75% and 88% of the relative radius, while homologous HSA19 chromatin was observed in the nuclear interior with a maximum DNA content between 38% and 58% (Table 2, Fig. 5).

II.3.3.3. Radial distribution of human chromosome 18 and 19 homologous CTs.[11]

Table 2:

Species	HSA18 homologues #	HSA19 homologues #	HSA1q32→1qter homologues#	Nuclei with conserved radial arrangement‡
HSA	88%	48%	-	31/31 (100%)
PTR	86%	58%	-	38/41 (92.7%)
GGO	85%	60%	-	30/30 (100%)
PPY	75%	38%	-	31/31 (100%)
HLA	90%	64%	-	43/43 (100%)
SOE	79%*	42%§	62%	34/34 (100%)
CJA	82%*	51%§	65%	38/38 (100%)
SSC	86%*	54%§	79%	33/35 (94.3%)

Peaks of maximum DNA content at the relative distance from the nuclear center.

* These painted CTs contain also HSA8p homologous chromosome segments.

§ These values indicate average values of two independent experiments (compare Figs. 5 and 6).

‡ Individual nuclei where CTs 18 gravity centers show a more peripheral location than CTs 19.

The findings obtained for human and great apes lymphoblastoid cell nuclei are fully consistent with previous studies of human lymphocytes and show that transformed lymphoblastoid cell lines retain the distinctly different radial arrangement of HSA18 and HSA19 CTs observed in nuclei of both non-

[11] for more statistical analysis s. Chapter II.3.7

cycling B and T cells from peripheral blood and PHA stimulated, cycling normal T-lymphocytes (7, 8).

In lesser apes (gibbons) the HSA18 homologue is conserved but translocated, whereas the HSA19 homologue is fragmented (24). In the white-handed gibbon a HSA18 homologous segment is associated with a HSA1p32→q22 homologous segment to form the metacentric gibbon chromosome 5 (Fig. 1). Gibbon chromosomes 10 and 16 each carry one segment of HSA19 homologous chromatin, while gibbon chromosome 14 contains two HSA19 homologous segments, one of them including the centromeric heterochromatin (Fig. 1). According to these complex rearrangements most nuclei revealed four to eight painted regions homologous to HSA19 (Fig. 3e). These regions were located towards the nuclear interior with a content maximum at 64% of the relative radius (Figs. 3e and 5, Table 2). Some nuclei even showed one large cluster of a centrally located painted region (Fig. 3f). In contrast, HSA18 homologous chromatin was always located in proximity to the nuclear envelope with a DNA content maximum at 90% (Table 2, Fig. 5).

In New World monkeys, the HSA18 homologues are entirely conserved but translocated to the HSA8p (7.3 genes/Mbp; http://www.ensembl.org/Homo_sapiens/), (Fig. 1). This chromosome form represents the ancestral condition of this primate infraorder (22). The probes used for these species painted these chromosomes along their entire length, i.e. both HSA18 and HSA8p homologous materials. In the three New World monkey species included in this study the HSA18 and HSA8p homologous chromosome segments revealed maximum DNA contents at relative radii between 79% and 86% and were thus within the same range as found for the great and lesser apes. HSA19 homologous chromosomes or chromosome segments showed maximum DNA contents at relative radii between 42% and 54% (Table 2, Fig. 5). In the squirrel monkey HSA19 homologous chromatin is represented by SSC14q and SSC14p by a HSA1q32→qter homologous segment. Two color painting of squirrel monkey chromosomes 14p and 14q revealed a specific orientation of these CTs: HSA1q32→qter homologous

chromosome segments with a gene density of 9.5 genes/Mbp (http://www.ensembl.org/Homo_sapiens/) were typically located closer towards the nuclear periphery with a DNA content maximum at around 79% of the relative radius while the HSA19 homologous segments with a gene density of 20.5 genes/Mbp were located towards the nuclear centre with a maximum DNA content at 54% of the relative radius (Figs. 2h, 6). Similar radial orientations were observed in tamarin and marmoset cell nuclei (Fig. 6) where HSA19 and HSA1q32→qter homologous chromatin represent separate chromosome entities (Fig. 1).

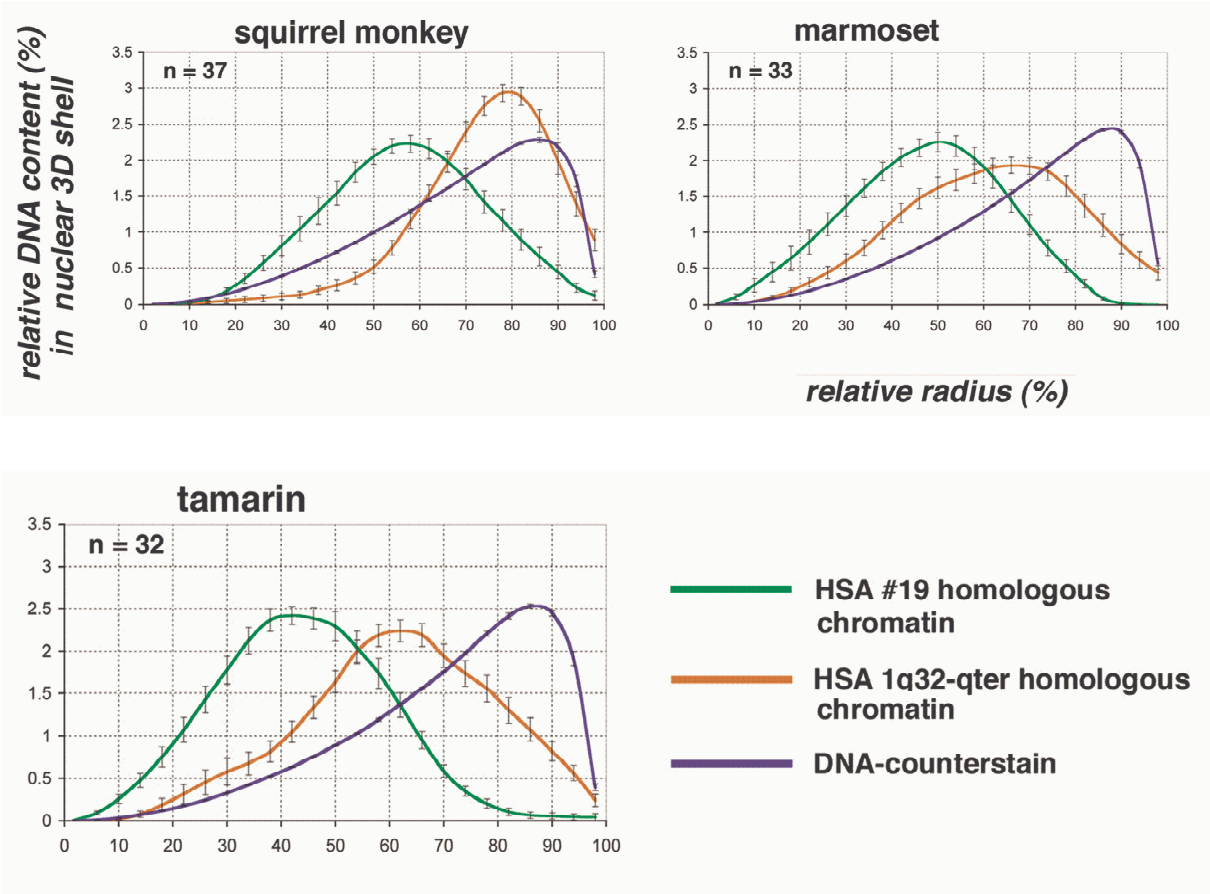

Figure 6. Quantitative 3D evaluation in New World monkey species nuclei with HSA19 and HSA1q32→qter homologues. Left, Quantitative 3D evaluation of SSC14 positioning in squirrel monkey cell nuclei after painting of SSC14p (red) with a HSA1q32→qter homologous probe and of SSC14q (green) with a HSA19 homologous probe (compare Fig. 1). Middle and right, Quantitative 3D evaluation after painting of

separate chromosomes homologous to HSA1q32→qter (red) and HSA19 (green) homologous segments in marmoset and tamarin cell nuclei (for the description of the abscissa and the ordinate see Fig. 5).

II.3.4. Discussion

Our results demonstrate that the distinctly different radial distribution patterns that have been previously found for CTs 18 and 19 in human lymphocyte and lymphoblastoid cell nuclei have been conserved for HSA18 and HSA19 homologous chromatin during higher primate evolution. In all species analyzed HSA18 homologous chromatin was found at the nuclear periphery and HSA19 homologous chromatin towards the nuclear interior. This radial distribution pattern was thus maintained over a period of at least 30 million of years, irrespective of the extensive chromosomal rearrangements that occurred during the evolution of higher primates. Our results fit the hypothesis that radial chromatin arrangements reflect differences in gene density (6). Additional evidence supporting this hypothesis is provided by our observation of a specific orientation of the relatively gene-poor HSA1q32→qter and the gene dense HSA19 homologous chromatin segment which form chromosome 14 in the squirrel monkey. This hypothesis also holds true for somatic translocation events. For example, a somatic t(18;19) translocated chromosome also maintained the original nuclear orientation of the translocation partners with a peripheral location of HSA18 and an internal location of the HSA19 region (8).

It is a well established fact that the positioning of genes close to heterochromatin blocks can strongly affect their transcription (25) and it has also been argued that heterochromatin blocks may play a role with regard to the evolving nuclear architecture (26). Chromosome translocations that join heterochromatic segments with gene-dense chromatin segments may therefore lead to radial chromatin shifts depending on the size and composition of the respective segments. For example, gene – poor chromatin and heterochromatin has often been noted at the nuclear periphery (5). Accordingly, the joining of a heterochromatin block with a gene-dense chromosome segment, previously

located in a gene-dense, interior nuclear compartment, may result in a positional shift of the latter towards the peripheral nuclear compartment, possibly affecting its transcriptional activity. Our present study provides two possible examples for such a shift. Firstly, the squirrel monkey chromosome 14p (homologous to HSA1q32→qter) is heteromorphic in the cell line used in this study (Fig. 2c). One 14 p-arm shows a large, additional heterochromatic band, which is neither present in the other homologous squirrel monkey chromosome 14 nor in the corresponding counterparts of marmoset chromosome 18 and tamarin chromosome 20 (Fig. 1). This additional band may possibly explain, why squirrel monkey 14p chromatin was distributed on average more towards the nuclear periphery (maximum DNA content at 79%) than marmoset 18 and tamarin 20 CTs showing their maximum DNA content at 65% and 62%, respectively (Table 2, Fig. 6). Secondly, we observed a more exterior position of CTs of HSA19 homologues in chimpanzee and gorilla (at relative radius of 58% and 60%, respectively) as compared to human and orangutan (at 48% and 38%, respectively; Table 2, Fig. 5). Chimpanzee and gorilla homologues contain large regions of terminal heterochromatin, (Fig. 2a) while these blocks are absent in the respective human and orangutan chromosomes (Fig. 1, arrows). It is intriguing to look for other examples of chromosome evolution as well as chromosomally rearranged tumor cells, where the chromatin context adjacent to a given gene-poor or gene-rich chromosome segment changes and to test the consequences for radial positioning and gene function.

Finally, the finding of specific radial CT arrangement is not limited to primate cell nuclei, but was also reported for chicken cell nuclei (9). In Gallus gallus domesticus microchromosomes are early replicating and considerably more gene-dense than the gene-poor and later replicating macrochromosomes. We noted the location of microchromosome territories preferentially in the nuclear interior surrounded by the more peripherally located macrochromosome territories. This gene density-correlated radial higher order chromatin arrangement in chicken cell nuclei shows that the evolutionary conservation of non-random radial arrangements is compatible with drastic changes in

karyotype evolution that have occurred before the separation of the evolutionary branches which led to present days mammals and birds. In this context it is interesting to note that syntenic regions of HSA19 have been assigned to chicken microchromosomes whereas syntenic regions of HSA18 have been assigned to the chicken macrochromosomes 2 and Z (27, 28).

The evidence for an evolutionary conservation of gene density correlated radial chromatin arrangements argues for a functional significance. Possible underlying molecular mechanisms responsible for the establishment and maintenance of these higher order chromatin arrangements remain to be elucidated. In this context it is interesting to test whether the density of expressed genes rather than of all genes plays a major role. The observation of different positions of the active and inactive X chromosome in female cell nuclei argues for such a possibility. In addition, the different CG content of gene – dense and gene – poor chromosome segments should be considered (29).

II.3.5. Acknowledgements

This study was supported by a stipend of the Japanese government, STA, to H.T. and a grant from the Deutsche Forschungsgemeinschaft to T.C.

II.3.6. References

1. Chevret, E., Volpi, E. V. & Sheer, D. (2000) Cytogenet. Cell Genet. 90, 13-21.

2. Cremer, T. & Cremer, C. (2001) Nat Rev Genet 2, 292-301.

3. Cremer, T., Kreth, G., Koester, H., Fink, R. H. A., Heintzmann, R., Cremer, M., Solovei, I. V., Zink, D. & Cremer, C. (2000) Critical Reviews in Eukaryotic Gene Expression 12, 179-212.

4. Lamond, A. I. & Earnshaw, W. C. (1998) Science 280, 547-553.

5. Leitch, A. R. (2000) Microbiol. Mol. Biol. Rev. 64, 138-152.

6. Boyle, S., Gilchrist, S., Bridger, J. M., Mahy, N. L., Ellis, J. A. & Bickmore, W. A. (2001) Hum Mol Genet 10, 211-219.

7. Cremer, M., v. Hase, J., Volm, T., Brero, A., Kreth, G., Walter, J., Fischer, C., Solovei, I., Cremer, C. & Cremer, T. (2001) Chromosome Res 9, 541-567.

8. Croft, J. A., Bridger, J. M., Boyle, S., Perry, P., Teague, P. & Bickmore, W. A. (1999) J. Cell Biol. 145, 1119-1131.

9. Habermann, F., Cremer, M., Walter, J., v.Hase, J., Bauer, K., Wienberg, J., Cremer, C., Cremer, T. & Solovei, I. (2001) Chromosome Res 9, 569-584.

10. Craig, J. M. & Bickmore, W. A. (1994) Nat Genet 7, 376-382.

11. Sadoni, N., Langer, S., Fauth, C., Bernardi, G., Cremer, T., Turner, B. M. & Zink, D. (1999) J. Cell Biol. 146, 1211-1226.

12. Jackson, D. A. (1995) Bioessays 17, 587-591.

13. Nakayasu, H. & Berezney, R. (1989) J. Cell Biol. 108, 1-11.

14. O'Keefe, R. T., Henderson, S. C. & Spector, D. L. (1992) J. Cell Biol. 116, 1095-1110.

15. Lander, E. S., Linton, L. M., Birren, B., Nusbaum, C., Zody, M. C., Baldwin, J., Devon, K., Dewar, K., Doyle, M., FitzHugh, et al. (2001) Nature 409, 860-921.

16. Müller, S., Neusser, M., O'Brien, P. C. M. & Wienberg, J. (2001) Chromosome Res 9, 689-693.

17. Müller, S., O'Brien, P. C., Ferguson-Smith, M. A. & Wienberg, J. (1997) Hum Genet 101, 149-153.

18. Solovei, I., Walter, J., Cremer, M., Habermann, F., Schermelleh, L. & Cremer, T. (2002) in FISH: a practical approach, eds. Squire, J., Beatty, B. & Mai, S. (Oxford University Press, Oxford). in press.

19. Telenius, H., Carter, N. P., Bebb, C. E., Nordenskjold, M., Ponder, P. A. I. & Tunnacliffe, A. (1992) Genomics 13, 718-725.

20. Stanyon, R., Consigliere, S., Müller, S., Morescalchi, A., Neusser, M. & Wienberg, J. (2000) Am J Primatol 50, 95-107.

21. Stanyon, R., Consigliere, S., Bigoni, F., Ferguson-Smith, M., O'Brien, P. C. & Wienberg, J. (2001) Chromosome Res 9, 97-106.

22. Wienberg, J. & Stanyon, R. (1998) ILAR J 39, 77-91.

23. Yunis, J. J. & Prakash, O. (1982) Science 215, 1525-1530.

24. Jauch, A., Wienberg, J., Stanyon, R., Arnold, N., Tofanelli, S., Ishida, T. & Cremer, T. (1992) Proc. Natl. Acad. Sci. USA 89, 8611-8615.

25. Brown, K. E., Baxter, J., Graf, D., Merkenschlager, M. & Fisher, A. G. (1999) Mol Cell 3, 207-217.

26. Manuelidis, L. (1990) Science 250, 1533-1540.

27. Burt, D. W., Bruley, C., Dunn, I. C., Jones, C. T., Ramage, A., Law, A. S., Morrice, D. R., Paton, I. R., Smith, J., Windsor, D. et al (1999) Nature 402, 411-413.

28. Schmid, M., Nanda, I., Guttenbach, M., Steinlein, C., Hoehn, M., Schartl, M., Haaf, T., Weigend, S., Fries, R., Buerstedde, J. M. et al. (2000) Cytogenet Cell Genet 90, 169-218.

29. Bernardi, G. (2001) Gene 276, 3-13

II.3.7. Statistische Aufbereitung der Primatenuntersuchung

Übersichtstabelle:

	$<r_{18}>$	Sd korr	$<r_{19}>$	SD korr	dist. in SD	dist. in SDM
Squirrel Monkey	75,4	15,27	55,5	16,55	0,88	6,49
Common Marmoset	76,9	8,49	53,0	12,59	1,57	10,08
Tamarin	80,7	11,60	60,2	9,33	1,38	7,91
White Handed Gibbon	72,0	15,84	52,8	14,57	0,89	6,05
Orang Utan	73,8	11,46	46,8	16,40	1,35	8,75
Gorilla	75,2	10,32	56,5	14,14	1,07	7,85
Chimpanzee	72,0	15,84	52,8	14,57	0,89	6,74
human	79,2	12,73	48,8	11,74	1,76	9,78

Tab.II.3.1. In obiger Tabelle werden in Reihenfolge der evolutionären Entfernung zum Menschen die mittleren radialen Erwartungswerte der Chromosomen #18 und #19 gezeigt. Dazu die Standardabweichungen der Radialwerte, bei denen eine Multiplikation um den Faktor Ö2 stattfand, um Auszugleichen, dass die Einzelmessungen in Wahrheit Mittelwerte von je 2 Homologen waren. In die Tabelle mit eingetragen wurden die Abstände der Verteilung der Chromosomen #18 und #19 in Standardabweichungen der Verteilungen und die Abstände der Mittelwerte in Einheiten der Fehler der Mittelwerte.

Eine andere Möglichkeit der statistischen Aufbereitung liegt darin, von allen Mittelwerten der Position der Chromosomen #18 und #19 einen Mittelwert mit Standardabweichung zu bilden Es ergibt sich so:

<r18>= 75,7 – 3,2 <r19>= 53,3 – 4,3

Damit wäre der Abstand der beiden Mittelwerte 4,18 Standardabweichungen Nach beiden Rechnungen wäre der Abstand der Mittelwerte voneinander hochsignifikant. Die zweite Rechnung hat den Vorzug, dass sie nicht vom Stichprobenumfang der einzelnen Spezies abhängt.

II.3.8. Formparameter von Chr. #18 und 19 in Primaten

Morphologische Parameter waren das Volumen, die Oberfläche, die Roundness und die Smoothness vgl. Kapitel II.1.2. Beim Vergleich der verschiedenen Spezies bei gleichen Territorien konnte keine Abhängigkeit der evolutionären Entfernung zum Menschen oder dem Lebensraum der Primaten gesehen werden. Beim Vergleich zwischen Chromosom #18 und #19 fällt aber eine Korrelation bei den Volumen und Oberflächen auf. Dies könnte von der individuellen Fixierung der Zellen beider Spezies abhängen: Das angewandte Verfahren lies die Zellen erst schrumpfen und dann wieder anschwellen. Eine Verbesserung wäre hier nötig.

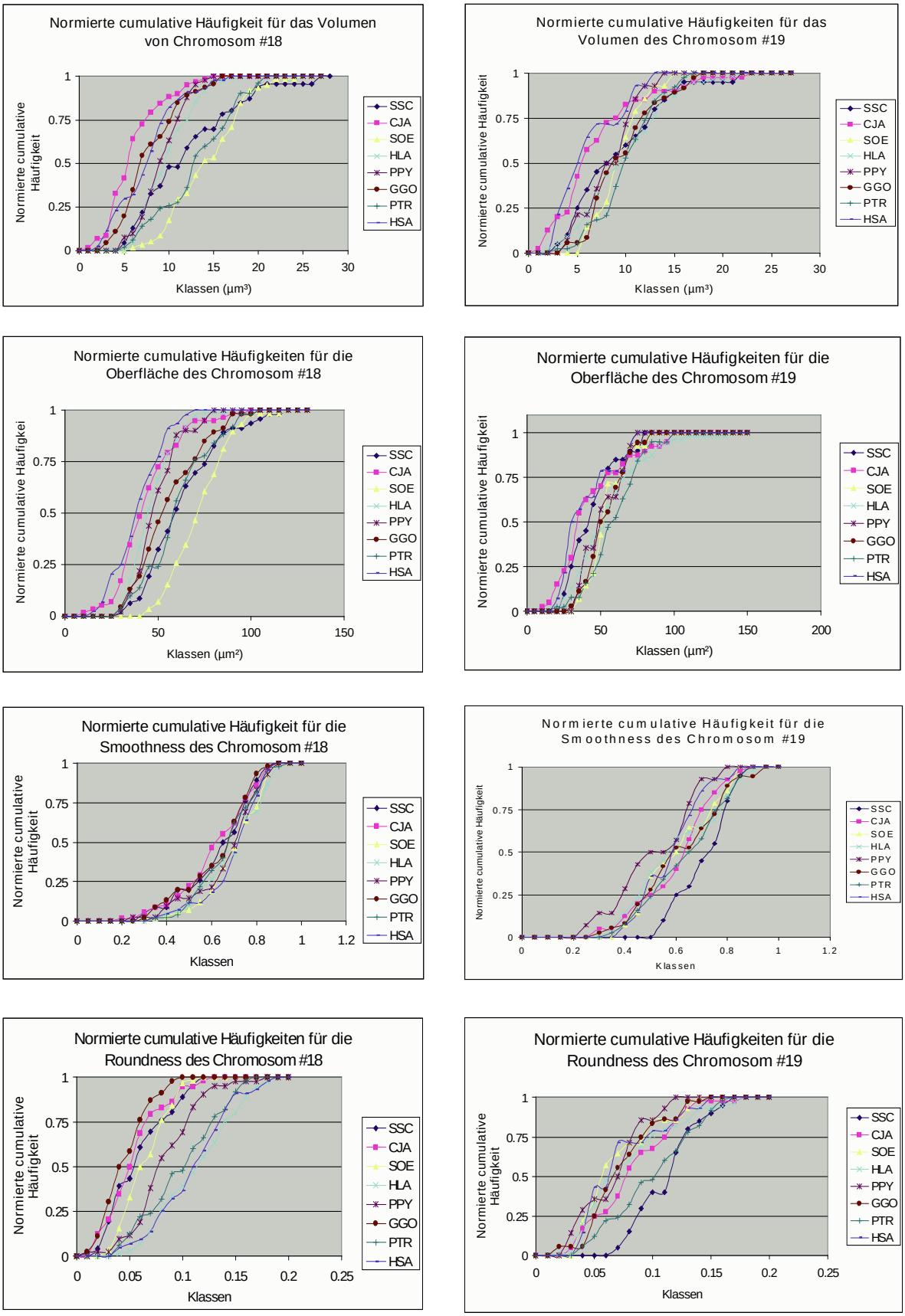

Abb.II.3.1. Im Vergleich lässt sich eine Korrelation im Volumen und der Oberfläche zwischen den CTs #18 und #19 finden. Dies könnte aber von der für jede Spezies individuellen Fixierung abhängen. Die Graphen stammen aus [Calcagno 2001][4].

[4]Unterstützung der Diplomarbeit durch J.v.Hase

II.3b. Arrangements of macro- and micro-chromosomes in chicken cells[12]

Felix A. Habermann [1,3], Marion Cremer [1], Joachim Walter [1], Gregor Kreth [2], Johann von Hase [2], Karin Bauer [1], Johannes Wienberg [1], Christoph Cremer [2], Thomas Cremer [1], and Irina Solovei [1*]

[1] Institute of Anthropology and Human Genetics, University of Munich (LMU), Munich, Germany; Tel: (+49) 89 2180 6713; Fax: (+49) 89 2180 6719; E-mail: irina.solovei@lrz.uni-muenchen.de; [2] Kirchhoff-Institute of Physics, University of Heidelberg, Heidelberg, Germany; [3] Present address: Chair of Animal Breeding, Technical University of Munich, Freising-Weihenstephan, Germany

* Correspondence

[12] Published in: Chromosome Research 9, pp. 569 – 584, 2001

Key words: chromosome arrangement, nuclear architecture, chicken interphase nuclei, 3D M-FISH.

II.3b.1. Abstract

Arrangements of chromosome territories in nuclei of chicken fibroblasts and neurons were analysed employing multicolor chromosome painting, laser confocal scanning microscopy and three-dimensional (3D) reconstruction. The chicken karyotype consists of 9 pairs of macrochromosomes and 30 pairs of microchromosomes. Although the latter represent only 23% of the chicken genome they contain almost 50% of its genes. We show that territories of microchromosomes in fibroblasts and neurons were clustered within the centre of the nucleus, while territories of the macrochromosomes were preferentially located towards the nuclear periphery. In contrast to these highly consistent radial arrangements the relative arrangements of macrochromosome territories with respect to each other (side-by-side arrangements) were variable. A stringent radial arrangement of macro- and microchromosomes was found in mitotic cells. Replication labelling studies revealed a pattern of DNA replication similar to mammalian cell nuclei: gene dense, early replicating chromatin mostly represented by microchromosomes, was located within the nuclear interior, surrounded by a rim of later replicating chromatin. These results support the evolutionary conservation of several features of higher order chromatin organization between mammals and birds despite the differences in their karyotypes.

II.3b.2. Introduction

The genomes of all presently existing vertebrate species have diverged from a common ancestor over a period of several hundred million years. The comparative analysis of the genome organization between remote species is a key tool for the delineation of evolutionary conserved features of this organization. While numerous studies have been carried out with regard to the evolutionary changes of genes and karyotypes in mammals (O'Brien et al.,

1999), data that allow a comparison of nuclear architecture between distant vertebrate species have been lacking so far. The divergence of birds and mammals from a common ancestor occurred about 300 – 350 million years ago (Hedges et al., 1996). The degree of conserved homologous chromosomal segments between humans and chicken revealed by genetic and physical mapping data is surprisingly high (Burt et al., 1999) while the karyotypes are strikingly different. The human genome consists of 2n = 46 chromosomes ranging from 279 Mb to 45 Mb (Lander et al., 2001) while the chicken, Gallus gallus domesticus, has 2n = 78 chromosomes with a size range between 250 Mb (Smith and Burt, 1998) and 3.5 Mb (Pichugin A.M. et al., 2001). The chicken chromosomes are classified somewhat arbitrarily into two major groups: the macrochromosomes comprise chromosome 1 – 8 and the sex chromosomes (ZZ, male or ZW, female) with a size ranging from 250 Mb to 30 Mb. The remaining smaller chromosomes are called microchromosomes and cannot be distinguished by conventional banding techniques. Microchromosomes represent approximately 23% of the female genome, are CG-rich and contain about 48% of all genes that have a high content of CpG islands (McQueen et al., 1996; McQueen et al., 1998; Smith et al., 2000; Smith and Burt, 1998). In average, microchromosomes appear to have a 2 - 4 times higher gene density than the macrochromosomes (Smith et al., 2000). The macrochromosomes are AT-rich and exhibit weak R-, C-, and T-banding (Schmid et al., 1989). The chicken genome (about 1200 Mb, Smith et al., 2000) is distinctly smaller than the human genome (3300 Mb, Lander et al., 2001). The smaller genome size in birds is mainly due to a lower content of repetitive sequences (Primmer et al., 1997).

The availability of specific DNA probes that delineate entire individual chromosomes and chromosomal subregions down to the level of individual gene loci has made possible detailed studies of chromosome structure and their arrangement in the nuclei of human cells. Recently, specific chromosome paint probes have also become available for all chicken macrochromosomes, several of the larger microchromosomes, and for fractions of smaller microchromosomes

(Griffin et al., 1999). The availability of this probe set has prompted us to study chromosome territory arrangements in chicken cell nuclei for comparison with the data known for human cells. The following questions were posed: (1) can we confirm a territorial organization of chromosomes in chicken cell nuclei? (2) Are neighbourhoods (side-by-side arrangements) of chicken chromosome territories fixed or variable as noted for several human cell types (see Cremer et al., 2001a, this issue)? (3) Do chicken nuclei exhibit specific radial arrangements of chromosome territories depending on different parameters such as chromosome size, gene density and replication timing as observed in humans and other mammalian species (see Cremer et al., 2001a, this issue)? We performed multi-colour FISH on three-dimensionally (3D) preserved nuclei of embryonic chicken fibroblasts and neurons. In addition, replication labelling with halogenated thymidine analogues was employed to study the nuclear distribution of early and mid-to-late replicating chromatin.

II.3b.3. Materials and Methods

II.3b.3.1. Cell Culture

Embryonic chicken fibroblasts were isolated from 5–6 day old chicken embryos and grown at 39°C and 3% CO_2 in Dulbecco's minimal essential medium (DMEM) containing 4,5 mg/ml glucose and 2 mM L-glutamine, supplemented with 10% fetal calf serum (FCS) and 100 U/ml penicillin / 100 µg/ml streptomycin. Primary neuronal cell cultures were prepared from the telencephalon of 7-day-old chicken embryos as described by Pettmann et al., 1979. Cerebral hemispheres were mechanically dissociated by passing through a nylon mesh (mesh size 48 µm). The resulting cell suspension was seeded at an approximate cell density of 4×10^4 cells / cm^2 on poly-L-lysine (MW 70 - 100 kD, Sigma, Germany) coated coverslips and cultured in 80% DMEM and 20% fetal calf serum for 6 days. Medium was changed every 24 hours. The outgrowth of neurites started 12 hours after seeding, building up a branched network during the time of cultivation. Chicken lymphoblastoid cell line DT-40 was kindly provided by Dr.J.-M. Buerstedde (Heinrich-Pette Institute for Experimental Virology and

Immunology, University of Hamburg) and was grown in RPMI 1640 supplemented with 10 % FCS and 2 % chicken serum.

II.3b.3.2. Generation of labelled pools of chromosome-specific painting probes

For multicolor FISH, we prepared pools containing several chromosome specific painting probes. These probes were obtained from flow-sorted chicken chromosomes (Griffin et al., 1999) and amplified by DOP-PCR using the 6MW primer (Telenius et al., 1992). Probe pools were re-amplified by stringent DOP-PCR and subsequently labelled with biotin- or digoxigenin-dUTP (Roche, Germany) by DOP-PCR or with estradiol-dUTP (Roche, Germany) using a standard nick-translation protocol. Two sets of probe pools were prepared: (I) Probe pools for differential painting of the macrochromosomes 1 – 6 and Z by combinatorial labelling: Pool Ia including chromosomes 1, 4, 5 and 6 was labelled with biotin-dUTP; pool Ib including chromosomes 2, 4, 6, and Z was labelled with digoxigenin-dUTP; pool Ic including chromosomes 3, 5, 6, and Z was labelled with estradiol-dUTP. (II) To study the size-correlated distribution of chromosome territories, three other probe pools were prepared: Pool IIa detecting the macrochromosomes 1-5 and Z was labelled with biotin-dUTP; pool IIb detecting the medium-sized chromosomes 6-10 was labelled with estradiol-dUTP; pool IIc detecting 19 microchromosomes was labelled with digoxigenin-dUTP. The pool of medium-sized chromosomes 6 – 10 takes into account that chromosome 6 is notably smaller than chromosome 5 and that chromosome 10 is notably larger than the remaining microchromosomes (see Figure 1B, 2A).

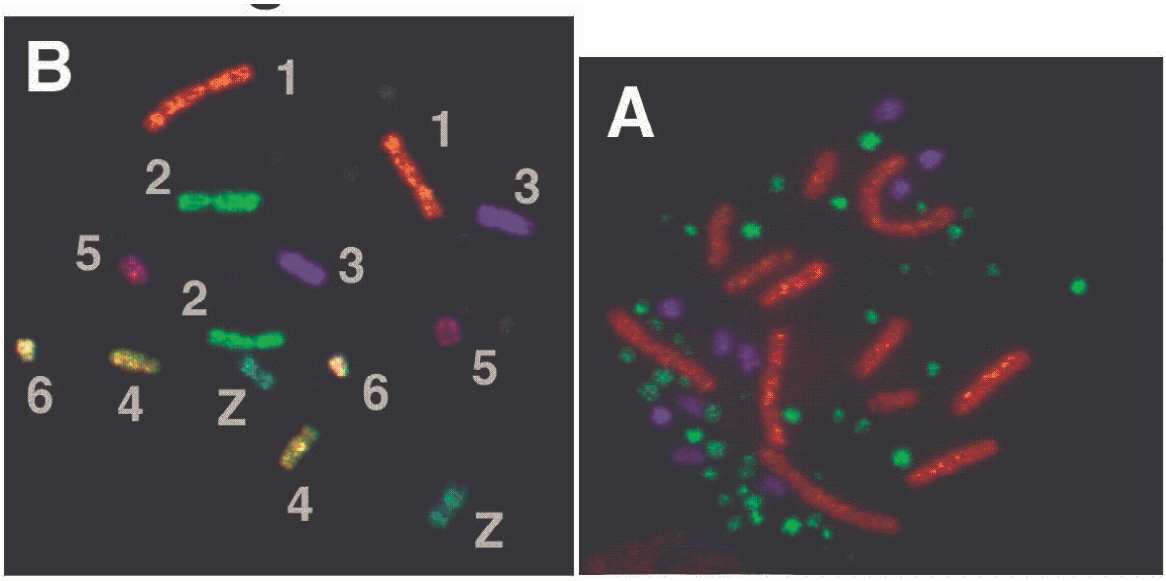

(B) Chicken (ZZ) metaphase spread after 7-color painting. False colours were attributed to the painted chromosomes 1-6 and Z depending on the different combinations of fluorochromes explained in (A). . (A) Chromosome painting of a chicken (ZZ) metaphase spread.

II.3b.3.3. Fluorescence in situ hybridization on metaphase spreads (2D FISH)

The labelled probe pools were mixed with a 10-fold excess of chicken Cot-1 DNA, ethanol-precipitated and re-suspended in 50% deionised formamide, 10% dextran sulphate and 1xSSC to a final concentration of 20 - 40 ng/µl for each single probe. Probes were denatured at 75°C for 5 min and allowed to pre-anneal for 20 min at 37°C before hybridization. Metaphase spreads from fibroblasts and DT-40 cells were prepared following standard protocols. Slides with metaphase spreads were denatured in 70% formamide/2xSSC, pH 7.0 at 70°C for 2 min, dehydrated in an ethanol series and air-dried before probe loading. Hybridization was performed at 37°C for 72 hours. Post-hybridization washes included 2xSSC at 37°C and 0.1xSSC at 60°C. Biotin was detected by Avidin-Cy3 (Dianova, Germany), digoxigenin by a monoclonal mouse anti-digoxigenin antibody (Roche, Germany) and a FITC-conjugated sheep anti-mouse antibody. Estradiol was detected by an anti-estradiol antiserum from rabbit (Roche) and a Cy5-

conjugated goat-anti-rabbit antibody (Dianova, Germany). Chromosomes were counterstained with DAPI and mounted in Vectashield (Vector Laboratories, UK).

II.3b.3.4. FISH on three-dimensionally preserved nuclei (3D-FISH)

A detailed protocol for 3D-FISH employed in our laboratory is described elsewhere (Solovei et al., 2001 in press). Cells were seeded on coverslips (thickness 0.170 ± 0.01 mm) in quadruple cell culture chambers (Quadriperm, Heraeus, Germany) and cultured for 72 hours (fibroblasts) or 6 days (neurons). Cells were fixed under isotonic conditions in 1.3% paraformaldehyde in 0.5xPBS for 15 min at RT. Permeabilization steps included (1) treatment with 0.5% Triton X100 for 20 min, (2) incubation in 20% glycerol in PBS for 30 min, (3) repeated freezing in liquid nitrogen and thawing at RT, and (4) incubation in 0.1N HCl for 5 min. Coverslips with cells were kept in 50% formamide/2xSSC at 4^{o}C until hybridization. Hybridization conditions, post-hybridization washings and detection procedures were essentially the same as described for 2D FISH on metaphase chromosomes with the exception that cells were strictly prevented from drying. Therefore, after denaturation of cells in 70% formamide/2xSSC, pH 7.0 at 72°C for 2 min they were immediately quenched in ice-cold 50% formamide/2xSSC before probe loading.

II.3b.3.5. Replication labelling of Dt-40 cells and fibroblasts

For replication banding of chicken metaphase chromosomes asynchronously growing DT-40 cells were incubated for 1 hour with the thymidine analogue iododeoxyuridine (IdU, Sigma, final concentration 1 µM). Cells were washed twice with PBS and further incubated in RPMI medium. Six hours after the end of the first label cells were exposed to chlorodeoxyuridine (CldU, Sigma, final concentration 1 µM) for 1 hour and washed twice again with PBS. After further growth in label-free RPMI medium for 4 hours metaphase spreads were prepared following standard protocols. The same labelling protocol was employed for the delineation of early and later replicating chromatin in 3D-preserved nuclei of proliferating chicken fibroblasts with the modification that the interval between the two labels was 5 hours and cells were fixed immediately after the second pulse. For detection of IdU and CldU the DNA of metaphase chromosomes and 3D-

preserved fibroblast nuclei was denatured in 70% formamide at 72°C as described above. Incorporated IdU was detected using mouse-anti-BrdU (Clone B44, Becton Dickinson, UK) and Alexa 488-conjugated goat anti-mouse antibody (Molecular Probes, NL); CldU was detected using a monoclonal rat-anti-CldU antibody (Clone Bu/75, Oxford Biotechnology, UK) and Cy3-conjugated goat-anti-rat antibody (Amersham, UK). IdU and CldU were detected sequentially to avoid antibody cross-reactions (for a detailed description see Solovei et al., 2001 in press).

II.3b.3.6. Microscopy

Metaphase spreads were analysed using an epifluorescence microscope (Axioplan II, Zeiss, Germany) equipped with a PlanApochromat 100x/1.4 oil immersion objective and filter sets for DAPI, FITC, Cy3 and Cy5. Digital images were acquired by a CCD-camera (CoolView, Photonic Science, UK) using CytoVision software (Applied Imaging, UK). The 8 bit greyscale single channel images were overlaid to a RGB image assigning a false colour to each channel. Light optical serial sections of cell nuclei were recorded by a confocal microscope (LSM 410, Zeiss) equipped with a PlanApochromat 63x/1.4 oil-immersion objective, three laser channels (excitation lines 488 nm, 543 nm, 633 nm), and the following emission filters: 510–525 nm bandpass for FITC, 575–640 nm bandpass for Cy3, and 665 nm longpass for Cy5. For each focus plane, the three fluorochromes were recorded sequentially generating 8-bit grayscale images. Pixel size was 50 x 50 nm; the axial distance between optical sections was 250 nm. To obtain an improved signal-to-noise ratio each section image was averaged from 32 successive scans.

II.3b.3.7. Digital image processing

The confocal image stacks were corrected for chromatic shift and subjected to deconvolution using the software Huygens 2 (Scientific Volume Imaging b. v., Hilversum, NL), running on a silicon graphics O2 workstation, OS IRIX 6.5. For deconvolution a theoretical point spread function was applied considering the pixel size, the distance between the optical sections, the numerical aperture of the objective, pinhole size, refractive indices of mounting medium and immersion oil as well as the signal-to-noise ratio. The deconvolved image stacks were used to generate three-dimensional reconstructions of chromosome territories by surface rendering using 3D image software Imaris (version 2.7, Bitplane AG, Switzerland). Chromosome assignment for combinatorially labelled chromosomes was done by visual inspection of the resulting pure or mixed colours.

II.3b.3.8. Quantitative analysis of the size-correlated distribution of chromosome territories

For a quantitative evaluation of the chromatin distribution from the three chromosome sets for large, medium-sized, and microchromosomes (described as probe pools IIa – c in Methods) – a central optical section from each nucleus was analysed (for detailed description see Cremer et al., 2001a, this issue).

II.3b.3.9. Simulation of the chromosome territory arrangement in ellipsoid cell nuclei

To obtain a statistical distribution of chromosome territories that would be expected as a consequence of geometrical constraints, computer simulations were performed using the “spherical 1-Mbp chromatin domain (SCD) model” (for details see (Cremer and Cremer, 2001b; Cremer et al., 2000; Kreth et al., 2001 in press). The simulation experiments assumed an ellipsoid nuclear shape with half axes of 4:2:2 µm and took into account the approximate size of chicken chromosomes according to Smith and Burt, 1998. Chicken chromosomes were divided into three groups: (i) the macrochromosomes 1 – 4 and Z, (ii) the medium-sized chromosomes 5 – 8 and W, (iii) a set of 19 microchromosome pairs ranging in size from 14Mb down to 4 Mb. Each group of chromosome

territories was visualized in a separate colour by applying virtual microscopy techniques (Cremer et al., 2001a). For a quantitative evaluation a central section from each nucleus was analysed in exactly the same way as described for light optical sections of painted chicken nuclei.

II.3b.4. Results

II.3b.4.1. Variable side-by-side arrangements and structural features of macrochromosome territories 1-6 and Z

For differential painting of the 6 largest autosomes and the Z-chromosome by multi-colour FISH a combinatorial labelling scheme was established as shown in Figure 1A.

(A) Scheme of combinatorial labelling for 7-color FISH experiments (for details see Methods).

For this purpose the labelled probe pools were first tested individually and in combination on metaphase spreads. The concentration of individual chromosome-specific paint probes within each pool was adjusted to achieve a strong and rather homogeneous signal intensity on each painted chromosome. These adjusted pools were mixed and hybridised to metaphase spreads. Each chromosome could be identified visually based on its distinct fluorescence pattern (Figure 1B).

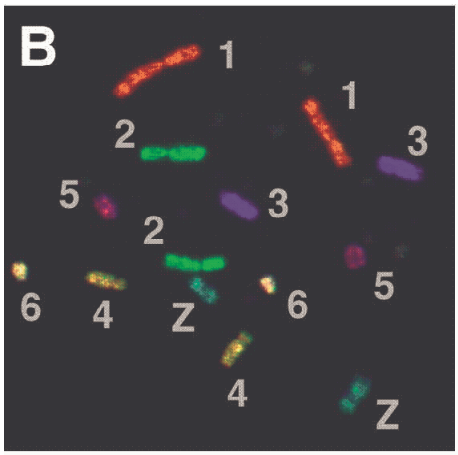

(B) Chicken (ZZ) metaphase spread after 7-color painting. False colours were attributed to the painted chromosomes 1-6 and Z depending on the different combinations of fluorochromes explained in (A)

The same probe pools were hybridised to 3D-preserved nuclei of fibroblasts and neurons. Observations of different optical sections demonstrated that each macrochromosome occupied a distinct territory (Figure 1D, E, G, H, I) with clear boundaries between adjacent territories. Deconvolution of the image stacks showed that the territories were built up of chromatin domains that have the appearance of granules (Figure 1E, H) with diameters of roughly 300 to 600 nm.

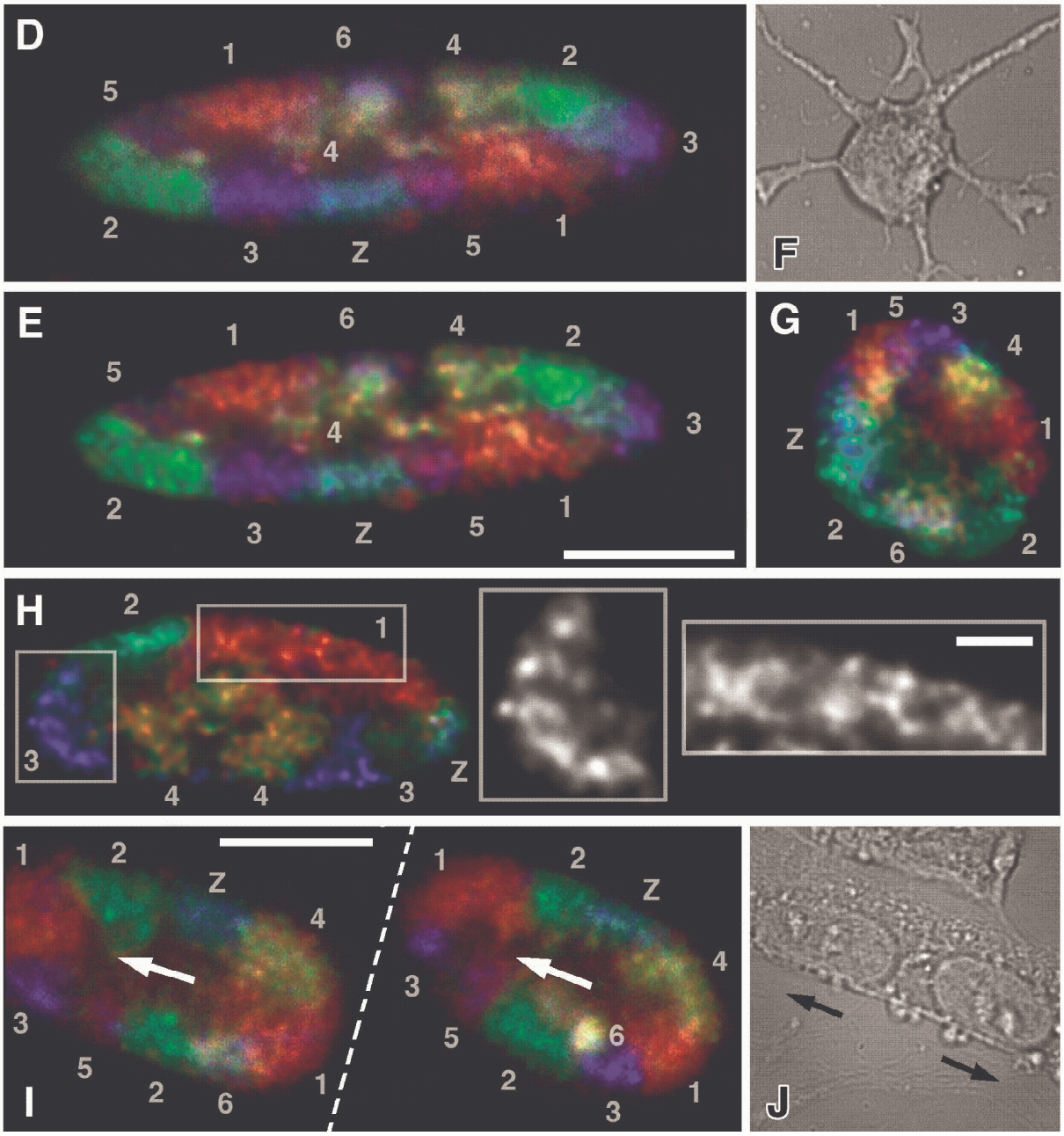

(D) Mid plane optical section through a chicken (ZW) fibroblast nucleus with seven pairs of painted chromosomes. All macrochromosomes occupy distinct territories and are arranged along the nuclear periphery. Note that only one of the two chromosome 6 territories is represented in this section. (E) After deconvolution of the same section, the granular substructure of the chromosome territories becomes apparent. (F) Transmission light image of a chicken neuronal cell showing an axon and several dendrites. (G) Central light optical section through the nucleus of the cell shown in (F) after seven-colour

painting of the macrochromosomes 1 - 6 and Z and deconvolution. Painted chromosome territories are seen at the nuclear periphery. The unstained area in the centre of the section corresponds to a large nucleolus and space occupied by microchromosomes (compare with Figure 2C). (H) Mid plane confocal section of another fibroblast nucleus after deconvolution. Macrochromosomes represented in this section are also situated at the periphery of the nucleus, but their side-by-side arrangement is different from that in the nucleus shown on (D) and (E). The granular substructure of chromosome territories 1 and 3 is exemplified at higher magnification (boxes). (I) and (J), two daughter fibroblast nuclei show a mirror-like symmetrical distribution of macrochromosomes. To facilitate comparison of the chromosome arrangements, the right nucleus in (J) was rotated at 180° in (I). The bar on (E) and (I) is 5 mm, the bar on the insertion in (H) is 1 mm

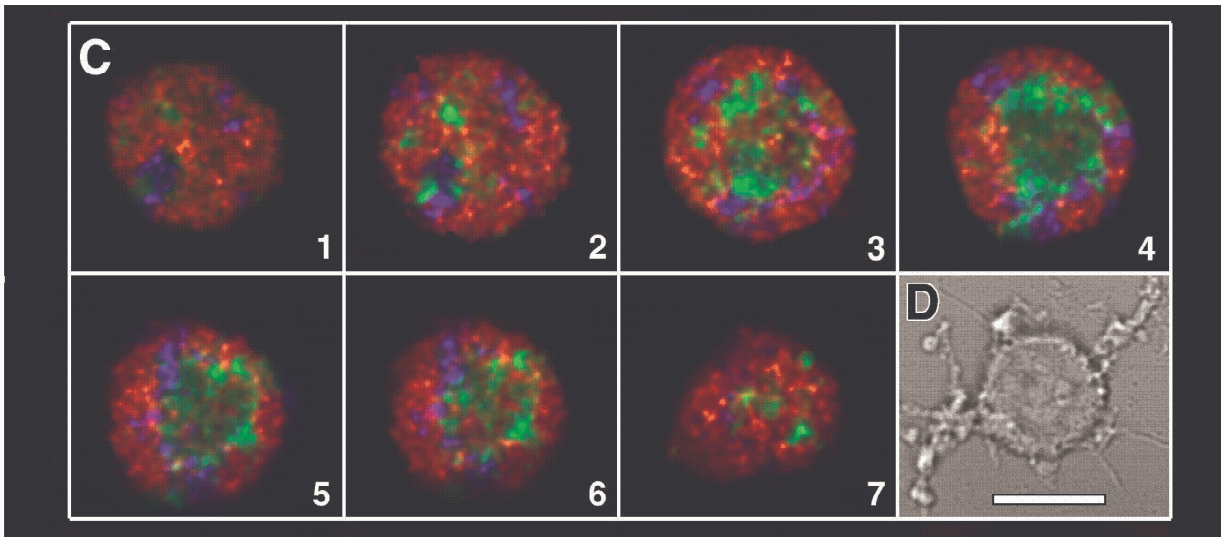

(C) Gallery of deconvolved images from confocal serial sections obtained after three-colour painting of macrochromosomes, medium-sized chromosomes and microchromosomes. Every second optical section is shown, the distance between sections is 500 nm. Macrochromosomes (red) and medium-sized chromosomes (blue) are situated peripherally, while microchromosomes (green) are located more centrally except for a few clusters that expand towards the nuclear periphery (e.g., optical section #4, 6). The central part of the nucleus on the mid plane sections (#4, 5) is devoid of chromatin due to the centrally located large nucleolus. (D) Transmission light image.

Chromatin domains of similar size and morphology were also found in optical sections of chicken fibroblast nuclei stained with propidium iodide (data not

shown), as well as in nuclei labelled with halogenated thymidine analogues (Figure 4C).

The spatial arrangement of differentially painted macrochromosomes in chicken nuclei was studied using confocal serial sections from 20 fibroblasts and 20 neurons. The side-by-side arrangement of the macrochromosome territories, e.g. the relative arrangement of chromosome territories with respect to each other, varied from cell to cell (compare, e.g. Figure 1E, H and I). The territories of homologous chromosomes were found separate in most instances, although homologous associations were also observed (see Figure 1H, chromosome 1 and 4 territories). Sister nuclei in binucleated fibroblasts showed strikingly similar - either congruent or mirror-like symmetrical - arrangements of macrochromosome territories. (Figure 1I and J). However, the comparison of different pairs of sister nuclei confirmed the high intercellular variability of side by side chromosome territory arrangements observed in mononucleated fibroblasts and neurons (data not shown).

II.3b.4.2. Distinct radial arrangements of macro- and microchromosome territories

To study the question whether the radial position of chromosome territories within the nucleus is correlated with their DNA content, chicken chromosomes were assigned to three categories according to their size. Each category was stained with a separate fluorochrome by preparing three chromosome paint pools: Pool IIa labelled the macrochromosomes 1-5 and Z, pool IIb labelled the medium-sized chromosomes 6–10 (e. g. the macrochromosomes 6 - 8 and the two largest microchromosome pairs) and pool IIc labelled 19 microchromosome pairs. (Figure 1C, 2B). The chromosomes painted by these three probe pools account for about 95% of the chicken genome (according to Smith and Burt, 1998). Three-colour FISH on metaphase spreads demonstrated strong signals for each pool without cross-hybridization (Figure 2A). The same three probe pools were hybridised to three-dimensionally preserved nuclei from neurons and fibroblasts. While the cultured neurons did not show any proliferative activity, about 10% of

the fibroblasts were in S-phase as revealed by BrdU pulse labelling (data not shown). A series of confocal sections through a neuron nucleus is shown in Figure 2C, a central section through a fibroblast nucleus is shown in Figure 2F. The image stacks were used to compute 3D reconstructions that can be rotated and viewed from different sides (Figure 2E, G). The visualization of the three chromosome pools revealed a consistent radial arrangement pattern. In both, fibroblast and neuronal cells, the sets of large chromosomes (1 – 5, Z) and medium-sized chromosomes (6 – 10) were found predominantly at the periphery of the nucleus, while the set of 19 microchromosome pairs formed clusters predominantly located in the inner part of the nucleus. However, some microchromosomes reached the surface of the nucleus forming small microchromosomal patches between macrochromosomes (Figure 2 C, E, F, and G).

(E) Three-dimensional reconstruction by surface rendering, top view (1) and bottom view (2). (F, G) Distribution of chromosome territories in the nucleus of a fibroblast. Mid plane optical section (F) and three-dimensional reconstruction (G) shown from top (left) and from bottom (right). Note a peripheral localization of macrochromosomes (red) and medium-sized (blue) chromosomes and a more central position of most microchromosomes (green).

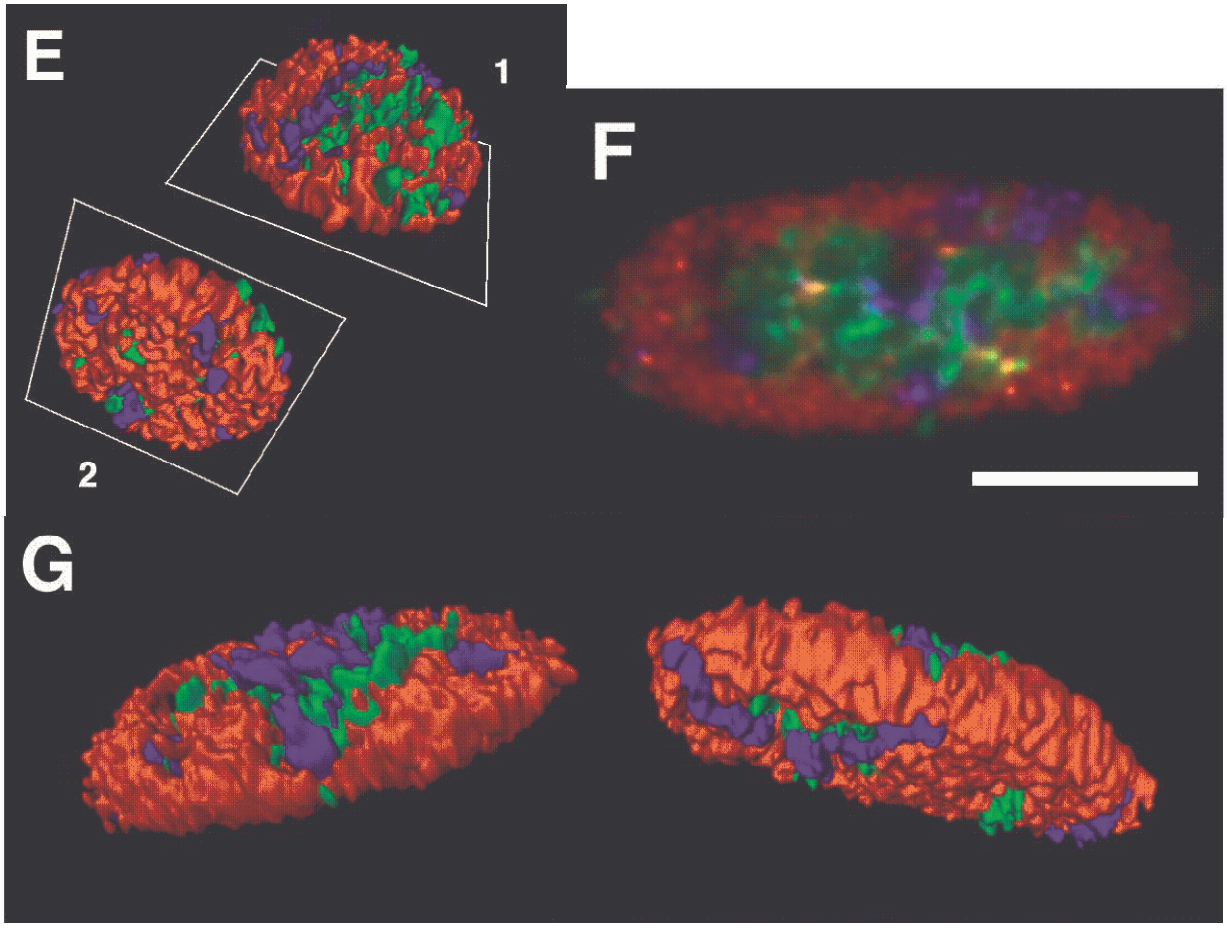

The distribution of the three chromosome sets was quantitatively analysed in 21 neuron nuclei and 28 fibroblast nuclei evaluating a central optical section of each nucleus. The resulting graphs are shown in Figure 3. Fibroblast nuclei showed an almost identical distribution for the macro- and the medium-sized chromosome territories with a maximum DNA content at approximately 80% of the relative radius. In neurons, the distribution of the macrochromosomes 1 – 5 and Z showed a maximum DNA content at 78% of the relative radius, while the distribution of the medium-sized chromosome territories was shifted slightly towards the interior with a maximum DNA content at 73% of the relative radius. In comparison to the larger chromosome territories, in both cell types the territories of the microchromosome set were clearly shifted towards the centre of the nuclear section with a peak of the DNA content at 62% in neurons and at 55% in fibroblasts. In neurons, the centre of the nucleus was typically occupied by one large nucleolus (Figure 2C, optical section #4), while the positions of

nucleoli (1-2 per nucleus) in fibroblasts varied. Accordingly, in neuron nuclei the peak of the distribution curve for the microchromosome pool was shifted somewhat more to the periphery than in fibroblasts.

II.3b.4.3. Three-dimensional simulation of statistically distributed large, medium-sized and small chromosome territories in ellipsoid cell nuclei

To compare the observed radial distribution of large, medium-sized and small chromosome territories with a statistical distribution resulting from geometrical constraints, the distribution of the three chromosome groups was simulated in 50 ellipsoid model cell nuclei and quantitatively analysed evaluating a virtual central section of each model nucleus. An example for such a virtual microscopic section is shown in Figure 2H. The results of these computer simulations were opposite to the results of the FISH experiments: The large territories were predominantly located in the nuclear centre with a peak of the maximum DNA content at 55 %, while the smaller chromosome territories were predominantly located at the nuclear periphery with a maximum DNA content at around 80 % of the nuclear radius.

II.3b.4.4. Distribution of macro- and microchromosomes in mitotic cells

The probe pools for macro- and microchromosomes were also used for the analysis of the radial arrangement of chicken chromosomes in 3D preserved mitotic cells in growing fibroblast cultures. Late prophase and prometaphase rosettes presented a strikingly consistent size-correlated distribution of chromosomes: a central, round or star-shaped cluster of microchromosomes encircled by macrochromosomes (Figure 5A, B). This order was maintained throughout metaphase, anaphase (Figure 5C, D) and telophase.

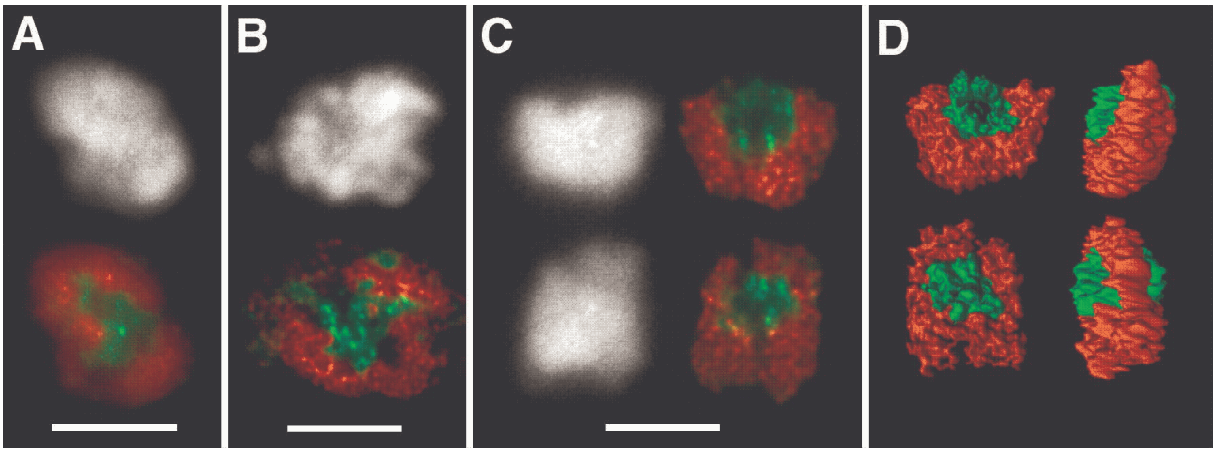

Figure 5. Maintenance of the size-correlated distribution of chromosomes through the cell cycle. (A – D) Distribution of microchromosomes (green) and macrochromosomes (red) in prophase nuclei (A), prometaphase rosettes (B), and late anaphase rosettes (C, D) from embryonic chicken fibroblasts. Note peripheral position of macrochromosomes and central location of microchromosomes throughout all stages of mitosis. Black and white figures show counterstaining with DAPI. A three-dimensional reconstruction (surface rendering) of anaphase rosettes from (C) is shown on (D): top (left) and lateral (right) views. Bars: 5 µm.

II.3b.4.5. The distribution of early and late replicating chromatin during S-phase

To define early and late replicating chromatin in metaphase chromosomes from DT-40 cells double replication labelling experiments with IdU and CldU were performed (for labelling schemes see Materials and Methods). In the following we use the terms “early” to assign chromatin replication roughly to the first half of S-phase (i. e. labelled with the first labelling pulse) and “late” to the second half of S-phase (i. e. labelled by the second labelling pulse), respectively. This pragmatic definition does not refer to the specific labelling patterns described for different stages of S-phase in mammalian cell nuclei (O'Keefe et al., 1992). We showed that chicken microchromosomes predominantly consist of early replicating chromatin, while most of the chromatin of macrochromosomes replicates late (Figure 4H). Some microchromosomes also contain late replicating chromatin (Figure 4H, I, arrows).

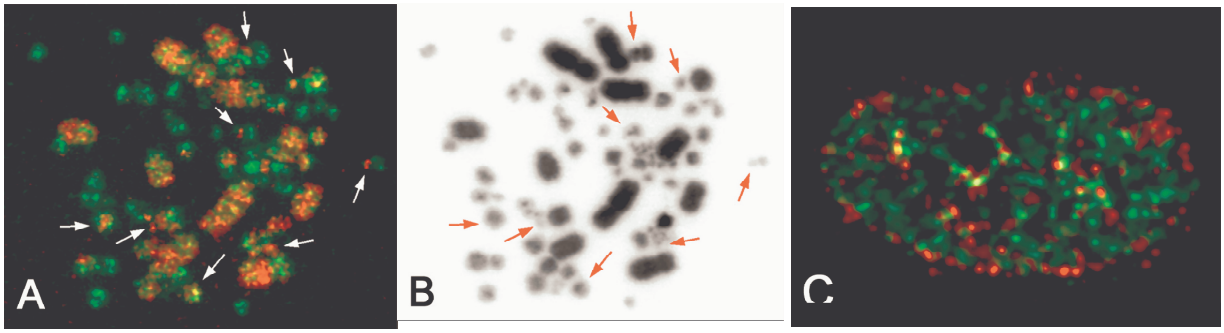

Figure 4. (A) Metaphase chromosome spread from a DT-40 cell after double replication labelling. Early replicating chromatin (green) is observed mainly in micro- and medium-sized chromosomes, while macrochromosomes contain mostly later replicating chromatin (red). Arrows show small sites of late replicating chromatin on some microchromosomes. (B) Inverted DAPI image of the metaphase spread. Arrows show the same microchromosomes as shown in (A). (C) Light optical section through the mid part of a double replication labelled primary chicken fibroblast nucleus. Note a rim of late replicating chromatin foci (red) at the nuclear periphery. Early replicating chromatin foci (green) together with some late replicating foci are located in the nuclear interior. Bars = 5 mm.

To study the spatial arrangement of early and late replicating chromatin in three-dimensionally preserved nuclei of embryonic chicken fibroblasts, asynchronously cells were double labelled with IdU and CldU (for description see Material & Methods) and fixed immediately after the second label. As shown in Figure 4K late replicating chromatin was preferentially located at the periphery of the nucleus, while early replicating chromatin occupied mostly the nuclear interior. Hence, the distribution of early and late replicating chromatin is congruent with the distinct radial position of small and large chicken chromosome territories.

II.3b.5. Discussion

II.3b.5.1. Macro- and microchromosome territories show morphological characteristics similar to mammalian chromosome territories.

Chromosome territories in interphase nuclei of chicken embryonic fibroblasts and neuronal cells displayed variable shapes and were built up from focal chromatin domains of a size roughly between 300 – 600 nm. These focal domains are comparable in size to the ~1 Mb chromatin domains previously described in human chromosome territories (Cremer and Cremer, 2001b; Cremer et al., 2000; Zink et al., 1998). These ~1 Mb chromatin domains are presently not well defined at the electron microscopic level. They are maintained throughout the cell cycle. During S-phase they recruit replication factors and represent at this time period replication foci (Leonhardt et al., 2000). In mitosis, several adjacent domains form chromosome bands (Sadoni et al., 1999).

II.3b.5.2. Side-by-side arrangements of macrochromosome territories are variable

Based on the visual inspection of fibroblast and neuronal nuclei after multicolor painting of the seven largest macrochromosomes, we conclude that neighbourhoods between non-homologous as well as homologous macrochromosome territories are variable. Territories of homologous macrochromosomes were in most cases separated even in remote nuclear positions, although associations were also observed. We also could not notice any obvious difference between side by side arrangements of chromosome territories and proliferating activity of the cells: in both, cycling fibroblasts and non-proliferating neurons, the side-by-side arrangement of macrochromosome territories varied from cell to cell. These findings are in agreement with previous studies of different human cell types demonstrating a pronounced cell-to-cell variability of chromosome territory neighbourhoods (Cremer et al., 2001a; Dietzel et al., 1995; Emmerich et al., 1989; Lesko et al., 1995; Popp et al., 1990; Sun et al., 2000; Sun and Yokota, 1999). However, based on presently available data, the possibility remains that specific chromosome segments have a high

probability, even a functional necessity to be placed close to each other in certain cell types, at certain stages of the cell cycle or in terminally differentiated cells.

II.3b.5.3. Radial arrangements of macro- and microchromosomes are highly consistent in interphase nuclei and mitotic figures

In contrast to the pronounced intercellular variability observed for side-by-side arrangements of homologous and non-homologous chromosome territories, the radial arrangements of macro- and microchromosomes were highly consistent. Macrochromosome territories were located mostly towards the nuclear periphery, while microchromosome territories formed a few distinct clusters located towards the nuclear centre. This was observed in proliferating chicken fibroblasts as well in non-proliferating neurons suggesting that this radial arrangement may be a general motif of chicken cell types. In parallel, dividing fibroblasts displayed a stringent radial chromosome arrangement in all stages of mitosis - a central microchromosome cluster surrounded by a ring of macrochromosomes.

Such a size-correlated arrangement of mitotic chromosomes was first noted on squashed preparations of proliferating tissues from different species including chicken (for references see White, 1961). In these studies, the preferential location of small chromosomes in the central part and of large chromosomes in the periphery of metaphase plates was described. The squashing technique (Mcgregor and Varley, 1988) preserves the in vivo arrangement of mitotic chromosomes to a certain degree. Despite the fact that the commonly used spreading technique employing colcemide and hypotonic treatment is much more destructive, a similar distribution pattern of large and small chromosomes was also observed in metaphase spreads from human lymphocytes and fibroblasts (for references see Cremer et al., 2001a, this issue). These findings suggest that chromosome arrangements noted in mitotic cells correlate to some extent with chromosome territory arrangements in interphase nuclei.

The mechanisms that maintain the observed radial arrangements of micro- and macrochromosomes in chicken cells from one cell cycle to the other are not known. Computer simulations of chromosome territories in ellipsoid cell nuclei show that these radial arrangements of macro- and microchromosome territories cannot be explained by a statistical distribution of large and small chromosome territories influenced by topological constraints.

Epigenetic mechanisms, including DNA-methylation and histone acetylation, apparently play a major role in higher order chromatin architecture and gene expression (Rice and Allis, 2001; Wade, 2001) but their potential contribution to the intranuclear arrangements of chromosome territories has not been studied so far. Gene-poor, mid-to-late replicating chromatin may - in contrast to early replicating, gene dense chromatin - carry binding sites for the reconstituting nuclear lamina during telophase (Pyrpasopoulou et al., 1996). This could push early replicating gene-dense chromatin into a more interior position, a finding also observed in mammalian cell nuclei (Sadoni et al., 1999; Schermelleh et al., 2001 and references therein). However, late replicating chromatin was also observed around the nucleoli. At present, the system of molecular “addresses” that may account for the formation of separate higher order chromatin compartments formed by polarized chromosome territories (Sadoni et al., 1999; Sadoni et al., 2001) is mainly subject to speculations.

To some extent the size-correlated radial arrangement of chromosome territories in interphase cell nuclei may be due to the organization of the mitotic spindle (see following Figure 5E – H).

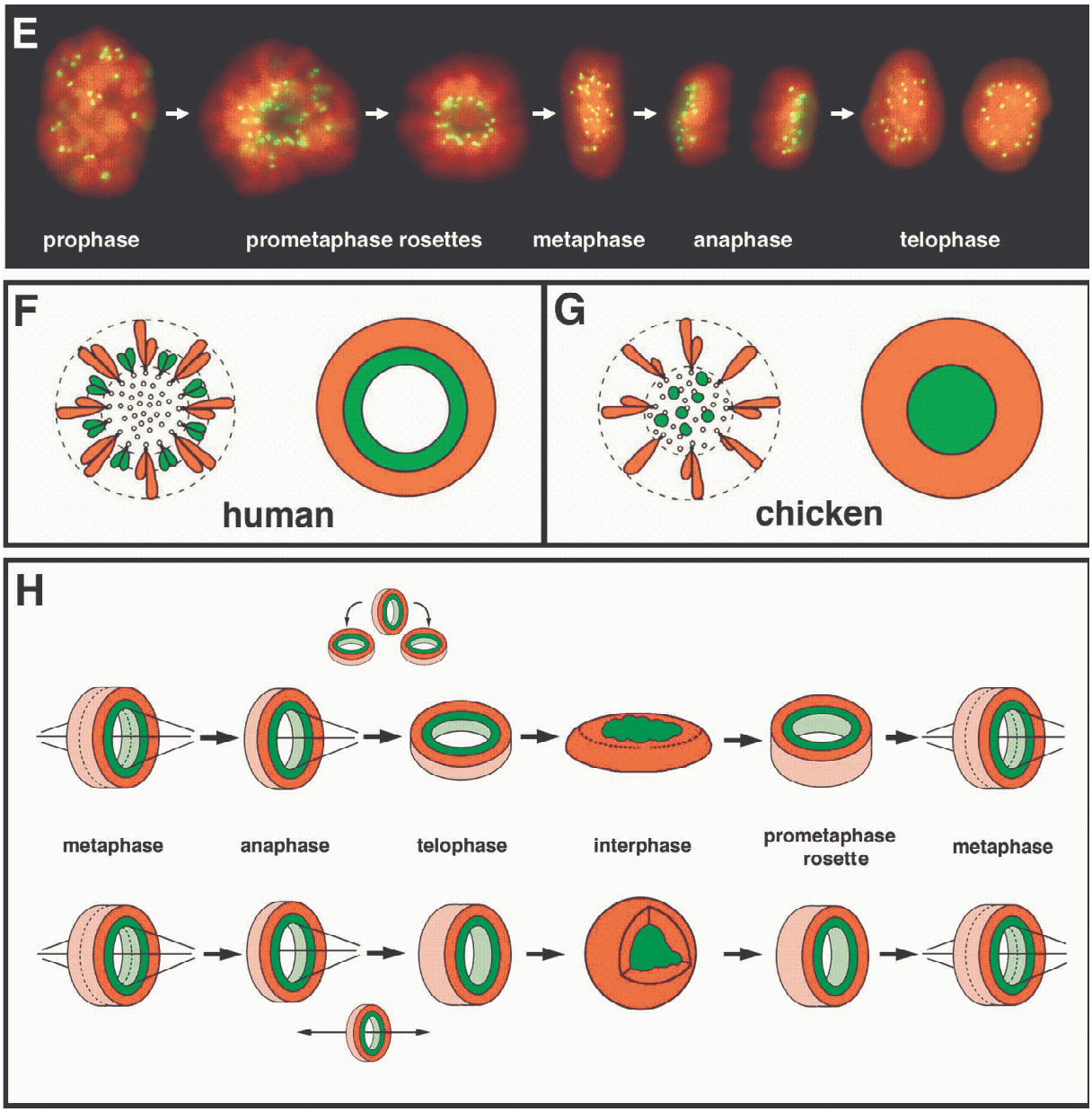

(E) Arrangement of chromosomes and centromeres through mitosis in adherently growing human cells (primary fibroblasts). Chromosomes were stained with DAPI (red); location of centromeres (green) was defined with antibodies against CENP-C (kind gift from W.C. Earnshaw, University of Edinburgh). At the beginning of the prophase, centromeres are predominantly situated at the nuclear periphery. At the end of the prometaphase, all centromeres become attached to microtubules and form a ring like structure around the bundle of central microtubules of the mitotic spindle. This ring-like arrangement of centromeres persists during the metaphase and anaphase. At the end of the telophase – beginning of the G1 stage, most of the centromeres return to the periphery

of the nucleus. (F, G) Scheme illustrating the arrangement of large (shown in red) and small chromosomes (green) in metaphase rosettes of human (F) and chicken (G) cells. In human cells (F), all chromosomes abut the tight bundle of microtubules of the mitotic spindle. The centromeres of all chromosomes form a ring in the equatorial plane of the spindle (compare with prometaphase rosette on E). The gravity centres of small chromosomes are situated closer to the spindle axis than the gravity centres of large chromosomes. In chicken cells (G), the macrochromosomes surround the bundle of central microtubules, while the microchromosomes are predominantly located between the central microtubules of the spindle. (H) Scheme illustrating the hypothesis that the radial arrangement of chromosome territories in the cell nucleus has its origin in the chromosome arrangement in the preceding metaphase plate and is maintained to a great extent during the entire cell cycle. Metaphase as well as anaphase rosettes of flat, adherently growing cells (upper row) are typically perpendicular to the substratum. During telophase, the separated rosettes decline until they are parallel to the substratum. The formation of a spherical nucleus (lower row) requires an expansion of the decondensing chromatin along the spindle axis.

The central part of a mitotic spindle in vertebrates consists of a tight bundle of microtubules stretching between the two centrioles. In species with very small chromosomes (like birds), the latter may find enough space between the central microtubules of the spindle, and may therefore be located centrally, while larger chromosomes occupy a ring-shaped zone outside the central bundle of microtubules (Figure 5G; Östergren, 1945; White, 1961). In human cells, even smaller chromosomes may be large enough to be excluded from the spindle centre and hence to abut the tight bundle of central spindle microtubules (Bajer and Molé-Bajer, 1972; Chaly and Brown, 1988; Nagele et al., 1995; Östergren, 1945; Rieder and Salmon, 1994). Consequently, centromeres of all human chromosomes form a ring in the equatorial plane of the spindle (Figure 5E, F), while the gravity centres of small chromosomes are situated closer to the spindle axis than the gravity centres of large chromosomes (Figure 5F). The radial chromosome arrangement in the mitotic cells may be reinforced by the spindle and provide the starting point for the radial arrangements of chromosome

territories in the reforming daughter cell nuclei (see Figure 5H). Metaphase as well as anaphase rosettes of flat cells adherently growing in vitro are typically perpendicular to the substratum (e. g. a coverslip, Figure 5E, H upper row). After separation of chromatids the two anaphase rosettes move to the opposite spindle poles. During telophase the two sister rosettes decline until they are parallel to the substratum (Figure 5E, H upper row) and chromosomes start to decondense. The formation of a spherical nucleus (Figure 5H lower row) requires an expansion of the decondensing chromatin along the spindle axis. While side-by-side arrangements of chromosomes may change when a cell enters mitosis and forms the metaphase plate, the side-by-side arrangements established during telophase – early G1 are likely maintained to a large extent during the entire interphase (Boveri, 1909 and our own unpublished observations).

In humans, the radial position of some chromosome territories cannot be explained by the action of the spindle. For example, in human lymphocyte nuclei chromosome territories #18, 19, and Y show a distinctly different positions: #18 and Y are located at the nuclear periphery and #19 in the nuclear centre (Cremer et al., 2001a; Croft et al., 1999). This distribution does not fit a simple correlation of chromosome DNA content and radial CT positioning and further emphasizes a need for specific interactions between chromatin and other nuclear structures (lamina etc.) in order to establish higher order chromatin arrangements.

II.3b.5.4. Correlation of higher order chromatin arrangements with replication timing and gene density

Our data confirm previous observations (McQueen et al., 1998; Ponce de Leon et al., 1992; Schmid et al., 1989) that microchromosomes are predominantly early replicating with a small proportion of late-replicating segments. These late replicating segments may partly coincide with the heterochromatin blocks visualized by C-banding (Schmid et al., 1989). The preferential position of mid-late replicating chromatin at the nuclear periphery and the central position of early replicating chromatin previously observed in mammalian cell nuclei (Ferreira et al., 1997; Sadoni et al., 1999) was confirmed for chicken cells by double replication labelling experiments. In humans, the majority of smaller autosomes are early replicating. In comparison to the later replicating larger chromosomes, they have a higher average content of CpG islands (Craig and Bickmore, 1994) and a higher gene density as predicted by the estimation of ESTs (Deloukas et al., 1998). A specific radial chromatin arrangement with regards to the preferential positioning of relatively gene dense, early replicating chromatin in the nuclear interior and later replicating, relatively gene poor chromatin at the nuclear periphery, seems to be an evolutionary conserved motif for the organization of the nucleus in both chicken and human cells. It should be noted that we did not detect in chicken cell nuclei a rim of mid-late replicating chromatin around the nucleoli while such a rim is typically observed around nucleoli in human cells (O'Keefe et al., 1992; Sadoni et al., 1999). This difference may reflect the fact that the chicken genome bears much less heterochromatin than the human genome.

Future comparative studies could help to gain more insight into evolutionary conserved cell cycle and cell type specific motifs of higher order chromatin arrangements. The chromosome specific paint probes generated from Gallus gallus domesticus can identify orthologous chromosomes of other bird species with distinctly different karyotypes. Thus, chicken chromosome paint probes or painting pools could be used to identify the distribution pattern of orthologous

genomic segments in nuclei of different bird species. Species with highly divergent karyotypes offer a way to analyse the contribution of chromosome size, gene density and replication timing as key factors for a conserved radial arrangement of chromatin.

II.3b.6. Acknowledgements

We thank Dr. W.C. Earnshaw (University of Edinburgh, UK) for providing antibodies against CENP-C. We are grateful to Dr. J.-M. Buerstedde (University of Hamburg, Germany) for the generous gift of DT-40 cells. This work was supported by grants from the Deutsche Forschungsgemeinschaft to T. Cremer (Cr 59/20-1), from the European Community to C. Cremer (FIGH-CT1999-00011) and to J.Wienberg (BIO4-CT98-0228, AVIANOME), from the Bundesministerium für Bildung und Forschung to J. Wienberg (DLR01 KW 96142). G.K. received a grant from the Deutsche Forschungsgemeinschaft for graduates “modelling and scientific computing”:

II.3b.7. Verschieden ausdifferenzierte Hühnerzellen

In der Arbeit von Felix Habermann wurden Fibroblasten- und Neuronenzellen von Hühnern (Gallus domesticus) untersucht. Es wurden die großen Chromosomen (1-5 &Z), die mittleren (6-10) und die meisten Mikrochromosomen untersucht. In vorliegendem Zusatz wurden 4 verschiedene Zelltypen von Hühnern untersucht und dabei das Chromsom 1 (groß) und das Chromosom 8 (mittelgroß) betrachtet. Die Zelltypen waren: multipotente Vorläuferzellen (d.h. nicht ausdifferenzierte Zellen), Macrophagenzellen, Monoblastenzellen und Proerythoblastenzellen. In allen Zelltypen war besonders

Chromosom #1 am Rand. Chromosom 8 nahm eine weniger periphere Position ein.

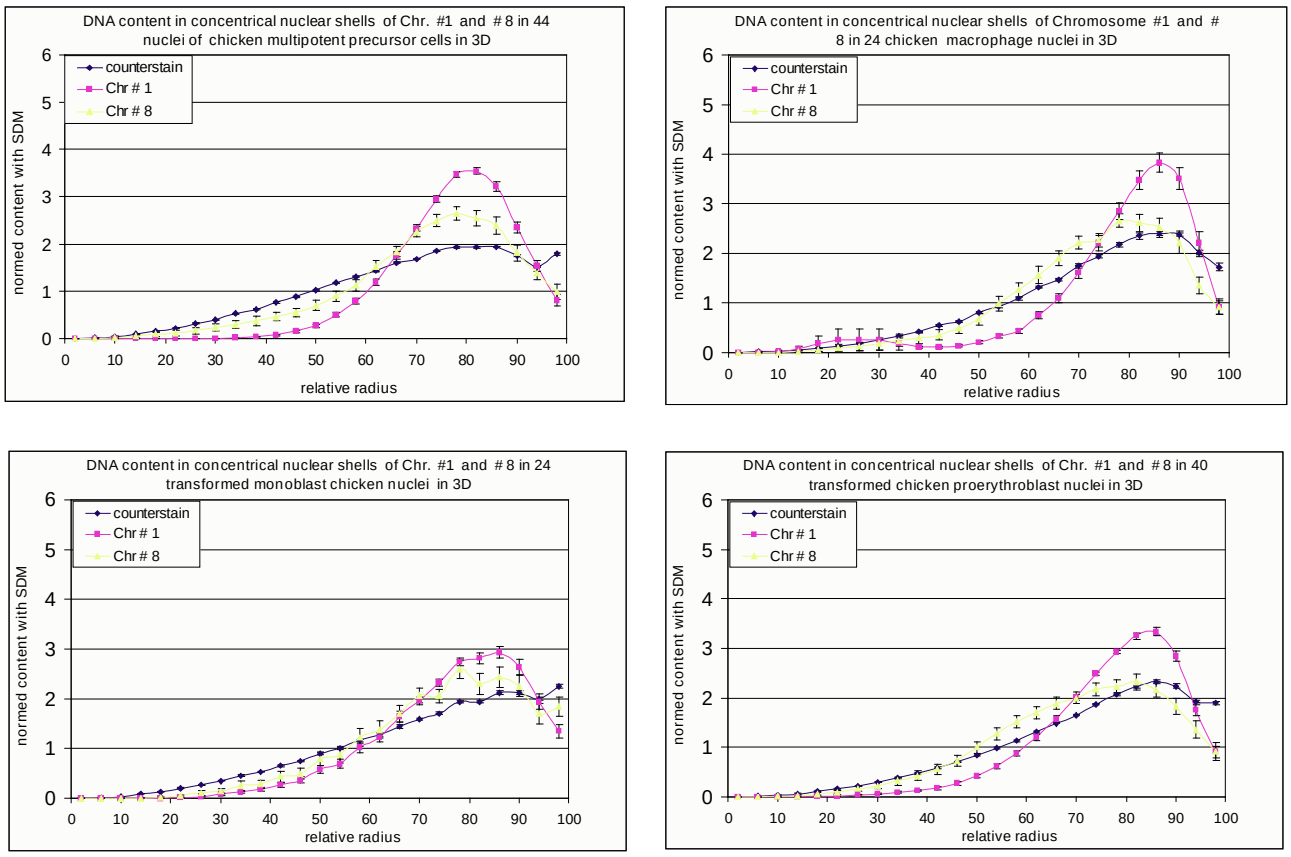

Abb.II.3.2. Die 4 Diagramme stimmen gut überein. Demnach war Chromosom #1 immer peripher. In den Markophagen- und Proerythoblastenzellen lag Chromosom #8 etwas weiter innen.

II.4. Position der Chromosomenterritorien in Krebszellen

II.4.1. Beschreibung von Krebs: [s. z.B. Wizelman 2002]

Eine Krebszelle ist eine Zelle des Organismus, die aufgrund von normalerweise 6 bis 7 Mutationen (Chromosomenaberrationen) sich unkontrolliert vermehrt und nie in Apoptose übergeht. Apoptose ist ein Sterbeprogramm das jede Zelle hat und das bei bestimmten Umständen wie es z.B. nach DNA-Strangbrüchen eintritt. Ursache für derartige Mutationen kann UV- Strahlung aus der Sonne sein, die auf die ungeschützte Haut fällt, oder Röntgenstrahlung, oder Radioaktivität oder schon ein Virusbefall: denn Viren können ihre eigene DNA in die befallene Zelle einschleusen. Aber Mutationen können auch während der Zellteilung entstehen. Es gleicht genetisch kein Krebsfall einem anderen, und im Laufe der unkontrollierten Vermehrung der Krebszellen ereignen sich noch viele chromosomale, (d.h. kariotypische) Umbauten (d.h. Aberrationen).

II.4.2. Einteilung der Chromosomenaberrationen:

Es gibt konstitutionelle wie somatische Chromosomenaberrationen (CA). Nicht alle CAs führen zu Krebs. Eine CA kann auch den Zelltod oder eine Minderleistung der Zelle bedeuten oder folgenlos bleiben. Im günstigen Fall kann eine CA eine bessere Anpassung an die Umwelt hervorrufen. Bei konstitutionellen Aberrationen sind die Keimzellen selbst betroffen. Die Aberration kann dann an die nachkommende Generation weitergegeben werden. Bei den somatischen CAs sind die Keimzellen nicht betroffen. Ein Krebspatient könnte also auch gesunde Kinder bekommen.
Bei numerischen CAs ändert sich die Anzahl der Chromosomen von der Norm. Zum Beispiel kann jedes Chromosom statt 2 mal auch 1mal oder 3 mal vorkommen.
Bei strukturellen CAs kommen Umbauten innerhalb eines oder mehrerer Chromosomen vor. Für den Fall von balancierten Umbauten, das sind solche bei denen die DNA-Menge nicht verändert wird, entsteht häufig kein Krankheitsbild. Translokationen sind Verbindungen von DNA Sequenzen, die nicht zusammengehören. Sie können z.B. nach Doppelstrangbrüchen auftreten und sind Verbindungen verschiedener Chromosomen.

II.4.3. Die untersuchten Krebsarten:

Die nachfolgende Tabelle soll einen Überblick auf molekularer Ebene über die untersuchten Karzinome geben. Es ist jeweils nach der grauen Zeile in der Tabelle zu Beginn der gesunde

Zelltyp aufgeführt, von denen sich in den nachfolgenden Zeilen aufgeführt, die sich daraus entwickelten Krebsarten ergaben. So entstanden aus normalen (sprich: gesunden) Lymphozytenzellen Jurkat- und Hodgkin Zellen (zwei Leukämiearten). Aus Keratinocytenzellen entstanden Meljuso Zellen, eine Art Hautkrebs. Aus Gebärmutterzellen entstanden HeLa- Zellen. Aus Dickdarmzellen (colon ephitelial) entstanden vier Krebstypen: DLD-1, RKO, SW480 und SW620. Aus Fibroblastenzellen sind seltene Fibrosarkomzellen entstanden und schließlich wurden Glioblastomzellen untersucht.

Tissue origin of cells and name of tumor cell lines	structural aberrations and copy number imbalancies		references* (listed in cases where data from previous publications are used)
	chromosome 18	chromosome 19	
Normal peripheral lymphocytes	2 normal copies	2 normal copies	
Jurkat T-lymphocyte derived cell from acute T cell leukemia	der(18)t(X;18)(q11;p11.2); (10/10)		(Müller et al)
	monosomy 18p	2 normal copies	
HDLM-2 Hodgkin disease derived cell line	1 normal copy der(18)t(rDNA::18p11.2-q23::9p24-pter) (Macleod)	1 normal copy der(17)t(19;9;19;17) (8/10) der(2)t(2;13;19;12) (8/10) der(6)t(6/19) (5/10) der(19)t(19;5;1)	(Macleod) SKY(Joos)
	balanced	trisomy 19	
Normal diploid keratinocytes	2 normal copies	2 normal copies	
MelJuso Melanoma derived cell line	der(9;18)t(9;18)(q11;p11); (10/15)	der(1;19)t(1;19)(p11;q11) ; (15/15) der(4;19)t(4;19)(q11;p11);(6/15) der(19)t(19;22)(p11;q?); (7/15) der(18;19)t(18;19)(q11;p11)(2/15)	(Müller et al)
	monosomy 18p	balanced	
Normal diploid Cervix epithelial cells	2 normal copies	2 normal copies	
HeLa Cervix carcinoma derived	1 normal copy der(18)delq der(14)t14;18)	1 normal copy der(19)t(13;19) der(19)t(19;20)	
	unbalanced	unbalanced	
Normal diploid colon epithelial cells	2 normal copies	2 normal copies	

DLD1 Colon adeno-carcinoma Derived	2 normal copies	2 normal copies	(Abdel Rahman)
RKO Colon adeno-carcinoma Derived	2 normal copies	2 normal copies	Cahill, 1998
SW480 Colon adeno-carcinoma Derived	der(18)del(18)(q12); (15/15)	Der(8;19)t(8;19)(p11;q11); (15/15) Der(19)t(19;8;19;5)(p;q;q;p),(15/15)	Abdel-Rahman Müller Melcher
	unbalanced 1 x normal copy monosomy 18q (CGH and bar code and Melcher) (trisomy 18p laut CGH and Melcher)	unbalanced 1 x normal copy partial trisomy for 19q? (trisomy for 19p, tetrasomy 19q laut CGH, 19q deleted laut Melcher)	
SW620 Colon adeno-carcinoma Derived	der(18)del(18)(q12); der(18)t(17;18)(p11.2;q12)		
	unbalanced monosomy for 18q (CGH and bar code) 18p balanced (CGH) trisomy 18p (bar code)	balanced (CGH and bar code)	Müller et al. Melcher
Normal diploid fibroblasts	2 normal copies	2 normal copies	
HT-1080 Fibrosarcoma derived	2 normal copies	2 normal copies	
T98G Glioblastoma derived	M-FISH und CGH abwarten		

Tabelle II.4.1. In obigem Tabellenwerk ist eine Übersicht über die Untersuchten Krebsarten gegeben. In der linken Spalte steht der Zelltyp, in der zweiten die Umbauten, die Chromosom #18 betreffen, in der dritten Spalte die Umbauten, die Chromosom #19 betreffen. Hierbei deutet „t“ auf Translokationen hin. In der vierten und letzten Spalte sind Literaturhinweise aus von dort übernommenen Angaben. Die Tabelle wurde freundlicherweise von M.Cremer zur Verfügung gestellt.

Im Anhang ist auf den Seiten 10-14 Material über Krebszellen enthalten. Auf S.11 des Anhangs ist eine 3D-Rekonstruktion einer Hela-Zelle im Vergleich zu einer DLD-1 Zelle gezeigt: Während bei der Hela- Zelle die Territorien 18 in Trisomie und die Territorien 19 länglich zerklüftet vorlagen, konnten für die DLD-1 Zellen keine äußerlichen Besonderheiten gefunden werden. Die Verteilungsgraphen können im Anhang auf den Seiten 12 bis 14 eingesehen werden.

II.4.4. Radiale Positionen der Chromosomenterritorien in Krebszellen im Spiegel chromosomaler Aberrationen

Manchmal gebrauchte Abkürzungen: Chromosomenterritorien (CT), chromosomale Aberrationen (CA), Translokationen (TL)

Krebsart	Chromosom 18	Chromosom 19
Jurkat	Nur Translokation mit X Graph unauffällig; auch unauffällig in CT 1-5	2 normale Homologe Graph unauffällig; auch unauffällig in CT 17-20.
Hodgkin	Ein homolog normal, das andere balanciert Graph unauffällig	1 homolog normal, das andere mit hochkomplexen umbauten mit inaktivem Chromatin. Trisomie Graph: leicht nach außen verschoben.
Meljuso	Translocation mit CT 9 Graph unauffällig	Balancierte aber zahlreiche TLs. Betroffen: CT #19, 4, 1, 22,. Graph zu CT #19 leicht nach außen, zu #4 unauffällig
HeLa	1 homolog normal, das andere hat eine TL mit CT #14 Graph mit starken Tendenzen nach Innen.	1 homolog normal, das andere hat TLs mit CTs #13 und #20 Graph unauffällig
Colon DLD-1: Zellkerne flach	2 normale Homologe. Graph ähnlich wie normale Fibroblasten- Verteilung	2 normale Homologe Graph etwas nach außen verschoben.
Colon RKO	2 normale Homologe Graph entspricht einer Zufallsverteilung	2 normale Homologe Graph unauffällig
Colon SW 480	1 normales Homolog, ansonsten unbalancierte	1 normales Homolog, ansonsten unbalancierte

	CAs Graph nach Innen verschoben	CAs Graph normal
Colon SW 620 (Metastase zu SW 480)	Translokationen mit CT #17, unbalancierte Cas, in #18q Monosomie, in 18p trisomie Graph normal	Balancierte Cas Graph normal
Fibrosarkomzellen HT-1080	2 normale Homologe vorläufige Graphen:eher zentral, äußerst zerklüftet	2 normale Homologe Graphen: abzuwarten; eher normale Verteilung
Glioblastomzellen T98G	CAs: abzuwarten Graphen: Zufallsverteilung	Cas: abzuwarten. Graphen: Zufallsverteilung

Tab.II.4.2. In obigem Tabellenwerk ist ein Vergleich zwischen Chromosomenaberrationen und den zugehörigen Positionen der Chromosomenterritorien gegeben.

Bei allen Serien gab es für jedes Territorium Nähe zum Zellkernrand. Der Grund liegt wohl darin, dass, wie in Kapitel II.5. an 8 Lymphozytenterritorien gezeigt wird, die Centromere aller Territorien am Zellkernrand liegen.

Die DLD-1 Zellen sind flache Colon Zellen. Sie wurden sowohl in 2D als auch in 3D ausgewertet.

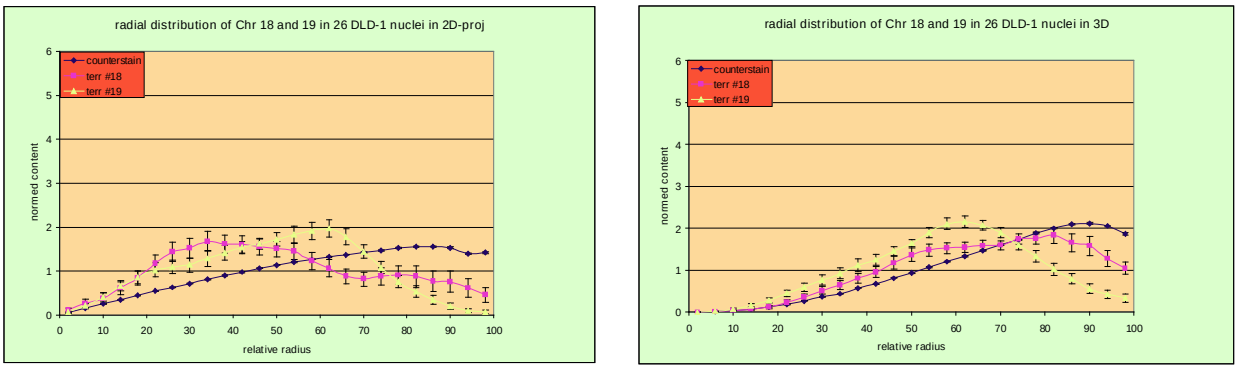

Abb.II.4.1.In beiden Diagrammen liegen beide Chromosomen zentraler als die Gegenfärbung. Chromosom 19 liegt in beiden Auswertungen bei mittelgroßen Radialwerten. Chromosom 18 liegt in 2D Zentral, in 3D nicht. Also liegt Chr. 18 lateral zentral aber von der Höhe her an der Kernlamina (Kernrand). Chr 19 lag nicht so sehr an der Lamina.

Insgesamt ergibt sich aus dem Vergleich zwischen Chromosomalen Umbauten und der resultierenden Position meistens eine Korrelation. Aufgrund des großen Aufwandes einer FISH und des Aufwandes einer digitalen Auswertung wird die Untersuchung der Position der Chromosomen zur Krebsdiagnose eher nicht zum klinischem Alltag gehören.

II.5. Position der Chromosomen und deren Centromere in Lymphozyten (s. [Weierich 2002])

II.5.1. Position der Centromere in G0 Kernen

Centromere bilden im Metaphasechromosom den Bereich, von dem die einzelnen Arme ausgehen und die beiden Schwesterchromatiden miteinander verbunden sind Wo aber ihre Position während der G0-Interphase liegt, ist Gegenstand dieses Kapitels. Im Anhang auf S.16f sind die Verteilungen der Chromosomen und Centromere zu #1, 11, 12, 15, 17, 18, 20, X in Lymphozyten gezeigt. In allen 8 Serien lagen die Centromere in 3D am Zellkernrand. Besonders interessant waren die Chromosomen #15, 17, und 20: Denn diese Territorien liegen laut den Radialverteilungen bevorzugt im Zellkerninneren. Diese Verteilungen widersprechen sich nicht, denn die Centromere können am Rand des Territoriums liegen (s. Anhang S.18f) Zum Vergleich wurden auch die Positionen aller Centromere in menschlichen Fibroblasten sowie in Lymphozyten von Menschen und Mäusen untersucht (Pancentromerische Probe):

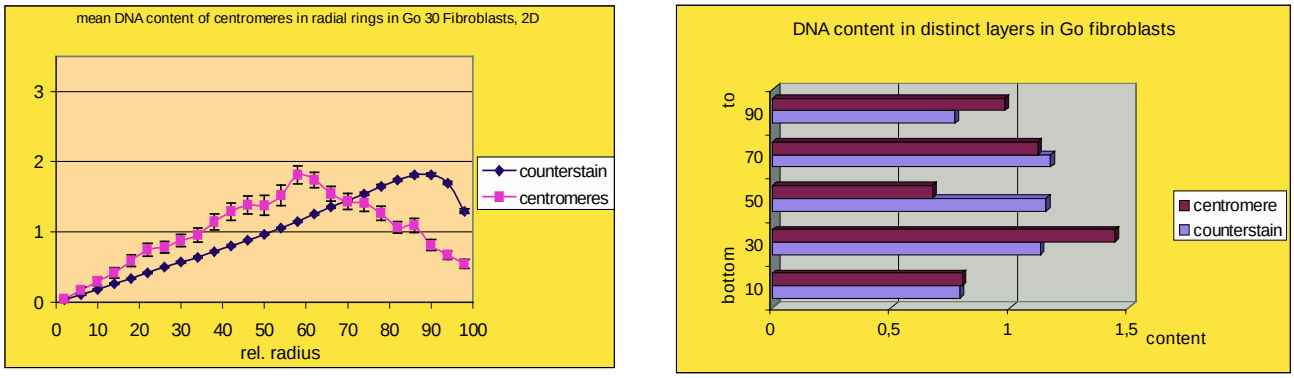

Abb.II.5.1. Oben links sind die Verteilungen der Centromere in menschlichen Fibroblasten gezeigt. Sie lagen, in 2D betrachtet, in Unterschied zu den Lymphozyten etwa auf halbem Weg zum Zellkernrand. In der 1D-Projektion rechts erkennt man, dass die Centromere auf halber Höhe zwischen Schwerpunktsebene und Zellkernrand liegen

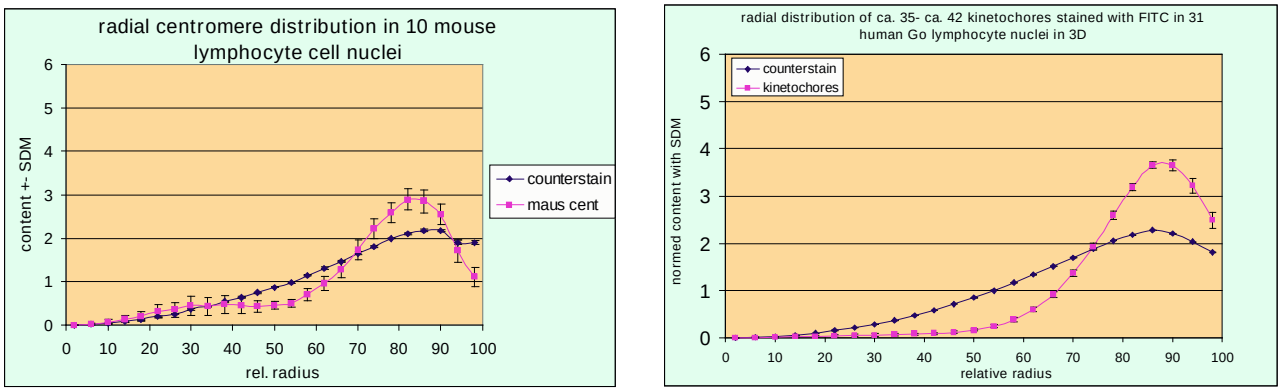

Abb.II.5.2. Maus- und menschnliche Centromerregionen sind vergleichbar im Kern gelegen. Wie an den menschlichen Lymphozyten (rechts) die Kinetochoren (ein Teil der Centromere) liegen die Centromere der Maus (links) besonders am Zellkernrand.

II.5.3. Position der Centromere im Territorium

Mit Ausnahme von Chromosom X lagen alle Centromere am Territoriumsrand (s. Anhang auf S. 18f.). Bei Chromosom 15 schienen die Centromere sogar als mit den Territorien nicht zusammenhängend. Beim Chromosom X lagen die Centromere im Inneren des Territoriums. vgl. dazu auch [Dietzel 94].

II.5.4. Position von Telomeren

Es wurde auch die Position aller Telomere in Fibroblasten, Lymphozyten und Maus-lymphozyten bestimmt. Telomere bilden die Enden der Chromosomen und sind nur ca. 10-15kb groß. Die Telomere ragen von den Centromeren aus gesehen mit Ausnahme bei den Mauslymphozyten erwartungsgemäß in den Kern hinein.

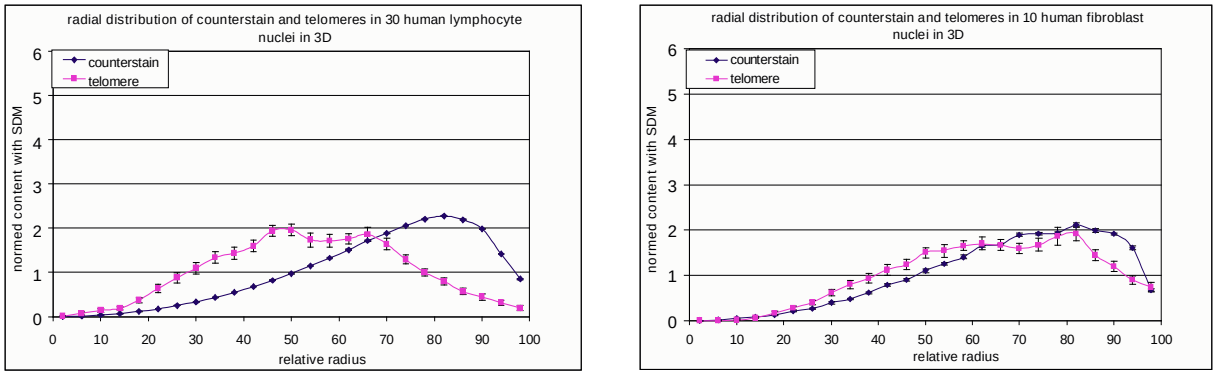

Abb.II.5.3. Besonders im linken Schaubild sieht man, dass die Telomere von Lymphozyten eher in mittleren bis kleinen Radialpositionen liegen. Bei den Fibroblasten ist das nicht ganz so deutlich. Eine 2D-Auswertung zu machen wurde hier versäumt, würde aber aus der Erfahrung mit in 3D ausgewerteten 2D-Objekten (s. Einleitung) es auch zeigen

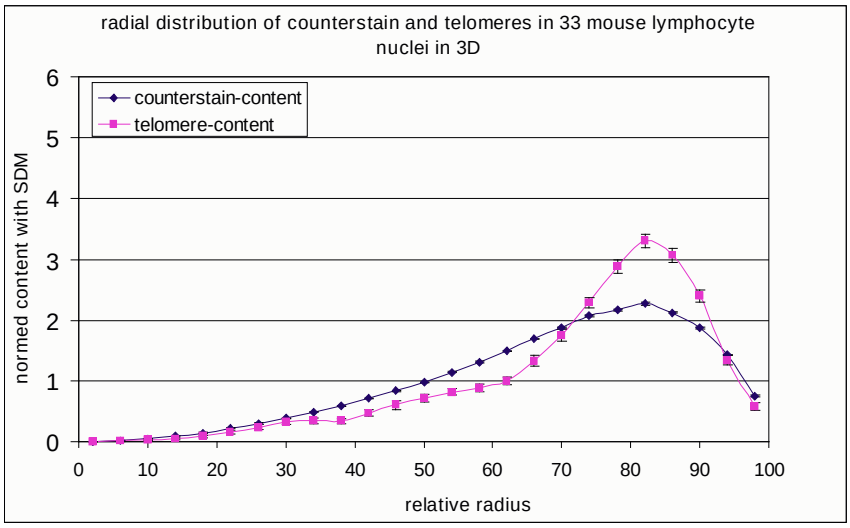

Abb.II.5.4.In Abweichung vom Muster im Menschen ist hier bei der Maus die Position der Telomere peripher.

Zur Erklärung der Telomerverteilung in Mauslymphozyten: Die Chromosomen der Mauslymphozyten sind acrozentrisch. Das bedeutet, dass die Entfernung der Telomere von den Centromeren geringer als beim Menschen ist.

II.5.5. Abstände der Territorien voneinander

Es wurden auch alle auftretenden Abstände zwischen Chromosomenmittelpunkt und Centromermittelpunkt gemessen. Es können dabei 6 verschiedene Abstände auftreten: ein Abstand zwischen den Territorien, einer zwischen den Centromeren, zwei Abstände zwischen Territorium und Centromer des selben Chromosoms und zwei Abstände zwischen Territorium und Centromer des jeweils anderen Chromosoms, s.Skizze:

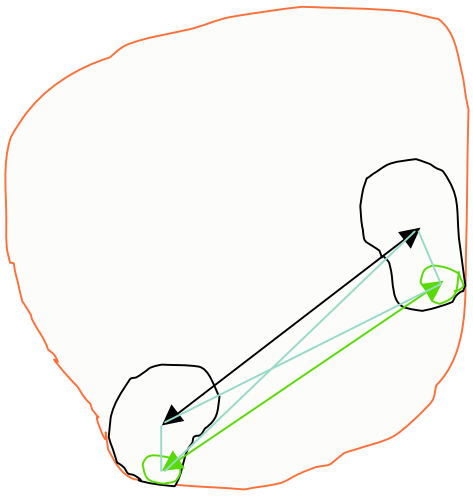

Abb.II.5.5. Ein Beispielskern: in Rot die Kernhülle, in Schwarz die Territorienränder, in Grün die Centromere. Es sind 6 verschiedene Abstände möglich und eingezeichnet.

Es wurden nicht die Abstände zwischen verschiedenen Chromosomen gemessen. Wollte man hier systematisch alles erfassen, würde der Aufwand exponentiell mit der Anzahl der betrachteten Chromosomen anwachsen. Bei Verdacht einer besonderen Verteilung, z.B. wenn eine Translokation zwischen zwei Chromosomen als Ursache einer Krankheit feststeht, mag man nachmessen. Die gefundenen Graphen stehen im Anhang auf S. 21f. Hier scheinen die Abstände zwischen den beiden Chromosom #15 Homologen besonders scharf um den Wert 4,5 µm zu liegen.

II.5.6. Zu erwartende Abstände bei statistisch verteilten Territorien

Zum besseren Vergleich mit dem Fall einer statistischen Verteilung wird hier noch der Abstand zweier statistisch verteilter simulierter Homologenpaare gegeben (Chr #6 und #7). Die Stichprobe umfasste dabei 50 Kerne:

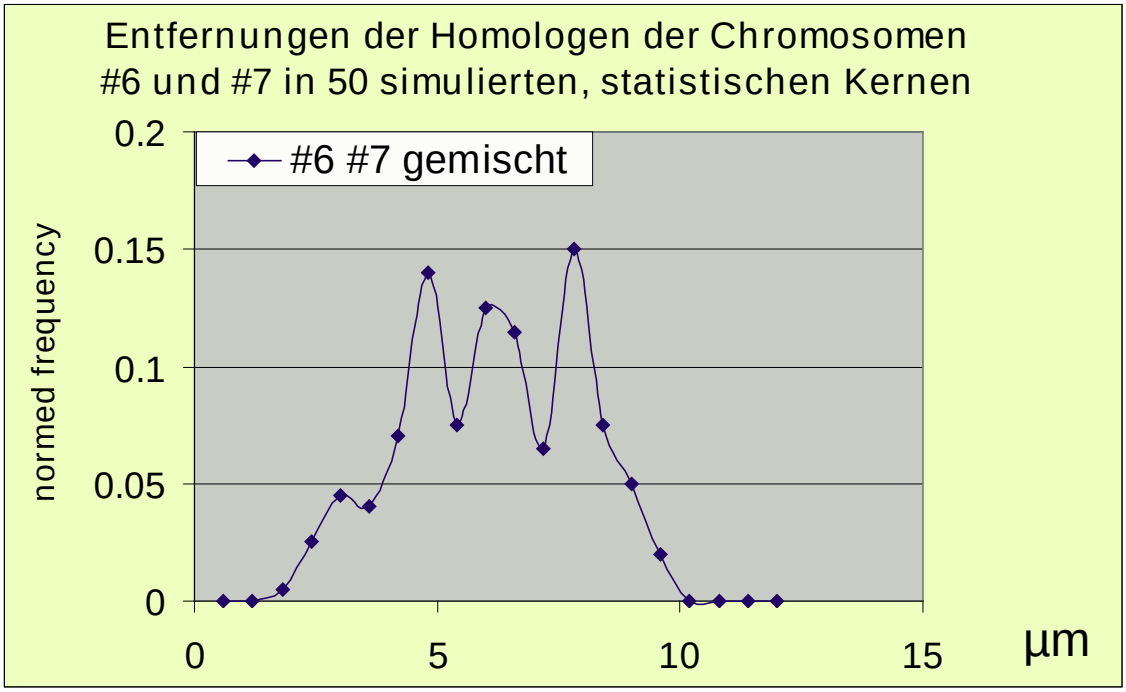

Abb.II.5.6. in obigem Graph ist das Ergebnis der Abstände der Schwerpunkte simulierter, statistisch verteilter Chromosomen in 50 Kernen statistisch aufbereitet. Insgesamt ergaben sich 200 Abstände (4x50, s. Abb II.5.5). Der Verlauf der Verteilung verläuft in etwa glockenförmig.

II.5.7. Zu erwartende Abstände bei Territorien auf Kugeloberflächen

Will man die auftretenden Abstände auf einer Kugeloberfläche bestimmen, so kann man wie folgt vorgehen: o.B.d.A. lege man auf einen der Punkte immer den Nordpol. Der andere Punkt liege in J Breitengraden Entfernung. In dieser Entfernung vom Nordpol gibt es eine Anzahl Punkte A(J), die proportional zum Umfang des Breitengrades ist, also zu 2pR•sin(J). Der Abstand d(J) der Punkte voneinander erstreckt sich nicht entlang der Kugeloberfläche sondern führt durch die Kugel durch und beträgt 2R•sin(J/2) (s.Skizze)

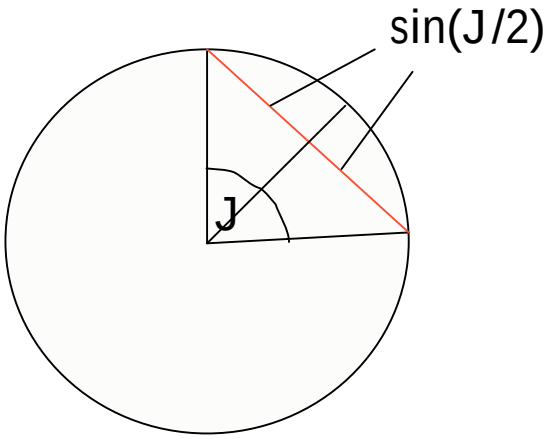

Abb.II.5.7. In obiger Abbildung soll erklärt werden, wie die Länge der Sehne bei bekanntem J bestimmt wird. J wird durch den Eintritts- und Austrittsort bestimmt. Eingezeichnet ist ferner die Winkelhalbierende von J die mit der Sehne einen rechten Winkel eingeht.

Die Umkehrabbildung von d(J) wird leicht als J = 2 arcsin (d/2R) bestimmt. Nun lässt sich das gesuchte H(d) als H(d(J)) bilden und erhält als Häufigkeitsverteilung der Abstände:

$$H(d)=2p\bullet\sin(\arcsin(d/(2R)) \qquad \text{mit } 0<J<p.$$

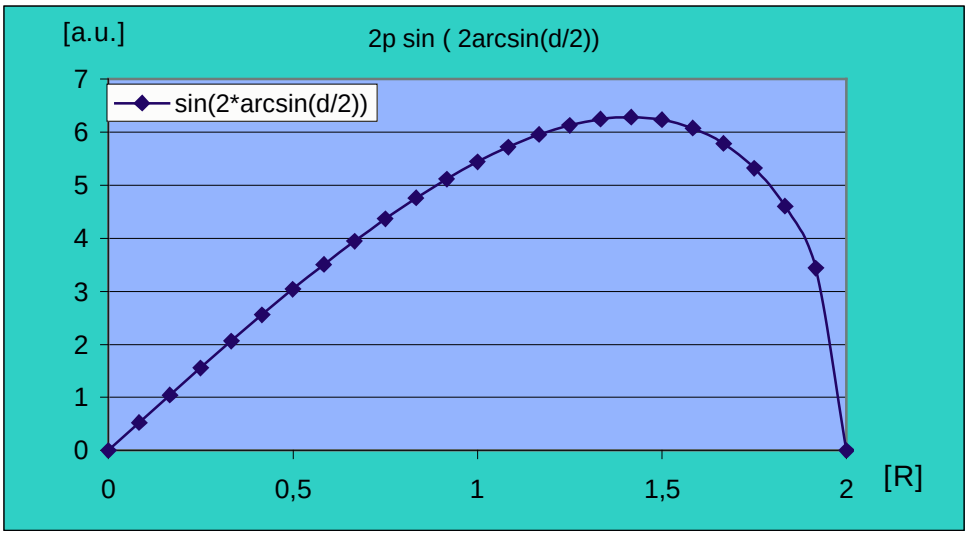

Abb.II.5.8. Obiger Graph stellt dar, wie häufig Abstände zu erwarten sind, wenn die Endpunkte der Abstände ungefähr auf einer radialen Schale liegen.

Anhand dieses Vergleiches beurteilt man die auftretenden Abstände als statistisch verteilt bis auf die Homologene des Chromosoms #15 und vielleicht noch #11, wobei die Anzahl der gemessenen Abstände für beide Kurven nur 18 betrug.

II.6. Verteilung der Kinetochoren in Lymphozyten im Verlauf des Zellzyklusses

[s.Dühring 2002]

II.6.1. Biologische Einleitung zu den Kinetochoren

Wie in der Einleitung bereits dargelegt wurde, gibt es für eine Zelle verschiedene Entwicklungsphasen. Eine Zelle kann grundsätzlich im Teilungszyklus sein (G1, S, G2, Metaphase, G1), oder stabil die G0 Phase halten. Von der Metaphase absehend, wurde die Position der Kinetochoren in allen Stadien der Interphase vor allem in Lymphozyten untersucht. Kinetochoren sind Proteine, die im Centromer eingebaut sind und mit welchen die Mikrotubuli der Spindelapparate verbunden sind, um in der Metaphase die Schwesternchromatiden für je einen neuen Zellkern zu trennen. Die Kinetochoren wurden mit Antikörpern kenntlich gemacht und es wurde versucht, alle Kinetochoren zu markieren. Als Bild ergaben sich in der G1 Phase einzelne Signale nahe an der Auflösungsgrenze des Mikroskops. In der G2 Phase sah man die Punkte paarweise auftreten, nachdem sie in der davor liegenden S Phase dupliziert worden waren (Bilder s. Anhang S. 24f). Die Phasen wurden anhand dreier Kriterien bestimmt: der Ki-67 Markierung, der BrdU-Markierung und der Kerngröße. Die Anzahl der beobachteten Signale hätte in der G0 Phase und den anderen untersuchten Phasen außer der G2 Phase, maximal 46 Kinetochoren betragen können und in der G2 Phase 92. Aber nur in der G1 Phase ergaben sich fast 100 % der Signale. in der G0 Phase waren es nur 30% und in den anderen Phasen etwa 70 %. Dühring [Dühring 2002] vermutet eine Agglomeration der Kinetochore vor allem in der G0 Phase.

Die Verteilung der Kinetochoren (s. Anhang S.26f) war in der G0 Phase deutlich peripher, was eine Verbindung mit der Kernhülle nahelegt, während in den anderen Phasen auch Aufenthaltsmaxima bei mittleren Radien vorhanden waren. Dies könnte eine Verbindung mit den Nukleoli bedeuten. In der S Phase war die periphere Lage ausgeprägter als in der G1 und der G2 Phase.

II.6.2. Verteilung der Kinetochoren

Es wurde zum Vergleich auch die Verteilung von Kinetochoren in G0 Lymphozyten, die mit FISH gekennzeichnet waren, sowie die Verteilung in G0 Fibroblasten und in G0 Shep Zellen untersucht. Shep Zellen gehören zu einer Krebsart. Es wurde stets versucht, alle Kinetochoren zu markieren.

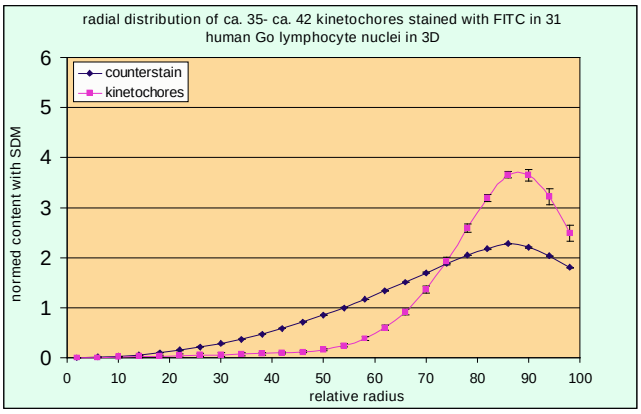

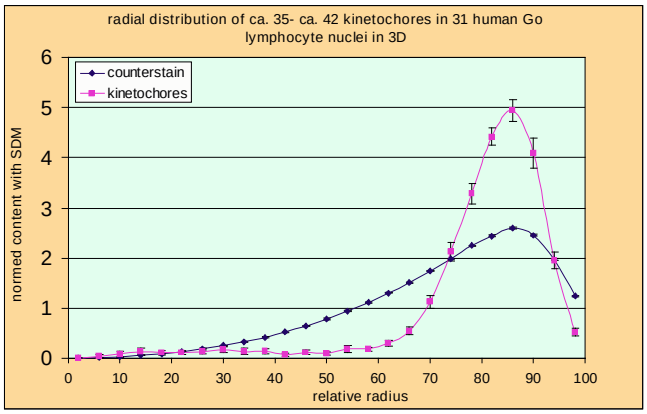

Abb.II.6.1. In beiden obigen Graphen ist die Kinetochorverteilung in menschlichen Lymphozyten zu sehen. Links mit FITC Markierung und rechts mit BrdU Pulsmarkierung

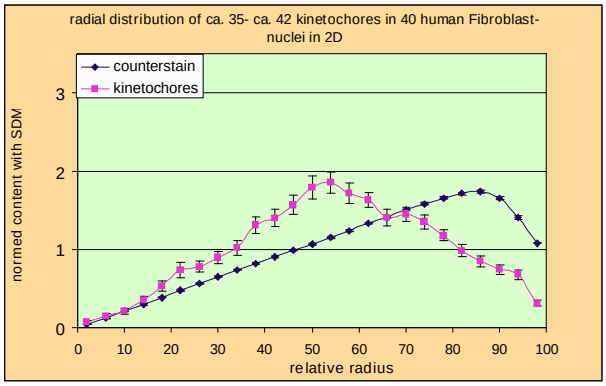

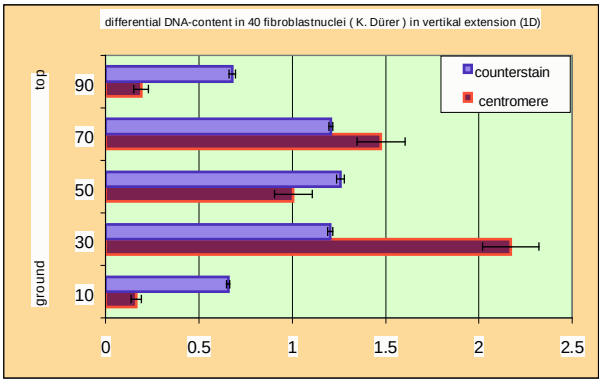

Abb.II.6.2. Verteilung der Kinetochoren in menschlichen G0-Fibroblasten. Der linke Graph zeigt die laterale Verteilung mit einem Maximum bei eher inneren Werten. Der rechte Graph zeigt die höhenabhängige Verteilung. Besonders in der unteren Subperipherie ist die Verteilung maximal.

Es wurde auch die Kinetochorverteilung in 2 G1 Shepzellen untersucht. Shepzellen sind wie Fibrobasten flach, bilden aber eine Krebsart. Ähnlich wie bei den Fibroblasten liegen die Kinetochoren auf dem Grund der Zellen.

Es steht aufgrund der hier dargelegten Ergebnisse fest, dass viele Kinetochoren in der Interphase im Teilungszyklus sich von der Kernmembran lösen und zu den Nucleoli oder einem anderen Ort im Kerninneren wandern.

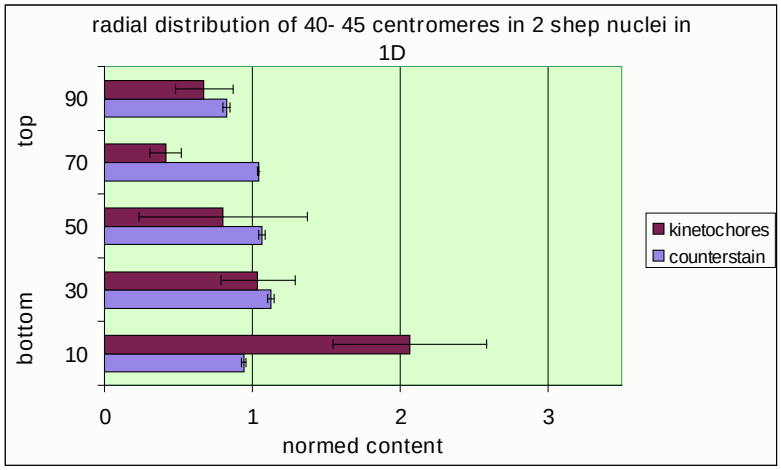

Abb.II.6.3. In 2 Shep Zellen lagen die Kinetochoren wie bei den Fibroblasten meistens auf dem Zellgrund.

II.7. Untersuchung der RNA-DNA -Korrelation in Fibroblasten

Es wurde die Korrelation zwischen dem Aufkommen von RNA und DNA mit 4 Methoden untersucht. Dabei stellte sich heraus, dass DNA gegenüber der RNA an der Kernmembran und in den Nucleoli überproportional vertreten ist. Im Rest des Kerns wurde keine Korrelation gefunden. In den Nucleoli gab es wenig DNA und noch weniger RNA.

II.7.1. Biologische Einleitung:

Die meisten Zellfunktionen werden von Proteinen erbracht. Die Informationen für die Aminosäuresequenz der Proteine werden von der mRNA und diese aus der RNA entnommen. Die RNA ist ein Komplement zur DNA, bei der die Base Thymin mit Uracil getauscht ist. Da nicht genau bekannt ist, in wie fern der Zellkern kompartimentiert [Cremer 2000, Cremer 2001] oder aber der Zellkern eine Art Reagenzglas ist, in dem alle Reaktionen an beliebigen Stellen stattfinden [Knoch 2002], ist es von Interesse zu prüfen, ob zum Beispiel die RNA Verteilung mit der DNA Verteilung korreliert, antikorreliert oder unkorreliert ist.

II.7.2. Material und Methoden

Anhand von 30 Fibroblastenaufnahmen im G0 Stadium, auf deren einem Kanal DNA mit GFP und auf deren anderem RNA mit BrUTP markiert war, wurde diese Frage angegangen. Zur Beantwortung wurden vier Bildbearbeitungswege eingeschlagen.

II.7.2.1. Untersuchung der RNA-DNA -Korrelation mit Hilfe der "ratio"- Methode

Eine in der Biologie gängige Praxis ist die punktweise Bildung der Ratio des einen Bildes zum anderen. Helle Zonen weisen auf ein Ungleichgewicht zwischen beiden Bildkanälen hin: es wurde einmal DNA/RNA und einmal RNA/DNA ermittelt. Es folgen nun die Bilder DNA/RNA:

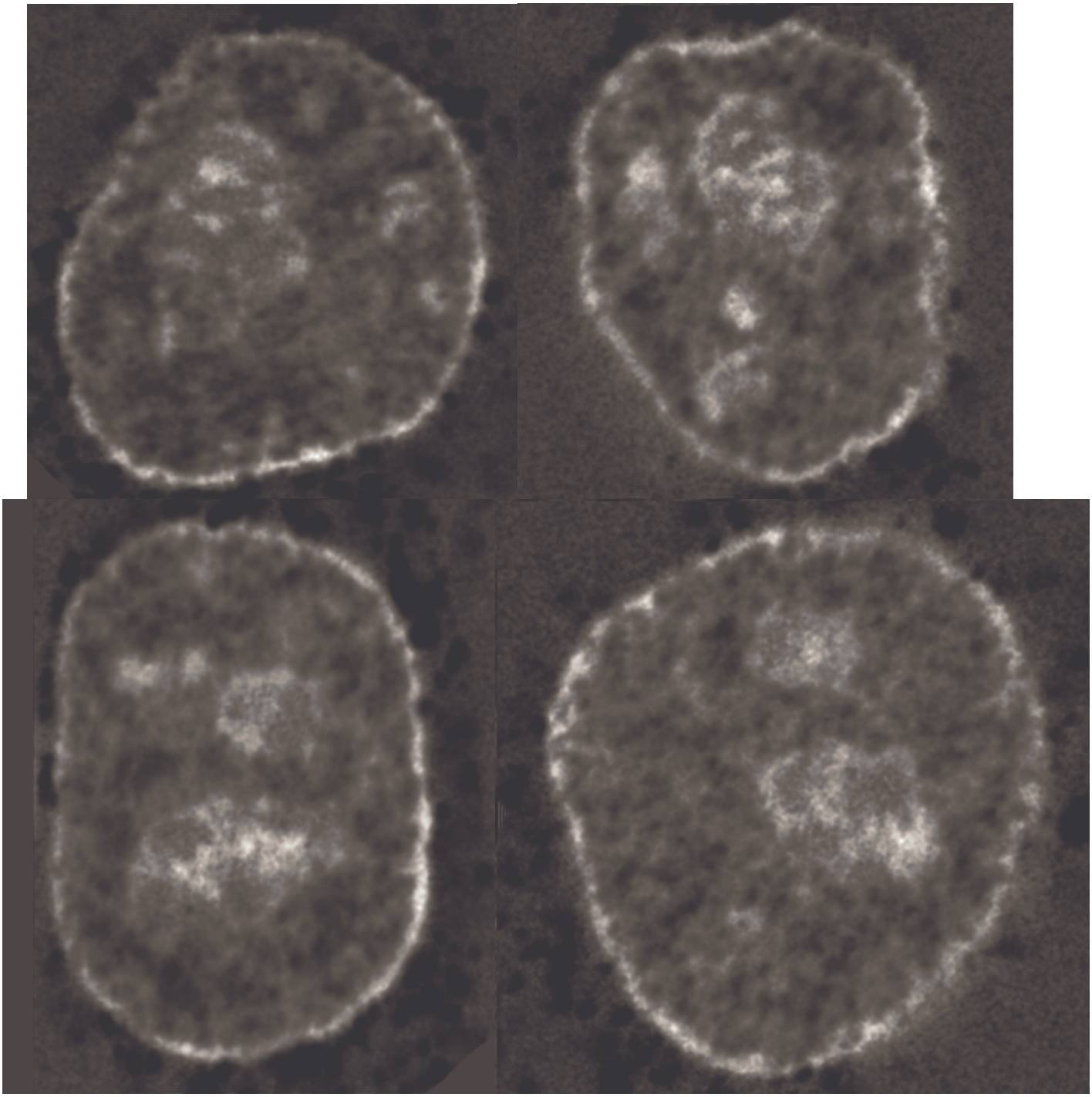

Abb.II.7.1. An 4 Beispielkernen ist das DNA-Bild durch das RNA-Bild dividiert worden. An hellen Stellen überwog die DNA. Dies ist regelmäßig am Kernrand und auch in den Nucleoli der Fall. An dunklen Stellen überwog die RNA. Solche Stellen wechseln sich ab.

Die Ratio- Methode eignet sich besonders, um Antikorrelationen sichtbar zu machen, denn Stellen mit Antikorrelation erscheinen in großer Helligkeit. Um extrem große Helligkeitsunterschiede zu vermeiden, wurde von den Helligkeiten Voxelweise die Wurzel gezogen. Außerdem wurde eine Division durch 0 vermieden. Die Stellen, an denen das RNA überwiegt sieht man am besten in Bildern RNA pro DNA, s.u.:

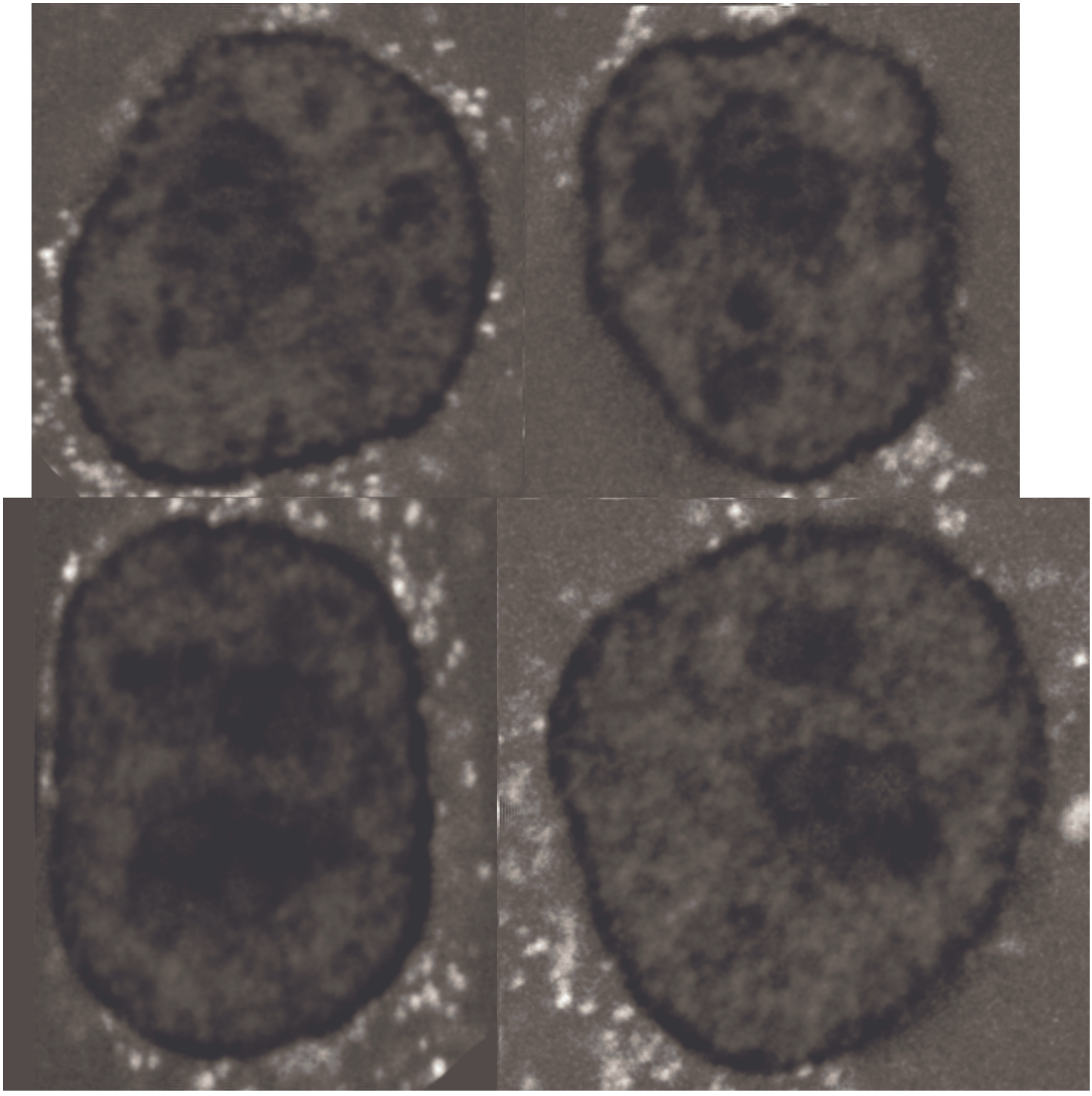

Abb.II.7.2. hier wurde das RNA-Bild punktweise mit dem DNA-Bild dividiert. Man erkennt, dass außerhalb der Kerne im Verhältnis zur DNA besonders viel RNA vorhanden ist.

Die original DNA- Bilder sehen dabei folgendermaßen aus:

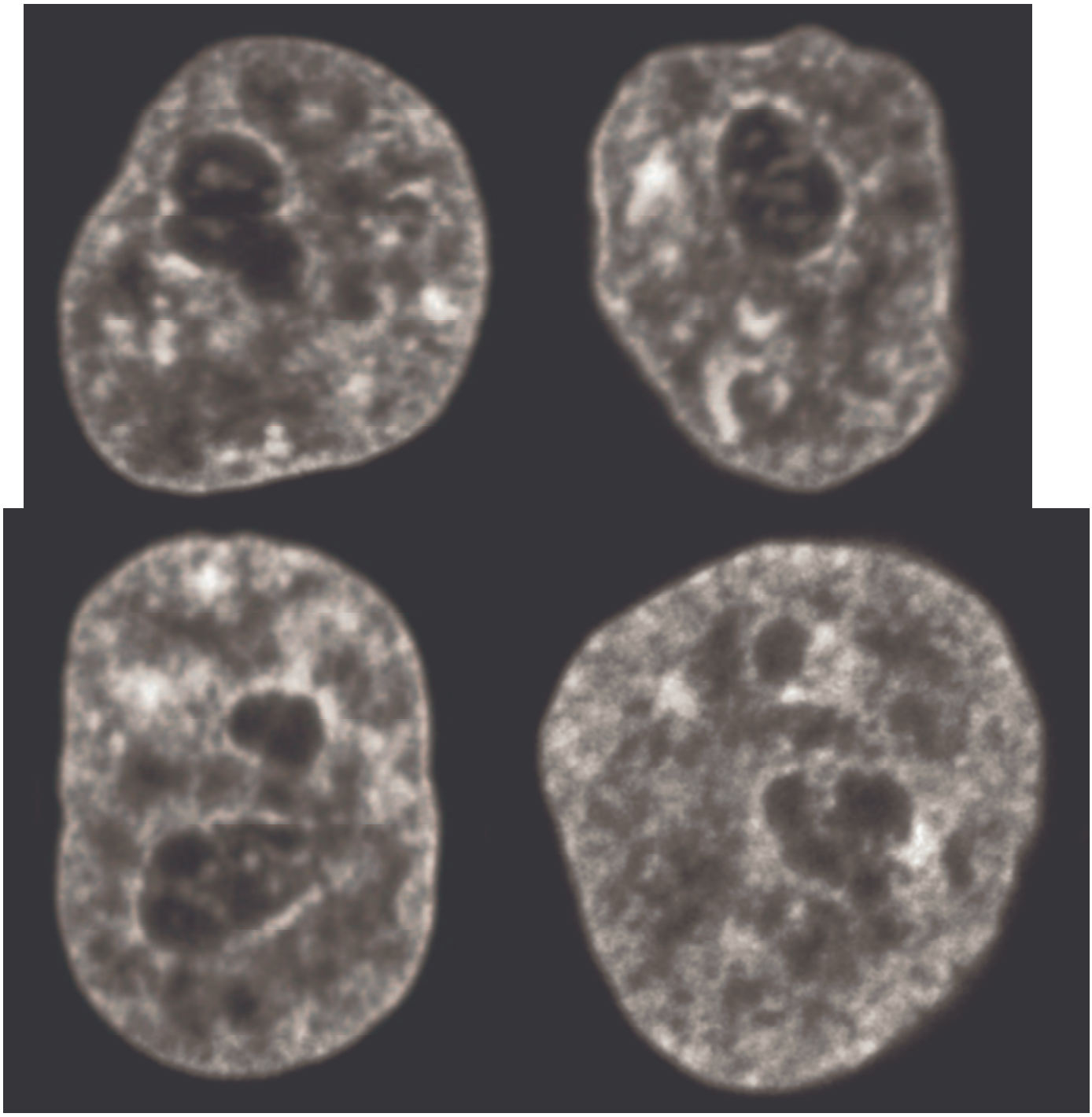

Abb.II.7.3. dies ist die DNA-Verteilung in den Zellkernen. Außerhalb des Kernes befindet sich überhaupt keine DNA und auch in den Nucleoli ist wenig DNA vorhanden

Die RNA- Originalbilder sehen folgendermaßen aus:

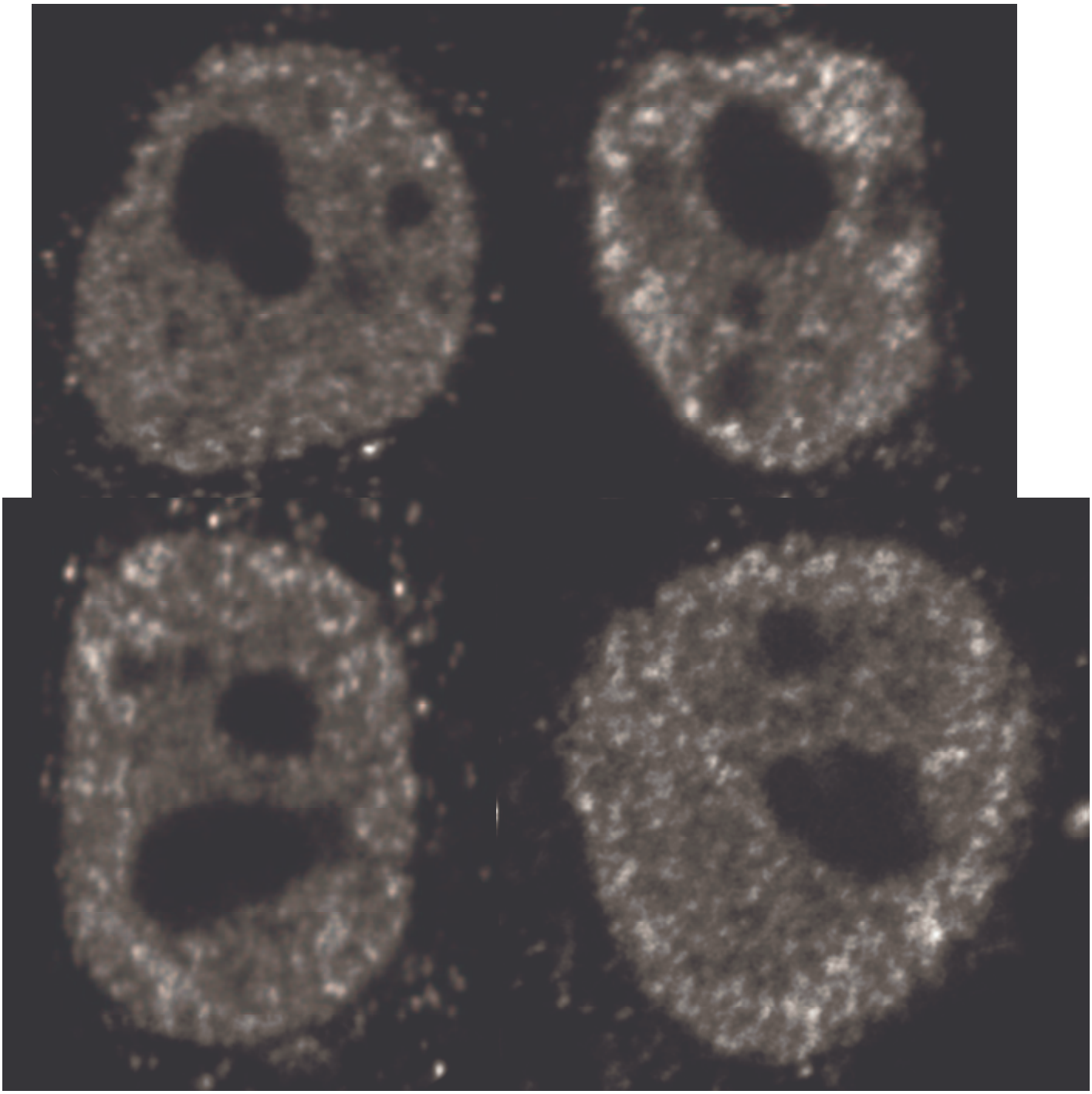

Abb.II.7.4. Die Abbildung der RNA kommt viel gesprenkelter vor als es die homogenere DNA ist. Bei allen vier Darstellungen wurden von links nach rechts, von oben nach und unten verwendet: Kern 1 Ebene 11, Kern 4 Ebene 13, Kern 2 Ebene 13, Kern 10 Ebene 18.

II.7.2.2. Untersuchung der RNA-DNA-Korrelation mithilfe von "line scans"

Die zweite Methode, die RNA-DNA Korrelation zu untersuchen, ging über sogenannte „line scans“. Ein line scan ist nichts anderes, als ein Helligkeitsprofil entlang einer Linie, die durch das Bild gelegt wird. Dieses Verfahren ist in der Biologie verbreitet. In diesem Fall wurden anhand von den vier Beispielkernen Farbbilder erstellt mit den Farben Rot für DNA und Türkis für die RNA. Es sollte die Korrelation der Helligkeitsschwankungen beider Farbkanäle untersucht werden, also ob die Maxima und Minima der Kurven an der gleichen Stelle liegen, oder um wieviel sie verschoben sind. Dies ist nichts anderes als eine visuelle Korrelationsanalyse der Farbkanäle in 1D mithilfe von Graphen.

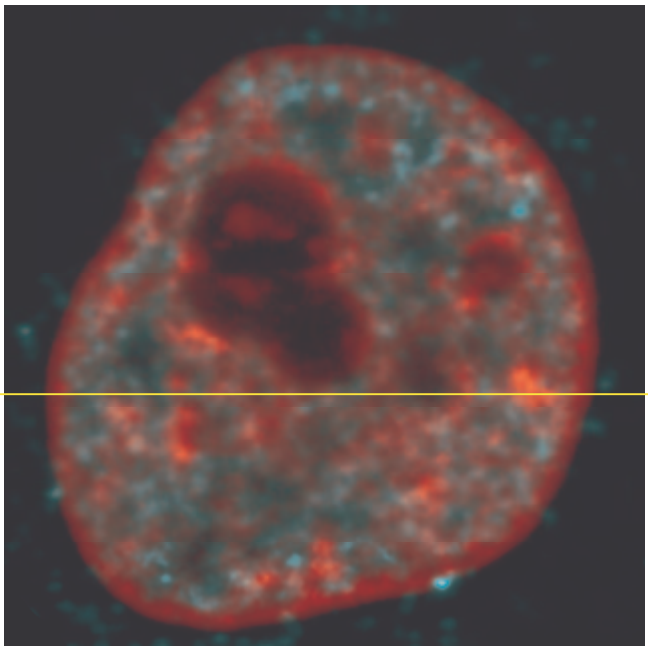

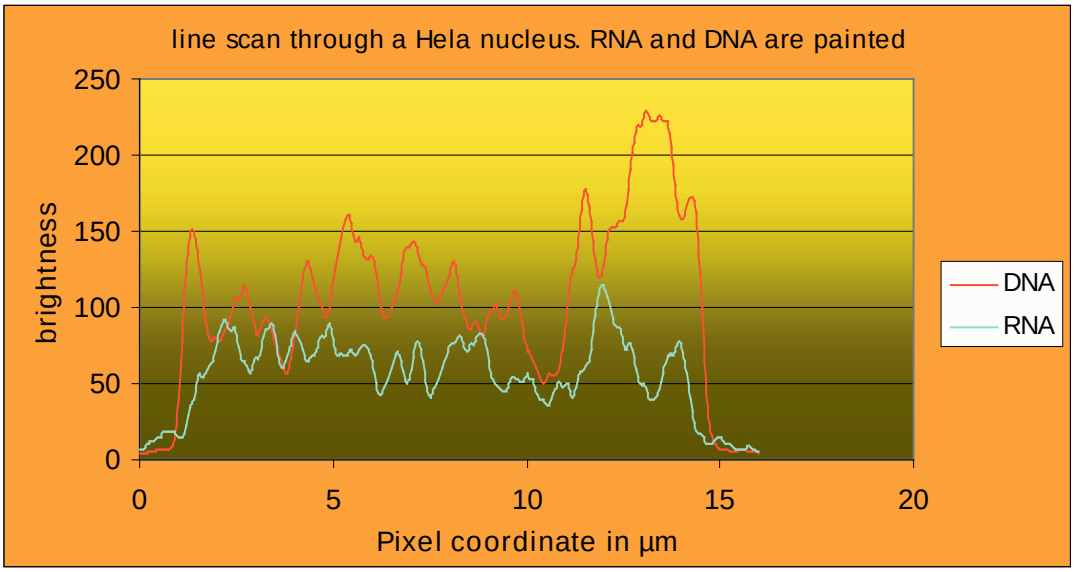

Abb.II.7.5. In obiger Abbildung ist Kern 1, Ebene 11, mit einem line scan abgebildet. Der Graph des line scans zeigt bei 12 µm und 8 µm eine Antikorrelation und bei 6µm und 4µm eine Korrelation in Größenbereichen um 1µm. Es gibt auch weitere Beispiele für Korrelationen und Antikorrelationen.

Weiter wurde Kern 2 Ebene 13, um 90° gedreht, gewählt:

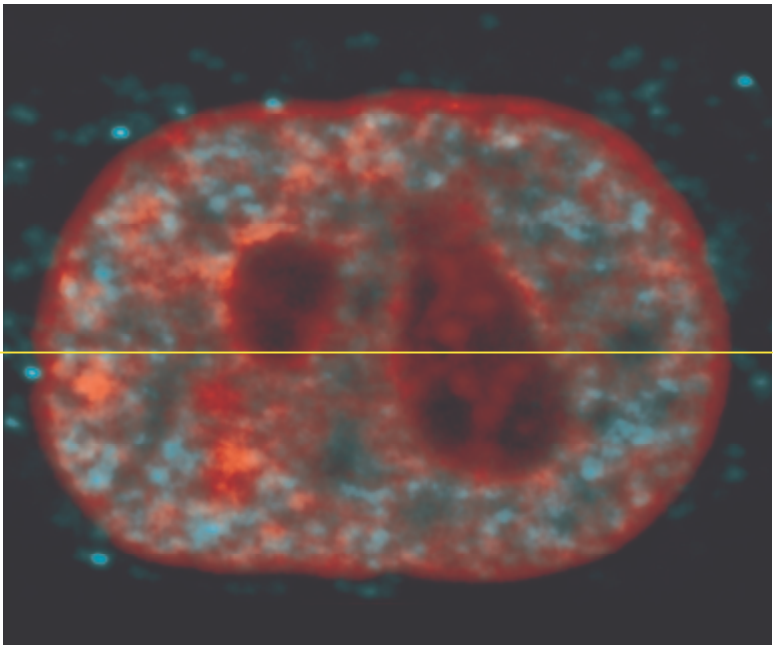

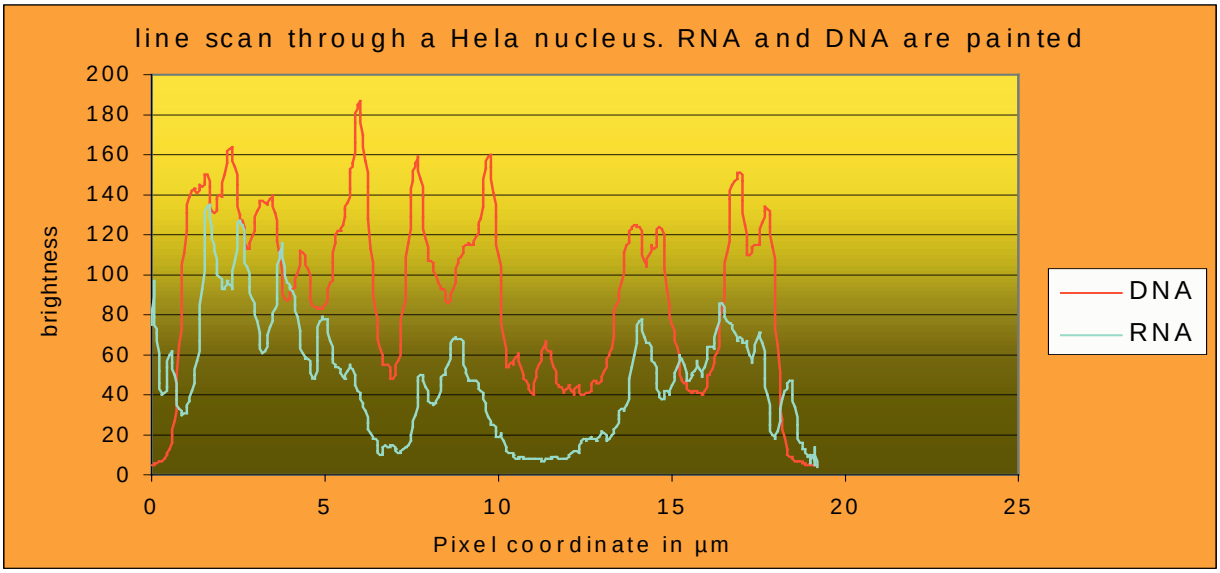

Abb.II.7.6. An diesem Kern sieht man auf der Ebene der Größen um 3 µm eine starke Korrelation. Die Spitzenwerte hingegen sind einmal antikorreliert und einmal unkorreliert.

Im nächsten Bild ist Kern 4 Ebene 13 mit line scan auf Höhe 203 dargestellt:

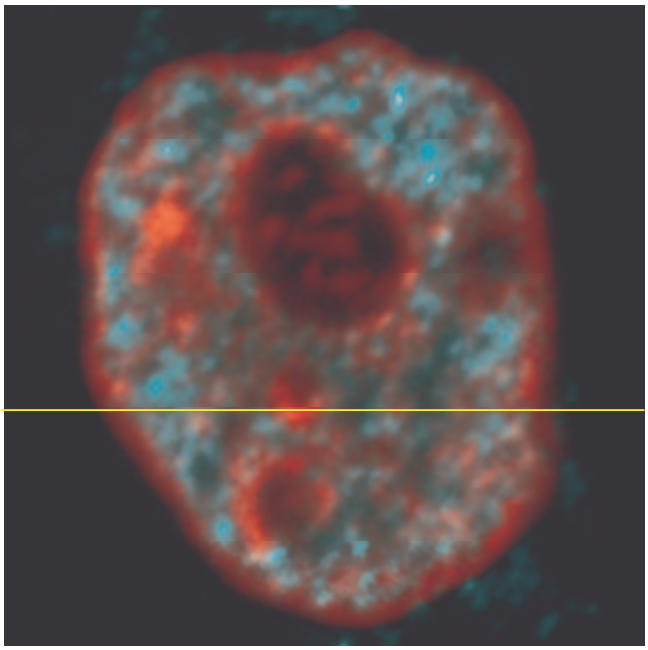

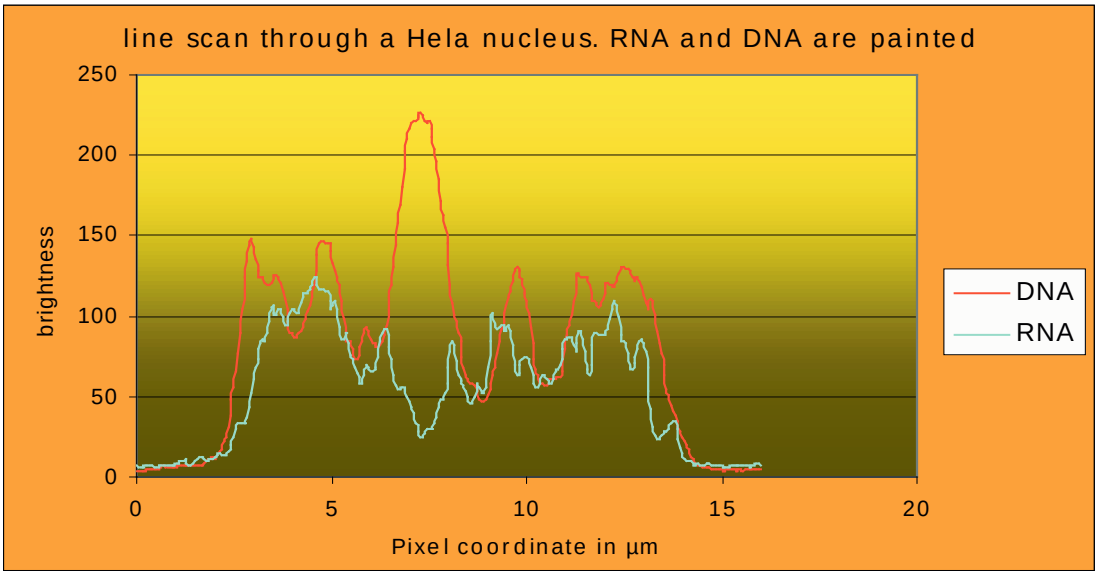

Abb.II.7.7. Aus obigem line scan resultiert außer für den Bereich um 7µm, wo es eine Antikorrelation zwischen DNA und RNA gibt, eine Korrelation für Größen um 2 bis 3µm. In kleineren Skalen schließt man eher auf Unkorreliertheit, da Maxima und Minima mehr oder weniger phasenverschoben auftreten.

Als nächstes Bild zu sehen ist: Kern 10, Ebene 18

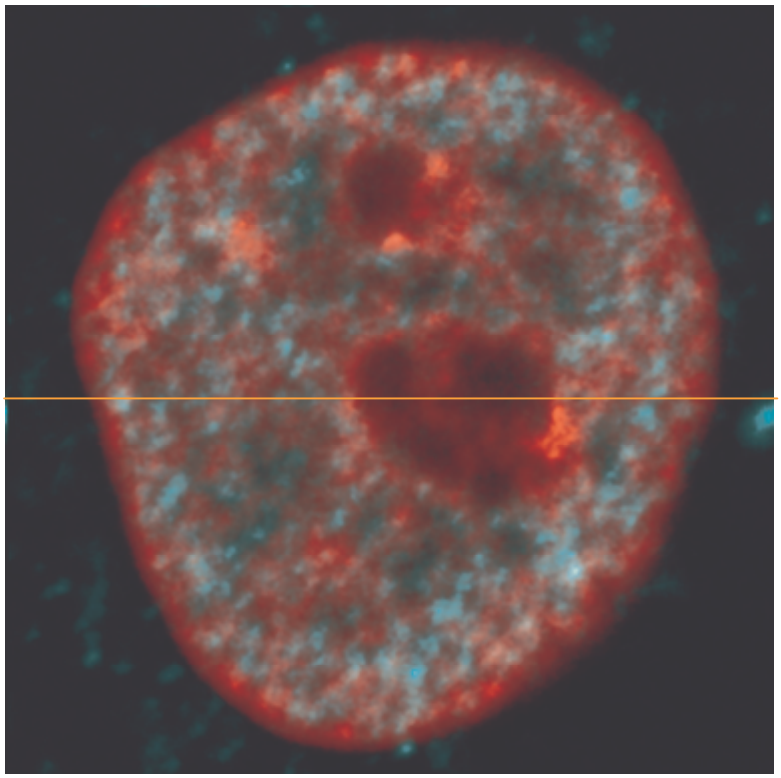

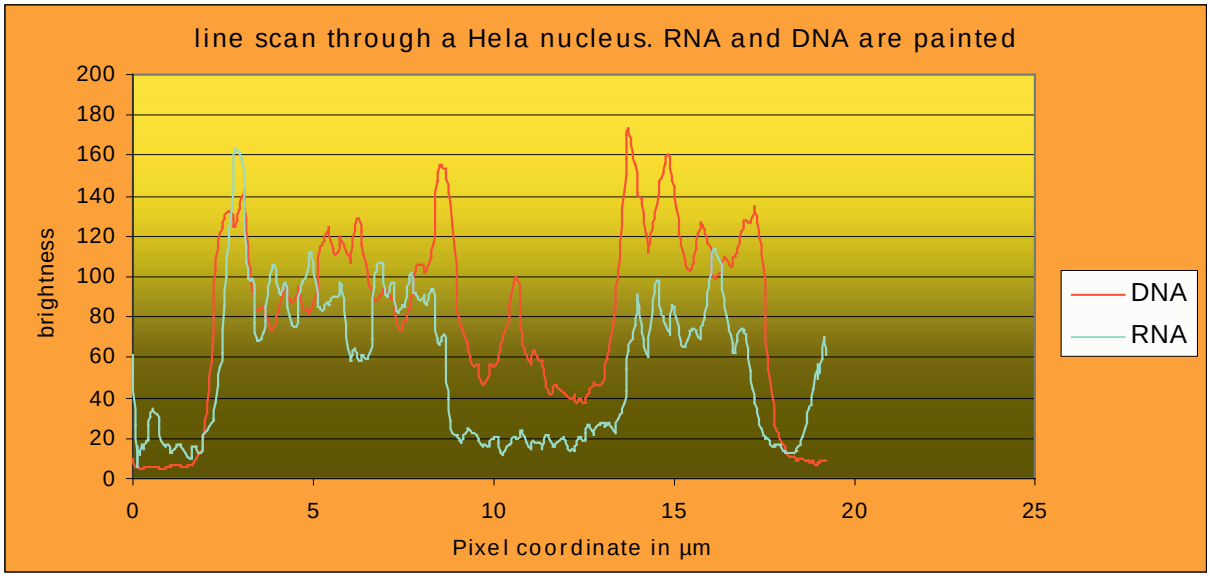

Abb.II.7.8. Der obige line scan zeigt im Größenbereich von 5µm eine deutliche Korrelation. Allerdings ist die Aussage trivial, da der line scan durch die Nucleoli führt. Im restlichen Bereich herrscht zwischen den beiden Graphen Unordnung und daher Unkorreliertheit.

Zuletzt wird noch ein line scan an Kern 10 durch die Tiefe gezeigt: die Weitenachse wurde als Tiefenachse benutzt und an Ebene 190 visualisiert:

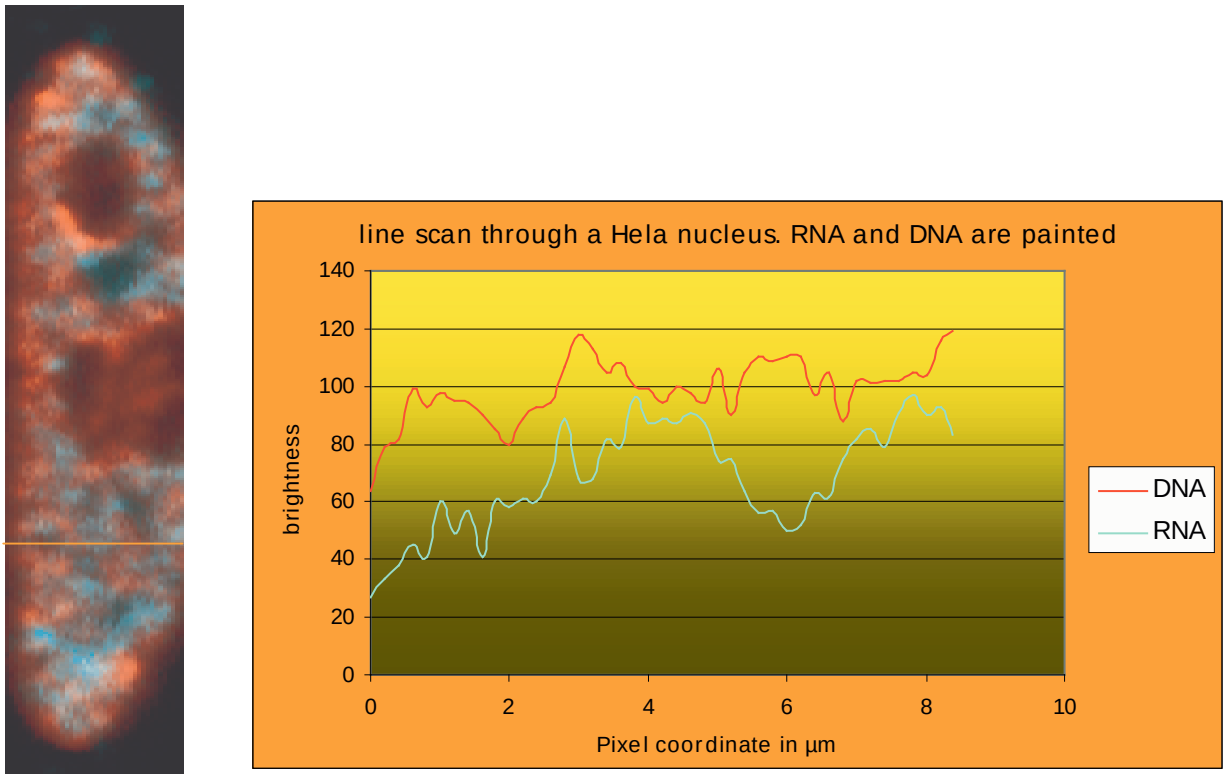

Abb.II.7.9. In obiger Abbildung sieht man eine Zunahme der DNA und RNA Dichte bei zunehmender Zellhöhe. Um die Koordinate 6µm sieht man hingegen eine Antikorrelation.

Im Ergebnis aller line scans kann man subjektiv zu unterschiedlichen Resultaten kommen. Zum Beispiel wertete [Verschure et al.1999] ihre line scans als Beleg für die Nachbarschaft von Replicationsfoci und naszenter DNA. Es ist möglich, dass obige Autoren sich vom visuellen Eindruck haben verleiten lassen: Tatsächlich erkennt man visuell Bereiche, in denen beide Farben vorkommen, nicht als solche, vielmehr erkennt man immer nur die vorherrschende Farbe. In dieser Arbeit wird die Meinung vertreten, dass aufgrund der line scans keine wirklich nennenswerten Korrelationen zu sehen sind, mit Ausnahme der durch die Nucleoli erzeugten Struktur. Sowohl der RNA- als auch der DNA- Gehalt sinken im Bereich der Nucleoli stark.

II.7.2.3. Quantisierung der "Ratio"- Methode

Die RNA und die DNA wurden mit Hilfe von Schwellwerten segmentiert und dann wurden zwei Binärbilder erstellt. Die RNA- Verteilung nahm ein geringeres Volumen ein als die DNA-Verteilung. Für alle Voxel mit RNA- Gehalt im RNA- Kanal wurde nun untersucht, ob auf der entsprechenden Stelle im DNA- Kanal ein DNA- Signal vorläge oder nicht. War dies der Fall, bekam das Voxel die Zahl „1“ für korreliert zugeordnet, war dies nicht der Fall, die Zahl „-1“ für antikorreliert (s. Abb. unten). Diese Zahlen wurden aufsummiert und durch die Anzahl an RNA- Voxel dividiert, so dass am Ende eine Fließkommazahl zwischen -1und 1 herauskam: -1, falls überall dort, wo RNA vorkam, kein DNA vorhanden war, und 1, falls überall, wo RNA vorkam, auch DNA vorhanden war. Der soeben geschilderte Berechnungsablauf wurde auf alle 30 Kerne angewandt und davon wurde eine kleine Statistik mit Mittelwert und Standardabweichung erstellt. Wiederholt wurde das Verfahren mit generell niedrigeren und generell höheren Schwellwerten.

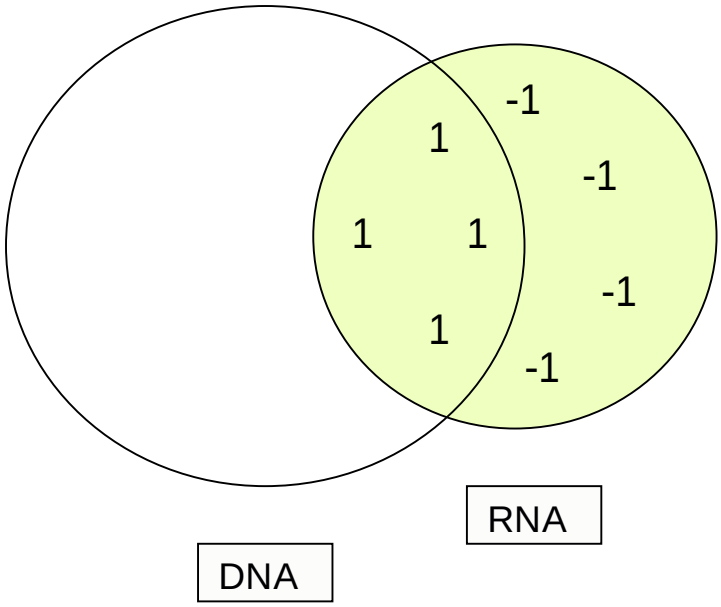

Abb.II.7.10. In obiger Abbildung wird die Zuweisung der Zahlen -1 und +1 für die Voxel erklärt. Demnach werden nur Voxel in Betracht gezogen, die zur RNA-Verteilung gehören (gelbes Gebiet). Davon werden mit „1“ alle Voxel numeriert, die gleichzeitig zur DNA gehören, und mit „-1“ alle diejenigen, die nicht zur DNA-Verteilung gehören. In obiger Skizze wäre die Summe 0 und damit würde die RNA-Verteilung zur DNA-Verteilung unkorreliert auftreten.

Als Ergebnis kam für den wahrscheinlichsten Schwellwert im Mittel etwa eine .0,0 heraus, d.h. ein unkorreliertes Ergebnis. Die Standardabweichung betrug ca. –0,3. Problematisch an dieser Methode ist allerdings die Schwellwertabhängigeit der Ergebnisse. Das Ergebnis liegt aber dieser Methode zufolge sicher zwischen +0.3 und –0.4

Korr bei v = 0.6	Korr bei v = 0.65	Korr bei v = 0.7
0.352035	0.139322	-0.196253
0.192622	-0.07956	-0.395168
-0.364203	-0.448362	-0.528112
0.081072	-0.174774	-0.579512
0.219342	-0.076778	-0.380787
0.195825	-0.160413	-0.571306
0.214039	-0.089156	-0.424231
-0.180405	-0.477098	-0.683802
-0.160995	-0.428419	-0.728565
0.382316	0.166642	-0.124991
0.225107	-0.136634	-0.50499
0.634986	0.460911	0.208289
0.066074	-0.311931	-0.635358
-0.035335	-0.325973	-0.556776
0.189942	-0.131492	-0.42715
0.264808	0.044326	-0.245728
-0.071731	-0.327216	-0.676319
0.25772	0.01338	-0.355569
0.597989	0.319027	-0.014373
0.743858	0.532278	0.22685
0.513903	0.232421	-0.046585
0.710587	0.550958	0.200573
0.513552	0.228016	-0.123476
0.303352	-0.016209	-0.42328
-0.136635	-0.422856	-0.7801

0.410846	0.126618	-0.199504
0.358698	0.004392	-0.334876
0.329202	0.008828	-0.404639
-0.134065	-0.557609	-0.957506
0.457206	0.136608	-0.213729
Mittelwert	Mittelwert	Mittelwert
0.23772373	-0.0400251	-0.36256577
SD	SD	SD
0.27484846	0.29259695	0.29126917
Median	Median	Median
0.24772187	-0.02811705	-0.3879775

Tab.II.7.1. Die Ergebnisse der Ortskorrelation sind in obigen Werten zu sehen: zuerst die Korrelationen der einzelnen 30 Bilder bei 3 verschiedenen Schwellwerten, dann die Mittelwerte, die Standardabweichungen und die Medianwerte. Die Ergebnisse sprechen für eine im Durchschnitt unkorrelierte Verteilung der DNA im Bereich der RNA.

II.7.2.4. Untersuchung der Phasenkorrelation der einzelnen Bildwellenlängen im Fourierraum. 3D Verallgemeinerung und Quantisierung der "line scan"- Methode

II.7.2.4.1. Einleitung

Die zu beschreibende Methode ist eine Erweiterung der line scan Methode von 1D auf 3D und eine quantitative Erfassung der sonst nur subjektiven Beurteilung der Profile.

Ausgenutzt wird der unter dem Namen diskrete Fourieranalyse bekannte Sachverhalt, dass nämlich ein beliebiges Bild aus komplexen Wellen verschiedener Wellenlängen zusammengesetzt gedacht werden kann. Dabei wird die Größe „d“ eines Objektes am ehesten durch die Bildwellenlänge 2d dargestellt, dessen Position dagegen durch die Phase der Wellen bestimmt aus denen das Objekt zusammengesetzt ist. Schwellwerte größer als 0 wurden nicht benötigt, da die Methode die vorhandenen Kontraste statt der absoluten Helligkeiten benutzt. Zusätzliche Schwellwerte würden nur künstliche scharfe Kontraste bewirken.

II.7.2.4.2. Vorgehensweise

Da bei einigen Bildstapeln einige Ebenen künstlich zueinander verschoben vorlagen, wurden die Ebenen der Bilder mit einem Korrelationsprogramm (von Rainer Heintzmann, MPI Göttingen) wieder in ihre korrekte Form geschoben. Zur Prüfung des Korrelationsprogrammes wurde dieses auf nicht verschobene Bildstapel simulierter Kerne angewandt. Die Bildstapel wurden dabei mit einer Genauigkeit von 0,5 Pixel oder sogar weniger verändert. Der chromatische Shift wurde grob um eine Ebene korrigiert.

Als nächstes wurden sowohl der Kanal mit der DNA als auch der Kanal mit der RNA fourier transformiert. Die beiden transformierten Bilder wurden miteinander multipliziert, nachdem von einem der Kanäle das konjugiert Komplexe gebildet worden war. Das erhaltene komplexe Bild ist wie folgt zu interpretieren: Der Nullvektor war in der Bildmitte. Der Winkel gegenüber dem Nullvektor war „j 1-j 2“. Die Entfernung zum Nullvektor war proportional zur Wellenfrequenz. Die Helligkeit an einem Punkt war proportional zu den Absolutbeträgen „r1•r2“ der beiden einfließenden Bilder.

Dies veranschaulicht die folgende Gleichung:

$$\begin{aligned}&[r1 \bullet \exp(\omega t + \varphi 1)] \bullet [r2 \bullet \exp(\omega t + \varphi 2)]^* \\ &= [r1 \bullet \exp(\omega t + \varphi 1)] \bullet [r2 \bullet \exp(-\omega t - \varphi 2)] \\ &= (r1 \bullet r2) \bullet \exp(\varphi 1 - \varphi 2)\end{aligned} \qquad \text{(II.7.1)}$$

Von den Phasendifferenzen, die zwischen -p und +p liegen, wurde der Kosinus gebildet, um einen Korrelationsgrad mit Werten zwischen –1 und +1 zu erhalten. Man erhielt ein Zweikanalbild mit Korrelation (j 1-j 2) und Amplitude (r1•r2) für jeden im Bild vorkommenden Wellenvektor

Die Bilddaten mussten nur noch sinnvoll zusammengefasst werden. Dazu wurde dieses komplexe Bild in konzentrische Schalen eingeteilt, welche Gebiete mit Wellenzahlen ähnlichen Betrages enthielten. Die Schalenober - und –untergrenzen wurden dabei so gewählt, dass die Wellenzahlen und die dazu reziproken Bildwellenlängen von Schalenobergrenze zu Schalenuntergrenze einen für alle Schalen konstanten Quotienten von 1,414 (Quadratwurzel von 2) bildeten, und bei der feineren Auswertung den Quotienten 1,189 (4.-te Wurzel aus 2). Diese Schalen wurden nach Innen pro Schale immer um den gleichen Faktor kleiner, s. Skizze:

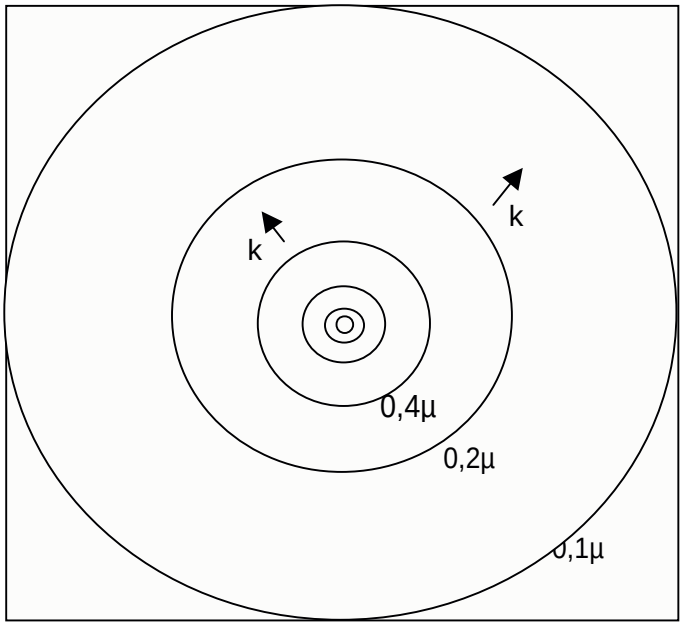

Abb.II.7.11. Bei dieser Bildeinteilung handelt es sich um konzentrische Schalen, die nach Innen jeweils die halbe Dicke haben. Ist das ursprüngliche Bild rechteckig, sieht die Einteilung Ellipsen vor. Entsprechendes gilt in 3D.

In axialer Richtung betrug die Schrittweite zwischen den konfokalen Ebenen 200nm. Daher betrug die kleinste Bildwellenlänge in axialer Richtung 400 nm. Lateral betrug die Voxelweite 50 nm, daher betrug die kleinste lateral vorkommende Bildwellenlänge 100 nm. Über das ganze Bild betrachtet blieb auf jeden Fall die Information für Bildwellenlängen über 400 nm voll erhalten.

II.7.2.4.3. Ergebnis

Im Ergebnis ergab sich für große Bildwellenlängen > 5µ eine starke Korrelation zwischen dem DNA - und dem RNA – Kanal. Dies bedeutet, dass beide, die RNA und die DNA großräumig im Kern verteilt sind. Um 1µm ergab sich eine leichte Antikorrelation (dass entspricht Gebilden um 500 nm Durchmesser wie den Replicationsfoci) wobei die kleineren Bildwellenlängen unkorreliert waren, s. Diagramm:

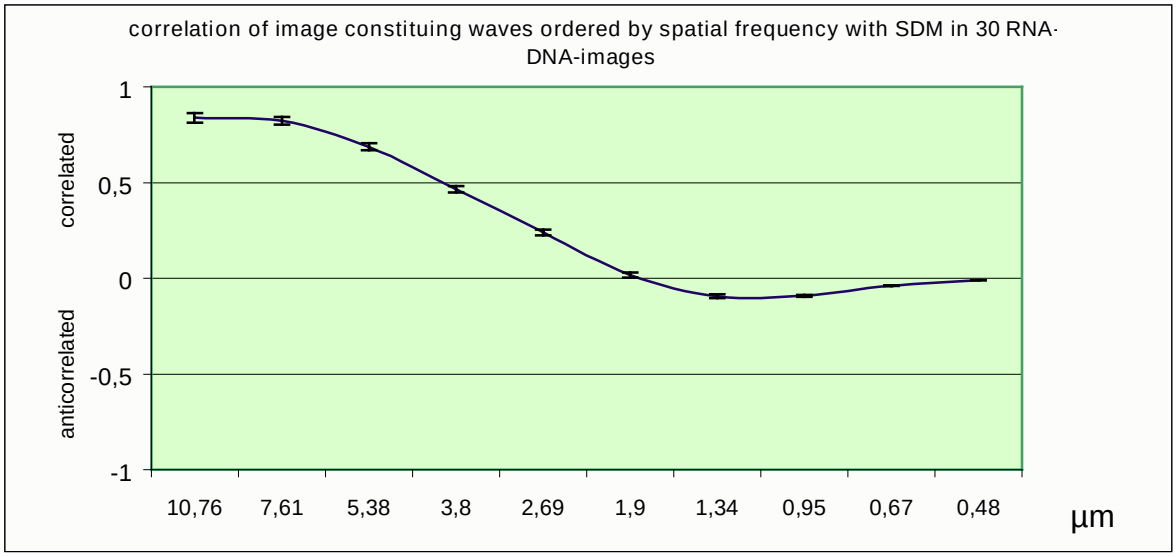

Abb.II.7.12. obiger Graph zeigt eine Korrelation für Bildwellenlängen l über 5µ (entspricht Strukturen über 2,5µ), eine leichte Antikorrelation um l = 1µ (entspricht Objekten der Größe 0,5µ wie Beispielsweise 1Mbp Replicationsfoci). Bei kleineren Wellenlängen ergibt sich keine Korrelation mehr.

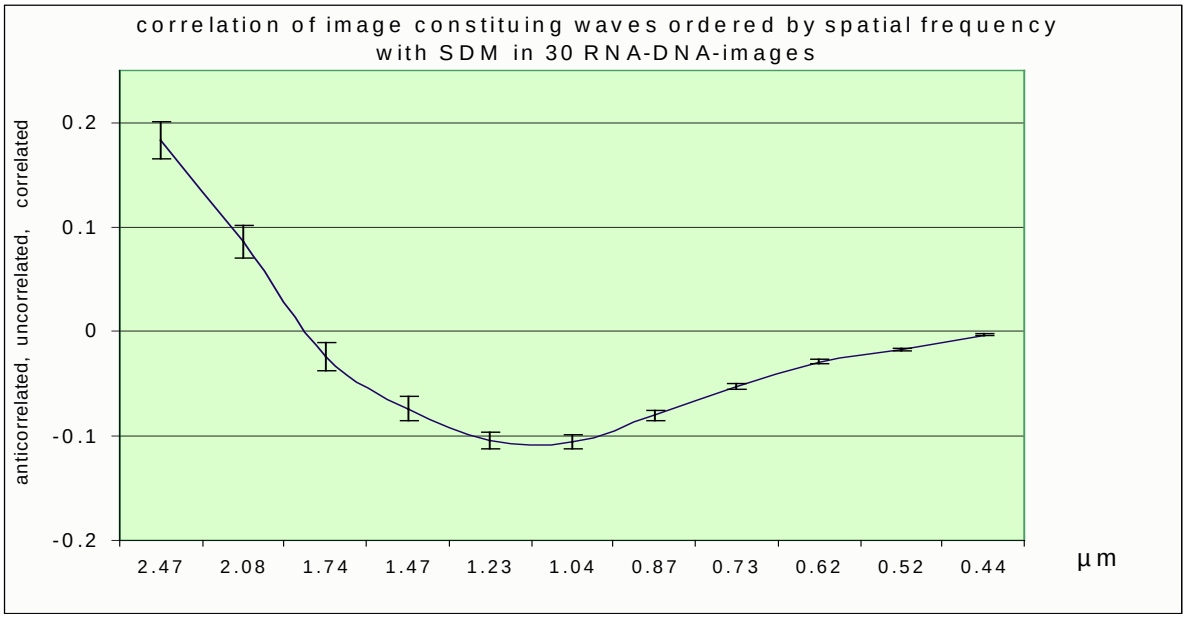

Abb.II.7.13. Hier ist ein vergrößerter Ausschnitt des darüber liegenden Diagrams zu sehen. Für Bildwellenlängen um 1µ ist eine statistisch signifikante aber kleine Abweichung der Kurve von der Unkorreliertheit 0 zu erkennen.

Eine Gewichtung der Phasendifferenzen (j 1-j 2) mit den Amplituden (r1•r2) aus Gleichung (1) brachte keine Veränderungen in den Graphen außer einer größeren Varianz.

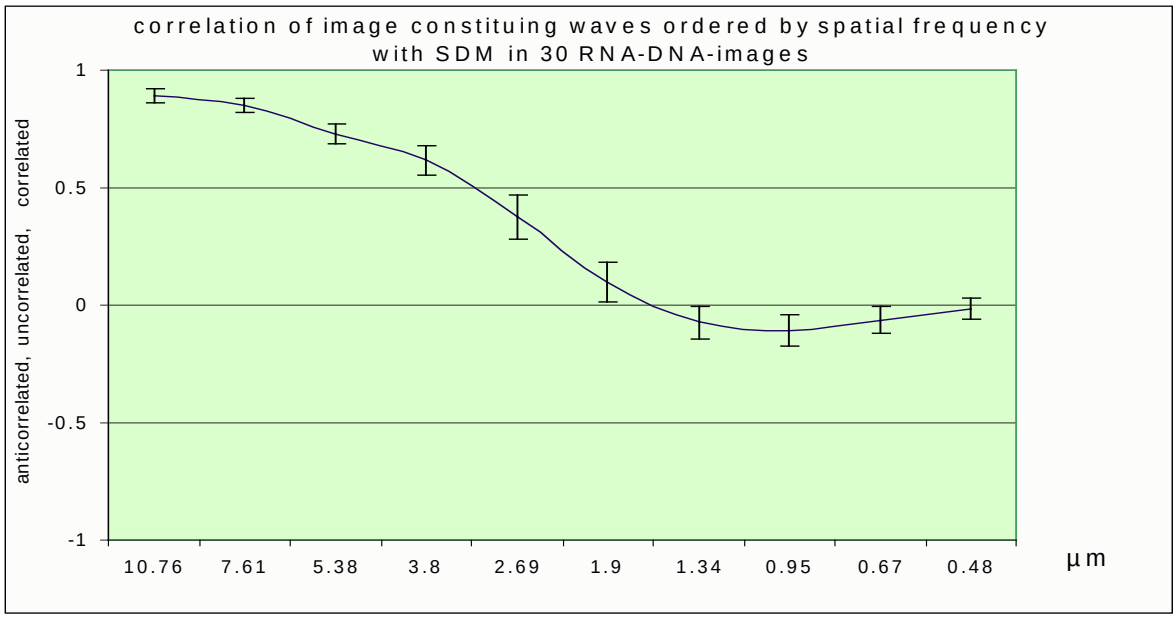

Abb.II.7.14. Bei Gewichtung der einzelnen Korrelationswerte mit der Amplitude ist eine Vergrößerung der Standardabweichung zu sehen.

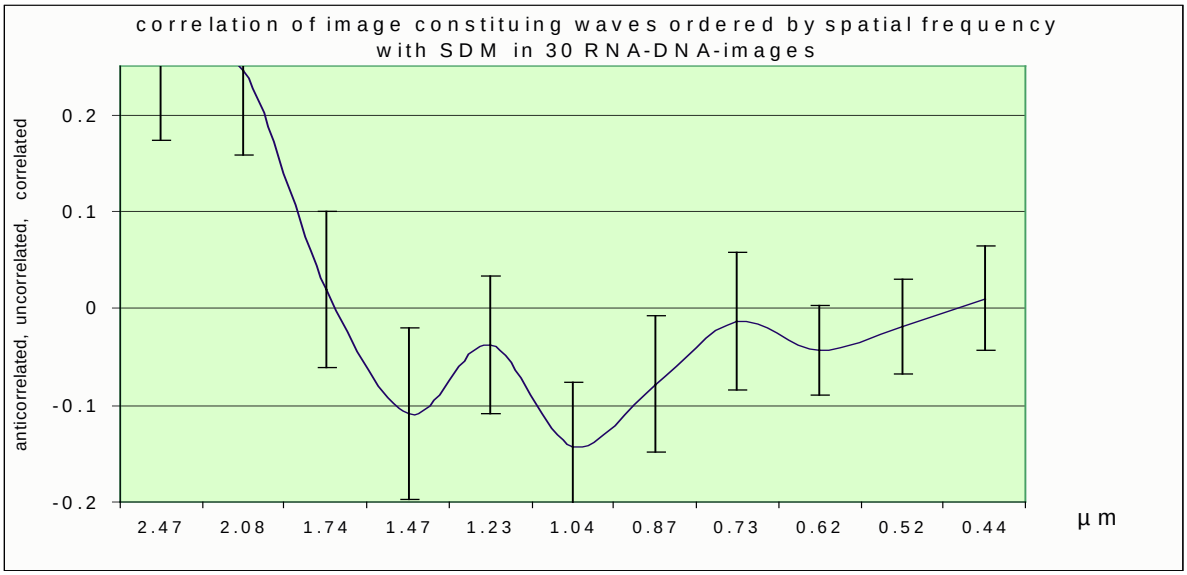

Abb.II.7.15. Besonders bei Betrachtung eines feineren Ausschnittes erkennt man die größere Varianz bei Berücksichtigung der Amplituden zu den zugehörigen Phasendifferenzen.

Die Messungen über alle 30 Kerne zeigen eine variable Antikorrelation von 0 bis –0,2 für Objektgrößen von ca. 0,5 µm Durchmesser.

II.7.2.4.4. Beweise für die Funktionstüchtigkeit der verwendeten Software

Der Beweis für das korrekte Funktionieren der angewandten Algorithmen wurde in mehreren Tests anhand simulierter Chromosomenterritorien in simulierten Zellkernen erbracht:

i) Wenn auf beiden Kanälen RNA und DNA die identischen Bilder eingegeben wurden, kam für alle Frequenzen die Korrelation +1 heraus.

ii) Wurden die beiden simulierten Bildstapel um eine Ebene gegeneinander verschoben, änderte sich die Korrelation besonders für kleine Bildwellenlängen von +1 gegen 0, siehe untenstehenden Graph:

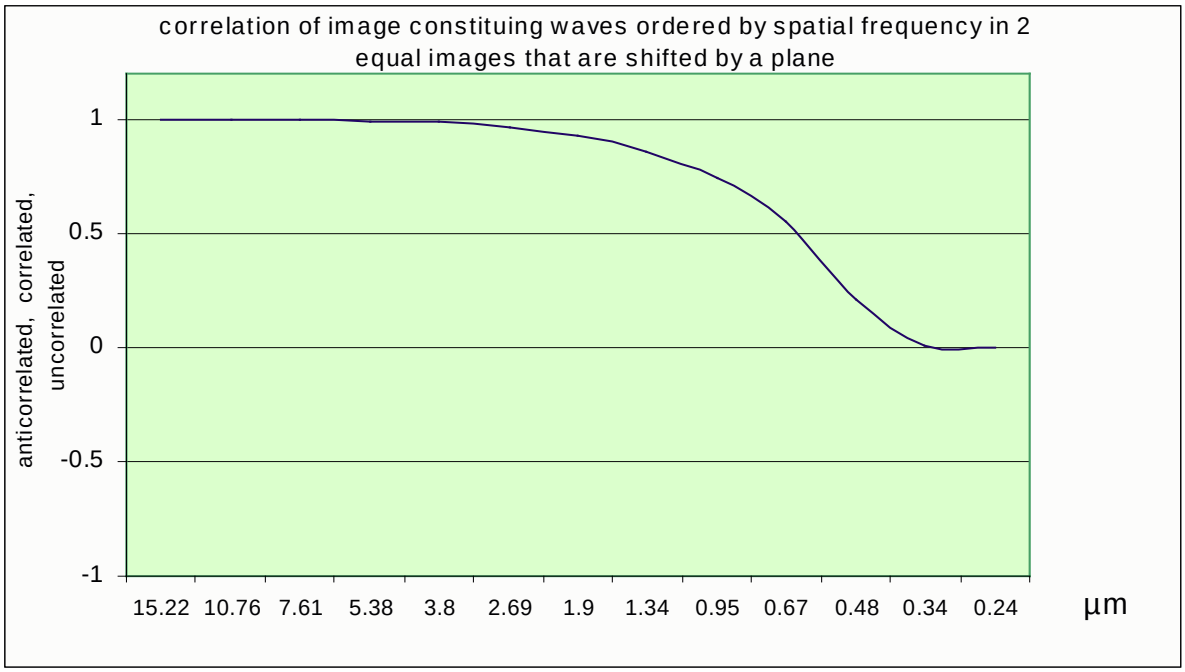

Abb.II.7.16. obiger Graph demonstriert, welche Ergebnisse die angewandten Algorithmen auf zwei simulierte, identische, jedoch um eine Ebene (entspricht 0,2µm) verschobene Bildstapel eines Kernes hervorbringen.

Dies war so zu erwarten, denn die Verschiebung um eine Ebene oder um 0,2µ ändert grosse Objekte nur zu einem kleinen Teil, kleine Objekte aber erheblich. Demnach wirkt sich der chromatische Shift auf kleine Objekte stark aus.

iii) Es wurden auf einem Kanal die ersten 23 simulierten Homologene sichtbar gemacht und im zweiten Kanal die Homologene 24 bis 46. Dabei ergab sich eine starke Antikorrelation bei 2,7µ, was Objektgrößen von 1,35µ entspricht. Da die Bilder erwartungsgemäß häufig eine Lücke neben einem Territorium aus der Hälfte der dargestellten Territorien beinhalten, kommt häufig die antikorrelierte Struktur der gemessenen Größe heraus.

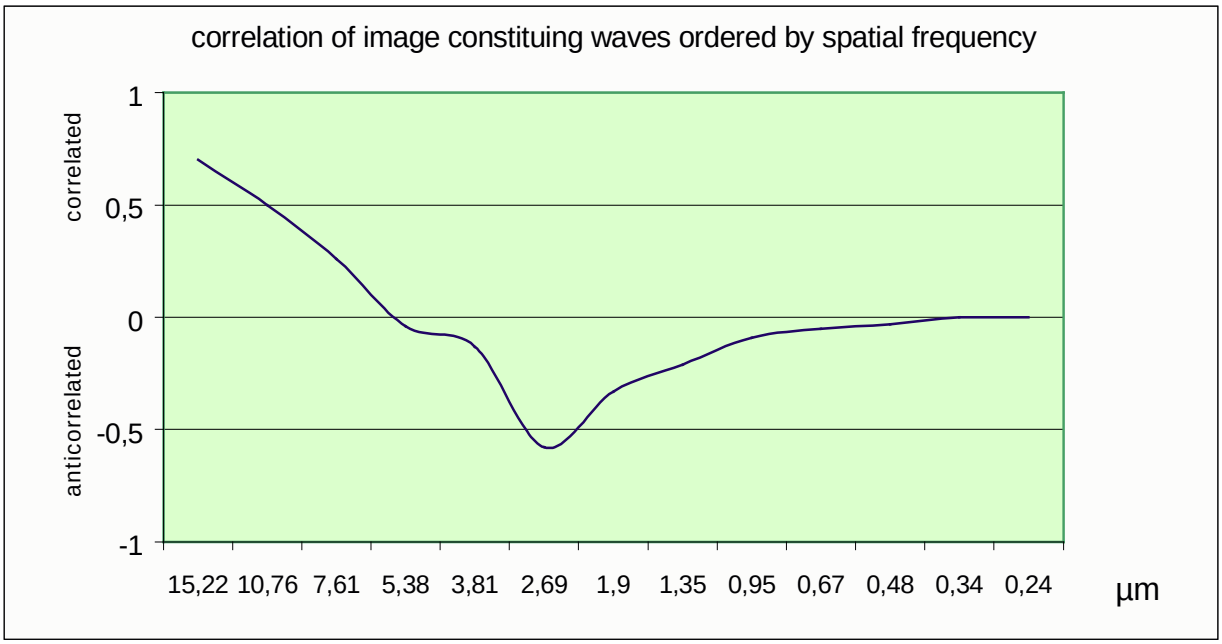

Abb.II.7.17. Wie zu erwarten ergab sich ein Korrelationsminimum bei l = 2,7µm, was Objektgrößen bzw. Lücken von 1,35µm entspricht. Da zum Argument 10,76 keine Voxel vorkamen, wurde an dieser Stelle interpoliert.

iv) Interessant war auch der fehlende Einfluss der PSF auf die Korrelationsmessungen, solange die einzelnen Korrelationen nicht mit ihrem Auftreten gewichtet wurden. Es traten selbst bei einer Gauß Glättung von 458 nm x 600 nm keine Abweichungen vom ungeglätteten Fall auf.

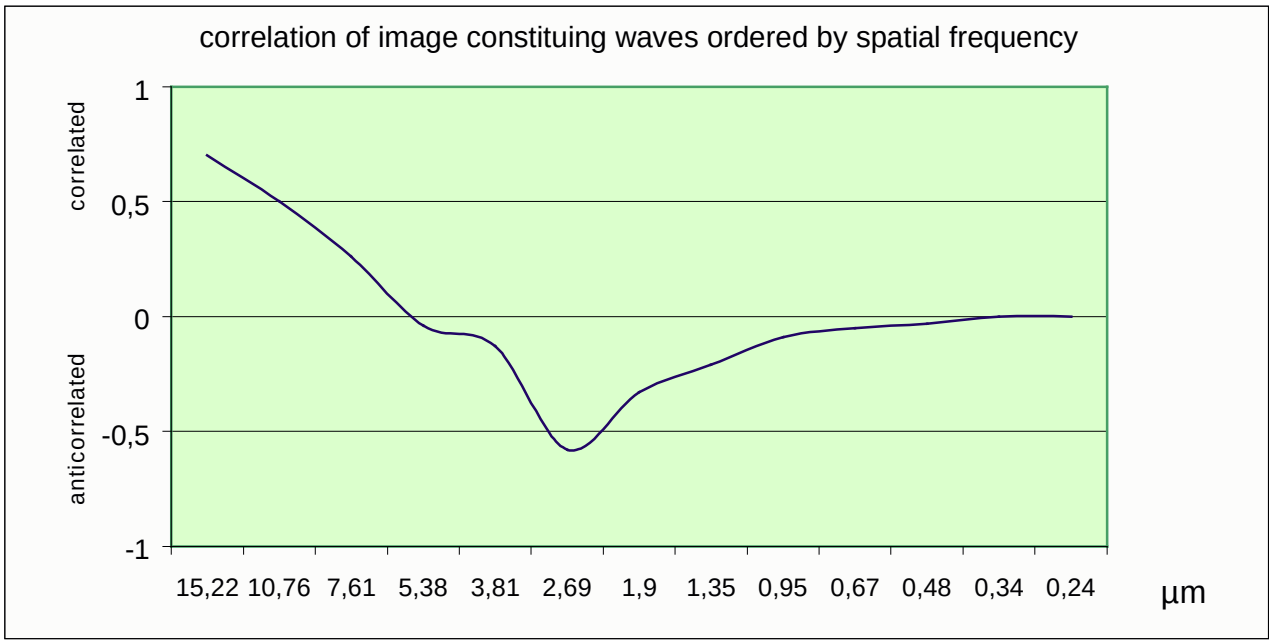

Abb.II.7.18. Obiger Graph beweist: Alle Messwerte stimmten mit denen ohne Glättung genau überein.

Das bedeutet, dass die PSF keinen Einfluss auf die Korrelationswerte nimmt, solange die einzelnen Korrelationswerte nicht mit ihrer Amplitude gewichtet wurden. Dies war so zu erwarten: denn die PSF als lineare Konvolution dämpft zwar die Amplituden, verändert aber nicht die Phasenbeziehungen die hier gemessen wurden. Allerdings dämpft der chromatische Shift Korrelationen oder Antikorrelationen von Objekten in der Größenordnung des chromatischen Shifts oder kleiner.

II.7.3. Zusammenfassende Ergebnisse der RNA-DNA Korrelations-analyse

Alle 4 Untersuchungsmethoden zusammenfassend kann man sagen, dass am inneren Kernrand viel DNA aber kaum RNA war. In den Nucleoli war wenig DNA vorhanden und noch weniger RNA. Leichte Antikorrelationen (-0,1) wurden auf dem Niveau von Größen um 0,5µm gefunden (Replikationsfoci?). Das letztgenannte Erbgebnis findet sich auch in [Verschure et al. 1999], wo die Beweislage allerdings verhältnismäßig schwach ausfiel.

III. Zusammenfassende Diskussion

In dieser Arbeit wurden die Positionen von Chromosomenterritorien (CT), deren Centromere und Telomere in verschiedenen Zellarten, Krebsarten, Spezies und verschiedenen Zell- Phasen der Interphase untersucht, wobei nicht alle diese Themen an allen Zellkernen untersucht werden konnten. Insgesamt lagen ca. 1500 Zellkerne zur Auswertung auf ca. 100 CDs vor. Die Auswertung wurde anhand verschiedener vielfach selbst entwickelter Computerprogramme getätigt, wobei die Auswertung nach interaktiver Wahl eines Parameters zur Festlegung der Schwellwerte automatisch verlief.

III.1. Vergleich verschiedener Zelltypen

III.1.1. Form der Zellkerne

Im Vergleich zwischen Fibroblasten, Lymphozyten und Neuronen muss zuerst gesagt werden, dass die Fibroblasten flach waren und daher nur lateral Raum für eine differenzierende Positionsbestimmung von großen Objekten wie CTs existierte. Daher wurde der Kern mittels einer Projektion ganz in ein 2D- Objekt verwandelt und der Kern in zum Kernrand konzentrische Ringe eingeteilt. Die Territorien lagen vor der Projektion so in der Höhe, dass sie entweder Kontakt mit der oben oder der unten gelegenen Kernmembran hatten. Die untersuchten Territorien in Fibroblasten zeigten eine Größenabhängigkeit derart, dass kleine Territorien 2D- lateral gesehen im Zellkerninneren und große Territorien am Zellkernrand lagen.

Die Lymphozyten waren nahezu kugelförmig, so dass in allen drei Koordinatenachsen Raum für eine Auswertung bestand (3D- Auswertung). Daher wurden die Lymphozyten in zur Kernhülle konzentrische Schalen eingeteilt. Die Neuronen sahen aus wie 2/3 einer Kugel und konnten ebenfalls in 3D ausgewertet werden.

III.1.2. Radiale Position der Chromosomen

Es zeigte sich, wie schon von [Boyle 2001] beschrieben, dass die gendichten Chromosomen eine zentrale Stellung und die genarmen eine periphere haben. Daher konnten die kleinen Chromosomen 18 und Y am Rand aufgefunden werden, in Abweichung zu der lateralen Stellung in Fibroblasten, wo sie in der radialen Darstellung zentral lagen. Bislang wurden Gene nur anhand ihrer Aktivität in Lymphozyten definiert. Da in Fibroblasten andere Gene aktiv sind, ist es denkbar,

dass dies der Grund für die abweichende Verteilung der beiden Zellarten Fibroblasten und Lymphozyten ist. Der Replikationszeitpunkt war ein etwas weniger zuverlässiger Parameter für die Territoriale Lage: obwohl in Fibroblasten das Chomosom Nr. 19 vor dem Chromosom Nr. 18 repliziert, ist deren Verteilung gleich [s. Bridger 2000].

In Neuronenkernen von Hühnern, die in 3D auswertbar sind und die eher taschenförmig sind, liegen die großen Territorien (1-5 & Z) außen, die mittelgroßen (6-10) ebenfalls außen und die Mikrochromosomen bei mittleren Radialwerten. Das Zentrum der Neuronenkerne wird von sehr großen Nucleoli ausgefüllt, s. [Habermann 2001]. Zusätzlich wurden auch vier Hühnerzelltypen verschiedener Entwicklungsstadien untersucht: multipotente Vorläuferzellen, Macrophagen, transformierte Monoblastenzellen und transformierte Proerythoblast Zellen. Angefärbt waren dabei die Chromosomen #1 und #8. Besonders Chromosom #1 hatte stets eine Randstellung im Kern. Chromosom #8, das kleiner ist, verteilte sich nicht immer am Rand, s. [Stadler 2002]. Ob Chromosom #8 genreicher als Chromosom #1 ist, oder welcher von beiden früher repliziert, ist nicht bekannt, kann aber aus den Verteilungsgraphen vermutet werden.

III.1.3. Formparameter von Chromosomenterritorien

Es wurden auch Formparameter von 7 Chromosomen (X aktiv und X inaktiv getrennt betrachtet) in Fibroblasten und 8 Chromosomen in Lymphozyten bestimmt. Bei den Fibroblasten sind besonders die homologen des aktiven und inaktiven X Chromosoms extremal. Als Formparameter wurde das Volumen pro Megabase, die Oberfläche pro Megabase$^{2/3}$, der Quotient aus V^2/O^3, die Smoothness und die Form des Histogramms hinzugenommen. Das Volumen betreffend fanden [Rinke 1995], [Eils 1996] und [Edelmann 96] allerdings keine nennenswerten Unterschiede (<2). Dies könnte daher rühren, dass sie für je beide Heterologen gleiche Schwellwerte gewählt haben. Dagegen wurden hier zwei individuelle Schwellwerte angewandt, wobei der Schwellwert des aktiven Homologes schon nach dem automatischen Schwellwertverfahren aber besonders nach interaktiver Prüfung regelmäßig niedriger als derjenige des inaktiven ausfiel. Die Lymphozyten erscheinen mit einer kleineren Oberfläche als die Fibroblasten. Allerdings wurden die Lymphozyten weniger schonend fixiert als die Fibroblasten. Daher könnten bei ihnen Feinstrukturen in der Oberfläche präparationsbedingt verschwunden sein.

III.2. Verteilung von Chromosomen in PC-Simulationen

Weiter wurden von Dr. Gregor Kreth PC-Simulationen von sphärischen menschlichen Zellkernen gemacht. Die radiale Lage der Territorien wurde anhand einer Wahrscheinlichkeitsfunktion, die im Exponenten das Produkt aus Radialwert und Gendichte enthält, gesetzt. An diesen Simulationen wurde erstmals die Gendichte mit der radialen Position in Verbindung gebracht derart, dass die gendichteren Chromosomen eher im Kernzentrum gesetzt wurden und die genarmen am Rand des Zellkerns, so wie es den experimentellen Lymphozyten entspricht. Auch wurden die Territorien in der Reihenfolge eingesetzt, in welcher die Chromosomen in experimentellen Kernen replizieren Mit einigen Ausnahmen, z.B. dem Chromosom #15 und #20, wurden die Chromosomen wie im Experiment in den Kern eingefügt. Man verspricht sich aus diesen nahe an den Experimenten heranreichenden simulierten Zellkernen bessere Vorhersagemöglichkeiten von beispielsweise Translokationsraten nach Doppelstrangbrüchen.

III.3. Radiale Chromosomenposition während der Evolution

Eine weitere Fragestellung war, ob die Position der Chromosomen Speziesabhängig sei oder nicht. Dazu wurden außer an dem Menschen noch an 7 weiteren Primaten mit unterschiedlicher evolutionärer Entfernung vom Menschen die Position der Chromosomen 18 und 19 untersucht, s.[Tanabe 2002]. Sie unterscheiden sich nicht wesentlich von der Verteilung im Menschen. Die kleinen Unterschiede sind dabei nicht mit der evolutionären Entfernung von bis zu 30 Millionen Jahren korreliert. Chromosomen, die Produkte einer Translokation waren, orientierten sich mit dem genreicheren Teil zur Kernmitte und mit dem genärmeren zur Kernperipherie.

Die Untersuchung von Hühnerfibroblasten und Hühnerneuronen bestätigte bei den großen, mittleren und den Mikrochromosomen das bekannte Muster beim Menschen mit den entsprechenden Chromosomen, sind aber schon seit 200-300 Millionen Jahren von der menschlichen Entwicklungslinie getrennt. Allerdings waren die Unterschiede nicht so deutlich: zum einen waren die Hühnerfibroblasten sehr schmal, und zum anderen hatten die Hühnerneuronen große Nucleoli in ihrer Mitte. Bei der Untersuchung der Formparameter konnte keine Abhängigkeit von der Spezies festgestellt werden. Jedoch war die Fixierung (Lufttrocknung und

hypertonisch angeschwollene Kerne durch Methanol Eisessig Fixierung) nicht schonend genug, um signifikante Aussagen zu treffen.

III.4. Karzinomzellen

Ein weiterer wichtiger Teil dieser Arbeit betrifft Karzinomzellen. Aus einer unendlichen Fülle von Krebssorten wurden 8 ausgewählt und an ihnen meistens die Position von Chromosom #18 und #19 geprüft. Jede Krebsart ist mit einer oder mehreren Mutationen verknüpft, aber nicht immer waren Chromosom #18 und #19 in der gleichen Weise betroffen. Wenn es Änderungen gab, war meistens Chromosom #18 statistisch verteilt. Änderungen im Karyotyp können mit FISH und konfokaler Mikroskopie deutlich sichtbar gemacht werden. So kann das homologe Chromatin eines Chromosoms in manchmal zahlreichen anderen Chromosomen gefunden werden. In so fern sind die Änderungen, die man im Mikroskop sehen kann oder histologisch erkennt, dramatischer als die Änderungen in den DNA-Verteilungsgraphen.

III.5. Position der Centromere in G0 Lymphozyten

Als chromosomale Substruktur wurden in G0 Zellen, besonders in Lymphozyten, die Verteilung der Centromere untersucht. Es stellte sich heraus, dass die Centromere in allen G0- Lymphozyten peripher liegen. Eine pancentromerische Anfärbung von Mauslymphozyten zeigte das gleiche Ergebnis. Dagegen ist die 2D Verteilung einer pancentromerischen Anfärbung in menschlichen Fibroblasten eher auf mittlere Radien konzentriert. Die Centromere liegen dabei außer beim X-Chromosom in Lymphozyten am Rand des Chromosoms, wie 3D- Rekonstruktionen zeigen. Es wurden ferner noch summarisch die Verteilungen der Telomere untersucht. In menschlichen Lymphozyten und in Fibroblasten waren sie eher auf mittlere Radien verteilt, bei den Mauslymphozyten eher am Zellkernrand. Deshalb ergibt sich folgendes Bild: In Lymphozyten sind die Chromosomen mit ihren Centromeren während der G0-Phase an der Kernhülle angeheftet. Von Ihnen erstrecken sich besonders bei den zentraleren Chromosomen die Telomerarme zum Zellkerninneren. Bei der Maus sind alle Chromosomen acrozentrisch, d.h. mit teilweise kurzen Telomerarmen ausgestattet.

III.6. Position der Centromere während des Zellzyklusses

Als Erweiterung der Untersuchung der Position der Centromere auf andere Phasen wurde die Verteilung der Kinetochoren in verschiedenen Zellstadien,

besonders in Lymphozyten untersucht. (An den Kinetochoren greifen die Mikrotubuli, welche die beiden Schwesternchromosomen für jeden zu bildenden Kern aufteilen, an.) Es wurden stets pankinetochore Anfärbungen gefertigt. Die Zellphasen wurden anhand von 3 Indikatoren bestimmt: An der Ki67 und BrdU Markierung sowie der Zellkerngröße. In G0 lagen alle Kinetochoren klar am Zellkernrand, in der S Phase waren sie noch bevorzugt am Rand, aber es war auch eine kleinere Menge in zentraleren Bereichen, vermutlich an den Oberflächen der Nucleoli. In der G1 und der G2 Phase waren die Kinetochoren noch ausgeglichener verteilt. Besonders in der G0 Phase aber auch in der S Phase wurden weniger Kinetochoren gesehen, als es der Homologenzahl entsprochen hätte. Man vermutet eine Clusterbildung verschiedener Kinetochoren. Die Untersuchung wies also auf strukturelle Umbauten in Lymphozyten während der Interphase hin. Nach [Dühring 2002] kann die gleiche Aussage auch für Fibroblasten gemacht werden.

III.7. Korrelation im Auftreten von DNA und RNA

Schließlich sei noch über die Korrelation im Auftreten von DNA und naszenter RNA gesprochen. Die Theorie des subkompartimentalisierten Zellkernes sieht außer Homologenterritorien auch Raum zwischen den Territorien vor, den ICD (Inter chromatin domain, s. [Cremer 2000, Cremer 2001b]). In diesem Raum seien verschiedene Proteine, welche die Genexpression ermöglichen. Es sollten sogar ICD- Kanäle in CTs hineinragen. Zur Überprüfung dieser Theorie wurde an lebenden Zellen die DNA mit GFP und die naszente RNA mit BrUTP markiert. Davon wurden konfokale Aufnahmen gemacht. Mit 4 Methoden wurden die Aufnahmen untersucht: erstens wurden durch Zellkernschnitte Profile von beiden Farben aufgenommen. Es sollte visuell geprüft werden, ob der Verlauf der beiden Farbkurven korreliert sei oder nicht. Nur im Bereich der Nucleoli konnte eine Korrelation festgestellt werden, weil sowohl die DNA als auch die RNA Intensität relativ gering waren. Diese Methode wurde per Software auf 3D erweitert und quantisiert und ergab die zweite Methode. Dabei ergab sich eine leichte aber signifikante Antikorrelation im Bildwellengrößenbereich von 1µm was Objekten der Größe von 500 nm entspricht. 500 nm ist die angenommene Größe der 1Mbp- Domänen. Demnach sind die 1Mbp-Domänen Nachbarn von naszenter RNA. Ein Problem bei dieser Untersuchungsmethode ist der unvermeidliche chromatische Shift. Ein Shift von 200 nm lässt korrelierte Objekte der Größe von 500 nm um 40% weniger korreliert

erscheinen lassen als sie es ohne chromatischen Shifts sind. Objekte um 200 nm würden ihre Korrelation zum Nachbarn ganz verlieren. Obwohl versucht worden war, durch verschieben der konfokalen Ebenen um 1 Ebene den chromatischen Shift zu korrigieren, blieb vermutlich immer noch chromatischer Shift übrig, da dieser nicht überall mit einer Ebene korrigiert werden kann. Die beschränkte Auflösung des Mikroskops wirkte sich dagegen anscheinend nicht negativ aus. Sicher wurden also leichte Antikorrelationen von RNA oder DNA- Objekten der Größe um 500 nm nachgewiesen. Die dritte Methode war die Ratio Methode. Dabei wird punktweise die Helligkeit des einen Farbkanals mit der des anderen dividiert. Dabei stellte sich heraus, dass am Kernrand ein besonders hoher relativer DNA Gehalt war und praktisch keine RNA. Tatsächlich ist das Chromatin am Zellkernrand dafür bekannt, dass es besonders konzentriert vorliegt und weitgehend inaktiv ist (an der Synthese der RNA wenig beteiligt). Als vierte Methode wurde die ratio- Methode quantisiert. Dabei konnten die Helligkeitsquotienten nur den Wert 1 oder -1 erhalten und es wurde über den ganzen Kern summiert. Im Rahmen der statistischen Genauigkeit wurde Unkorreliertheit gemessen. Die Ergebnisse sprechen eher gegen ein extremes ICD-Modell, bei dem die Transkription nur am Rande von kartoffelförmigen, „glatten“ CTs erfolgt. Nach einem solchen extremen Modell ihm wäre bereits bei konfokaler optischer Auflösung eine örtliche Aufteilung von RNA und DNA in distinkte Regionen zu erwarten gewesen. Dies war aber kaum der Fall. Die alternative ist ein Interphasen Zellkernmodell, wie es z.B. in [Cremer & Cremer 2001] beschrieben ist.

III.8. Ausblick

Der Mechanismus, welcher die Position der CTs und Teile davon festlegt, ist völlig unbekannt. Es könnte sich z.B. um ein Netz von Filamenten handeln, um eine Anheftung an der Kernmembran oder um eine Kraft, die mit der Transkription einhergeht. Biophysikalische Experimente könnten dank einer Markierung und einer laseroptischen Falle die Kraft bestimmen, die notwendig ist, die Territorien oder andere subnucleare Gebilde radial und lateral von ihren Plätzen zu bewegen. Weiter könnte bestimmt werden, ob diese Kraft abbricht oder nicht. Hat man ein bestimmtes Protein als Bindeprotein in Verdacht, etwa anhand einer veränderten Kernstruktur bei gleichzeitigem Mangel oder Überschuß dieses Proteins, könnte dieser an normalen Zellen mit biochemischen Mitteln manipuliert werden, um eine eventuell veränderte Kernstruktur nachzuweisen.

Neuere Nanoskopieverfahren (4 Pi Nanoskopie) mit besserer Auflösung bei weniger chromatischen Shift, und Anfärbetechniken, die auch in Lymphozyten die Form der Kernstrukturen besser bewahren, oder sogar spezifische in vivo Markierungen (Tripelhelicale Hybridisierungen) könnten die Erforschung der Chromosomen-territorien, des Nucleolus oder sogar der 1Mbp-Chromatindomänen weiter voranbringen.

IV. Literatur

IV.1.Artikel

Artikel, die für den Ergebnisteil besonders wichtig sind, sind unterstrichen.

Alcobia I, Dilao R, Parreira L (2000) Spatial associations of centromeres in the nuclei of hematopoietic cells: evidence for cell-type-specific organizational patterns. Blood 95: 1608-15.

Allison DC, Nestor AL (1999) Evidence for a relatively random array of human chromosomes on the mitotic ring. J Cell Biol 145: 1-14.

Bajer AS, Molé-Bajer J. (1972) Spindle dynamics and chromosome movements. In International review of cytology (Edited by Bourne G. H. and Danielli J. F.). Academic press, New York & London.

A.S. Belmont, S. Dietzel, A.C. Nye, Y.G. Strukov, T. Tumbar “Large-scale chromatin structure and function”, Current Opinion in Cell Biology, 11, pp 307-311, 1999

Bolzer A, Craig JM, Cremer T, Speicher MR (1999) A complete set of repeat-depleted, PCR-amplifiable, human chromosome- specific painting probes. Cytogenet. Cell Genet. 84: 233-40.

Boyle S, Gilchrist S, Bridger JM, Mahy NL, Ellis JA, Bickmore WA (2001) The spatial organization of human chromosomes within the nuclei of normal and emerin-mutant cells. Hum Mol Genet 10: 211-219.

Bridger JM, Boyle S, Kill IR, Bickmore WA (2000) Re-modelling of nuclear architecture in quiescent and senescent human fibroblasts. Curr Biol 10: 149-52.

Burt DW, Bruley C, Dunn IC et al. (1999) The dynamics of chromosome evolution in birds and mammals. Nature 402: 411-3.

Chaly N, Brown DL (1988) The prometaphase configuration and chromosome order in early mitosis. J Cell Sci 91: 325-35.

Chandley AC, Speed RM, Leitch AR (1996) Different distributions of homologous chromosomes in adult human Sertoli cells and in lymphocytes signify nuclear differentiation. J Cell Sci 109: 773-6.

Comings DE (1968) The rationale for an ordered arrangement of chromatin in the interphase nucleus. Am. J. Hum. Genet. 20: 440-60.

Comings DE (1980) Arrangement of chromatin in the nucleus. Hum. Genet. 53: 131-43.

Cooke HJ, Hindley J (1979) Cloning of human satellite III DNA: different components are on different chromosomes. Nucleic Acids Res 6: 3177-97.

Cooke HJ, Schmidtke J, Gosden JR (1982) Characterisation of a human Y chromosome repeated sequence and related sequences in higher primates. Chromosoma 87: 491-502.

Craig JM, Bickmore WA (1994) The distribution of CpG islands in mammalian chromosomes [see comments] [published erratum appears in Nat Genet 1994 Aug;7(4):551]. Nat Genet 7: 376-82.

Craig JM, Kraus J, Cremer T (1997) Removal of repetitive sequences from FISH probes using PCR-assisted affinity chromatography. Hum Genet 100: 472-6.

Cremer C, Cremer T, Gray JW (1982a) Induction of chromosome damage by ultraviolet light and caffeine: correlation of cytogenetic evaluation and flow karyotype. Cytometry 2: 287-90.

Cremer T, Baumann H, Nakanishi K, Cremer C (1984) Correlation between interphase and metaphase chromosome arrangements as studied by laser-uv-microbeam experiments. Chromosomes Today 8: 203-212.

Cremer T, Cremer C, Schneider T, Baumann H, Hens L, Kirsch-Volders M (1982b) Analysis of chromosome positions in the interphase nucleus of Chinese hamster cells by laser-UV-microirradiation experiments. Hum. Genet. 62: 201-9.

Cremer M, v. Hase J, Volm T et al. (2001a) General and cell type specific higher order chromatin arrangements in nuclei of diploid human cells. Chromosome Research 9, pp 541-567, 2001.

Cremer T, Cremer C (2001b) Chromosome Territories, Nuclear Architecture and Gene Regulation in Mammalian Cells. Nat Rev Genet 2: 292-301.

Cremer T, Kreth G, Koester H et al. (2000) Chromosome territories, interchromatin domain compartment, and nuclear matrix: an integrated view of the functional nuclear architecture. Critical Reviews in Eukaryotic Gene Expression 12: 179-212.

Cremer T, Kurz A, Zirbel R et al. (1993) Role of chromosome territories in the functional compartmentalization of the cell nucleus. Cold Spring Harb. Symp. Quant. Biol. 58: 777-92.

Cremer T, Landegent J, Bruckner A et al. (1986) Detection of chromosome aberrations in the human interphase nucleus by visualization of specific target

DNAs with radioactive and non- radioactive in situ hybridization techniques: diagnosis of trisomy 18 with probe L1.84. Hum. Genet. 74: 346-52.

Croft JA, Bridger JM, Boyle S, Perry P, Teague P, Bickmore WA (1999) Differences in the localization and morphology of chromosomes in the human nucleus. J. Cell Biol. 145: 1119-31.

Deloukas P, Schuler GD, Gyapay G et al. (1998) A physical map of 30,000 human genes. Science 282: 744-6.

Devilee P, Cremer T, Slagboom P et al. (1986) Two subsets of human alphoid repetitive DNA show distinct preferential localization in the pericentric regions of chromosomes 13, 18, and 21. Cytogenet Cell Genet 41: 193-201.

Dietzel S, Weilandt E, Eils R, Münkel C, Cremer C, Cremer T (1995) Three-dimensional distribution of centromeric or paracentromeric heterochromatin of chromosomes 1, 7, 15 and 17 in human lymphocyte nuclei studied with light microscopic axial tomography. Bioimaging 3: 121-133.

Dunham I, Lengauer C, Cremer T, Featherstone T (1992) Rapid generation of chromosome-specific alphoid DNA probes using the polymerase chain reaction. Hum Genet 88: 457-62.

Eils R, Dietzel S, Bertin E, Granzow M, Cremer C, Cremer T (1996): Three dimensional reconstruction of painted human interphase chromosomes: active and inactive X-chromosome territories have similar volumes but differ in shape and surface structur. J.of Cell Biology, 135: 1427-1440

Emmerich P, Loos P, Jauch A et al. (1989) Double in situ hybridization in combination with digital image analysis: a new approach to study interphase chromosome topography. Exp. Cell Res. 181: 126-40.

Ferguson M, Ward DC (1992) Cell cycle dependent chromosomal movement in pre-mitotic human T- lymphocyte nuclei. Chromosoma 101: 557-65.

Ferreira J, Paolella G, Ramos C, Lamond AI (1997) Spatial organization of large-scale chromatin domains in the nucleus: a magnified view of single chromosome territories. J Cell Biol 139: 1597-610.

Griffin DK, Habermann F, Masabanda J et al. (1999) Micro- and macrochromosome paints generated by flow cytometry and microdissection: tools for mapping the chicken genome. Cytogenet Cell Genet 87: 278-81.

Habermann F.A, M. Cremer, J. Walter , J.v. Hase, K.Bauer, J.Wienberg, C.Cremer, T.Cremer. "Arrangements of macro- and microchromosomes in chicken cells",

Chrom. Res. 9, pp 569-584, 2001.

Hager HD, Schroeder-Kurth TM, Vogel F (1982) Position of chromosomes in the human interphase nucleus. An analysis of nonhomologous chromatid translocations in lymphocyte cultures after Trenimon treatment and from patients with Fanconi's anemia and Bloom's syndrome. Hum Genet 61: 342-56.

Hartung J. (1991) Statistik, München, Wien.

Hedges SB, Parker PH, Sibley CG, Kumar S (1996) Continental break-up and the ordinal diversification of birds and mammals. Nature 381: 226-9.

Hens L, Kirsch-Volders M, Verschaeve L, Susanne C (1982) The central localization of the small and early replicating chromosomes in human diploid metaphase figures. Hum Genet 60: 249-56.

Higgins MJ, Wang HS, Shtromas I et al. (1985) Organization of a repetitive human 1.8 kb KpnI sequence localized in the heterochromatin of chromosome 15. Chromosoma 93: 77-86.

Höfers C, Baumann P, Hummer G, Jovin T, Arndt-Jovin D (1993) The localization of chromosome domains in human interphase nuclei. Three-dimensional distance determinations of fluorescence in situ hybridization signals from confocal laser scanning microscopy. Bioimaging 1: 96-106.

Hulsebos T, Schonk D, van Dalen I et al. (1988) Isolation and characterization of alphoid DNA sequences specific for the pericentric regions of chromosomes 4, 5, 9, and 19. Cytogenet Cell Genet 47: 144-8.

Knuth DE. (1981) The art of computer programming. Addison, Reading UK.

Koutna I, Kozubek S, Zaloudik J et al. (2000) Topography of genetic loci in tissue samples: towards new diagnostic tool using interphase FISH and high-resolution image analysis techniques. Anal Cell Pathol 20: 173-85.

Kreth, P. Edelmann, Ch. Münkel et al. "Translocation frequencies for X and Y chromosomes predicted by computer simulations of nuclear structure", Some Aspects of Chromosome Structure and Functions, Edts. R.C. Sobti, G. Obe, R.S. Athwal, pp 57-71, 2002.

Lander ES, Linton LM, Birren B et al. (2001) Initial sequencing and analysis of the human genome. International Human Genome Sequencing Consortium. Nature 409: 860-921.

Leitch AR (2000) Higher levels of organization in the interphase nucleus of cycling and differentiated cells. Microbiol Mol Biol Rev 64: 138-52.

Leitch AR, Brown JK, Mosgoller W, Schwarzacher T, Heslop-Harrison JS (1994) The spatial localization of homologous chromosomes in human fibroblasts at mitosis. Hum. Genet. 93: 275-80.

Leonhardt H, Rahn HP, Weinzierl P et al. (2000) Dynamics of DNA replication factories in living cells. J. Cell Biol. 149: 271-80.

Lesko SA, Callahan DE, LaVilla ME, Wang ZP, Ts'o PO (1995) The experimental homologous and heterologous separation distance histograms for the centromeres of chromosomes 7, 11, and 17 in interphase human T-lymphocytes. Exp. Cell Res. 219: 499-506.

McQueen HA, Fantes J, Cross SH, Clark VH, Archibald AL, Bird AP (1996) CpG islands of chicken are concentrated on microchromosomes. Nat Genet 12: 321-4.

McQueen HA, Siriaco G, Bird AP (1998) Chicken microchromosomes are hyperacetylated, early replicating, and gene rich. Genome Res 8: 621-30.

Manuelidis L (1985) Individual interphase chromosome domains revealed by in situ hybridization. Hum. Genet. 71: 288-93.

Manuelidis L (1990) A view of interphase chromosomes. Science 250: 1533-1540.

Marsden MPF & Laemmli UK (1979) Metaphase chromosome structure: evidence for a radial loop model, Cell, 17, 849-858.

Metropolis N, Rosenbluth AW, Rosenbluth MN, Teller AH, Teller E (1953) Equation of state calculations by fast computing machines. J. Chem. Phys. 21: 1087-1092.

Morton NE (1991) Parameters of the human genome. Proc. Natl. Acad. Sci. USA 88: 7474-6.

Mosgoller W, Leitch AR, Brown JK, Heslop-Harrison JS (1991) Chromosome arrangements in human fibroblasts at mitosis. Hum. Genet. 88: 27-33.

Moyzis RK, Albright KL, Bartholdi MF et al. (1987) Human chromosome-specific repetitive DNA sequences: novel markers for genetic analysis. Chromosoma 95: 375-86.

Münkel C, Eils R, Imhoff J, Dietzel S, Cremer C, Cremer T (1995) Simulation of the distribution of chromosome targets in cell nuclei under topological constraints. Bioimaging 3: 108-120.

Münkel C & Langowsky J, (1998) Chromosome structure predicted by a polymer model. Phys. Rev. E, 57, 5888-5896.

Nagele R, Freeman T, McMorrow L, Lee HY (1995) Precise spatial positioning of chromosomes during prometaphase: evidence for chromosomal order. Science 270: 1831-5.

Nagele RG, Freeman T, Fazekas J, Lee KM, Thomson Z, Lee HY (1998) Chromosome spatial order in human cells: evidence for early origin and faithful propagation. Chromosoma 107: 330-8.

Nagele RG, Freeman T, McMorrow L, Thomson Z, Kitson-Wind K, Lee H (1999) Chromosomes exhibit preferential positioning in nuclei of quiescent human cells. J Cell Sci 112: 525-35.

Nikiforova MN, Stringer JR, Blough R, Medvedovic M, Fagin JA, Nikiforov YE (2000) Proximity of chromosomal loci that participate in radiation-induced rearrangements in human cells [In Process Citation]. Science 290: 138-41.

O'Brien SJ, Menotti-Raymond M, Murphy WJ et al. (1999) The promise of comparative genomics in mammals. Science 286: 458-62, 479-81.

Ochs BA, Franke WW, Moll R, Grund C, Cremer M, Cremer T (1983) Epithelial character and morphologic diversity of cell cultures from human amniotic fluids examined by immunofluorescence microscopy and gel electrophoresis of cytoskeletal proteins. Differentiation 24: 153-73.

O'Keefe RT, Henderson SC, Spector DL (1992) Dynamic organization of DNA replication in mammalian cell nuclei: spatially and temporally defined replication of chromosome-specific alpha-satellite DNA sequences. J. Cell Biol. 116: 1095-110.

Östergren G (1945) Transverse equilibria on the spindle. Bot. Nat. 4: 467-468.

Pearson PL, Bobrow M, Vosa CG (1970) Technique for identifying Y chromosomes in human interphase nuclei. Nature 226: 78-80.

Pettmann B, Louis JC, Sensenbrenner M (1979) Morphological and biochemical maturation of neurones cultured in the absence of glial cells. Nature 281: 378-80.

Pichugin A.M., Galkina S.A., Potekhin A.A., Punina E.O., Rautian M.S., A.V. R (2001) The detection of the size of a smallest chicken (Gallus gallus domesticus) microchromosome by pulsed-field gel electrophoresis (PFGE). Genetika (Russ.) 37: 1-4.

Ponce de Leon FA, Li Y, Weng Z (1992) Early and late replicative chromosomal banding patterns of Gallus domesticus. J Hered 83: 36-42.

Popp S, Scholl HP, Loos P et al. (1990) Distribution of chromosome 18 and X centric heterochromatin in the interphase nucleus of cultured human cells. Exp Cell Res 189: 1-12.

Primmer CR, Raudsepp T, Chowdhary BP, Moller AP, Ellegren H (1997) Low frequency of microsatellites in the avian genome. Genome Res 7: 471-482.

Pyrpasopoulou A, Meier J, Maison C, Simos G, Georgatos SD (1996) The lamin B receptor (LBR) provides essential chromatin docking sites at the nuclear envelope. Embo J 15: 7108-19.

Rappold GA, Cremer T, Hager HD, Davies KE, Muller CR, Yang T (1984) Sex chromosome positions in human interphase nuclei as studied by in situ hybridization with chromosome specific DNA probes. Hum. Genet. 67: 317-25.

Rattner JB & Linn CC, (1985) Radial loops and helical coils coexist in metaphase chromosomes, Cell, 42, 291-296.

Rice JC, Allis CD (2001) Histone methylation versus histone acetylation: new insights into epigenetic regulation. Curr Opin Cell Biol 13: 263-73.

Rieder CL, Salmon ED (1994) Motile kinetochores and polar ejection forces dictate chromosome position on the vertebrate mitotic spindle. J Cell Biol 124: 223-33.

Rinke B, (1995): Volume ratios of painted chromosome territories 5, 7, X in female human cell nuclei studied with confocal laser scanning microscopy and the Cavalieri estimator.; Bioimaging 3;1-11

Rocchi M, Miller DA, Miller OJ, Baldini A (1989) Human alpha-DNA clone specific for chromosome 12. Cytogenet cell Genet 51: 1067.

Sadoni N, Langer S, Fauth C et al. (1999) Nuclear organization of mammalian genomes. Polar chromosome territories build up functionally distinct higher order compartments. J Cell Biol 146: 1211-26.

Sadoni N, Sullivan KF, Weinzierl P, Stelzer EH, Zink D (2001) Large-scale chromatin fibers of living cells display a discontinuous functional organization. Chromosoma 110: 39-51.

Schardin M, Cremer T, Hager HD, Lang M (1985) Specific staining of human chromosomes in Chinese hamster x man hybrid cell lines demonstrates interphase chromosome territories. Hum Genet 71: 281-7.

Schermelleh L, Solovei I, Zink D, Cremer T (2001) Two-colour fluorescence labelling of early and mid-to-late replicating chromatin in living cells. Chromosome Res. 9: 77-80.

Schermelleh L, Thalhammer S, Heckl W et al. (1999) Laser microdissection and laser pressure catapulting for the generation of chromosome-specific paint probes. Biotechniques 27: 362-7.

Schmid M, Enderle E, Schindler D, Schempp W (1989) Chromosome banding and DNA replication patterns in bird karyotypes. Cytogenet Cell Genet 52: 139-46.

Schwarzacher H. (1976) Chromosomes in mitosis and interphase. Springer, Berlin, Heidelberg, New York.

Skalnikova M, Kozubek S, Lukasova E et al. (2000) Spatial arrangement of genes, centromeres and chromosomes in human blood cell nuclei and its changes during the cell cycle, differentiation and after irradiation. Chromosome Res 8: 487-99.

Smith J, Bruley CK, Paton IR et al. (2000) Differences in gene density on chicken macrochromosomes and microchromosomes. Anim Genet 31: 96-103.

Smith J, Burt DW (1998) Parameters of the chicken genome (Gallus gallus). Anim Genet 29: 290-4.

Solovei I, Walter J, Cremer M, Habermann F, Schermelleh L, Cremer T. (2001 in press) FISH on three-dimensionally preserved nuclei. In FISH: a practical approach (Edited by Squire J., Beatty B. and Mai S.). Oxford University Press, Oxford.

Spaeter M (1975) [Non-random position of homologous chromosomes (no. 9 and YY) in interphase nuclei of human fibroblasts (author's transl)]. Humangenetik 27: 111-8.

Sun HB, Shen J, Yokota H (2000) Size-dependent positioning of human chromosomes in interphase nuclei. Biophys J 79: 184-90.

Sun HB, Yokota H (1999) Correlated positioning of homologous chromosomes in daughter fibroblast cells. Chromosome Res 7: 603-10.

Tanabe H, Müller S, Neusser M, Hase J.v, Calcagno E, Cremer M, Solovei I, Cremer C. Cremer T.(2002): “Evolutionary conservation of chromosome territory arrangements in cell nuclei from higher primates” In Proceedings of National Academy of Sciences, Vol 99 No 7 pp. 4424-4429, 2002.

Telenius H, Pelmear AH, Tunnacliffe A et al. (1992) Cytogenetic analysis by chromosome painting using DOP-PCR amplified flow-sorted chromosomes. Genes Chromosomes Cancer 4: 257-63.

Verschure P J, van der Kraan I, Manders E. M.M., van Driel R. (1999) Spatial Relationship between Transcription Sites and Chromosome Territories Journal of Cell Biology, Vol 147, No1

Visser A.E., F. Jaunin, S. Fakan, J.A. Aten " High resolution analysis of interpase chromosome domains", J. of cell Science, 113, pp 2585-2593, 2000

Vogel F, Schroeder TM (1974) The internal order of the interphase nucleus. Humangenetik 25: 265-97.

Vourc'h C, Taruscio D, Boyle AL, Ward DC (1993) Cell cycle-dependent distribution of telomeres, centromeres, and chromosome-specific subsatellite domains in the interphase nucleus of mouse lymphocytes. Exp Cell Res 205: 142-51.

Wade PA (2001) Methyl CpG binding proteins: coupling chromatin architecture to gene regulation. Oncogene 20: 3166-73.

Waye JS, England SB, Willard HF (1987) Genomic organization of alpha satellite DNA on human chromosome 7: evidence for two distinct alphoid domains on a single chromosome. Mol Cell Biol 7: 349-56.

White MJ. (1961) The chromosomes. In Methuen`monographs on biological subjects (Edited by Ltd. M. a. C.).

Willard HF, Waye JS (1987) Chromosome-specific subsets of human alpha satellite DNA: Analysis of sequence divergence within and between chromosomal subsets and evidence for an ancestral pentameric repeat. L Mol Evol 25: 207-214.

Willard HF, Waye JS, Skolnick MH, Schwartz CE, Powers VE, England SB (1986) REstriction length polymorphisms at the centromeres of human chromosomes using chromosome specific alpha satellite DNA. Proc Natl Acad Sci U S A 83: 5611_5615.

Wollenberg C, Kiefaber MP, Zang KD (1982a) Quantitative studies on the arrangement of human metaphase chromosomes. IX. Arrangement of chromosomes with and without spindle apparatus. Hum Genet 62: 310-5.

Zink D, Cremer T, Saffrich R et al. (1998) Structure and dynamics of human interphase chromosome territories in vivo. Hum Genet 102: 241-51.

IV.2. Dissertationen und Diplomarbeiten

Bolzer A (2002): Analyse der Chromosomenverteilung in menschlichen Fibroblasten mittels 3D-Vielfarbenfluoreszens in situ Hybridisierung.(Dissertation)

Brero, A. (1999): Größenabhängige Verteilung von Chromosomenterritorien in menschlichen Fibroblasten, Diploma thesis, faculty of Biology at the Ludwig- Maximilians-Universität München

Calcagno, V. (2001): Quantitative Bildanalyse von Zellkernen: Radiale Position und Morphologie spezifischer Chromosomenterritorien

Dühring K. (2002): Verteilung von Centromeren in Zellkernen verschiedener humaner Zelltypen im Verlauf des Zellzyklus, Diploma thesis, faculty of Biology at the Ludwig Maximilians-Universität München

Edelmann P. (1996): Dreidimensionale Bildverarbeitung zur Rekonstruktion der Morphologie von Interphase-Chromosomen aus Daten der konfokalen Laser-Scanning-Mikroskopie, Diploma thesis, faculty of Biology at the Ruprecht-Karls-Universität Heidelberg

Habermann F (2000): Untersuchungen zur Anordnung von Makro und Mikrochromosomen im Zellkern embryonaler Fibroblasten und Neuronen von Gallus Domesticus, Dissertation Ludwig-Maximilians-University

Hase, J.v. (1999): Quantitative Bildanalyse der DNA-Verteilung spezifischer Chromosomenterritorien im Zellkern, Diploma thesis Ruprecht-Karls-University Heidelberg

Knoch, T.A.(2002): Dissertation, Ruprecht Karls Universität Heidelberg

Kreth, G. (1997): Diploma Thesis, Ruprecht Karls Universität Heidelberg

Kreth, G. (2001): Simulation von Chromosomenterritorien und virtuelle Mikroskopie, Dissertation, Ruprecht-Karls-University Heidelberg

Krug, R. (1999): Digitale Bildanalyse der 3D-Chromatinstruktur in menschlichen Zellkernen: Volumengetreue Segmentierung von Replicationsfoci in experimentellen und simulierten konfokalen Datensätzen, Diploma thesis Ruprecht Karls University Heidelberg

Weierich, C. 2002: Untersuchung zur räumlichen Beziehung von Zentromeren und Chromosomenterritorien in Zellkernen humaner Lymphozyten, Diploma thesis, faculty of Biology at the Ludwig Maximilians-Universität München

Wizelman, L. (2002): Untersuchungen zur räumlichen Anordnung von Chomosomen-territorien mit hoher und niedriger Gendichte in Tumorzellen, Diploma thesis, faculty of Biology at the Ludwig Maximilians-Universität München

IV.3. Lehrbücher

Alberts B. Bray D. Johnson A. Lewis J. Raff M. Roberts K. Walter P. (1999): Lehrbuch der Molekularen Zellbiologie

Czihak G., Langer H. Ziegler H (1981): Biologie, ein Lehrbuch

Macgregor H, Varley J. (1988) Working with animal chromosomes. 2nd edition. John Wiley & Sons.

Wolfe, Stephen L.(1993): Molecular and cellular biology

V. Danksagung

Bedanken möchte ich mich bei allen sehr herzlich, die am Zustandekommen meiner Doktorarbeit beigetragen haben.

Mein herzlicher Dank gilt vor allem Prof. Dr. Dr. Christoph Cremer, der die vorliegende Untersuchung als Dissertation annahm und diese während des Entstehens mit weiterführenden Hinweisen begleitete und bereicherte.

Dank schulde ich auch den Mitarbeitern der Arbeitsgruppe Angewandte Physik am Kirchoff Institut für Physik der Universität Heidelberg, Dipl. Phys. Vincenzo Calcagno und Stefan Stein.

Dankbar erwähne ich auch die Hilfestellung, die mir von seiten von Dr. Gregor Kreth sowie von Dipl. Ing. Heinz Eipel, Florian Staier, Dr. Benno Albrecht, Dr. Dott. Antonio-Virgilio Failla, Dipl. Phys. Andreas Schweitzer, Dipl. Phys. Udo Spöri, Dipl. Biol. Georg-Lars Hildenbrand, Dipl. Phys. Christian Wagner, Dipl. Phys. Nick Kepper und Priv. Dozent Dr. M. Hausmann zuteil wurde. Wichtige Bildbearbeitungstools stammen von Peter Edelmann, Rainer Heintzmann und Boris Schädler.

Sehr zu danken habe ich auch der Forschungsgruppe unter Leitung von Prof. Dr. Thomas Cremer vom Institut für Anthropologie und Humangenetik der Universität München. Ihre biologischen Experimente bestimmten, was ich auswerten konnte.

Zellen gezüchtet und aufgenommen haben für meine Untersuchung Frau Dr. Marion Cremer, Dipl. Phys. Alessandro Brero, Dr. Irina Solovei, Dr. Felix Habermann, Dipl. Biol. Monika Hofbauer, Dr. Hideyuki Tanabe, Dipl. Biol. Christine Ahrens, Dipl. Biol. Klaus Dühring, Dipl. Biol. Claudia Weierich, Dipl. Biol. Leah Wizelman, Dipl. Biol. Sonja Stadler, Dipl. Biol. Katrin Küpper und Dipl. Biol. Babett Wagler. Wichtige Hinweise für die Entwicklung der in meiner Arbeit verfolgten Fragestellung verdanke ich Prof. Dr. Thomas Cremer.

Finanziell wurde ich von der Europäischen Union, dem Land Baden Württemberg und der VW- Stiftung gefördert, was ich hier ebenfalls dankbar erwähnen möchte.

Herzlich danke ich auch meinen Eltern und meinen Geschwistern für die Anteilnahme und menschliche Unterstützung während der Vorbereitungszeit vorliegender Dissertation.

Erklärung

Ich versichere hiermit, dass ich die vorgelegte Dissertation selbst verfasst und mich keiner anderen als der von mir ausdrücklich bezeichneten Quellen und Hilfen bedient habe.

(Johann von Hase)

Heidelberg, 14.10.02

Appendix

Comparison fibroblast-lymphocytes

P.3,4: In the following an accumulative presentation graph is shown. The left site indicate inner territories and graphs, the right site outer territories

P.4: In the right diagram the radial expectation values of each territory is reported with the respect standard deviation

Distribution of territorial gravity centers in fibroblast nuclei I

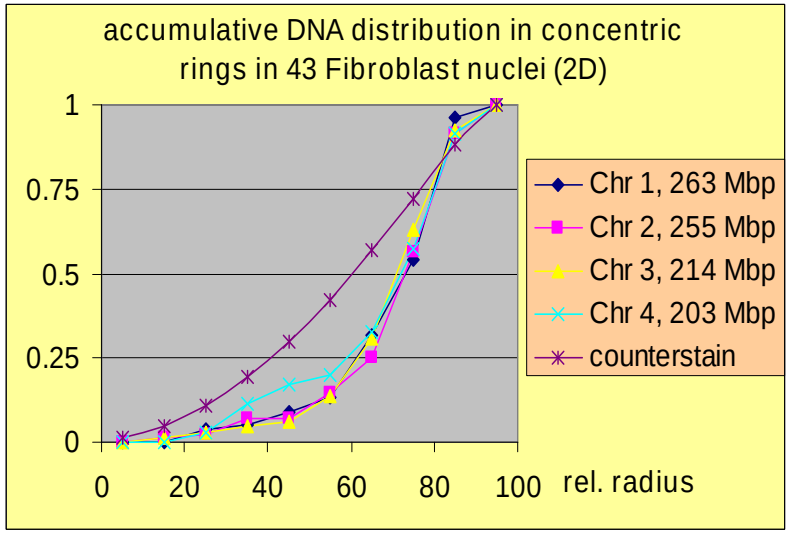

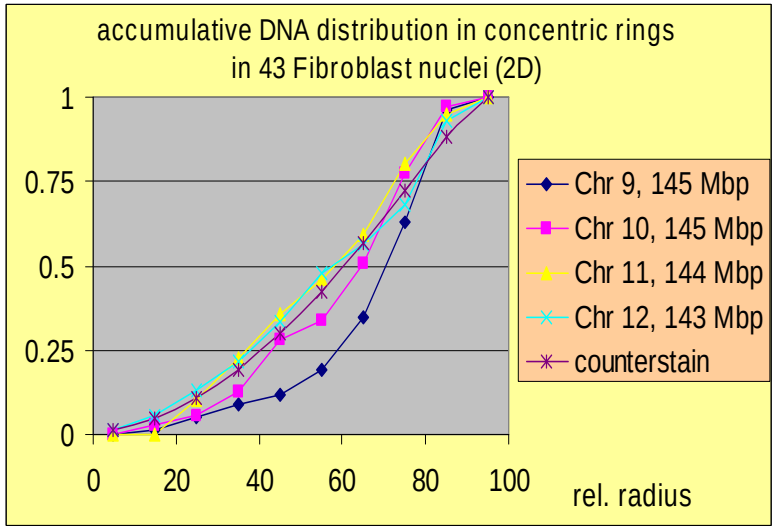

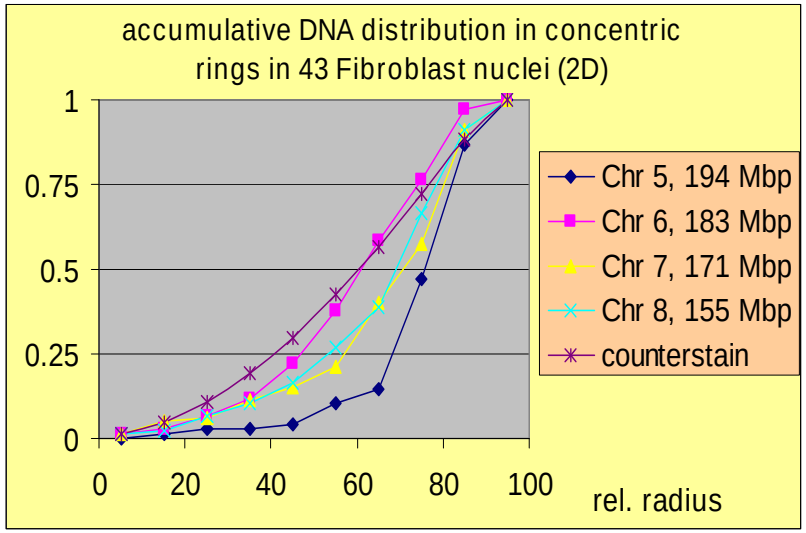

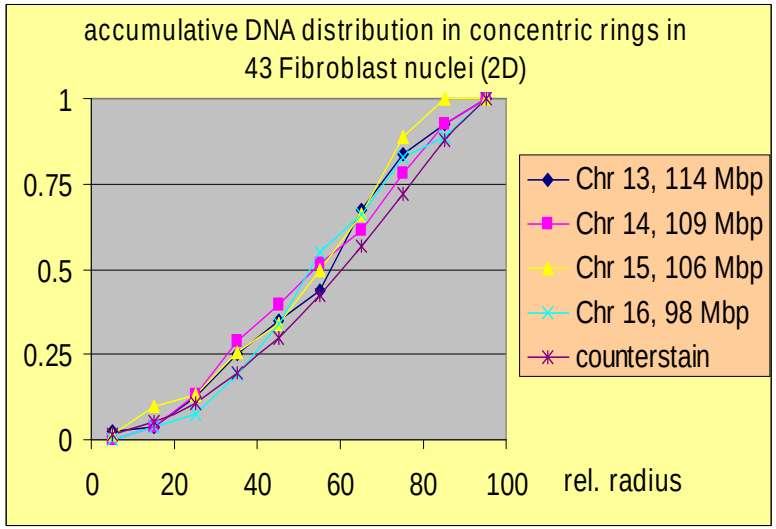

Distribution of territorial gravity centers in fibroblast nuclei II

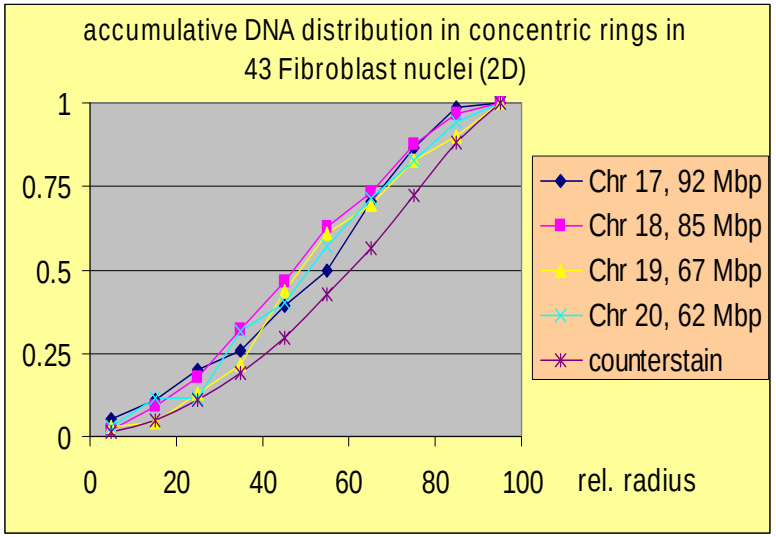

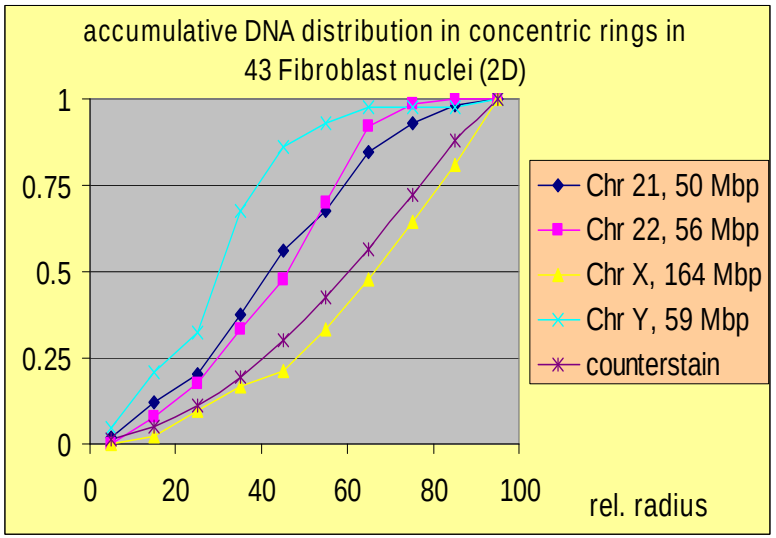

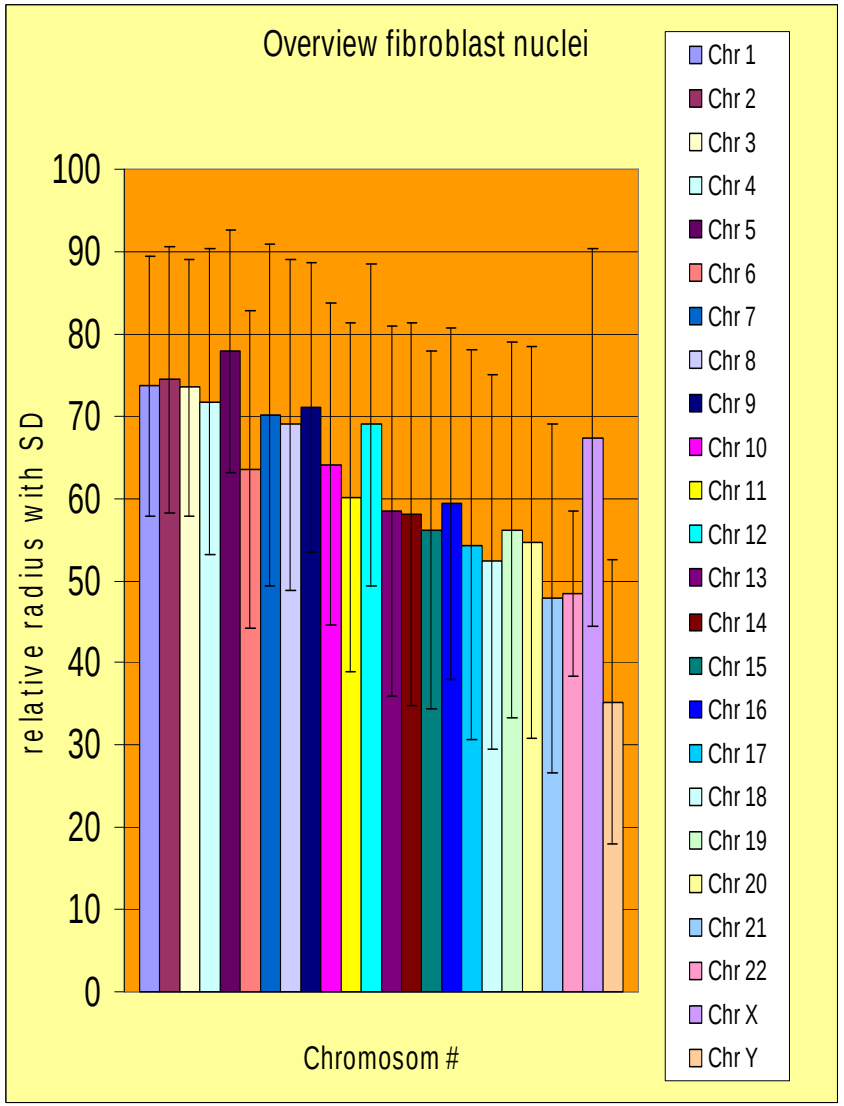

Comparison between human lymphocyte nuclei and computer models of spherical human nuclei

P.6: 1Mbp subdomains are connected by entropic like spring potentials

P.7: A 3D reconstruction of simulated territories applying the virtual microscopy method

P.8, 9: the comparison between lymphocytes and simulated nuclei fits for many territories, for #15 and #20 not.

Spherical 1-Mbp Chromatin Domain (SCD) model

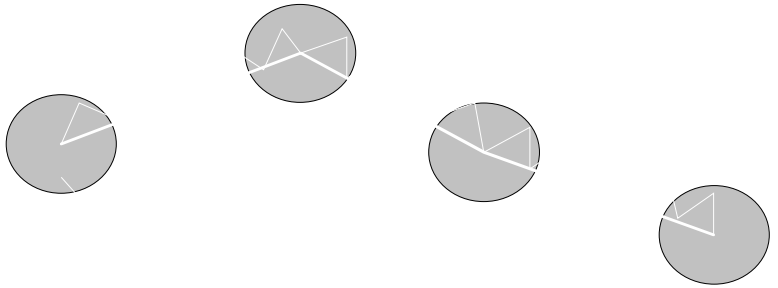

visualized: chromosome #1 territories

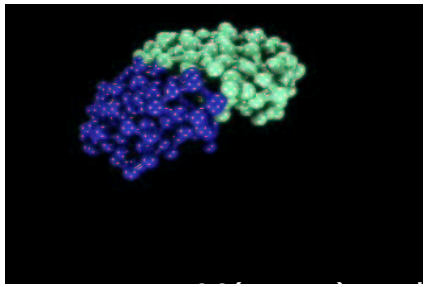

visualized: chromosome X (green) and Y (red)

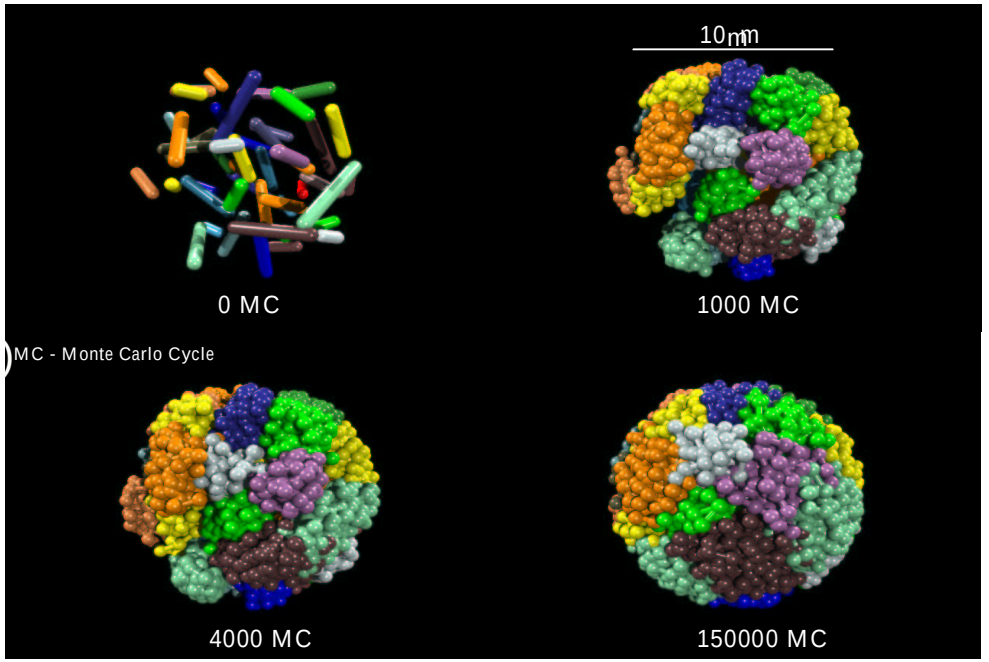

Simulated distribution of chromosome territories regarding the specific gene density of each chromosome

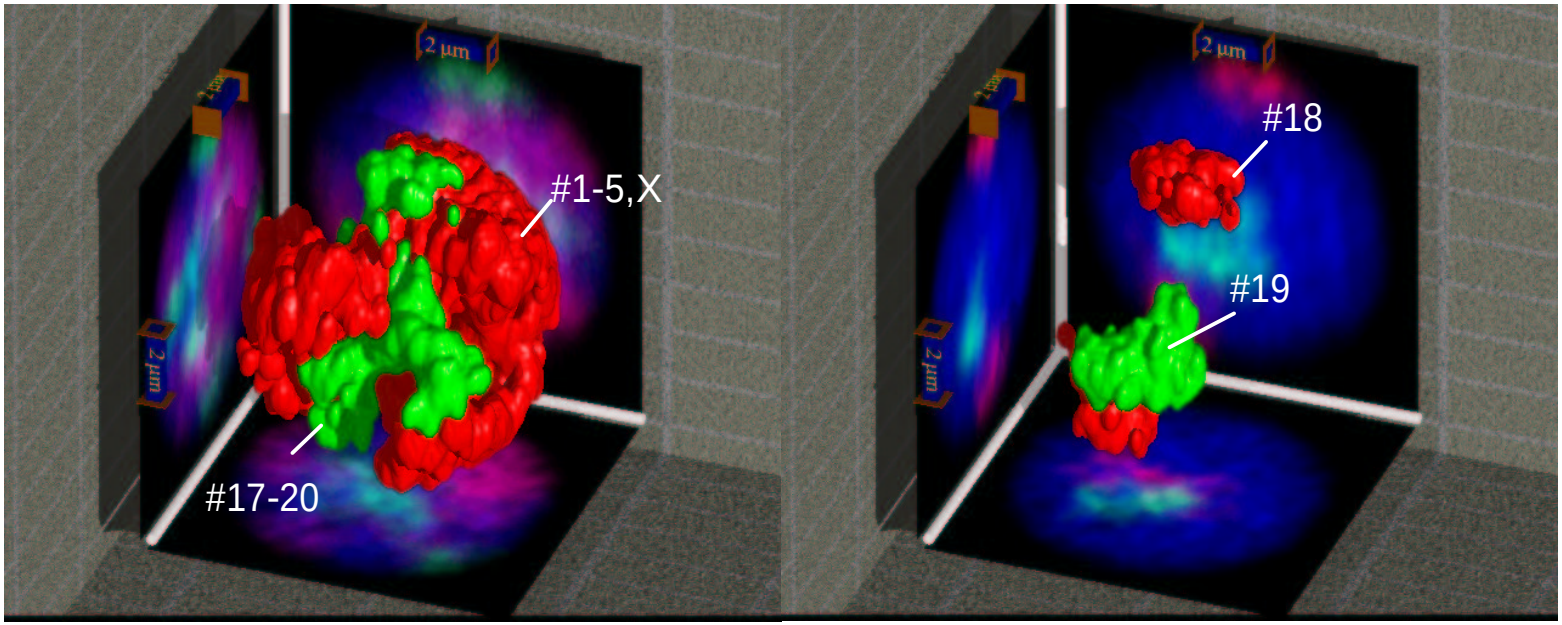

J. Finsterle, G. Kreth

Lymphocytes

Simulated spherical nuclei

Mapping of CT groups: comparison (#1,2,3,4,5,X) and (#17,18,19,20)

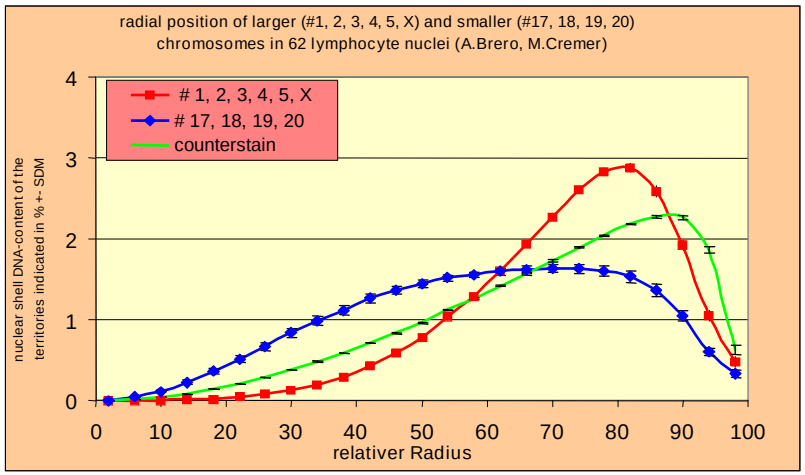

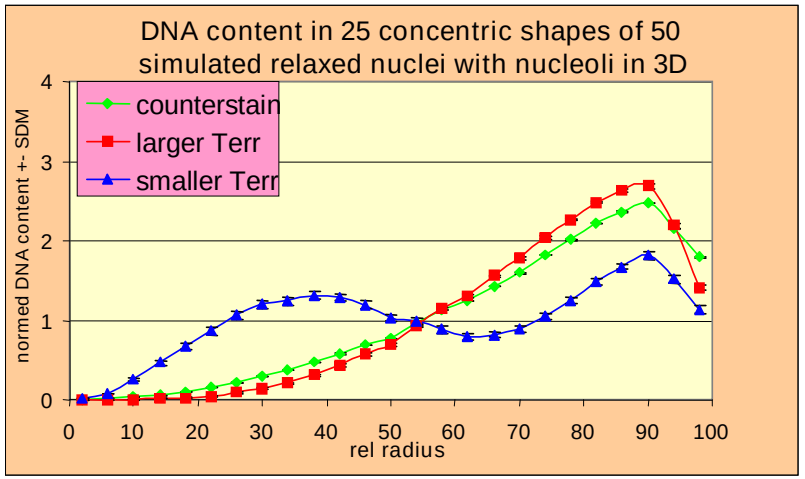

Mapping of CTs: comparison (#18) and (#19)

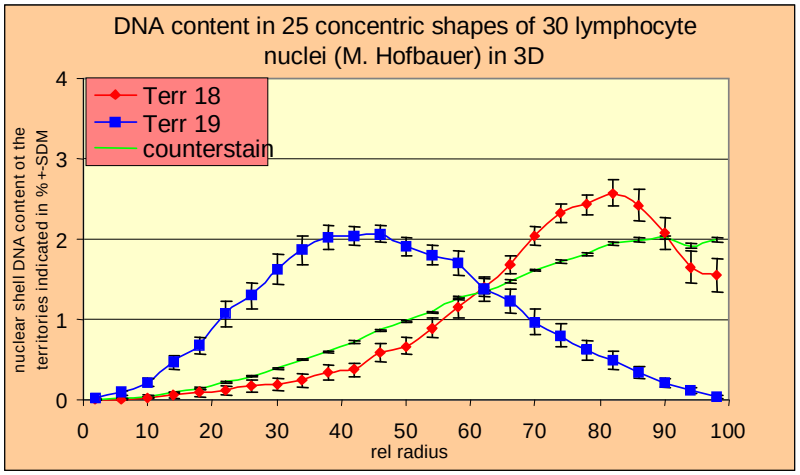

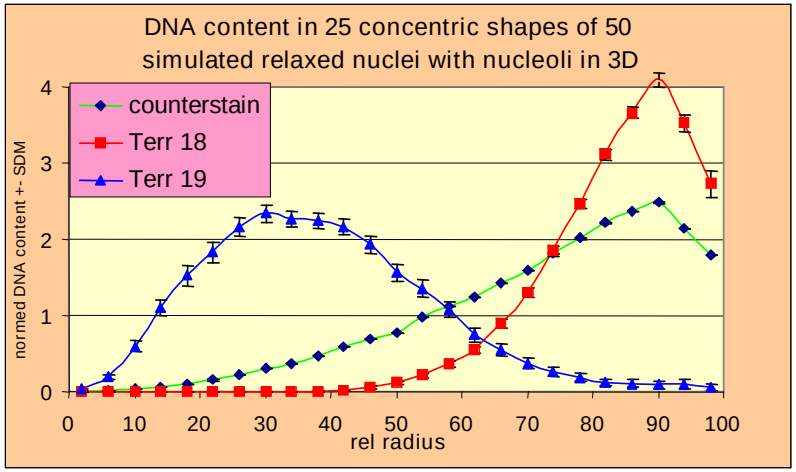

Lymphocytes

Spherical, simulated nuclei

Mapping of CTs: (#15)

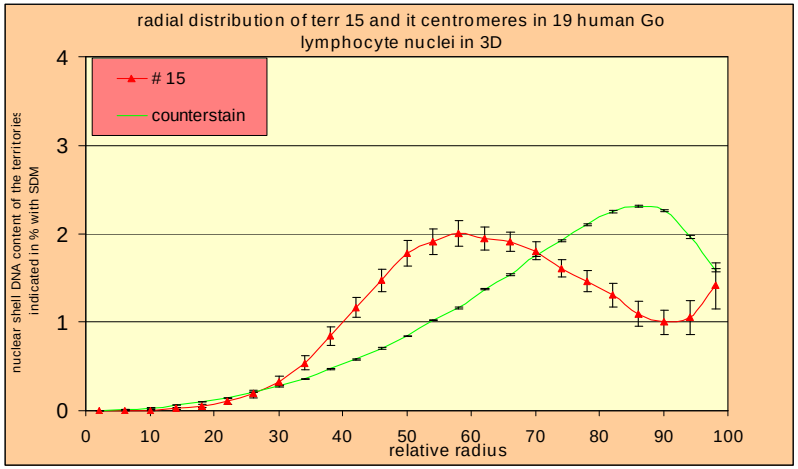

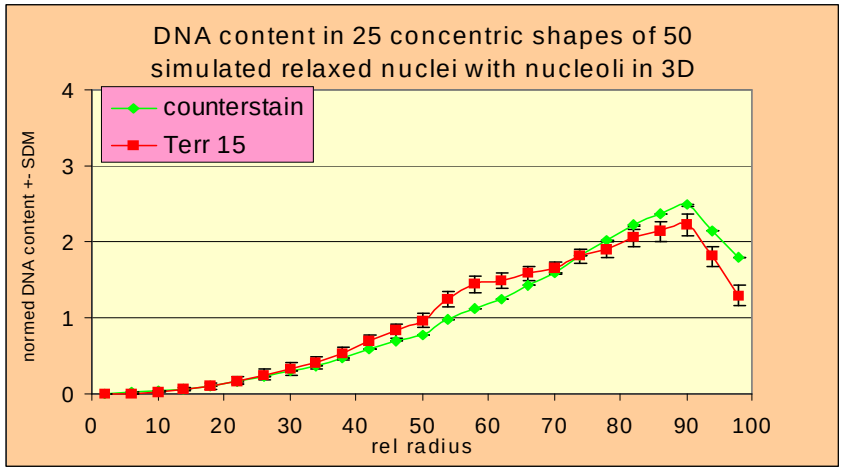

Mapping of CTs: (Y)

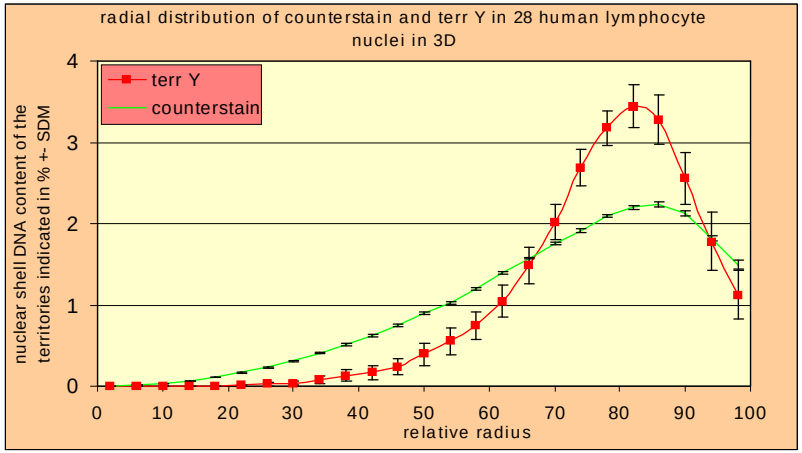

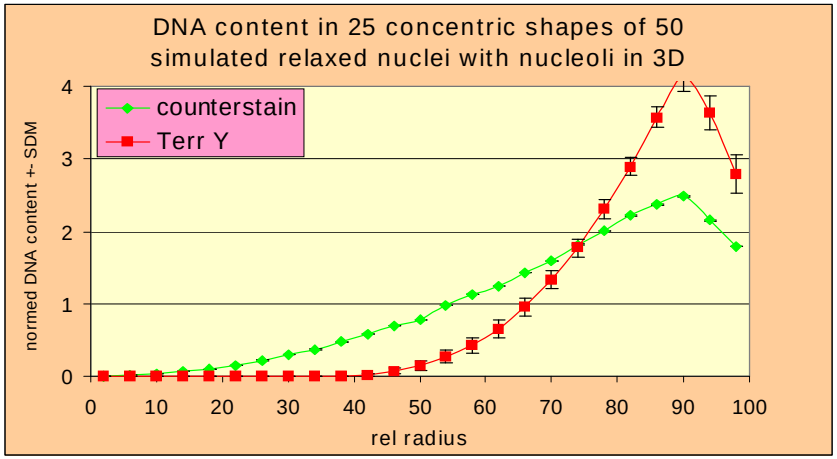

chromosomal position in cancer cells

P.11: cancer cells in comparison. In Hela cells a translocation or a trisomie could be found, in the case of DLD-1 no translocations were observed

P.12-14: different cancer species show different distribution graphs. The most common anomality was that of Chr #18 which was not always located clearly at the periphery.

Hela

DLD-1

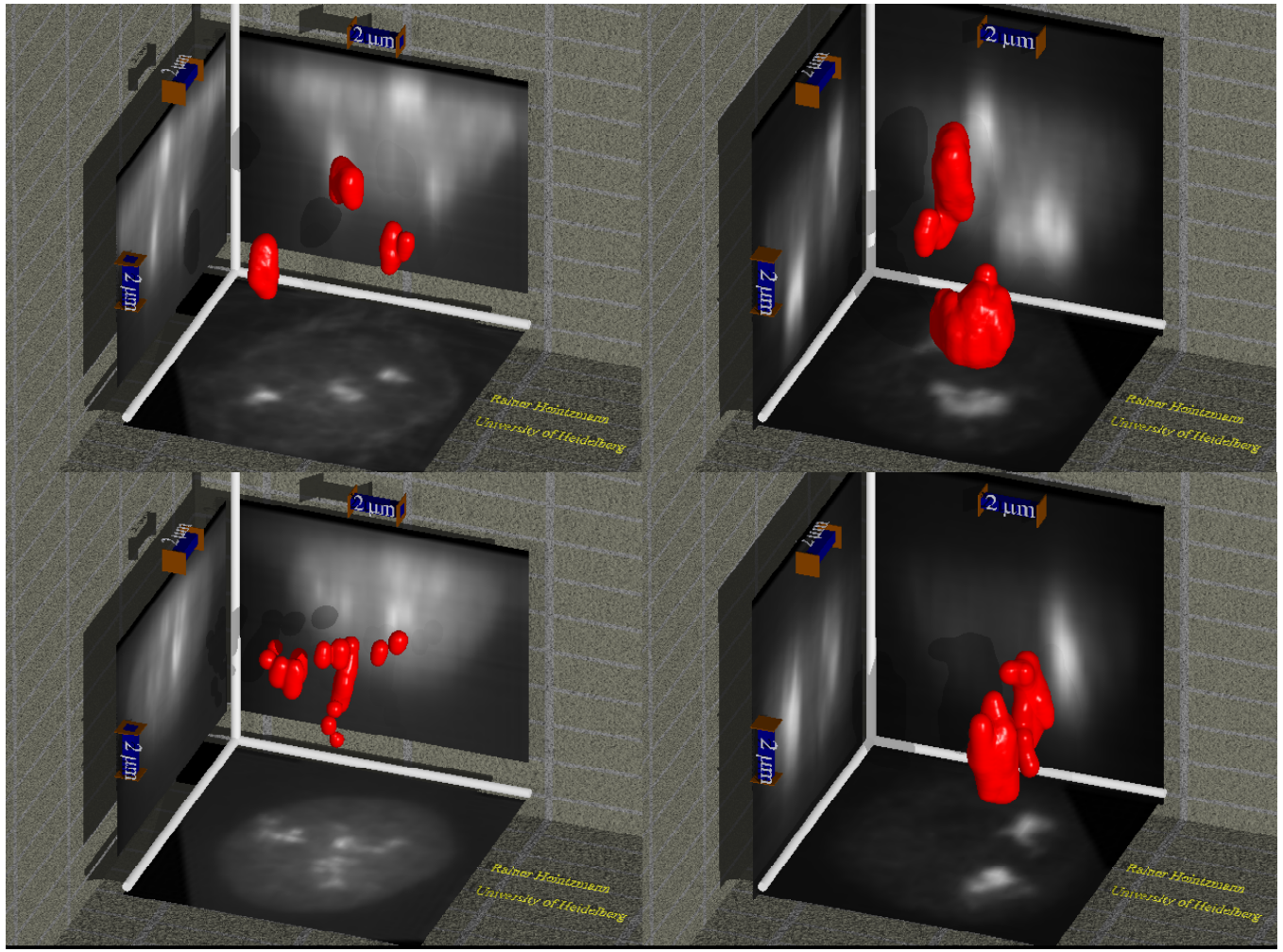

Chr #18

Chr #19

Territorial position in cancer cells I, in 3D

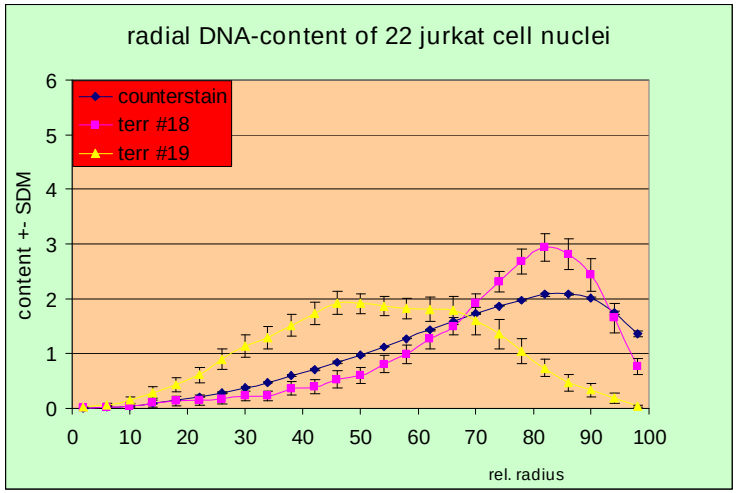

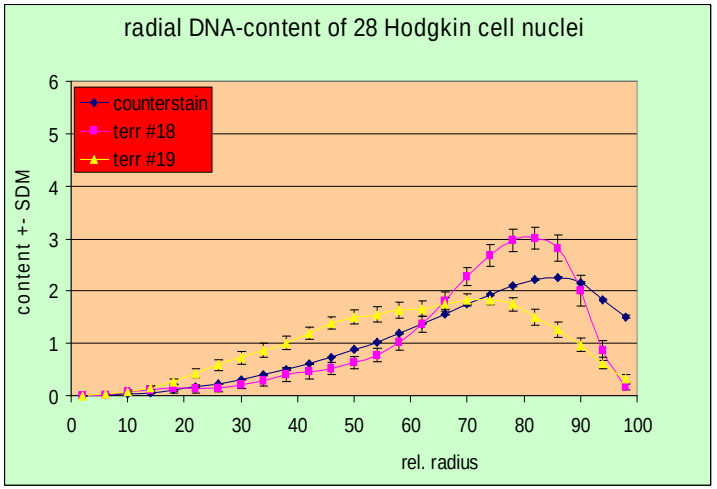

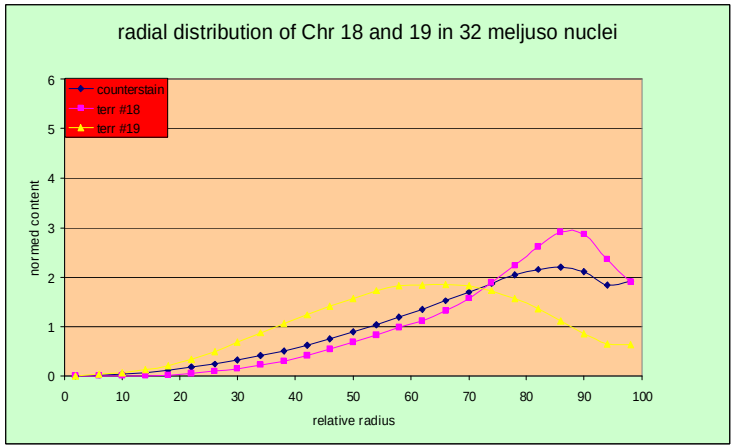

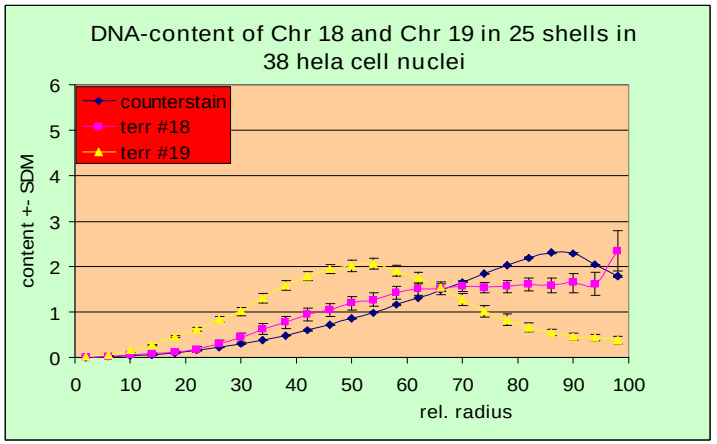

Territorial position in cancer cells II, most in 3D

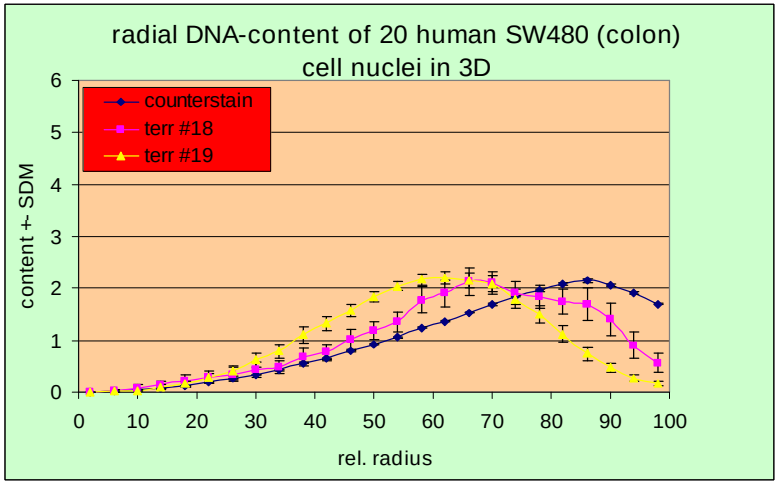

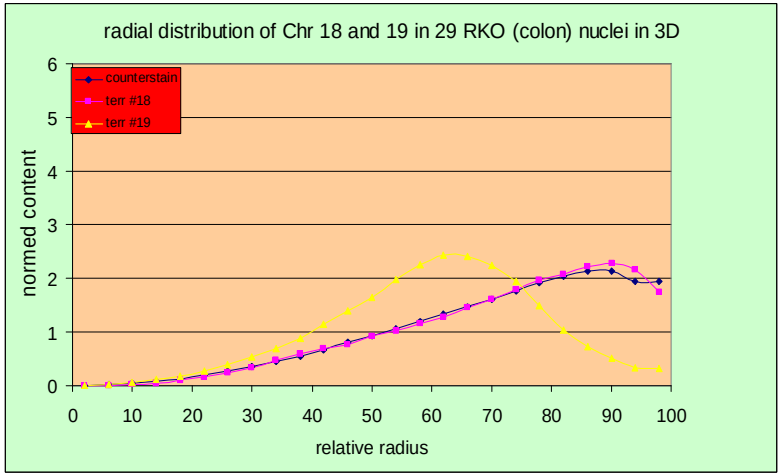

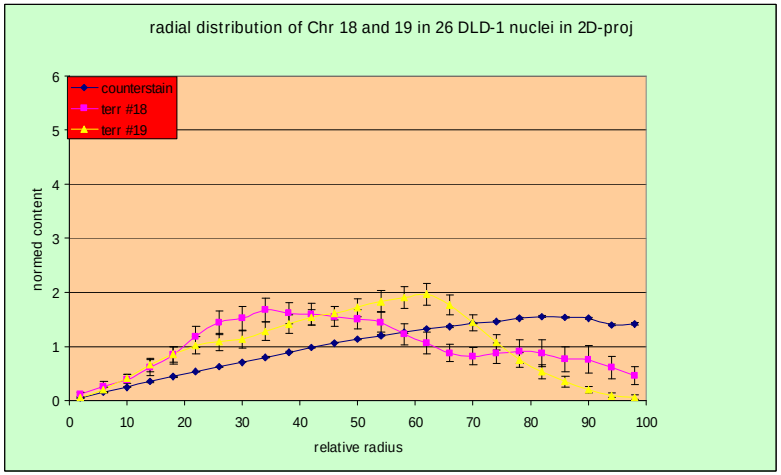

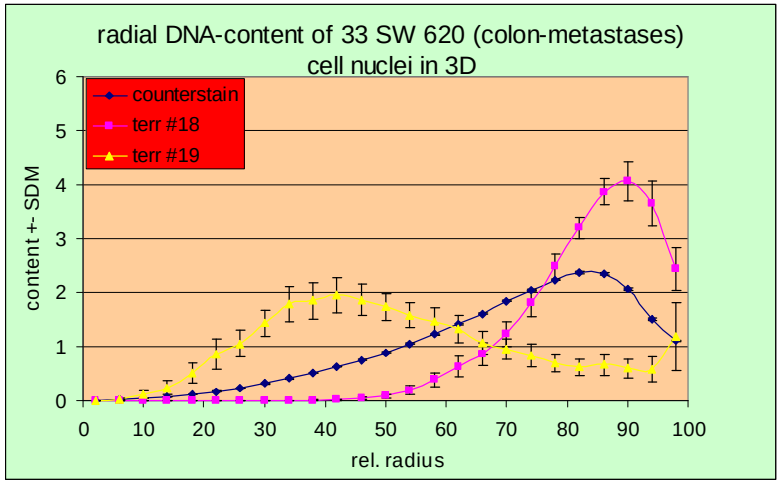

Territorial position in cancer cells III in 3D

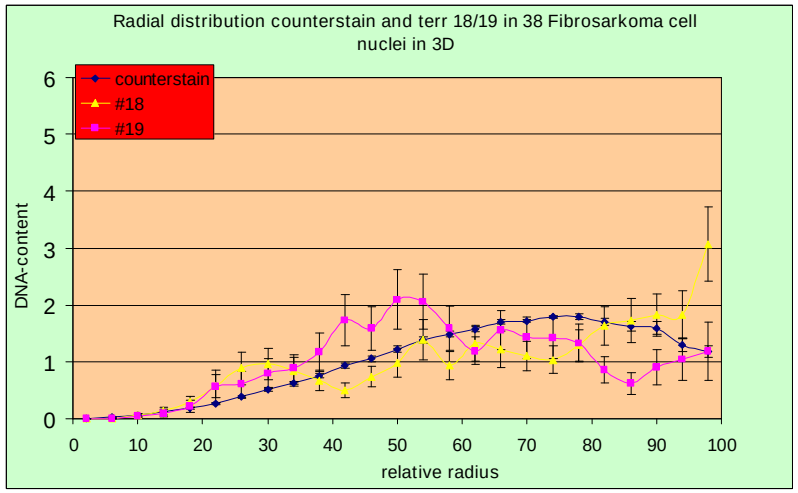

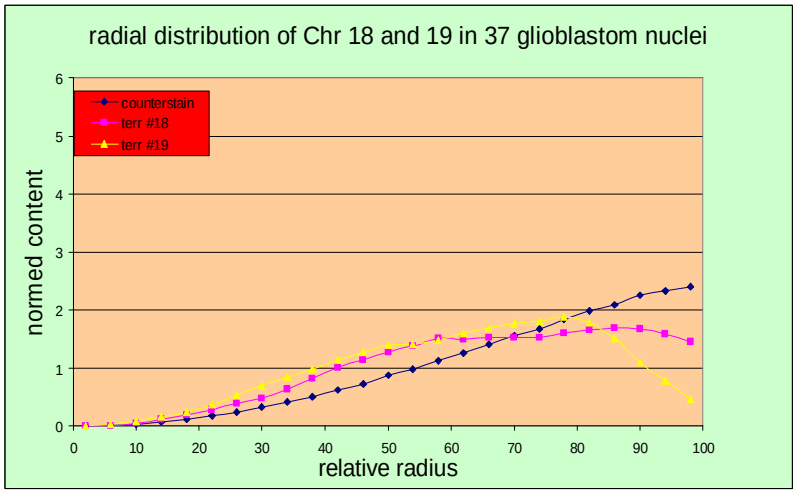

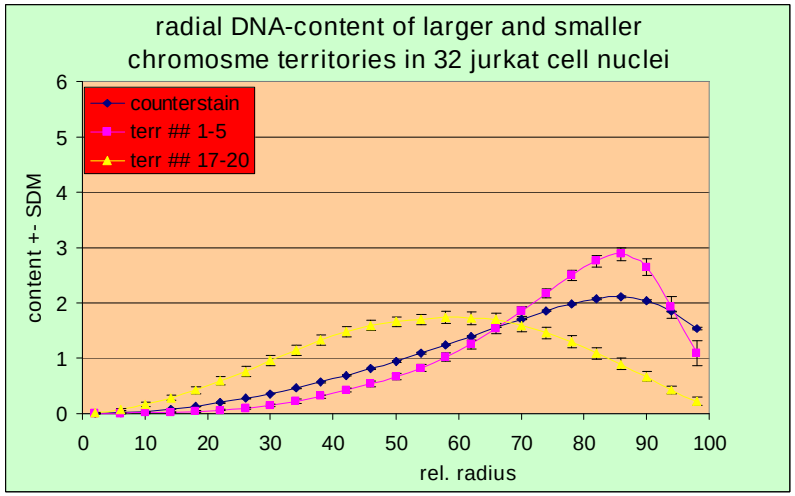

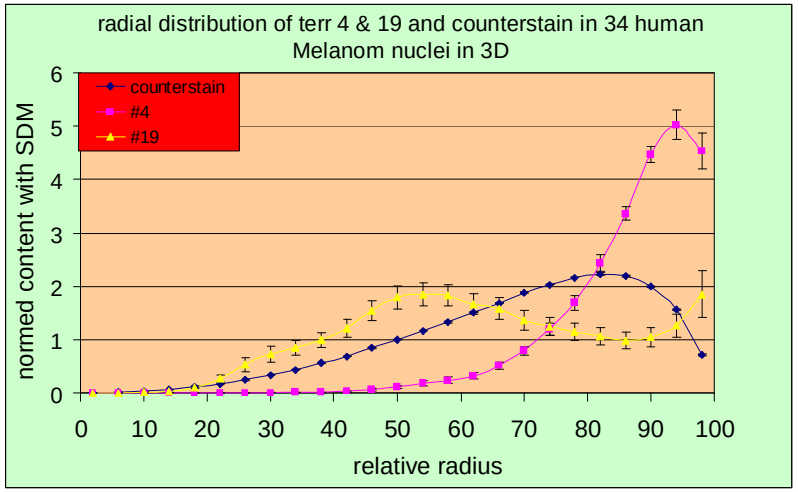

The centromere as chromosomal subregion and its position in lymphocyte nuclei

P.16, 17: The distribution of centromeres is always peripheral, independent from the position of the residual territory.

P.18, 19: The pictures show that except of territory X the centromere region is always at the periphery of the territory. The colors green and blue belong to the same color channel.

Centromeres I

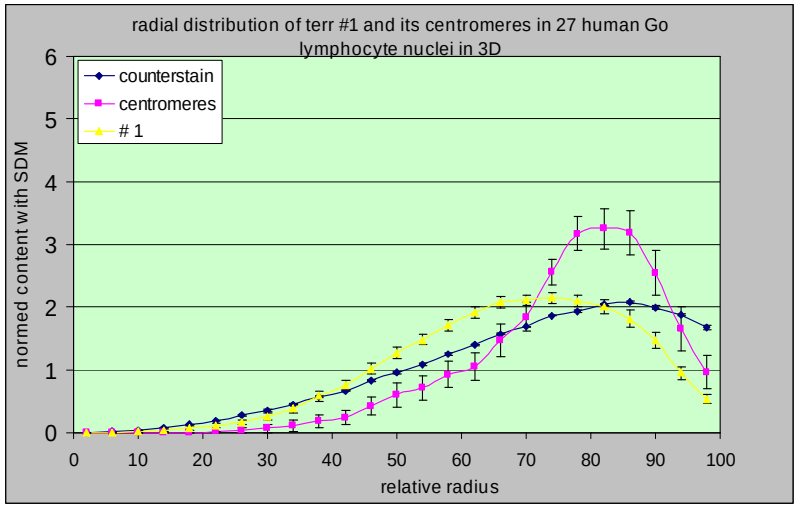

CTs #1

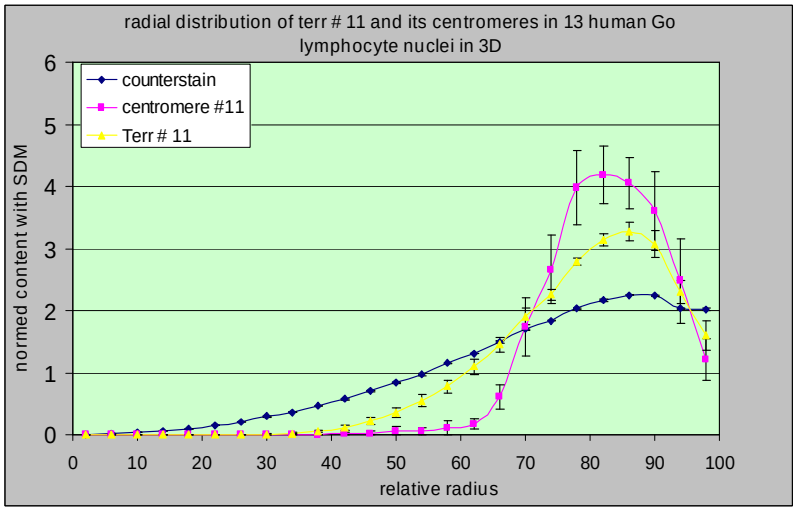

CTs #11

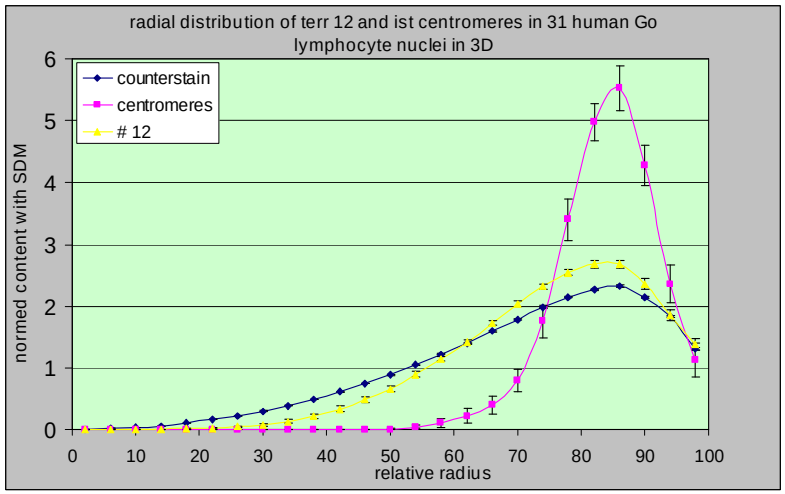

CTs #12

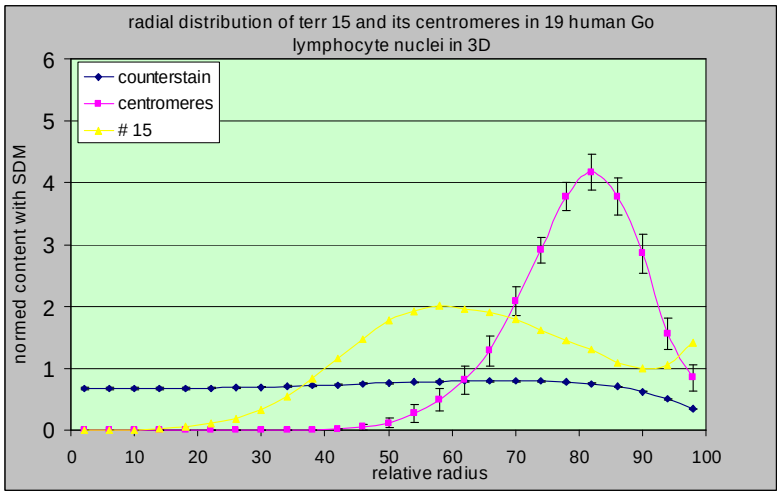

CTs #15

Centromeres II

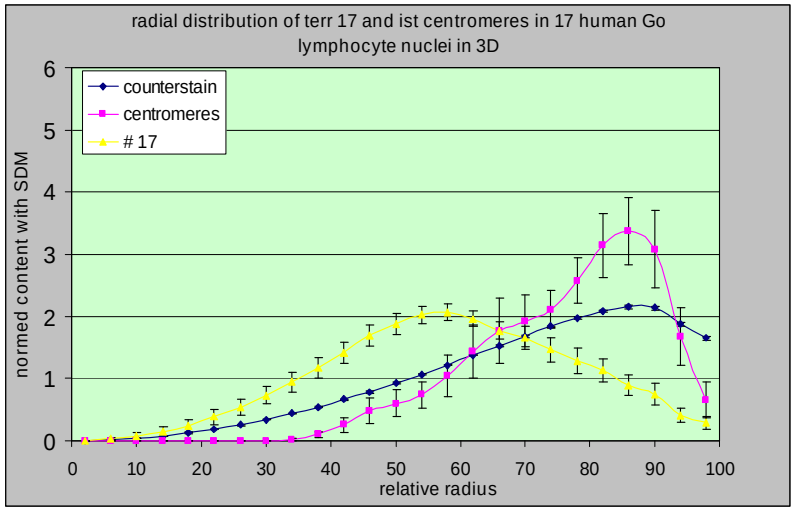

CTs #17

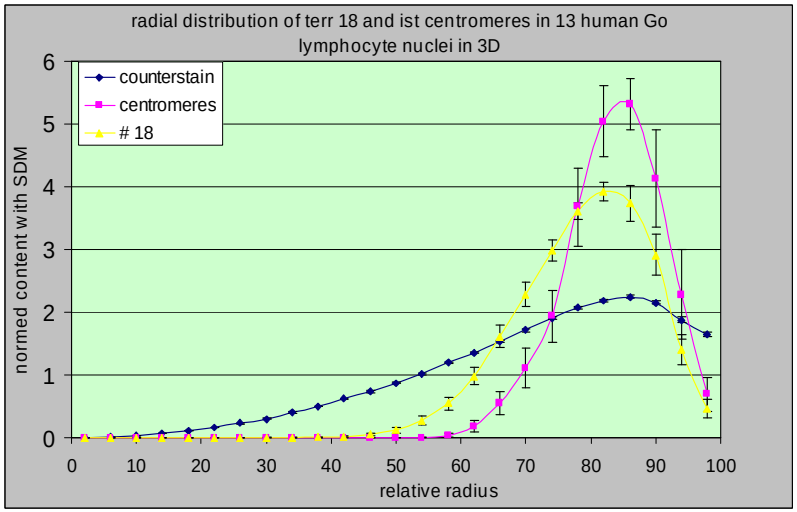

CTs #18

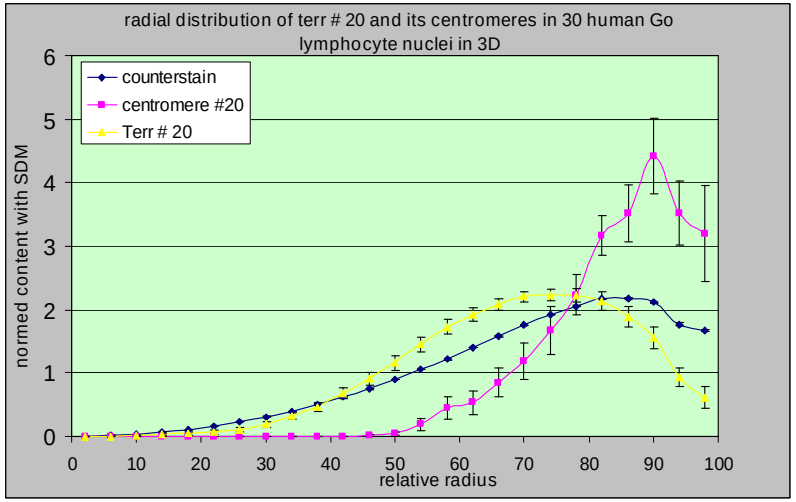

CTs #20

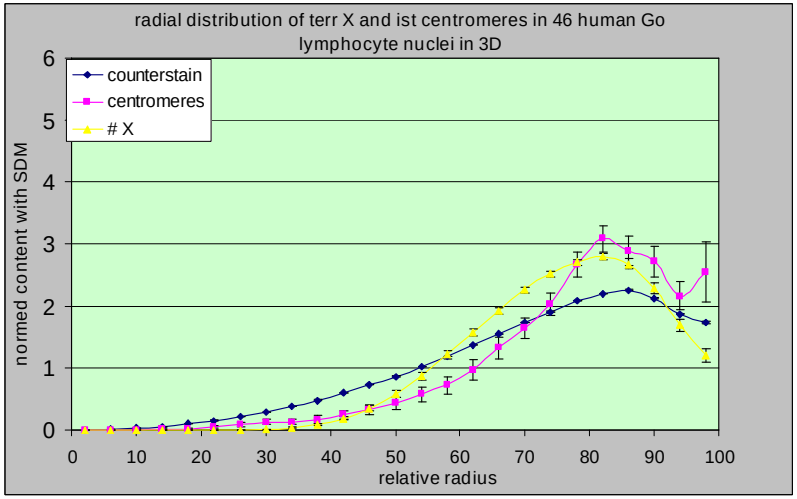

CTs #X

CTs and centromeres I

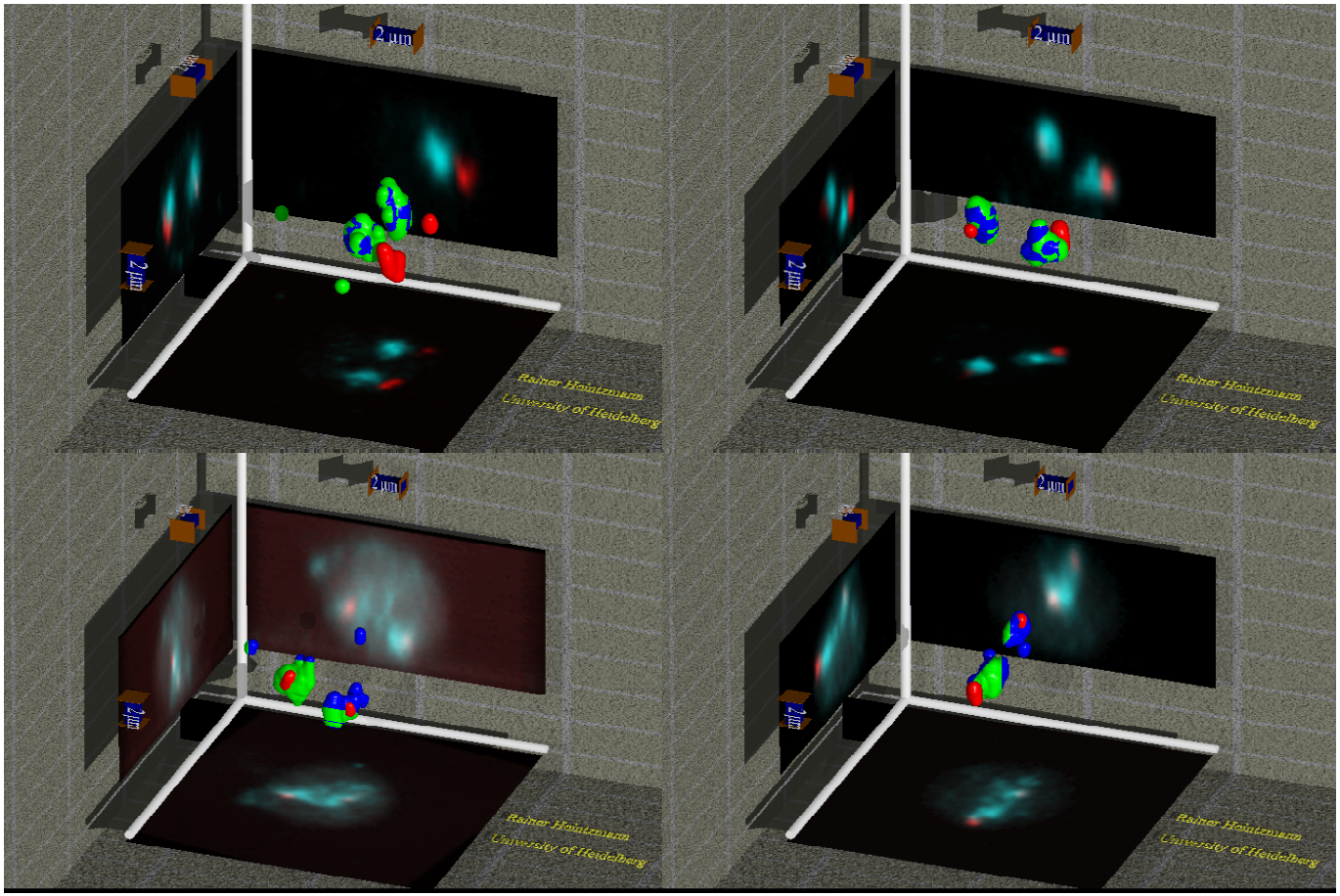

CTs #15

CTs #17

red: Centromere,

green and blue: CT

CTs and centromeres II

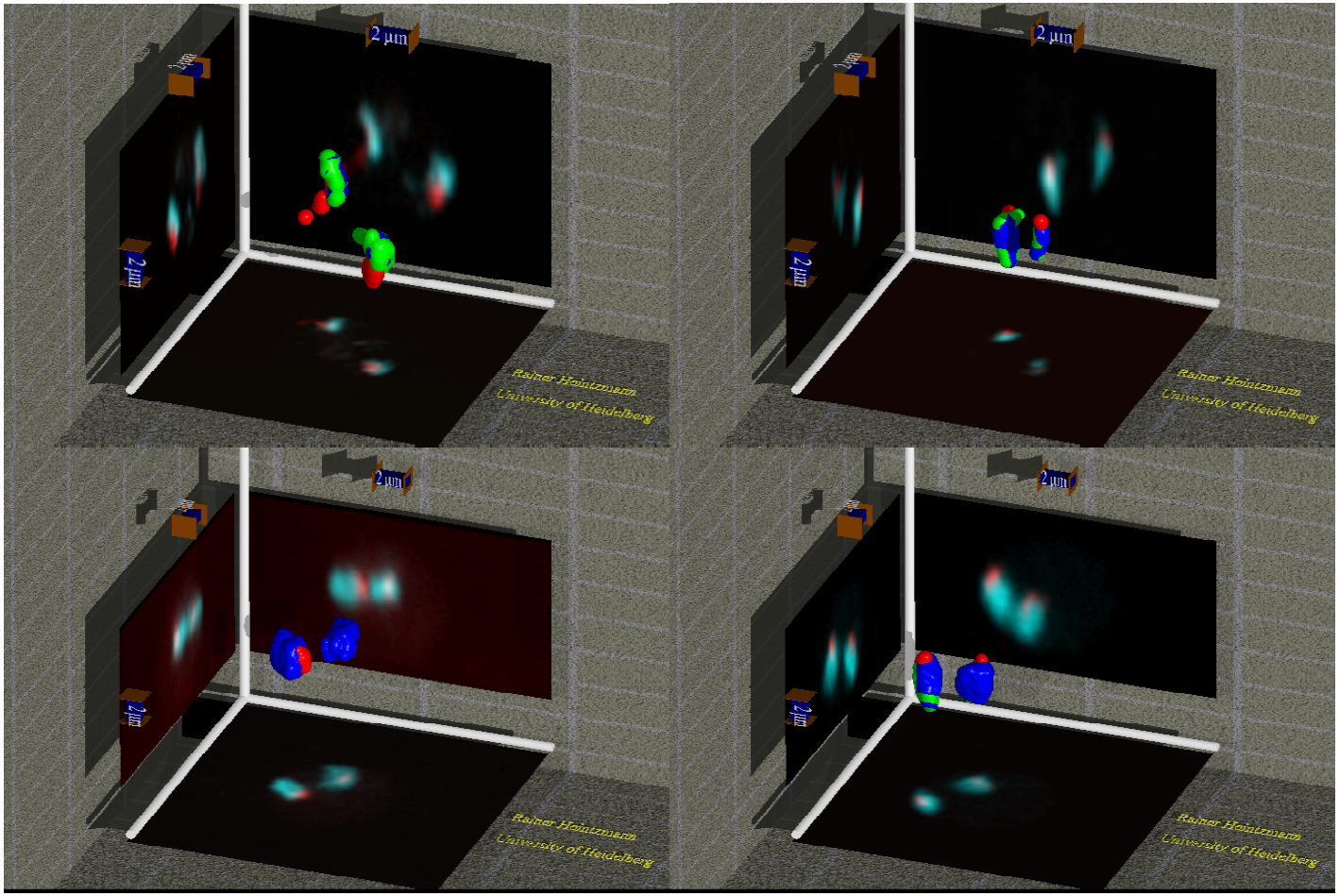

CTs #18

CTs #X

red: Centromere,

green and blue: CT

P.21, 22: the graphs show all distances that occur
between the centromeres and the territory center:
between the centers of territories („territories“),
between the centromeres („centromeres“), and
between the centromeres and territorial centers
(„mixed“). Of special interest is the left maximum at
about 0 to 3 µm distances: It represents the centromer
and territorial center distance of the same territory.
(see Fig II.5.5)

Distances centromere - CT I

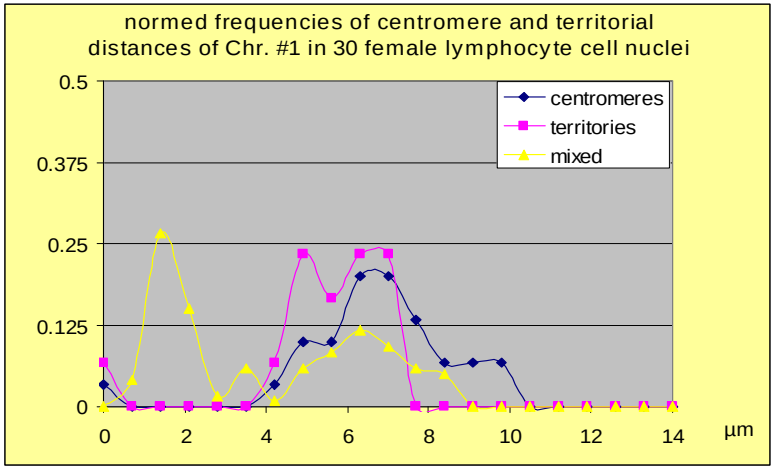

CTs #1

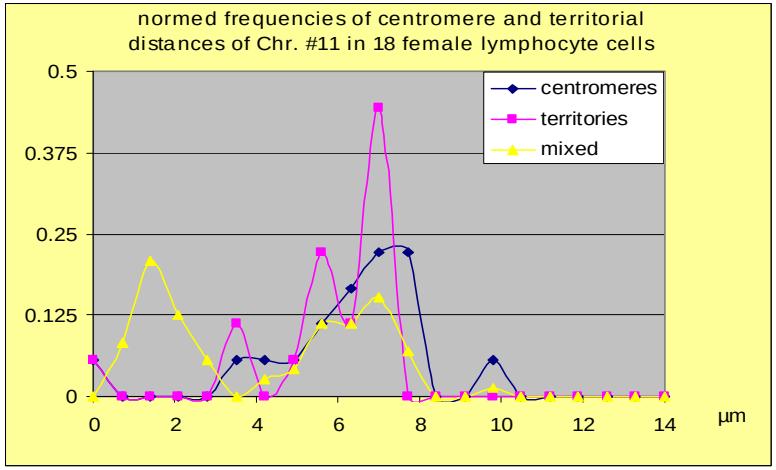

CTs #11

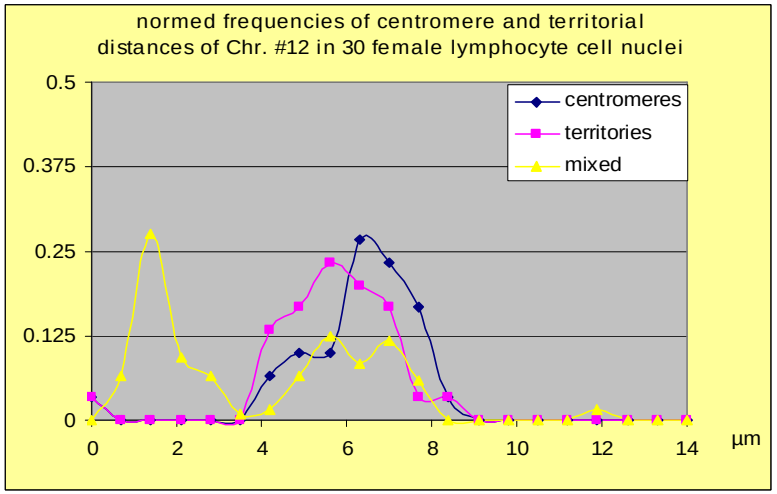

CTs #12

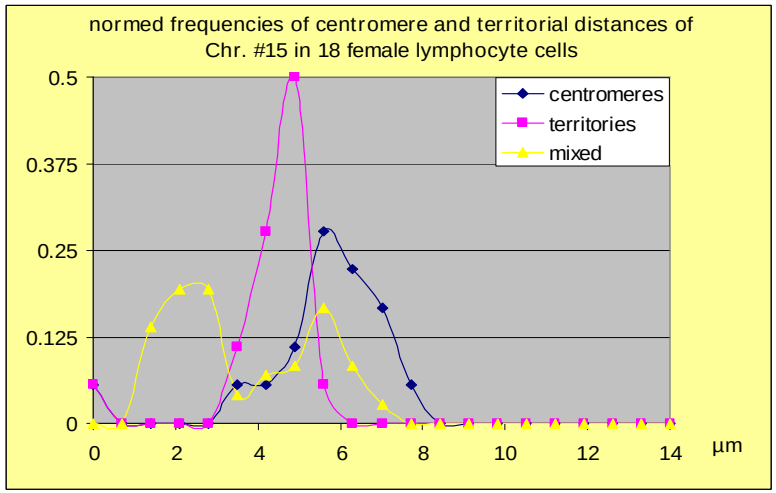

CTs #15

Distances centromere - CT II

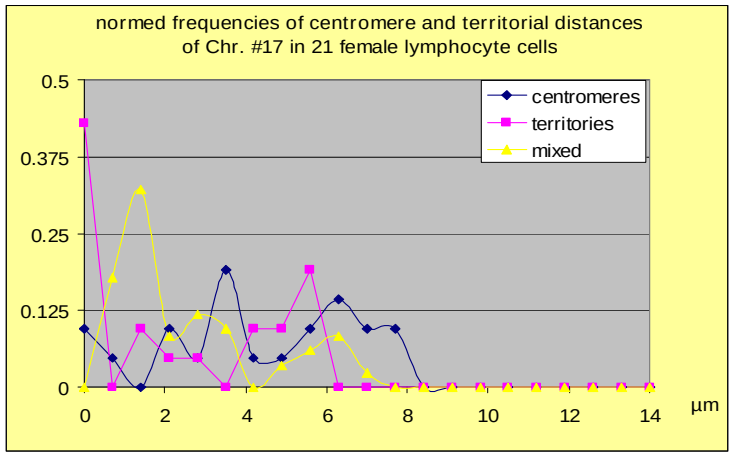

CTs #17

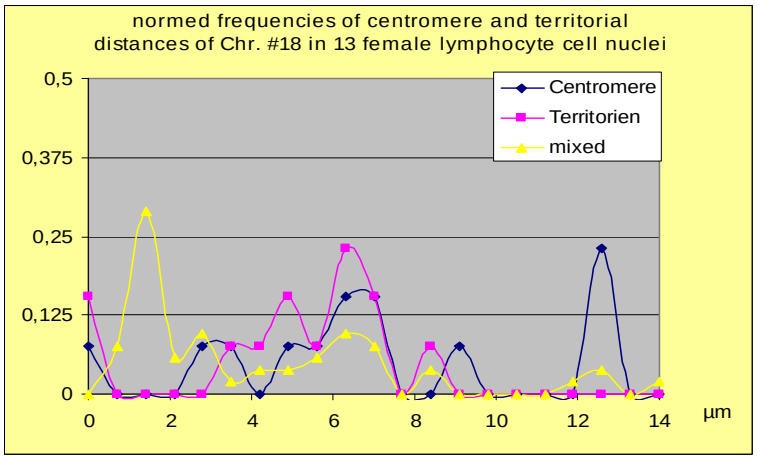

CTs #18

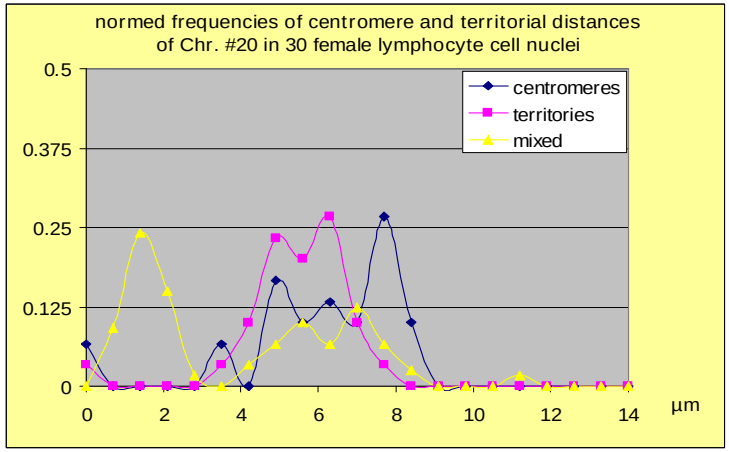

CTs #20

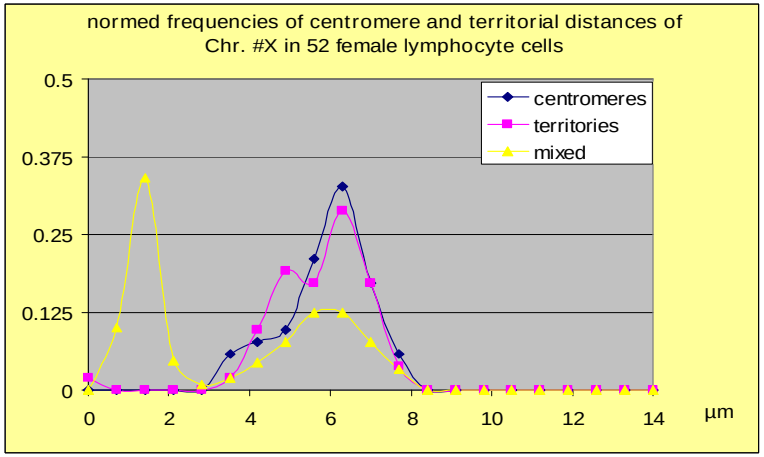

CTs #X

Kinetochore distribution in lymphocytes during the cell-cycle

P.24: all kinetochores can be seen as single spots during the G1 -phase.

P.25: nearly all kinetochores appear doubled and elongated in the G2 phase.

P.26, 27: the graphs show in the G0 phase a clear peripheral position of kinetochores. In the other phases also in the center of the nucleus some kinetochores are located. Maybe they are attached at the nucleolus.

Kinetochores of lymphocytes in G1

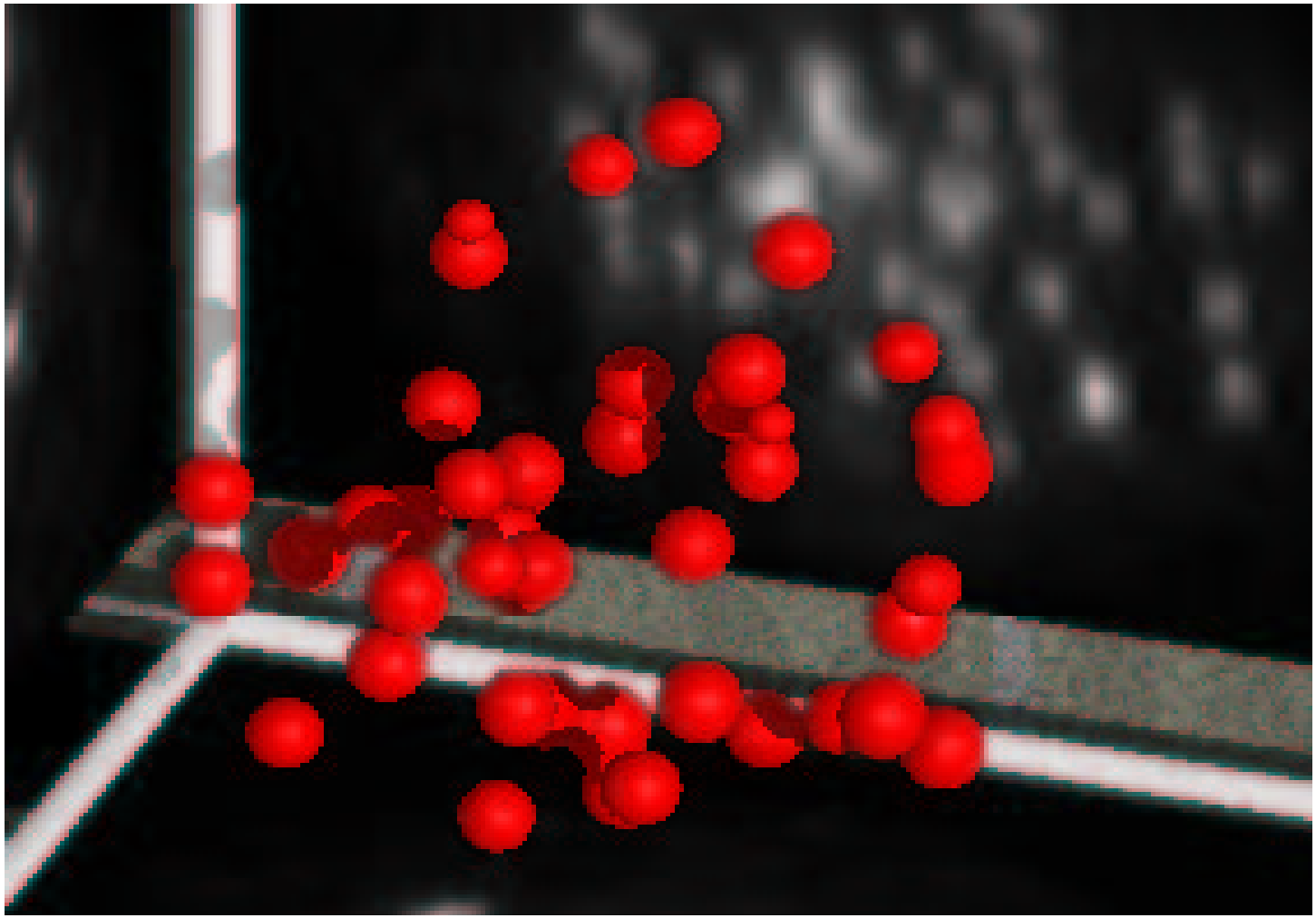

Kinetochores in lymphocytes in G2

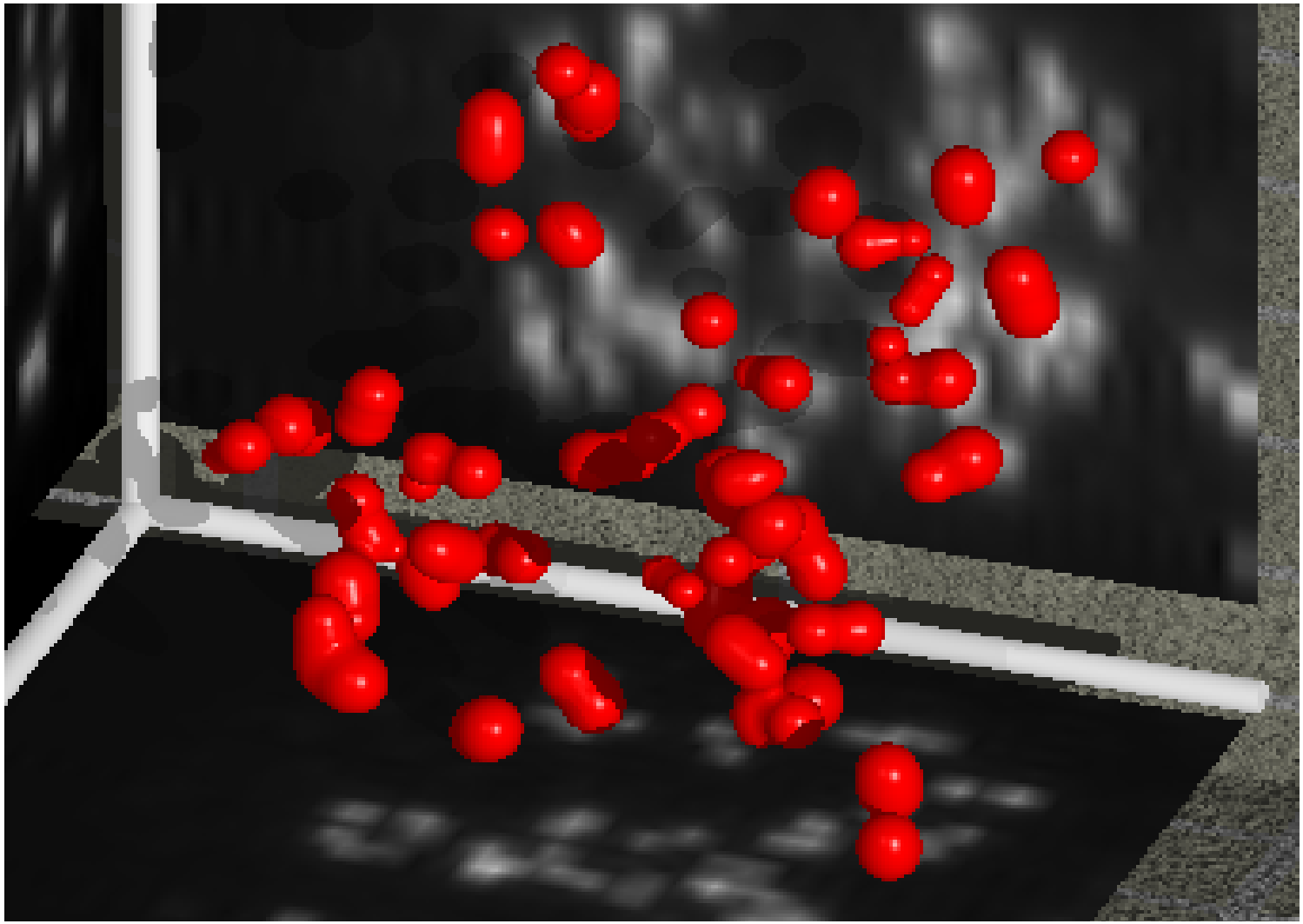

Graphs of kinetochores I

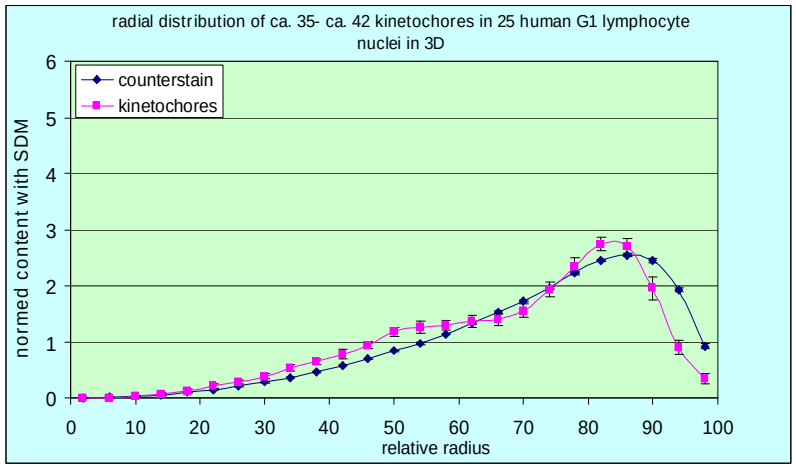

G1-Phase

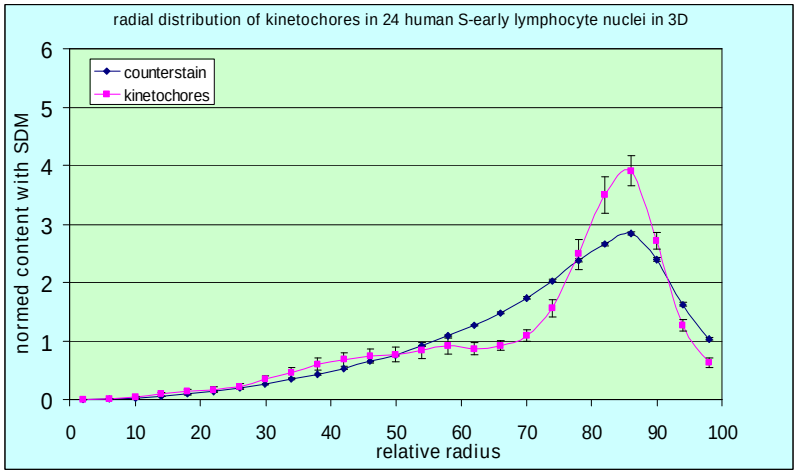

early S

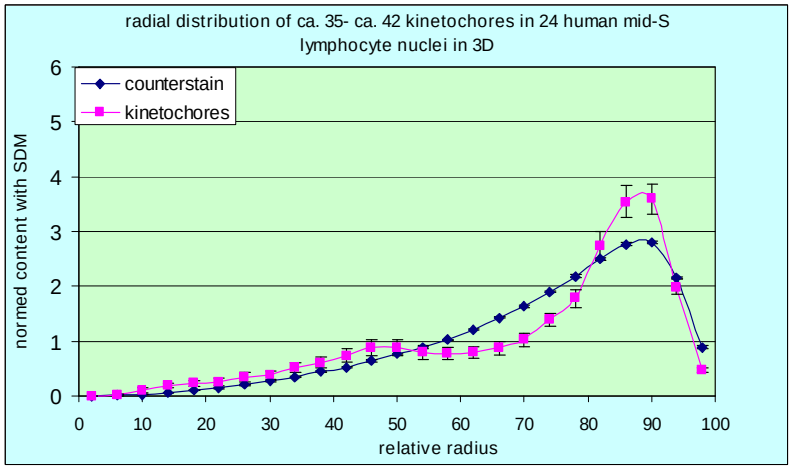

mid S

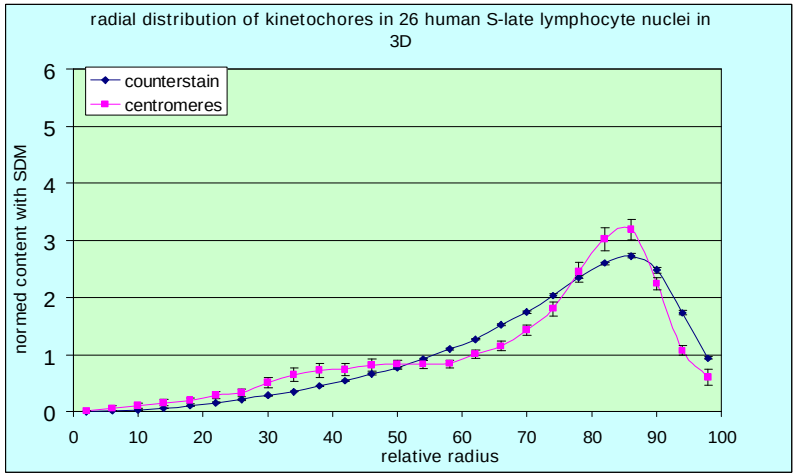

late S

Graphs of kinetochores II

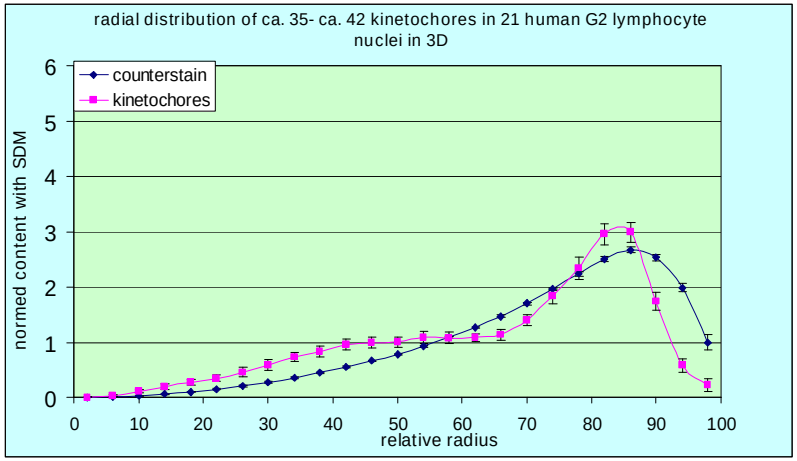

G2

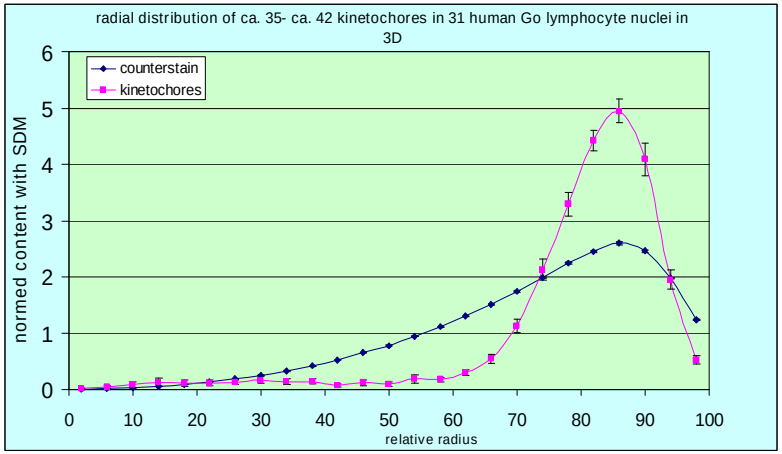

G0

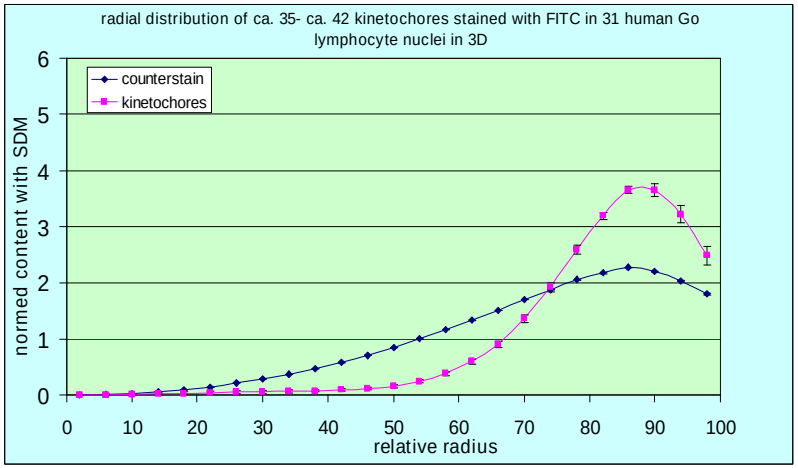

G0-Fitc

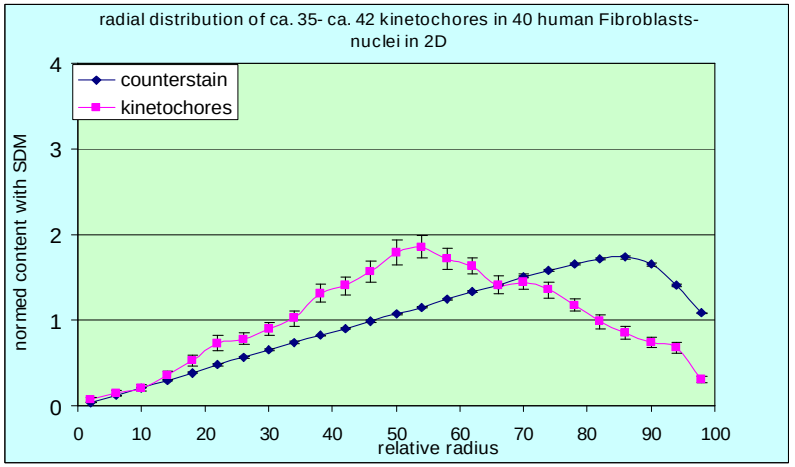

G0 in fibroblasts